8-2020

Volume I. Introduction to DUNE

B. Abi

R. Acciarri

M.A. Acero

G. Adamov

D. Adams

See next page for additional authors

Authors

B. Abi, R. Acciarri, M.A. Acero, G. Adamov, D. Adams, M. Adinolfi, Z. Ahmad, J. Ahmed, T. Alion, S. Alonso Monsalve, C. Alt, J. Anderson, C. Andreopoulos, M. Andrews, F. Andrianala, S. Andringa, A. Ankowski, M. Antonova, S. Antusch, A. Aranda-Fernandez, A. Ariga, L.O. Arnold, M.A. Arroyave, J. Asaadi, A. Aurisano, V. Aushev, D. Autiero, F. Azfar, H. Back, J.J. Back, C. Backhouse, P. Baesso, L. Bagby, R. Bajou, S. Balasubramanian, P. Baldi, B. Bambah, F. Barao, G. Barenboim, G. Barker, Wayne A. Barkhouse, C. Barnes, G. Barr, J. Barranco Monarca, N. Barros, J.L. Barrow, A. Bashyal, V. Basque, F. Bay, J. Bazo Alba, J.F. Beacom, E. Bechetoille, B. Behera, L. Bellantoni, G. Bellettini, V. Bellini, O. Beltramello, D. Belver, N. Benekos, F. Bento Neves, J. Berger, S. Berkman, P. Bernardini, R.M. Berner, H. Berns, S. Bertolucci, M. Betancourt, Y. Bezawada, M. Bhattacharjee, B. Bhuyan, S. Biagi, J. Bian, M. Biassoni, K. Biery, B. Bilki, M. Bishai, A. Bitadze, A. Blake, B. Blanco Siffert, F. Blaszczyk, G. Blazey, E. Blucher, J. Boissevain, S. Bolognesi, T. Bolton, M. Bonesini, M. Bongrand, F. Bonini, A. Booth, C. Booth, S. Bordoni, A. Borkum, T. Boschi, N. Bostan, P. Bour, S. Boyd, D. Boyden, J. Bracinik, D. Braga, D. Brailsford, A. Brandt, J. Bremer, C. Brew, E. Brianne, S.J. Brice, C. Brizzolari, C. Bromberg, G. Brooijmans, J. Brooke, A. Bross, G. Brunetti, N. Buchanan, H. Budd, D. Caiulo, P. Calafiura, J. Calcutt, M. Calin, S. Calvez, E. Calvo, L. Camilleri, A. Caminata, M. Campanelli, D. Caratelli, G. Carini, B. Carlus, P. Carniti, I. Caro Terrazas, H. Carranza, A. Castillo, C. Castromonte, C. Cattadori, F. Cavalier, F. Cavanna, S. Centro, G. Cerati, A. Cervelli, A. Cervera Villanueva, M. Chalifour, C. Chang, E. Chardonnet, A. Chatterjee, S. Chattopadhyay, J. Chaves, H. Chen, M. Chen, Y. Chen, D. Cherdack, C. Chi, S. Childress, A. Chiriacescu, K. Cho, S. Choubey, A. Christensen, D. Christian, G. Christodoulou, E. Church, P. Clarke, T.E. Coan, A.G. Cocco, J. Coelho, E. Conley, J. Conrad, M. Convery, L. Corwin, P. Cotte, L. Cremaldi, L. Cremonesi, J.I. Crespo-Anad, E. Cristaldo, R. Cross, C. Cuesta, Y. Cui, D. Cussans, M. Dabrowski, H. Da Motta, L. Da Silva Peres, Q. David, G.S. Davies, S. Davini, J. Dawson, K. De, R.M. De Almeida, P. Debbins, I. De Bonis, M. Decowski, A. De Gouvea, P.C. De Holanda, I.L. De Icaza Astiz, A. Deisting, P. De Jong, A. Delbart, D. Delepine, M. Delgado, A. Dell'Acqua, P. De Lurgio, J.R. De Mello Neto, D.M. DeMuth, S. Dennis, C. Densham, G. Deptuch, A. De Roeck, V. De Romeri, J. De Vries, R. Dharmapalan, M. Dias, F. Diaz, J. Diaz, S. Di Domizio, L. Di Giulio, P. Ding, L. Di Noto, C. Distefano, R. Diurba, M. Diwan, Z. Djurcic, N. Dokania, M. Dolinski, L. Domine, D. Douglas, F. Drielsma, D. Duchesneau, K. Duffy, P. Dunne, T. Durkin, H. Duyang, O. Dvornikov, D. Dwyer, A. Dyshkant, M. Eads, D. Edmunds, J. Eisch, S. Emery, A. Ereditato, C. Escobar, L. Escudero Sanchez, J.J. Evans, E. Ewart, A.C. Ezeribe, K. Fahey, A. Falcone, C. Farnese, Y. Farzan, J. Felix, E. Fernandez-Martinez, P. Fernandez Menendez, F. Ferraro, L. Fields, A. Filkins, F. Filthaut, R.S. Fitzpatrick, W. Flanagan, B. Fleming, R. Flight, J. Fowler, W. Fox, J. Franc, K. Francis, D. Franco, J. Freeman, J. Freestone, J. Fried, A. Friedland, S. Fuess, I. Furic, A.P. Furmanski, A. Gago, H. Gallagher, A. Gallego-Ros, N. Gallice, V. Galymov, E. Gamberini, T. Gamble, R. Gandhi, R. Gandrajula, S. Gao, D. Garcia-Gamez, M.Á. Garc?eris, S. Gardiner, D. Gastler, G. Ge, B. Gelli, A. Gendotti, S. Gent, Z. Ghorbani-Moghaddam, D. Gibin, I. Gil-Botella, C. Girerd, A. Giri, D. Gnani, O. Gogota, M. Gold, S. Gollapinni, K. Gollwitzer, R.A. Gomes, L. Gomez Bermeo, L.S. Gomez Fajardo, F. Gonnella, J. Gonzalez-Cuevas, M.C. Goodman, O. Goodwin, S. Goswami, C. Gotti, E. Goudzovski, C. Grace, M. Graham, E. Gramellini, R. Gran, E. Granados, A. Grant, C. Grant, D. Gratieri, P. Green, S. Green, L. Greenler, M. Greenwood, J. Greer, C. Griffith, M. Groh, J. Grudzinski, K. Grzelak, W. Gu, V. Guarino, R. Guenette, A. Guglielmi, B. Guo, K. Guthikonda, R. Gutierrez, P. Guzowski, M.M. Guzzo, S. Gwon, A. Habig, A. Hackenburg, H. Hadavand, R. Haenni, A. Hahn, J. Haigh, J. Haiston, T. Hamernik, P. Hamilton, J. Han, K. Harder, D.A. Harris, J. Hartnell, T. Hasegawa, R. Hatcher, E. Hazen, A. Heavey, K.M. Heeger, K. Hennessy, S. Henry, M. Hernandez Morquecho, K. Herner, L. Hertel, A.S. Hesam, J. Hewes, A. Higuera Pichardo, T. Hill, S.J. Hillier, A. Himmel, J. Hoff, C. Hohl, A. Holin, E. Hoppe, G.A. Horton-Smith, M. Hostert, A. Hourlier, B. Howard, R. Howell, J. Huang, J. Huang, J. Hugon, G. Iles, A.M. Iliescu, R. Illingworth, A. Ioannisian, R. Itay, A. Izmaylov, E. James, B. Jargowsky, F. Jediny, C. Jesús-Valls, X. Ji, L. Jiang, S. Jiménez, A. Jipa, A. Joglekar, C. Johnson, R. Johnson, B. Jones, S. Jones, C. Jung, T. Junk, Y. Jwa, M. Kabirnezhad, A. Kaboth, I. Kadenko, F. Kamiya, G. Karagiorgi, A. Karcher, M. Karolak, Y. Karyotakis, S. Kasai, S.P. Kasetti, L. Kashur, N. Kazaryan, E. Kearns, P. Keener, K.J. Kelly, E. Kemp, W. Ketchum, S. Kettell, M. Khabibullin, A. Khotjantsev, A.

Khvedelidze, D. Kim, B. King, B. Kirby, M. Kirby, J. Klein, K. Koehler, L.W. Koerner, S. Kohn, P.P. Koller, M. Kordosky, T. Kosc, U. Kose, V. Kostelecky, K. Kothekar, F. Krennrich, I. Kreslo, Y. Kudenko, V. Kudryavtsev, S. Kulagin, J. Kumar, R. Kumar, C. Kuruppu, V. Kus, T. Kutter, A. Lambert, K. Lande, C.E. Lane, K. Lang, T. Langford, P. Lasorak, D. Last, C. Lastoria, A. Laundrie, A. Lawrence, I. Lazanu, R. LaZur, T. Le, J. Learned, P. LeBrun, G. Lehmann Miotto, R. Lehnert, M. Leigui de Oliveira, M. Leitner, M. Leyton, L. Li, S. Li, S. Li, T. Li, Y. Li, H. Liao, C. Lin, S. Lin, A. Lister, B.R. Littlejohn, J. Liu, S. Lockwitz, T. Loew, M. Lokajicek, I. Lomidze, K. Long, K. Loo, D. Lorca, T. Lord, J. LoSecco, W.C. Louis, K. Luk, X. Luo, N. Lurkin, T. Lux, V.P. Luzio, D. MacFarland, A. Machado, P. Machado, C. Macias, J. Macier, A. Maddalena, P. Madigan, S. Magill, K. Mahn, A. Maio, J.A. Maloney, G. Mandrioli, J.C. Maneira, L. Manenti, S. Manly, A. Mann, K. Manolopoulos, M. Manrique Plata, A. Marchionni, W. Marciano, D. Marfatia, C. Mariani, J. Maricic, F. Marinho, A.D. Marino, M. Marshak, C. Marshall, J. Marshall, J. Marteau, J. Martin-Albo, N. Martinez, D.A. Martinez Caicedo, S. Martynenko, K. Mason, A. Mastbaum, M. Masud, S. Matsuno, J. Matthews, C. Mauger, N. Mauri, K. Mavrokoridis, R. Mazza, A. Mazzacane, E. Mazzucato, E. McCluskey, N. McConkey, K.S. McFarland, C. McGrew, A. McNab, A. Mefodiev, P. Mehta, P. Melas, M. Mellinato, O. Mena, S. Menary, H. Mendez, A. Menegolli, G. Meng, M. Messier, W. Metcalf, M. Mewes, H. Meyer, T. Miao, G. Michna, T. Miedema, J. Migenda, R. Milincic, W. Miller, J. Mills, C. Milne, O. Mineev, O.G. Miranda, S. Miryala, C. Mishra, S. Mishra, A. Mislivec, D. Mladenov, I. Mocioiu, K. Moffat, N. Moggi, R. Mohanta, T.A. Mohayai, N. Mokhov, J.A. Molina, L. Molina Bueno, A. Montanari, C. Montanari, D. Montanari, L.M. Montano Zetina, J. Moon, M. Mooney, A. Moor, D. Moreno, B. Morgan, C. Morris, C. Mossey, E. Motuk, C.A. Moura, J. Mousseau, W. Mu, L. Mualem, J. Mueller, M. Muether, S. Mufson, F. Muheim, A. Muir, M. Mulhearn, H. Muramatsu, S. Murphy, J. Musser, J. Nachtman, S. Nagu, M. Nalbandyan, R. Nandakumar, D. Naples, S. Narita, D. Navas-Nicolas, N. Nayak, M. Nebot-Guinot, L. Necib, K. Negishi, J.K. Nelson, J. Nesbit, M. Nessi, D. Newbold, M. Newcomer, D. Newhart, R. Nichol, E. Niner, K. Nishimura, A. Norman, R. Northrop, P. Novella, J.A. Nowak, M. Oberling, A. Olivares Del Campo, A. Olivier, Y. Onel, Y. Onishchuk, J. Ott, L. Pagani, S. Pakvasa, O. Palamara, S. Palestini, J.M. Paley, M. Pallavicini, C. Palomares, E. Pantic, V. Paolone, V. Papadimitriou, R. Papaleo, A. Papanestis, S. Paramesvaran, S. Parke, Z. Parsa, M. Parvu, S. Pascoli, L. Pasqualini, J. Pasternak, J. Pater, C. Patrick, L. Patrizii, R.B. Patterson, S. Patton, T. Patzak, A. Paudel, B. Paulos, L. Paulucci, Z. Pavlovic, G. Pawloski, D. Payne, V. Pec, S.J. Peeters, Y. Penichot, E. Pennacchio, A. Penzo, O.L. Peres, J. Perry, D. Pershey, G. Pessina, G. Petrillo, C. Petta, R. Petti, F. Piastra, L. Pickering, F. Pietropaolo, J. Pillow, R. Plunkett, R. Poling, X. Pons, N. Poonthottathil, S. Pordes, M. Potekhin, R. Potenza, B.V. Potukuchi, J. Pozimski, M. Pozzato, S. Prakash, T. Prakash, S. Prince, G. Prior, D. Pugnere, K. Qi, X. Qian, J. Raaf, R. Raboanary, V. Radeka, J. Rademacker, B. Radics, A. Rafique, E. Raguzin, M. Rai, M. Rajaoalisoa, I. Rakhno, H. Rakotondramanana, L. Rakotondravohitra, Y. Ramachers, R. Rameika, M. Ramirez Delgado, B. Ramson, A. Rappoldi, G. Raselli, P. Ratoff, S. Ravat, H. Razafinime, J. Real, B. Rebel, D. Redondo, M. Reggiani-Guzzo, T. Rehak, J. Reichenbacher, S.D. Reitzner, A. Renshaw, S. Rescia, F. Resnati, A. Reynolds, G. Riccobene, L.C. Rice, K. Rielage, Y. Rigaut, D. Rivera, L. Rochester, M. Roda, P. Rodrigues, M. Rodriguez Alonso, J. Rodriguez Rondon, A. Roeth, H. Rogers, S. Rosauro-Alcaraz, M. Rossella, J. Rout, S. Roy, A. Rubbia, C. Rubbia, B. Russell, J. Russell, D. Ruterbories, R. Saakyan, S. Sacerdoti, T. Safford, N. Sahu, P. Sala, N. Samios, M. Sanchez, D.A. Sanders, D. Sankey, S. Santana, M. Santos-Maldonado, N. Saoulidou, P. Sapienza, C. Sarasty, I. Sarcevic, G. Savage, V. Savinov, A. Scaramelli, A. Scarff, A. Scarpelli, T. Schaffer, H. Schellman, P. Schlabach, D. Schmitz, K. Scholberg, A. Schukraft, E. Segreto, J. Sensenig, I. Seong, A. Sergi, F. Sergiampietri, D. Sgalaberna, M. Shaevitz, S. Shafaq, M. Shamma, H.R. Sharma, R. Sharma, T. Shaw, C. Shepherd-Themistocleous, S. Shin, D. Shooltz, R. Shrock, L. Simard, N. Simos, J. Sinclair, G. Sinev, J. Singh, J. Singh, V. Singh, R. Sipos, F. Sippach, G. Sirri, A. Sitraka, K. Siyeon, D. Smargianaki, A. Smith, A. Smith, E. Smith, P. Smith, J. Smolik, M. Smy, P. Snopok, M. Soares Nunes, H. Sobel, M. Soderberg, C.J. Solano Salinas, S. Söldner-Rembold, N. Solomey, V. Solovov, W.E. Sondheim, M. Sorel, J. Soto-Oton, A. Sousa, K. Soustruznik, F. Spagliardi, M. Spanu, J. Spitz, N.J. Spooner, K. Spurgeon, R. Staley, M. Stancari, L. Stanco, H. Steiner, J. Stewart, B. Stillwell, J. Stock, F. Stocker, T. Stokes, M. Strait, T. Strauss, S. Striganov, A. Stuart, D. Summers, A. Surdo, V. Susic, L. Suter, C. Sutera, R. Svoboda, B. Szczerbinska, A. Szelc, R. Talaga, H. Tanaka, B. Tapia Oregui, A. Tapper, S. Tariq, E. Tatar, R. Tayloe, A. Teklu, M. Tenti, K. Terao, C.A. Ternes, F.

Terranova, G. Testera, A. Thea, J.L. Thompson, C. Thorn, S. Timm, A. Tonazzo, M. Torti, M. Tortola, F. Tortorici, D. Totani, M. Toups, C. Touramanis, J. Trevor, W.H. Trzaska, Y.T. Tsai, Z. Tsamalaidze, K. Tsang, N. Tsverava, S. Tufanli, C. Tull, E. Tyley, M. Tzanov, M.A. Uchida, J. Urheim, T. Usher, M. Vagins, P. Vahle, G. Valdiviesso, E. Valencia, Z. Vallari, J.W. Valle, S. Vallecorsa, R. Van Berg, R.G. Van de Water, D. Vanegas Forero, F. Varanini, D. Vargas, G. Varner, J. Vasel, G. Vasseur, K. Vaziri, S. Ventura, A. Verdugo, S. Vergani, M.A. Vermeulen, M. Verzocchi, H. Vieira de Souza, C. Vignoli, C. Vilela, B. Viren, T. Vrba, T. Wachala, A.V. Waldron, M. Wallbank, H. Wang, J. Wang, Y. Wang, Y. Wang, K. Warburton, D. Warner, M. Wascko, D. Waters, A. Watson, P. Weatherly, A. Weber, M. Weber, H. Wei, A. Weinstein, D. Wenman, M. Wetstein, M.R. While, A. White, L.H. Whitehead, D. Whittington, M.J. Wilking, C. Wilkinson, Z. Williams, F. Wilson, R.J. Wilson, J. Wolcott, T. Wongjirad, K. Wood, L. Wood, E. Worcester, M. Worcester, C. Wret, W. Wu, W. Wu, Y. Xiao, G. Yang, T. Yang, N. Yershov, K. Yonehara, Tim Young, B. Yu, J. Yu, J. Zalesak, L. Zambelli, B. Zamorano, A. Zani, L. Zazueta, G. Zeller, J. Zennamo, K. Zeug, C. Zhang, M. Zhao, E. Zhivun, G. Zhu, E.D. Zimmerman, M. Zito, S. Zucchelli, J. Zuklin, V. Zutshi, and R. Zwaska

Journal of Instrumentation

Volume I. Introduction to DUNE

To cite this article: B. Abi *et al* 2020 *JINST* **15** T08008

JINST

Published by IOP Publishing for Sissa Medialab

Received: *April 10, 2020*
Accepted: *April 21, 2020*
Published: *August 27, 2020*

Deep Underground Neutrino Experiment (DUNE) Far detector technical design report

Volume I
Introduction to DUNE

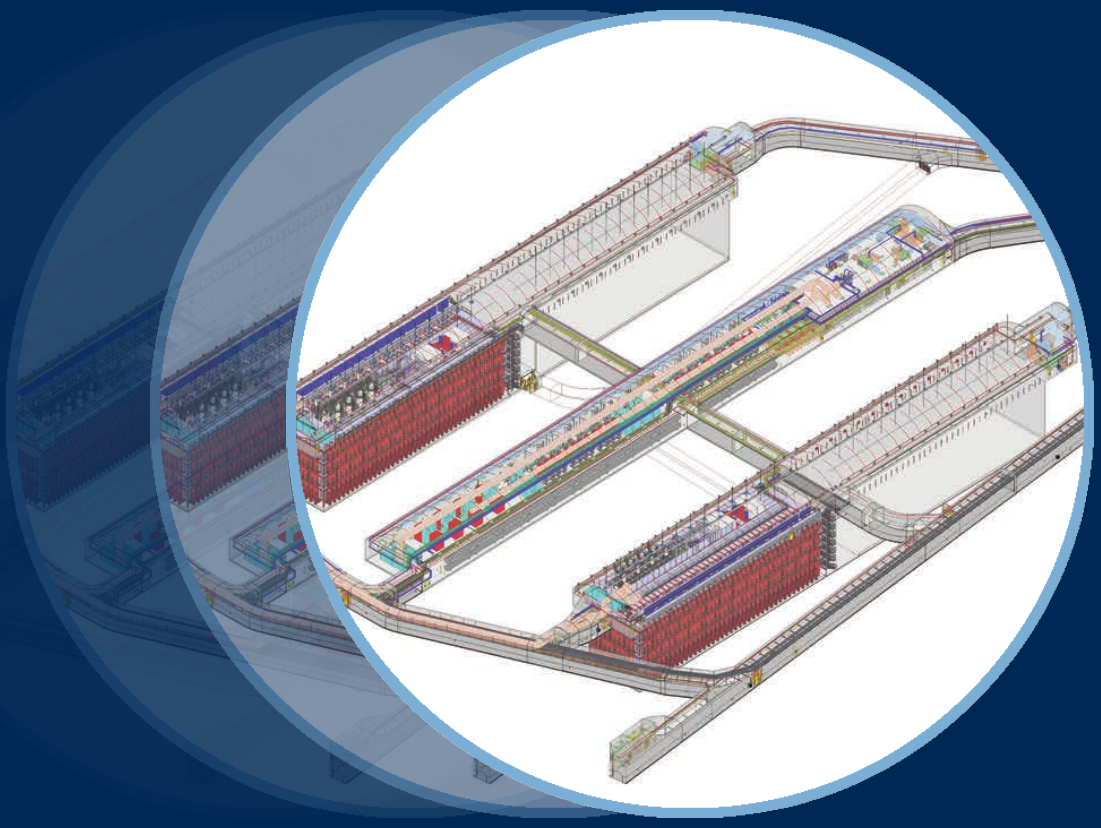

The DUNE collaboration

DEEP UNDERGROUND NEUTRINO EXPERIMENT

https://doi.org/10.1088/1748-0221/15/08/T08008

Contents

2020 JINST 15 T08008

2020 JINST 15 T08008

List of Figures

2020 JINST 15 T08008

2020 JINST 15 T08008

List of Tables

A roadmap of the DUNE technical design report

The Deep Underground Neutrino Experiment (DUNE) far detector (FD) technical design report (TDR) describes the proposed physics program, detector designs, and management structures and procedures at the technical design stage.

The TDR is composed of five volumes, as follows:

- Volume I (Introduction to DUNE) provides an overview of all of DUNE for science policy professionals.
- Volume II (DUNE physics) describes the DUNE physics program.
- Volume III (DUNE far detector technical coordination) outlines DUNE management structures, methodologies, procedures, requirements, and risks.
- Volume IV (The DUNE far detector single-phase technology) and Volume V (The DUNE Far Detector Dual-Phase Technology) describe the two FD liquid argon time-projection chamber (LArTPC) technologies.

The text includes terms that hyperlink to definitions in a volume-specific glossary. These terms appear underlined in some online browsers, if enabled in the browser's settings.

2020 JINST 15 T08008

Chapter 1

Executive summary

1.1 Overview

1.1.1 The DUNE science program

The preponderance of matter over antimatter in the early universe, the dynamics of the supernova neutrino bursts (SNBs) that produced the heavy elements necessary for life, and whether protons eventually decay — these mysteries at the forefront of particle physics and astrophysics are key to understanding the early evolution of our universe, its current state, and its eventual fate. The DUNE is an international world-class experiment dedicated to addressing these questions.

Experiments carried out over the past half century have revealed that neutrinos are found in three states, or *flavors*, and can transform from one flavor into another. These results indicate that each neutrino flavor state is a mixture of three different nonzero mass states, and to date offer the most compelling evidence for physics beyond the standard model. In a single experiment, DUNE will enable a broad exploration of the three-flavor model of neutrino physics with unprecedented detail. Chief among its potential discoveries is that of matter-antimatter asymmetries (through the mechanism of charge-parity symmetry violation (CPV)) in neutrino flavor mixing — a step toward unraveling the mystery of matter generation in the early universe. Independently, determination of the unknown neutrino mass ordering and precise measurement of neutrino mixing parameters by DUNE may reveal new fundamental symmetries of nature.

Neutrinos emitted in the first few seconds of a core-collapse supernova carry with them the potential for great insight into the evolution of the universe. DUNE's capability to collect and analyze this high-statistics neutrino signal from a supernova within the Milky Way would provide a rare opportunity to peer inside a newly formed neutron star and potentially witness the birth of a black hole.

Grand unified theories (GUTs), which attempt to describe the unification of the known forces, predict rates for proton decay that cover a range directly accessible with the next generation of large underground detectors such as the DUNE far detector. The experiment's sensitivity to key proton decay channels will offer unique opportunities for the ground-breaking discovery of this phenomenon.

2020 JINST 15 T08008

1.1.2 The DUNE detectors and supporting facilities

To achieve its goals, the international DUNE experiment, hosted by the U.S. Department of Energy's Fermi National Accelerator Laboratory (Fermilab) in Illinois, comprises three central components: (1) a new, high-intensity neutrino source generated from a megawatt-class proton accelerator at Fermilab, (2) a massive FD situated 1.5 km underground at the Sanford Underground Research Facility (SURF) in South Dakota, and (3) a composite near detector (ND) installed just downstream of the neutrino source. Figure 1.1 illustrates the layout of these components. The far detector, the subject of this TDR, will be a modular LArTPC with a fiducial (sensitive) mass of 40 kt[1] (40 Gg) of liquid argon (LAr), a cryogenic liquid that must be kept at 88 K (−185°C). This detector will be able to uniquely reconstruct neutrino interactions with image-like precision and unprecedented resolution [1].

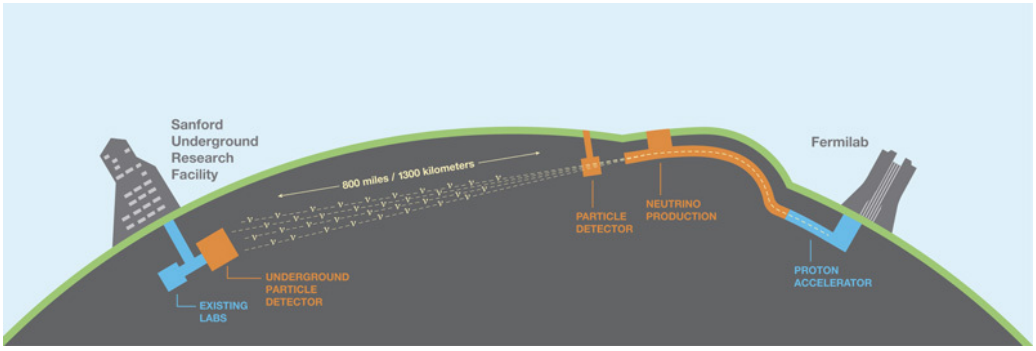

Figure 1.1. Cartoon illustrating the configuration of the LBNF beamline at Fermilab, in Illinois, and the DUNE detectors in Illinois and South Dakota, separated by 1300 km.

The Long-Baseline Neutrino Facility (LBNF) project, also hosted by Fermilab, provides the beamline and the civil construction, called conventional facilities (CF), for the DUNE experiment. The organization and management of LBNF is separate from that of the experiment; its design and construction are organized as a U.S. DOE/Fermilab project incorporating international partners.

The LBNF beamline at Fermilab will deliver the world's most intense neutrino beam to the near and far detectors in an on-axis configuration. The upgrade to the Proton Improvement Plan II (PIP-II) [2], a leading-edge, superconducting, linear proton accelerator under construction at Fermilab, will deliver between 1.0 and 1.2 MW of proton beam power from the Fermilab Main Injector to LBNF, which will aim and focus the beam, whereupon the protons, in a wide energy band of 60 GeV to 120 GeV, will collide with a high-power production target, creating a secondary beam from which the intense neutrino flux will emerge, traveling in the direction of the DUNE detectors (figure 1.2). A further planned upgrade of the accelerator complex could provide up to 2.4 MW of beam power by 2030, potentially extending the DUNE science reach. The upgrade will also increase the reliability of the Fermilab accelerator complex and provide the flexibility to produce customized beams tailored to specific scientific needs.

The intense, wide-band neutrino beam, the massive LArTPC detector at the far site, and the composite (i.e., multi-purpose) ND will provide a rich ancillary science program for the DUNE

[1]For comparison, this is nearly twice the mass of the Statue of Liberty and nearly four times that of the Eiffel Tower.

2020 JINST 15 T08008

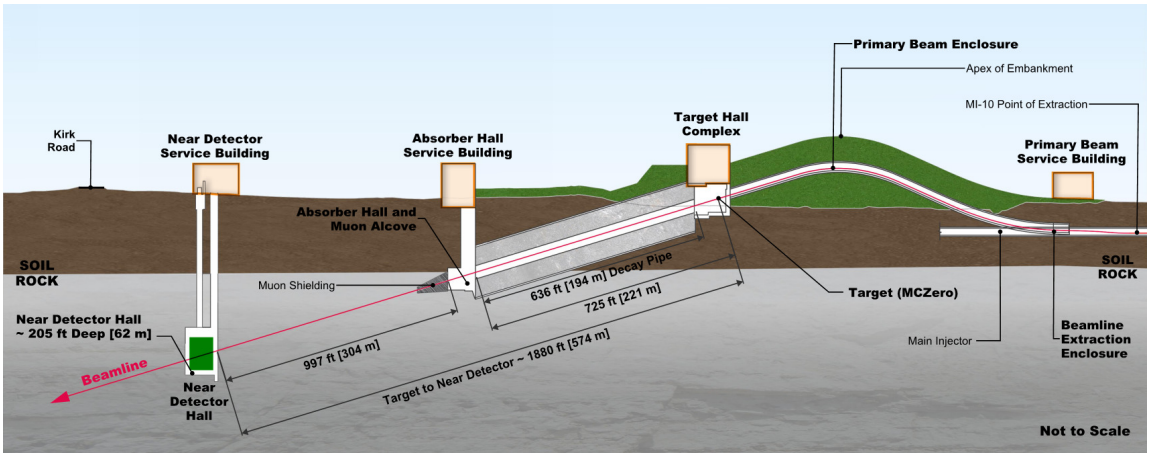

Figure 1.2. Neutrino beamline and DUNE near detector hall at Fermilab in Illinois.

experiment, beyond its primary goals, including accelerator-based neutrino flavor-transition measurements with sensitivity to physics beyond the standard model, measurements of tau neutrino appearance, measurements of neutrino oscillation phenomena using atmospheric neutrinos, and a rich neutrino interaction physics program using the DUNE ND, including a wide range of measurements of neutrino cross sections, studies of nuclear effects, and searches for dark matter. Further advances in LArTPC technology during FD construction may open up possibilities to observe very low-energy phenomena such as solar neutrinos or even the diffuse supernova neutrino flux — measurements that require a sensitivity that is presently beyond our reach.

1.1.3 The DUNE collaboration

The DUNE collaboration is a global organization with more than 1000 scientists and engineers from 31 countries (figure 1.3). It represents the combination of several worldwide efforts that developed independent paths toward a next-generation long-baseline neutrino experiment over the last decade. DUNE was formed in April 2015, combining the strengths of the LBNE project in the U.S. and the Long Baseline Neutrino Observatory (LBNO) project in Europe, adding many new international partners in the process. DUNE thus represents the convergence of a substantial fraction of the worldwide neutrino-physics community around the opportunity provided by the large investment planned by the U.S. DOE and Fermilab to support a significant expansion of the underground infrastructure at SURF in South Dakota and to create a megawatt neutrino-beam facility at Fermilab.

1.1.4 Strategy for the DUNE far detector design

DUNE and LBNF have developed the strategy presented in this TDR to meet the requirements laid out in the report of the U.S. Particle Physics Project Prioritization Panel (P5) in 2014. The strategy also takes into account the recommendations of the European Strategy for Particle Physics (ESPP) adopted by the European Organization for Nuclear Research (CERN) Council in 2013, which classified the long-baseline neutrino program as one of the four scientific objectives requiring significant resources, sizable collaborations, and sustained commitment.

2020 JINST 15 T08008

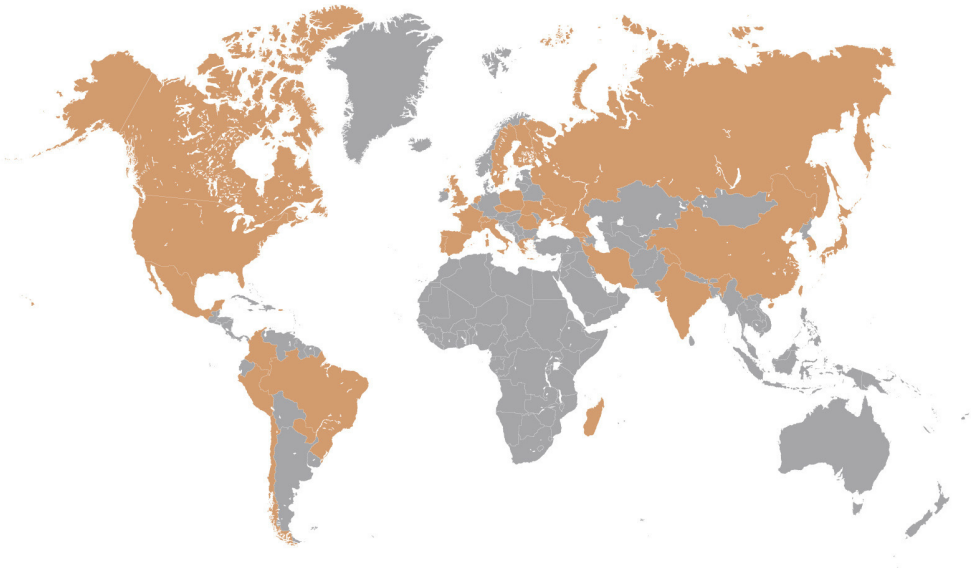

Figure 1.3. The international DUNE collaboration. Countries with DUNE membership are in light brown.

The P5 report [3] set the goal of determining leptonic CPV with a precision of three standard deviations ($3\,\sigma$) or greater (i.e., a precision of at least 0.03 %), over more than 75 % of the range of possible values (0 through 2π) of the unknown CP-violating phase δ_{CP}. It is impossible to provide coverage of 100 % since CPV effects vanish as the value of δ_{CP} approaches 0 or π. Based partly on this goal, the report stated that "the minimum requirements to proceed are the identified capability to reach an exposure of 120 kt · MW · year [2] by the 2035 time frame, the far detector situated underground with cavern space for expansion to at least 40 kt LAr fiducial volume, and 1.2 MW beam power upgradable to multi-megawatt power. The experiment should have the demonstrated capability to search for supernova neutrino bursts (SNBs) and for proton decay, providing a significant improvement in discovery sensitivity over current searches for proton decay."

Here we briefly address how the LBNF and DUNE project (LBNF/DUNE) strategy and designs will satisfiy each of these requirements and deliver a world-leading neutrino program. The following chapters and the other volumes of this TDR elaborate on these concepts, providing a full picture of this ambitious enterprise.

Reach at least 120 kt · MW · year exposure by the 2035 timeframe and 1.2 MW beam power: To reach the necessary precision on its measurements, DUNE will need to collect a few thousand neutrino interactions over a period of about ten years. The number of interactions is the product of (1) the intensity of the neutrino beam, (2) the probability that a neutrino will oscillate (approximately 0.02), (3) the interaction cross section, and (4) the detector mass. Currently, the highest-power proton beam that a beam target can safely withstand is between 1 and 2 MW, which caps the achievable neutrino beam intensity. This points to a required a detector mass in the tens-of-kilotons range. The DUNE FD cryostats will hold 17.5 kt of LAr each, for a total of nearly 70 kt, of which

[2] 1 kt · MW · year is the amount of exposure a detector of target mass 1 kt of LAr would get in one year using a 1 MW proton beam to generate the neutrinos. Exposure increases linearly as each of the factors increases.

at least 40 kt will be encompassed by the four detector modules as fiducial mass. Higher usable fractions of the total volume are under study.

Moreover, the DUNE concept builds on the notion that a highly-performant detector technology with excellent neutrino energy reconstruction and background rejection capabilities can optimize sensitivity and cost with an on-axis exposure to an intense, wide-band, conventional (magnetic horn-focused) beam. The current generation of long-baseline neutrino experiments have benefited from narrow-band beam characteristics associated with off-axis detector deployment, which offers a low background rate in both electron neutrino (ν_e) appearance and muon neutrino (ν_μ) disappearance channels. However, this advantage comes at a cost of flux and spectral information relative to an on-axis detector configuration [1, 4].

Situated underground: given the rate of cosmic rays at the surface (165 kHz) and the neutrino beam parameters, the ratio of neutrino events to cosmic rays would be less than one to a million and the discovery potential for DUNE's oscillation physics goals would be vanishingly small. Roughly 1500 m underground at the SURF site, this ratio becomes slightly higher than 1, raising the discovery potential to a very achievable level. Supernova neutrinos have energies on the order of 100 times lower than beam neutrinos, and despite the fact that they arrive in a few-second burst, would be nearly impossible to identify on the surface. A meaningful search for nucleon decay is not possible at the surface. All three of the experiment's primary goals require significant overburden for the FD, which the SURF site provides.

Use of liquid argon (LAr): this requirement implies the use of the LArTPC technology, which enables finer resolution for kiloton-scale particle detectors than earlier technologies do. The enhanced resolution leads to greater efficiency in distinguishing signal events from background, which in turn leads to a reduction in the necessary size of the detector and potentially broadens the physics program. It is especially important for the long-baseline program with a wide-band neutrino beam. Additionally, the choice of LArTPC technology provides valuable complementarity to other existing and planned detectors pursuing many of the same goals. As an example, the sensitivity of DUNE to the ν_e component of supernova neutrino flux, prevalent in the neutronization phase of the explosion, provides distinct information relative to that provided by water or organic scintillator-based detectors in which electron antineutrino ($\bar{\nu}_e$) interactions dominate.

Sensitivity to CPV: the physics that DUNE will pursue demands measurements at the few-percent level. With just a FD, the neutrino fluxes would be known only to about 10 % and interaction rates to at best 20 %. To adequately reduce these uncertainties, is necessary to measure the neutrinos at a near location, e.g., 500 m from the neutrino source and at a far location, e.g., 1300 km away, using the same target nucleus in both detectors, and to extract the physics measurements from differences between the two. The ND can be smaller than the FD, but it must be multi-functional since the differences in the measurements are not due solely to oscillations. The detector rate is the product of the neutrino flux, the detector response, and the interaction cross section, the first two of which will differ between the ND and FD due to other factors as well, e.g., event rate and geometry. The ND must be able to measure the factors that go into the detector rate separately.

The optimal FD distance (baseline) to determine the mass hierarchy (MH), observe CPV, and observe δ_{CP} is between 1000 and 2000 km; at shorter baselines the optimal neutrino energy is lower, the second oscillation maximum is too low in energy to be visible, and charge parity (CP) sensitivity is reduced by ambiguities from the unknown mass ordering. At longer baselines CP sensitivity is

2020 JINST 15 T08008

harmed by matter effects that increase with baseline. The 1300 km baseline offered by locating the FD at SURF is optimized for the neutrino oscillation physics goals of the DUNE program.

The scientific basis for DUNE's foundational experimental design choices has been examined and validated through extensive review, undertaken at all stages of DUNE development. Recent experimental and theoretical developments have only strengthened the scientific case for DUNE and its basic configuration. The technical underpinnings for these choices have also been strengthened over time through a worldwide program of R&D and engineering development, as described in a suite of LBNF/DUNE project documents including this TDR, as well as through independent experiments and development activities.

1.2 The Long-Baseline Neutrino Facility (LBNF)

As mentioned above, the LBNF project will provide the beamline and the conventional facilities (CF) for both detectors of the DUNE experiment. At the far site, SURF in South Dakota, LBNF will construct a facility to house and provide infrastructure for the DUNE 10 kt fiducial mass FD modules; in particular LBNF is responsible for:

- the excavation of three underground caverns at SURF, north and south detector caverns and a central utility cavern (CUC) for the detector's ancillary systems; this requires the removal of 800 kt of rock;[3]
- free-standing, steel-supported cryostats to contain each detector module in a bath of 17.5 kt of LAr;
- the required cryogenics systems for rapidly deploying the first two modules;
- surface, shaft, and underground infrastructure at SURF to support installation, commissioning, and operation of the detector; and
- the LAr required to fill the first two cryostats.

DUNE intends to install the third and fourth FD modules as rapidly as funding will allow. When finished, the north and south caverns will each house two modules and the CUC will house cryogenics and data acquisition facilities for all four modules.

Figure 1.4 shows the cavern layout for the FD in the SURF underground area, also referred to as the 4850 (foot) level or 4850L.

1.3 The DUNE detectors

1.3.1 Far detector

The DUNE FD will consist of four LArTPC detector modules, each with a LAr mass in the sensitive region of the cryostat (fiducial mass) of at least 10 kt, installed approximately 1.5 km underground. excellent tracking and calorimetry performance, making it an ideal choice. Each LArTPC fits inside a cryostat of internal dimensions 15.1 m (w) × 14.0 m (h) × 62.0 m (l) containing a total LAr mass

[3]This is roughly the mass of the Golden Gate Bridge including its anchorage and approaches.

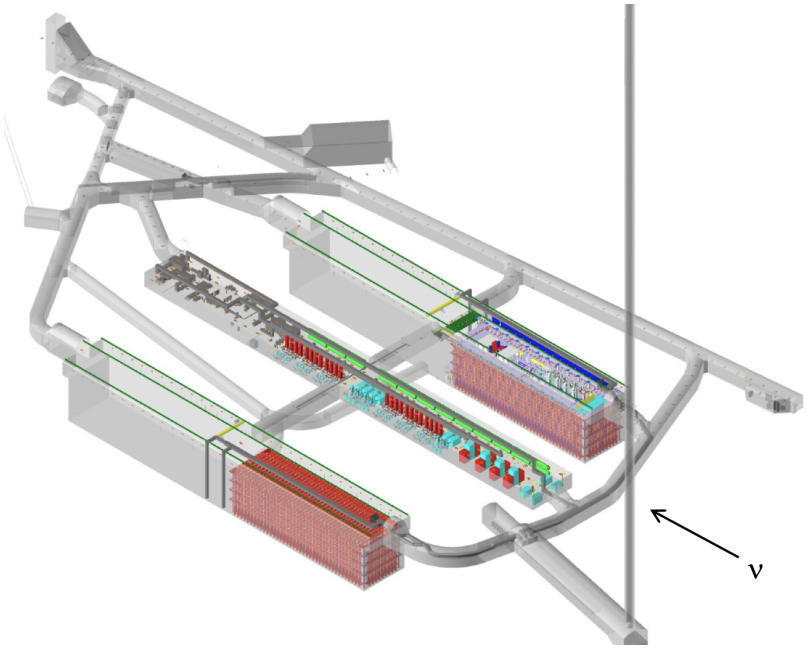

Figure 1.4. Underground caverns for the DUNE FD and cryogenics systems at SURF in South Dakota. The drawing shows the cryostats (red) for the first two FD modules in place at the 4850L. The Ross Shaft, the vertical shaft that will provide access to the DUNE underground area, appears on the right. Each cryostat is 65.8 m long (216 ft, approximately the length of two and a half tennis courts), 18.9 m wide, and 17.8 m tall (about three times as tall as an adult giraffe). The two detector caverns are each 144.5 m long, 19.8 m wide, and 28.0 m high, providing some room around the cryostats.

of about 17.5 kt. The design of the four identically sized modules is sufficiently flexible for staging construction and evolving the LArTPC technology.

DUNE is planning for and currently developing two LArTPC technologies: single-phase (SP) in which all the detector elements inside the cryostat are immersed in liquid; and dual-phase (DP), in which some components operate in a layer of gaseous argon above the liquid.

- In the SP technology, ionization charges drift horizontally in the LAr under the influence of an electric field (E field) towards a vertical anode, where they are read out. This design requires very low-noise electronics to achieve readout with a good signal-to-noise (S/N) ratio because no signal amplification occurs inside the cryostat. This technology was pioneered in the ICARUS project, and after several decades of worldwide R&D, is now mature. It is the technology used for Fermilab's currently operating MicroBooNE detector, as well as the SBND detector, which is under construction. Figure 1.5 shows the operating principle of an SP LArTPC.

- The DP technology was pioneered at a large scale by the WA105 DP demonstrator collaboration at CERN. It is less mature than the SP technology, and whereas it presents some challenges, it offers several advantages. Here, ionization charges drift vertically upward in LAr and are transferred into a layer of argon gas above the liquid. Devices called large electron multipliers (LEMs) amplify the signal charges in the gas phase before they reach

a horizontal anode. The gain achieved in the gas reduces the stringent requirements on the electronics noise and the overall design increases the possible drift length, which, in turn, requires a correspondingly higher voltage. Figure 1.6 shows the operating principle of a DP LArTPC.

In both technologies, the drift volumes are surrounded by a field cage (FC) that defines the active detector volume and ensures uniformity of the E field within that volume.

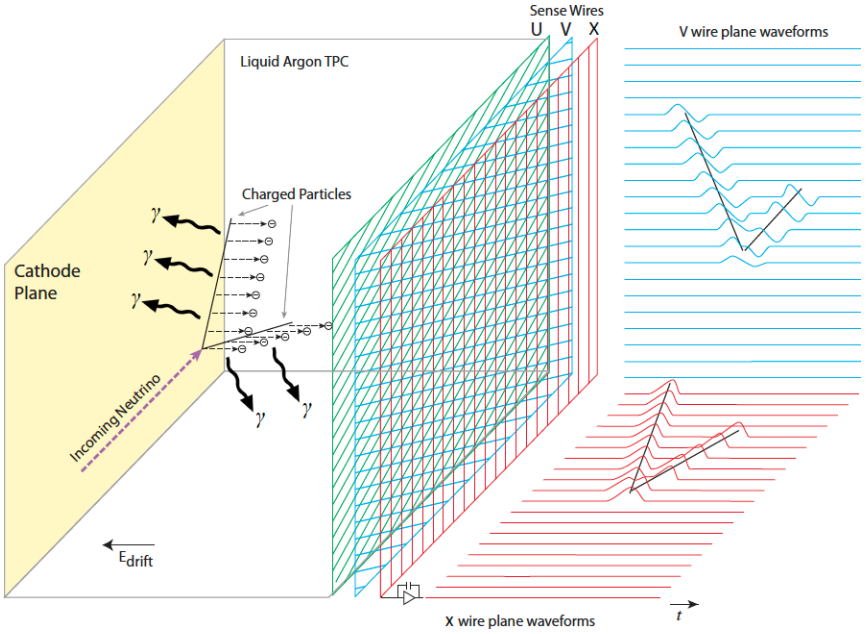

Figure 1.5. The general operating principle of the SP LArTPC. Negatively charged ionization electrons from the neutrino interaction drift horizontally opposite to the E field in the LAr and are collected on the anode, which is made up of the U, V and X sense wires. The right-hand side represents the time projections in two dimensions as the event occurs. Light (γ) detectors (not shown) will provide the t_0 of the interaction.

Argon is an excellent scintillator at a wavelength of 126.8 nm (UV), a property that both detector designs exploit. This fast scintillation light (photons), once shifted into the visible spectrum, is collected by photon detectors (PDs) in both designs. The light collection provides an initial start time (t_0) for every event recorded by the time projection chamber (TPC), indicating when the ionization electrons begin to drift. Comparing the time at which the ionization signal reaches the anode relative to this start time allows reconstruction of the event topology in the drift coordinate (i.e., horizontal and transverse to the beam for SP and vertical for DP); the precision of the measured t_0, therefore, directly corresponds to the precision of the spatial reconstruction in this direction.

Two key factors affect the performance of the DUNE LArTPCs: LAr purity and noise on the readout electronics. First, the LAr purity must be quite high to minimize charge and light attenuation over the longest drift lengths in the detector module. The SP and DP designs have slightly different purity requirements (expressed in minimum electron lifetimes of 3 ms versus 5 ms) due to the different maximum drift lengths. Second, the electronic readout of the LArTPC requires very low noise levels for the signal from the drifting electrons to be clearly discerned over the baseline of the

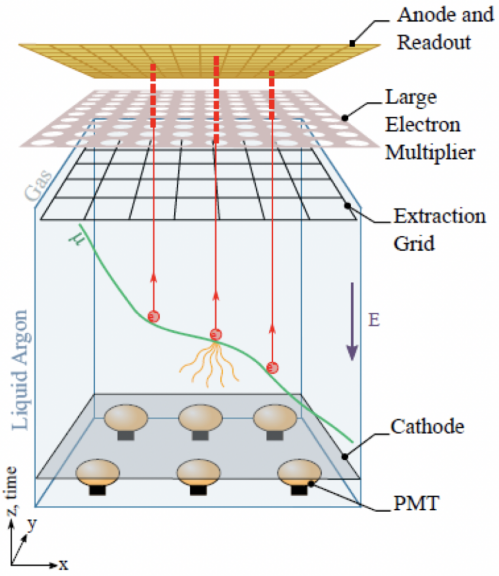

Figure 1.6. The general operating principle of the DP LArTPC. The ionization charges drift vertically upward in LAr and are transferred into a layer of argon gas above the liquid where they are amplified before collection on the anode. The light detectors (PMTs) sit under the cathode.

electronics. This requires using low-noise cryogenic electronics, especially in the case of the SP design.

The DUNE collaboration is committed to deploying both technologies. The full DUNE FD requires four modules. In this TDR, we describe plans for the first three modules: two SP modules, one of which will be the first module installed, and one DP module. The actual sequence of detector module installation will depend on results from the prototype detectors, described below, and on available resources. Plans for the fourth detector module, which may use a more advanced design, remain to be determined.

The plans for the SP and DP modules are described briefly in the following sections, more fully in Chapters 3 and 4, and finally in great detail in Volumes IV and V of this TDR.

1.3.1.1 A single-phase far detector module

The operating principle of an SP LArTPC (figure 1.5) has been demonstrated by ICARUS [5], MicroBooNE [6], ArgoNeuT [7], LArIAT [8], and ProtoDUNE-SP [9]. Charged particles passing through the TPC ionize the argon, and the ionization electrons drift in an E field to the anode planes. Figure 1.7 shows the configuration of a DUNE SP module. Each of the four drift volumes of LAr is subjected to a strong E field of 500 V/cm, corresponding to a cathode high voltage (HV) of 180 kV. The maximum drift length is 3.5 m.

An SP module is instrumented with three module-length (58.2 m) anode planes constructed from 6 m high by 2.3 m wide anode plane assemblies (APAs), stacked two APAs high and 25 wide, for 50 APAs per plane, and 150 total. Each APA consists of an alumninum frame with three layers of active wires, strung at angles chosen to reduce ambiguities in event reconstruction, that form a grid on each side of the APA. The relative voltage between the layers is chosen to ensure transparency to

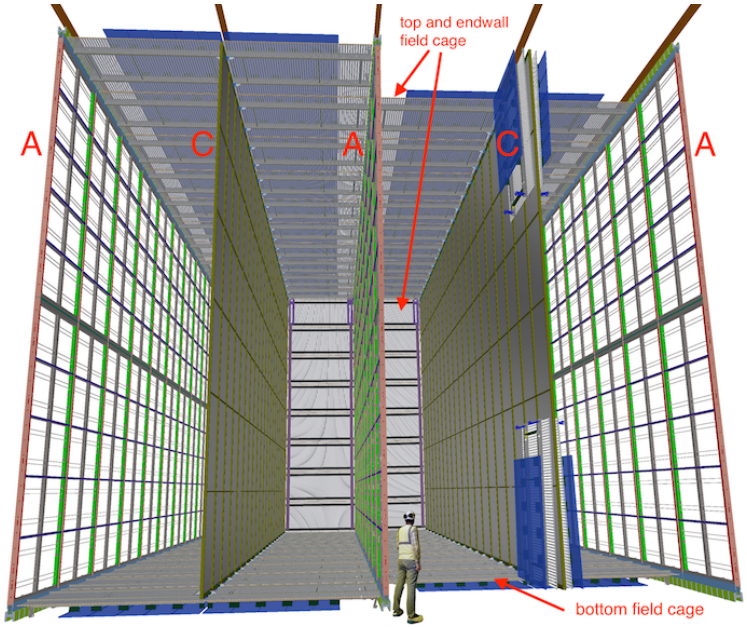

Figure 1.7. A 10 kt DUNE FD SP module, showing the alternating 58.2 m long (into the page), 12.0 m high anode (A) and cathode (C) planes, as well as the field cage (FC) that surrounds the drift regions between the anode and cathode planes. On the right-hand cathode plane, the foremost portion of the FC is shown in its undeployed (folded) state.

the drifting electrons of the first two layers (U and V). These layers produce bipolar induction signals as the electrons pass through them. The final layer (X) collects the drifting electrons, resulting in a unipolar signal. The pattern of ionization collected on the grid of anode wires provides the reconstruction in the remaining two coordinates perpendicular to the drift direction (figure 1.5).

Novel silicon photomultiplier (SiPM) based photon detectors (PDs) called ARAPUCAs[4] are placed in the inactive space between the innermost wire planes of the APAs, installed through slots in the APA frame. Each APA holds ten PD modules, for a total of 1500 per SP module. Of these, 500 are mounted in the APAs of the central anode plane and collect light from both directions, and 500 each are mounted in the outer APA frames and collect light from only the inner-facing direction.

1.3.1.2 A dual-phase far detector module

The DP operating principle, illustrated in figure 1.6, is very similar to that of the SP. Charged particles that traverse the active volume of the LArTPC ionize the medium while also producing scintillation light. The ionization electrons drift, in this case vertically, along an E field toward a segmented anode where they deposit their charge. Any scintillation light that is produced is measured in PDs that view the interior of the volume from below.

In this design, shown in figure 1.8, ionization electrons drift upward toward an extraction grid just below the liquid-vapor interface. After reaching the grid, an E field stronger than the 500 V/cm drift field extracts the electrons from the liquid up into the gas phase. Once in the gas,

[4] An "arapuca" is a South American bird trap; the name is used here as an analogy to the way the devices trap photons. These devices have been developed by DUNE collaborators in Brazil.

the electrons encounter micro-pattern gas detectors, called LEMs, with high-field regions in which they are amplified. The amplified charge is then collected and recorded on a 2D anode consisting of two sets of gold-plated copper strips that provide the x and y coordinates (and thus two views) of an event. An array of photomultiplier tubes (PMTs) coated with a wavelength-shifting material sits below the cathode to record the time (t_0) and pulse characteristics of the incident light.

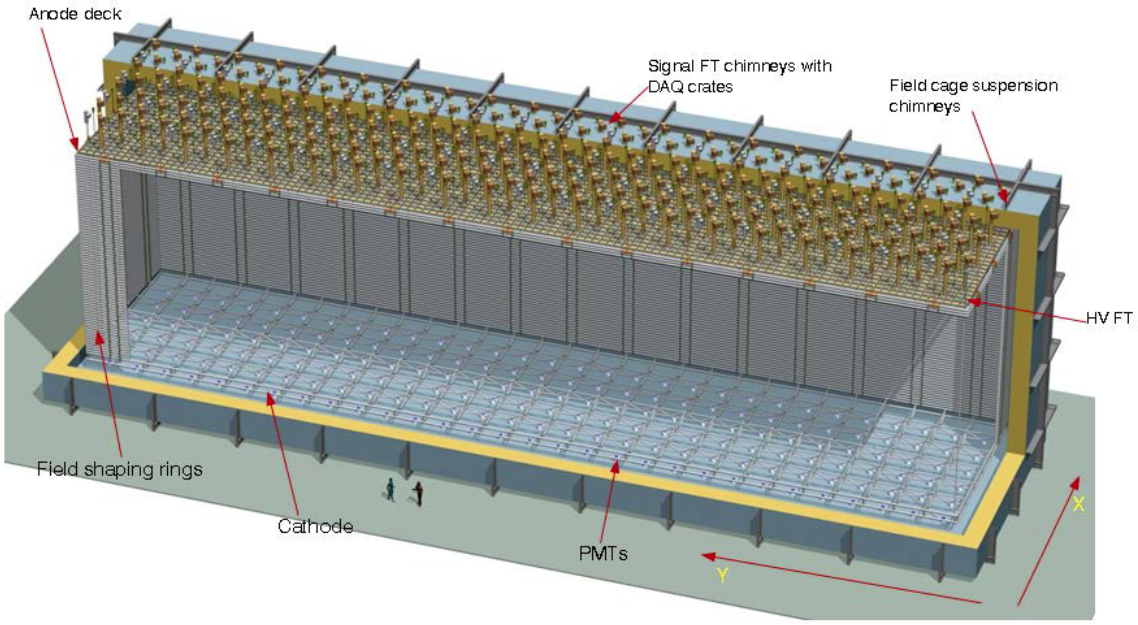

Figure 1.8. Schematic of a 10 kt DUNE FD DP detector module with cathode, PMTs, FC, and anode plane with SFT chimneys. The drift direction is vertical in the case of a DP module. The scale is indicated by the figures of two people standing in front of the model.

The extraction grid, LEM, and anode are assembled into three-layered sandwiches with precisely defined inter-stage distances and inter-alignment, which are then connected horizontally into 9 m^2 modular detection units called charge-readout planes (CRPs).

The precision tracking and calorimetry offered by both the SP and DP technologies provide excellent capabilities for identifying interactions of interest while mitigating sources of background. Whereas the SP design has multiple drift volumes, the DP module design allows a single, fully homogeneous LAr volume with a much longer drift length.

1.3.2 ProtoDUNEs: far detector prototypes

The DUNE collaboration has constructed and operated two large prototype detectors, ProtoDUNE-SP, and ProtoDUNE-DP, at CERN. Each is approximately one-twentieth the size of the planned FD modules but uses components identical in size to those of the full-scale module. ProtoDUNE-SP has the same 3.5 m maximum drift length as the full SP module. ProtoDUNE-DP has a 6 m maximum drift length, half that planned for the DP module. Figure 1.9 shows the two cryostats, ProtoDUNE-SP in the foreground and ProtoDUNE-DP at an angle in the rear. Figure 1.10 shows one of the two drift volumes of ProtoDUNE-SP on the left and the single drift volume of ProtoDUNE-DP on the right.

2020 JINST 15 T08008

Figure 1.9. ProtoDUNE-SP and ProtoDUNE-DP cryostats in the CERN Neutrino Platform in CERN's North Area.

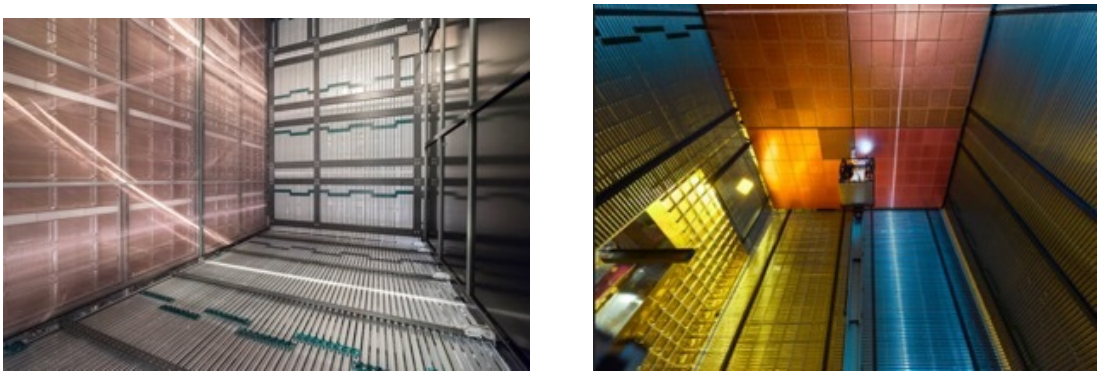

Figure 1.10. Left: view of one of the two drift volumes in ProtoDUNE-SP; the APA is on the left, the CPA is on the right, and two of the four the FC surfaces bounding the drift volume are at the center and bottom of the image. Right: the single ProtoDUNE-DP drift volume (still incomplete when the image was taken), looking up; the CRPs (orange) are at the top. Three sides of the surrounding FC are shown, but the cathode is not visible.

This massive prototyping program was undertaken with both engineering and scientific goals in mind, namely:

1. production of components: stress-test the production and quality assurance (QA) processes of detector components and mitigate the associated risks for the FD;
2. validation of installation procedures: test the interfaces between the detector elements and mitigate the associated risks for the FD;
3. operation of the detector with cosmic rays: validate the detector designs and performance; and
4. collection of test beam data: measure the physics response of the detector.

2020 JINST 15 T08008

Construction of the ProtoDUNE-SP detector was finished in July 2018 and filled with LAr the following month. It collected hadron beam and cosmic ray data during the fall of 2018 and continues to collect cosmic ray data. Construction of the ProtoDUNE-DP detector was complete in June of 2019, and the detector started operations in September 2019.

The data taken with ProtoDUNE-SP demonstrate the detector's excellent performance and have already provided valuable information on the design, calibration, and simulation of the DUNE FD. In all, 99.7 % of the 15360 TPC electronics channels are responsive in the LAr. The equivalent noise charge (ENC) amounts to $\approx$ 550 e^- on the collection wires and $\approx$ 650 e^- on the induction wires, roughly half of the allowed maximum. An average S/N of 38 for the collection plane is measured using cosmic-ray muons, while for the two induction planes, the S/N is 14 (U) and 17 (V), easily exceeding the requirement of 4 for the DUNE FD.

When an interaction occurs, we convert the charge deposited along the track to the energy loss (dE/dx) using stopping cosmic ray muons. Calibration constants have been derived with this method, which are applied to the energy deposits measured for the beam particles — muons, pions, protons, and positrons. Figure 1.11 (left) shows the calibrated dE/dx values as a function of the track residual range for protons in the 1 GeV/c beam, in good agreement with expectations.

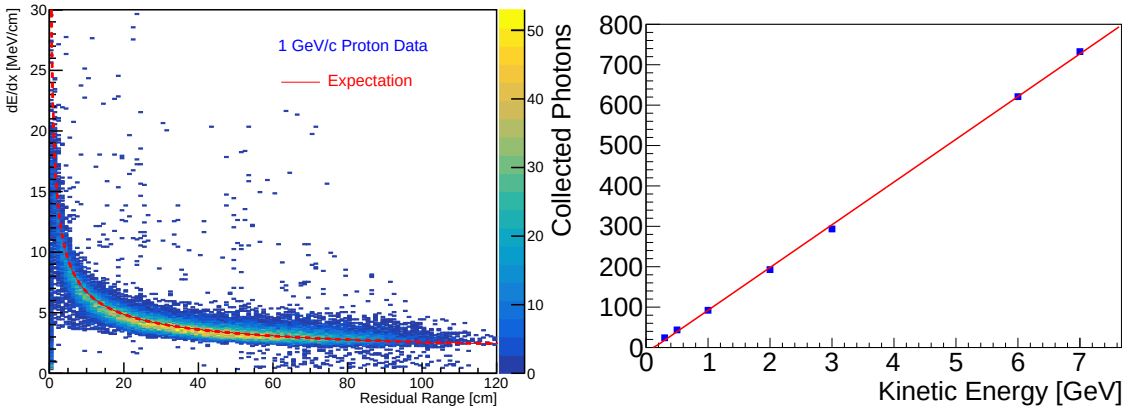

Figure 1.11. Left: calibrated dE/dx (energy loss over distance) versus residual range measured by a TPC for 1 GeV/c stopping protons. Right: response in ProtoDUNE-SP of an ARAPUCA PD module in APA3 as a function of incident electron kinetic energy.

The ProtoDUNE-SP beam run provides a unique set of high-quality data for detector performance characterization, physics studies, and calibration, and will allow us to perform hadron-argon cross section measurements, which are relevant for future DUNE neutrino oscillation analyses. Data collected during the beam run will also be used to characterize the photon detection system (PD system) response to light signals. Other useful data sets include beam data with triggers determined by the beam instrumentation; cosmic ray data from random triggers or from those in coincidence with the cosmic ray tagger (CRT) modules; and calibration data, with triggers enabling programmed light pulses. The response and gain for each of the 256 readout channels of the PD system have been determined from calibration data, and the initial analysis results indicate very good performance and stability for this system.

Figure 1.11 (right) shows the response of an ARAPUCA PD module (not corrected for geometry and detection efficiency) as a function of incident electron kinetic energy measured in

2020 JINST 15 T08008

ProtoDUNE-SP. This preliminary analysis demonstrates the achieved energy linearity for beam electrons contained in the detector. In addition to verifying the PD system response and calibration, ProtoDUNE-SP shows excellent correlation between TPC timing and the PD system timing. The latter will enable the further optimized physics reach of DUNE.

1.3.3 Near detector

Although not the subject of this TDR, an understanding of DUNE's capabilities would be impossible without some description of the ND's crucial contribution to the experiment. The ND will serve as the experiment's control, constraining systematic errors and measuring the initial unoscillated ν_μ and ν_e energy spectra (and that of the corresponding antineutrinos). Comparing the measured neutrino energy spectra near the beam source, before any oscillation takes place, and again at the far site allows us to disentangle the different energy-dependent effects that modulate the beam spectrum and to reduce the systematic uncertainties to the level required for discovering CPV. Its other key role in this arena is to measure neutrino-argon interactions with high precision using both gaseous and liquid argon, which will further reduce the systematic uncertainties associated with modeling these interactions.

The ND will have a physics program of its own, as well, independent of the FD. This program will include measuring neutrino interactions to explore the two pillars of the standard model: electroweak physics and quantum chromodynamics. It will also explore physics beyond the standard model, searching for non-standard interactions, sterile neutrinos, dark photons, and other exotic particles.

The ND will be located 574 m downstream from the neutrino beam source and will include three primary detector components, illustrated in figure 1.12:

- a LArTPC called ArgonCube;
- a high-pressure gaseous argon TPC (HPgTPC) surrounded by an electromagnetic calorimeter (ECAL) in a 0.5 T magnetic field, together called the multi-purpose detector (MPD); and
- an on-axis beam monitor called System for on-Axis Neutrino Detection (SAND).

These components serve important individual and overlapping functions in the mission of the ND. The first two can move off-axis relative to the beam, providing access to different neutrino energy spectra. The movement off-axis, called DUNE Precision Reaction-Independent Spectrum Measurement (DUNE-PRISM), provides a crucial extra degree of freedom for the ND measurements and is an integral part of the DUNE ND concept.

The ArgonCube detector contains the same target nucleus and shares some aspects of form and functionality with the FD. This similarity in target nucleus and, to some extent, technology, reduces sensitivity to nuclear effects and detector-driven systematic uncertainties in extracting the oscillation signal at the FD. ArgonCube is large enough to provide high statistics (1×10^8 ν_μ charged current events/year on-axis), and its volume is sufficiently large to provide good hadron containment. The tracking and energy resolution, combined with the LAr mass, will allow measurement of the neutrino beam using several techniques.

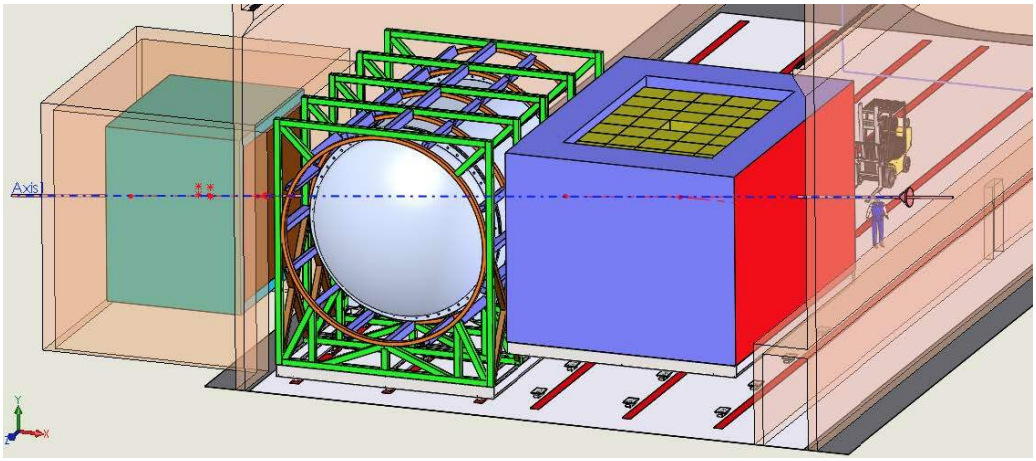

Figure 1.12. DUNE ND. The axis of the beam is shown as it enters from the right. Neutrinos first encounter the LArTPC (right), the MPD (center), and then the on-axis beam monitor (left).

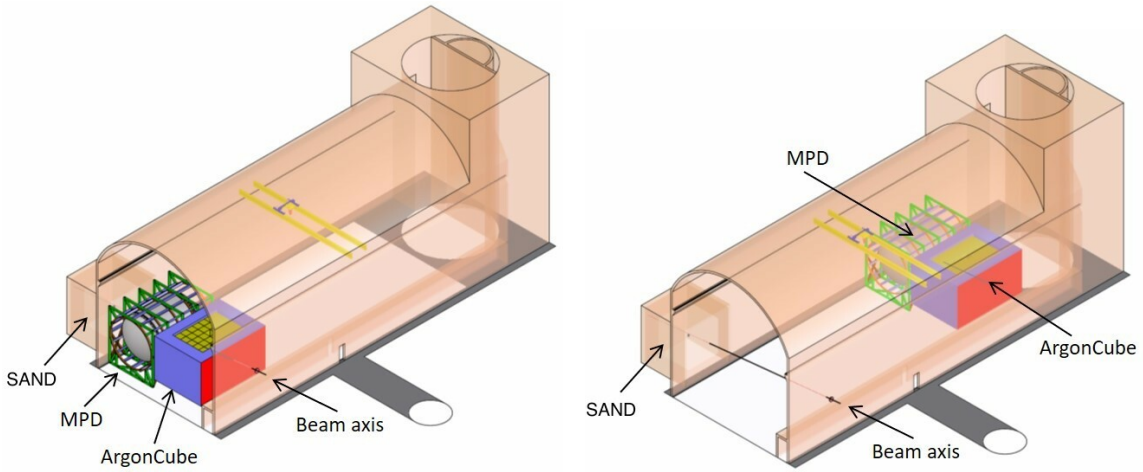

Figure 1.13. DUNE ND hall shown with component detectors all in the on-axis configuration (left) and with the LArTPC and MPD in an off-axis configuration (right). The beam monitor (SAND) is shown in position on the beam axis in both figures. The beam is shown entering the hall at the bottom traveling from right to left.

A LArTPC energy acceptance falls off for muons with a measured momentum higher than ~ 0.7 GeV/c because the muons will not be contained in the LArTPC volume. Since muon momentum is critical to determining the incoming neutrino's energy, a magnetic spectrometer is needed downstream of the LArTPC to measure the momentum and charge of the muons. In the DUNE ND concept, the MPD will make these measurements. The HPgTPC provides a lower density medium with excellent tracking resolution for muons from the LArTPC.

The LArTPC and MPD can be moved sideways up to 33 m to take data in positions off the beam axis (DUNE-PRISM). As the detectors move off-axis, the incident neutrino flux spectrum changes, with the mean energy dropping and the spectrum becoming more monochromatic. The DUNE concept is based on reconstructing the energy-dependent neutrino spectrum and comparing

measurements at the far and near sites. The ability to take measurements at the near site in off-axis locations will allow us to disentangle otherwise degenerate effects due to systematic biases of the energy reconstruction.

The final component of the DUNE ND suite is the beam monitor that remains on-axis at all times and serves as a dedicated neutrino spectrum monitor. It can also provide an excellent on-axis neutrino flux determination that can be used as an important point of comparison and a systematic crosscheck for the flux as determined by ArgonCube.

Chapter 5 of this TDR volume presents a more complete introduction to the ND and further details of the system can be found in the appendices. The DUNE collaboration is now in the process of finalizing studies for the ND Conceptual Design Report.

1.4 DUNE project organization and responsibilities

DUNE is the first large-scale science project to be built in the U.S. conceived as a fully international collaboration with majority international participation. As such, DUNE requires a new organizational and governance model that takes into account the international nature of the project and its relationship to LBNF. The model used by CERN to manage constructing and operating the LHC and its experiments served as a starting point for the management structure of both DUNE and LBNF, and our model continues to evolve as the DUNE project moves forward in concert with LBNF to build this experiment and the supporting facilities. The DUNE project is organized by the DUNE collaboration (section 1.5) with appropriate oversight from all its international stakeholders. In contrast, LBNF (section 1.2) is organized as a DOE-Fermilab project incorporating international partners.

A set of organizational structures has been established to coordinate the participating funding agencies, overseeing the LBNF and DUNE projects, and coordinating and communicating between the two. These structures and the relationships among them are shown in figure 1.14. They include the following committees:[5]

- International Neutrino Council

  The International Neutrino Council (INC) is part of the international project governance structure for the LBNF and the PIP-II projects. The INC comprises representatives from the international funding agencies and CERN that make major contributions to the infrastructure. The INC acts as the highest-level international advisory body to the U.S. DOE and the Fermilab directorate on anything related to the program, including coordination among the international partners. The associate director for HEP in the DOE Office of Science chairs the INC, and the INC includes the Fermilab director as a member. The council meets once a year and provides pertinent advice on the LBNF and PIP-II projects.

- Resources Review Board (RRB)

  A Resources Review Board (RRB) is part of DUNE's international project governance structure, established to coordinate among funding partners and oversee the DUNE project. It

[5]The LBNF Strategic Project Advisory Committee (LBNF SPAC) advises the Fermilab director on LBNF only, and thus is not described here. PIP-II is introduced in section 1.1.2.

2020 JINST 15 T08008

includes representatives from all funding agencies that sponsor the project and from Fermilab management. The RRB provides focused monitoring of the DUNE collaboration and also receives updates on the progress of LBNF, PIP-II, and the Short-Baseline Neutrino (SBN) program. The RRB receives periodic reports from both the Long-Baseline Neutrino Committee (LBNC) and Neutrino Cost Group (NCG), described here. A representative from the Fermilab directorate chairs the RRB and calls regular meetings to monitor progress on the DUNE project.

- Long-Baseline Neutrino Committee (LBNC)

  The Fermilab director has charged the LBNC to review the scientific, technical, and managerial progress, as well as plans and decisions associated with the DUNE project. The LBNC, comprising internationally prominent scientists with relevant expertise, provides regular external scientific peer review of the project. It also provides regular reports and candid assessments to the Fermilab director, which are also made available to the RRB, LBNF, and DUNE collaboration leadership, as well as the funding agencies that support these international projects. The LBNC reviews the TDRs for DUNE and, if acceptable, recommends endorsing the TDRs to the Fermilab director and the RRB. Upon request by the Fermilab director, the LBNC may task other DUNE and LBNF groups with providing more detailed reports and evaluations of specific systems. The chair of the LBNC participates as a delegate to both the Fermilab-managed RRB and the DOE-managed INC. At meetings of the RRB and INC, the LBNC chair reports on LBNC deliberations to the international delegates. The chair of the LBNC is an ex-officio member of Fermilab's Physics Advisory Committee.

- Neutrino Cost Group (NCG)

  The Fermilab director has charged the NCG to review the cost, schedule, and associated risks of the DUNE project and to provide regular reports to the Fermilab director and the RRB. This group comprises internationally prominent scientists with relevant experience. The NCG reviews the TDRs for DUNE and provides a recommendation to the Fermilab directorate and the RRB on endorsing the TDRs. The chair of the NCG participates as a delegate to both the RRB and INC. At meetings of the RRB and INC, the NCG chair reports on NCG deliberations to the international delegates.

- Experiment-Facility Interface Group (EFIG)

  Coordination between the DUNE and LBNF projects must be close and continuous to ensure the success of the combined enterprise. The Experimental Facilities Interface Group (EFIG) (green box in figure 1.14) oversees coordination between them, especially during design and construction, but will continue during experiment operations. This group examines interfaces between the detectors and their corresponding conventional facilities, between individual detector systems and the LBNF infrastructure, and between design and operation of the LBNF neutrino beamline, which may have issues that affect both LBNF and DUNE.

2020 JINST 15 T08008

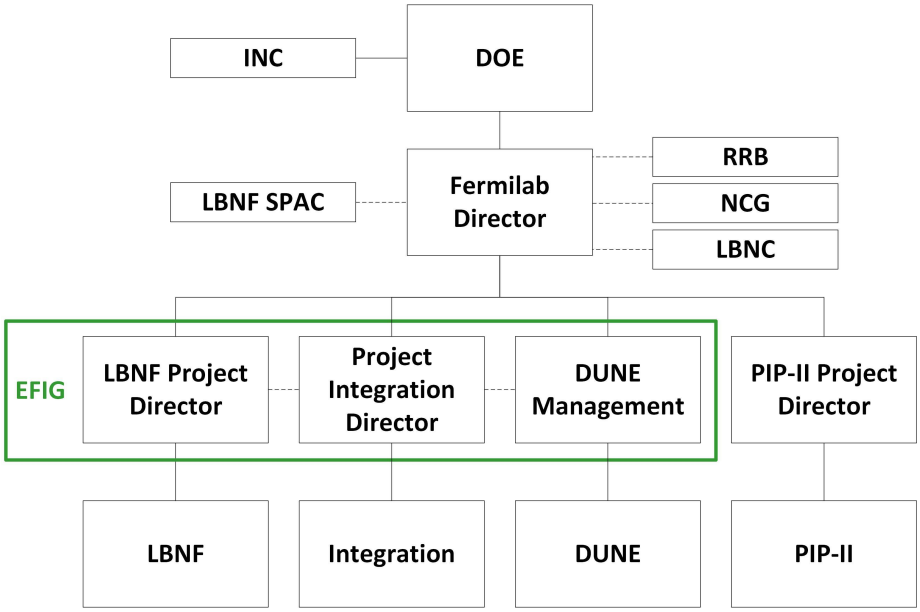

Figure 1.14. Top-level organization structure for oversight of the DUNE and LBNF projects, and flowdown.

1.5 DUNE collaboration organization and management

The DUNE collaboration organizes and manages DUNE in its entirety. Stakeholders include all collaborating institutions, the funding agencies participating in DUNE, and Fermilab as the host laboratory. All collaborating institutions have a representative on the DUNE institutional board (IB), which is responsible for establishing the governance rules of the collaboration and regulating governance-related issues. The collaboration is responsible for the design, construction, installation, commissioning, and operation of the detectors and prototypes used to pursue the scientific program. The DUNE executive board (EB), described below, is the primary management body of the collaboration and approves all significant strategic and technical decisions.

The top-level DUNE collaboration management team consists of two elected co-spokespersons, a technical coordinator (TC), and a resource coordinator (RC). The TC and RC are selected jointly by the co-spokespersons and the Fermilab director. The management team is responsible for the day-to-day management of the collaboration and for developing the overall collaboration strategy, which is presented for approval to the EB. The EB comprises the leaders of the main collaboration activities and currently includes the top-level management team, institutional board chair, physics coordinator, beam interface coordinator, computing coordinator, ND coordinator, and leaders of the FD consortia, described below. It is responsible for ensuring that all stakeholders in the collaboration have a voice in making decisions (see figure 1.15). Once the DUNE FD TDR is accepted, consortium leaders and coordinators of other major collaboration activities will become elected positions.

To carry out design and construction work for the DUNE FD, DUNE has formed consortia of institutions, each of which is responsible for an individual detector subsystem. A similar structure will be formed for the ND once the final detector concept is selected. The FD currently includes eleven consortia, including three specific to SP, three specific to DP, and five common to both

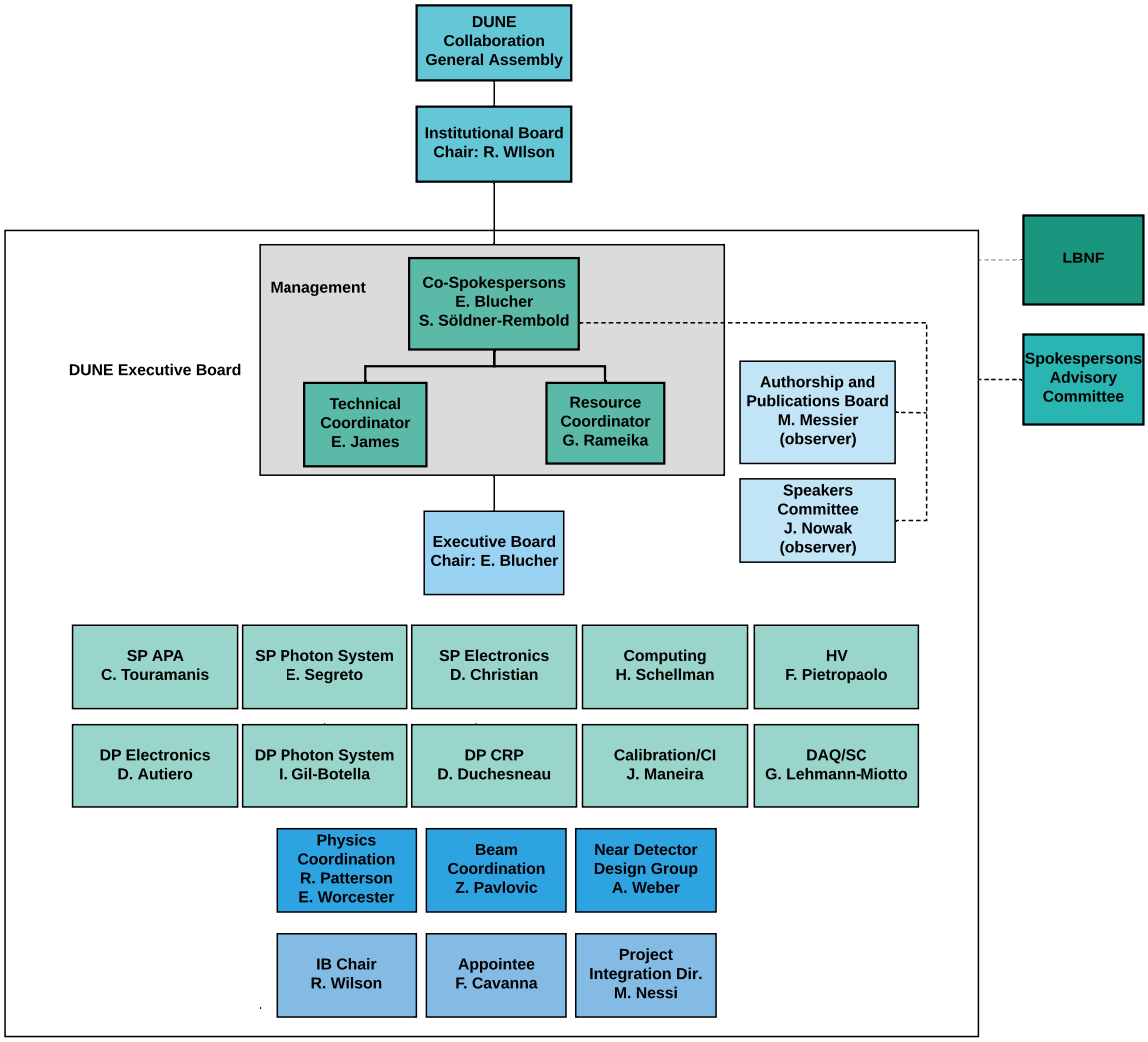

Figure 1.15. DUNE Executive Board.

technologies:

- (SP) anode plane assemblies (APAs),
- (SP) time projection chamber (TPC) electronics,
- (SP) photon detection system (PD system),
- (DP) charge-readout planes (CRPs),
- (DP) time projection chamber (TPC) electronics,
- (DP) photon detection system (PD system),
- (common) high voltage system (HVS),
- (common) data acquisition (DAQ),

2020 JINST 15 T08008

- (common) cryogenic instrumentation and slow controls (CISC),
- (common) calibration, and
- (common) computing.

Each consortium has an overall leader, a technical lead, and a consortium board with representatives from each participating institution. The consortia have full responsibility for their subsystems and for developing a work breakdown structure (WBS), and are expected to understand and document all interfaces with other systems, prepare final technical designs, and draft their own sections of the TDR. Following approval of the TDR, they will be responsible for constructing their respective detector subsystems.

Chapter 7 of this volume introduces the DUNE management and organization specifically as it relates to the FD; and Volume III, DUNE far detector technical coordination, of the TDR provides more detail.

1.6 Milestones for the first two far detector modules

The plan for construction and commissioning of the first two FD modules includes a set of key milestones and dates that will be finalized once the international project baseline is established. Table 1.1 shows some key dates and milestones (colored rows) and indicates how the detector consortia will add subsystem-specific milestones based on these dates (no background color).

The schedule for the design and construction of LBNF and DUNE has two critical parallel paths: one for the far site (SURF) and another for the near site (Fermilab). The schedule for initial work is driven by the design and construction of the conventional facilities (CF).

During the initial phase of the project, the far site CF has been given priority. Early far site preparation is complete as of fall 2019, following completion of the rehabilitation work on the Ross Shaft that leads to the DUNE underground area, and excavation can now begin. As each detector cavern is excavated and sufficient utilities are installed, the cryostat construction and cryogenics system installation begins, followed by detector installation, filling with LAr, and commissioning. The first detector module is scheduled to be operational in 2026.

U.S. DOE project management requires approval at critical decision (CD) milestones before allowing the LBNF/DUNE project to move on to the next step. CD-1R was granted in 2015, and CD-3A for LBNF far site construction was granted in 2016. In 2020, DUNE and LBNF will seek CD-2/3b and CD-2/3 for the near site. The project will conclude with CD-4 approval to start operations.

Table 1.1. DUNE schedule milestones for first two far detector modules. Key DUNE dates and milestones, defined for planning purposes in this TDR, are shown in orange. Dates will be finalized following establishment of the international project baseline.

Milestone	Date
Final design reviews	2020
Start of APA production	August 2020
Start photosensor procurement	July 2021
Start TPC electronics procurement	December 2021
Production readiness reviews	2022
South Dakota Logistics Warehouse available	April 2022
Start of ASIC/FEMB production	May 2022
Start of DAQ server procurement	September 2022
Beneficial occupancy of cavern 1 and CUC	October 2022
Finish assembly of initial PD modules (80)	March 2023
CUC DAQ room available	April 2023
Start of DAQ installation	May 2023
Start of FC production for detector module #1	September 2023
Start of CPA production for detector module #1	December 2023
Top of detector module #1 cryostat accessible	January 2024
Start TPC electronics installation on top of detector module #1	April 2024
Start FEMB installation on APAs for detector module #1	August 2024
Start of detector module #1 TPC installation	August 2024
Top of detector module #2 cryostat accessible	January 2025
Complete FEMB installation on APAs for detector module #1	March 2025
End DAQ installation	May 2025
End of detector module #1 TPC installation	May 2025
Start of detector module #2 TPC installation	August 2025
End of FC production for detector module #1	January 2026
End of APA production for detector module #1	April 2026
End detector module #2 TPC installation	May 2026
Start detector module #1 operations	July 2026

Chapter 2

DUNE physics

This chapter provides a brief introduction to DUNE physics. The text below closely follows the presentation in the introductory chapters of Volume II, where many more details may be found.

Presented here in summary form are (1) the scientific goals and opportunities, (2) the methodologies we have employed to evaluate the capabilities of DUNE to realize the science, and (3) the corresponding results for selected program elements.

2.1 Goals of the DUNE science program

The primary goals and ancillary science program elements listed in the previous chapter represent discovery opportunities at the forefront of particle physics and astrophysics. The DUNE has been designed to capitalize on these opportunities with a unique set of experimental conditions and capabilities. In this section we elaborate on elements of the science program that motivate the operating principles of DUNE that were presented in the previous chapter.

The focus of the presentation here is on physics opportunities offered by the DUNE FD. The DUNE ND will have its own physics program, only a small portion of which is covered here. The full ND physics program will be described in the ND conceptual design report (CDR), which is in progress as of this writing.

2.1.1 Neutrino oscillations: masses, mixing angles and CP violation

Neutrino oscillations imply nonzero neutrino masses and flavor-mixing in the leptonic charged current (CC) interactions. The nonzero neutrino mass is among the most important discoveries in fundamental particle physics of the twenty-first century. Understanding the mechanism behind nonzero neutrino masses is among the unresolved mysteries that drive particle physics today; they remain one of the few unambiguous facts that point to the existence of new particles and interactions, beyond those that make up the remarkable standard model of particle physics.

Almost all neutrino data can be understood within the three-flavor paradigm with massive neutrinos, the simplest extension of the standard model capable of reconciling theory with observations. It consists of introducing distinct, nonzero, masses for at least two neutrinos, while maintaining the remainder of the standard model. Hence, neutrinos interact only via the standard model CC and neutral current (NC) weak interactions. The neutrino mass eigenstates — defined as ν_1, ν_2, ν_3 with

2020 JINST 15 T08008

masses, m_1, m_2, m_3, respectively — are distinct from the neutrino CC interaction eigenstates, also referred to as the flavor eigenstates — ν_e, ν_μ, ν_τ, labeled according to the respective charged-lepton e, μ, τ to which they couple in the CC weak interaction. The flavor eigenstates can be expressed as linear combinations of the mass eigenstates: the coefficients of the respective linear combinations define a unitary 3×3 mixing matrix, the Pontecorvo-Maki-Nakagawa-Sakata (PMNS) matrix, as follows:

$$\begin{pmatrix} \nu_e \\ \nu_\mu \\ \nu_\tau \end{pmatrix} = \begin{pmatrix} U_{e1} & U_{e2} & U_{e3} \\ U_{\mu 1} & U_{\mu 2} & U_{\mu 3} \\ U_{\tau 1} & U_{\tau 2} & U_{\tau 3} \end{pmatrix} \begin{pmatrix} \nu_1 \\ \nu_2 \\ \nu_3 \end{pmatrix}. \tag{2.1}$$

Nonzero values for at least some of the off-diagonal elements, coupled with nonzero differences in the masses of ν_1, ν_2 and ν_3, lead to the phenomenon of neutrino oscillations, in which a neutrino — produced in a flavor eigenstate — acquires an oscillating probability of interacting as a different flavor (with an oscillation frequency proportional to the differences of the squares of the neutrino masses, $\Delta m^2_{ij} \equiv m^2_i - m^2_j$).

The PMNS matrix is the leptonic-equivalent of the Cabibbo-Kobayashi-Maskawa matrix (CKM matrix) that describes the CC interactions of quark mass eigenstates. If the neutrinos are Dirac fermions, the PMNS matrix, like the CKM matrix, can be unambiguously parameterized with three mixing angles and one complex phase.[1] By convention [10], the mixing angles are denoted θ_{12}, θ_{13}, and θ_{23}, defined as

$$\sin^2\theta_{12} \equiv \frac{|U_{e2}|^2}{1 - |U_{e3}|^2}, \tag{2.2}$$

$$\sin^2\theta_{23} \equiv \frac{|U_{\mu 3}|^2}{1 - |U_{e3}|^2}, \tag{2.3}$$

$$\sin^2\theta_{13} \equiv |U_{e3}|^2, \tag{2.4}$$

and one phase $\delta_{\rm CP}$, which in the conventions of [10], is given by

$$\delta_{\rm CP} \equiv -\arg(U_{e3}). \tag{2.5}$$

For values of $\delta_{\rm CP} \neq 0, \pi$, and assuming none of the $U_{\alpha i}$ vanish ($\alpha = e, \mu, \tau$, $i = 1, 2, 3$), the neutrino mixing matrix is complex and CP-invariance is violated in the lepton sector. This, in turn, manifests itself as different oscillation probabilities, in vacuum, for neutrinos and antineutrinos: $P(\nu_\alpha \to \nu_\beta) \neq P(\bar{\nu}_\alpha \to \bar{\nu}_\beta)$, $\alpha, \beta = e, \mu, \tau$, $\alpha \neq \beta$.

The central aim of the worldwide program of neutrino experiments past, present and planned, is to explore the phenomenology of neutrino oscillations in the context of the three-flavor paradigm, and, critically, to challenge its validity with measurements at progressively finer levels of precision. The world's neutrino data significantly constrain all of the oscillation parameters in the three-flavor paradigm, but with precision that varies considerably from one parameter to the next.

Critical questions remain open. The neutrino mass ordering — whether ν_3 is the heaviest ("normal" ordering) or the lightest ("inverted" ordering) — is unknown. Current data prefer the normal ordering, but the inverted one still provides a decent fit to the data. The angle θ_{23} is known to

[1] Additional nontrivial phases are present if neutrinos are Majorana fermions, but these do not affect oscillations at an observable level.

be close to the maximal-mixing value of $\pi/4$, but assuming it is not exactly so, the octant (whether $\sin^2\theta_{23} < 0.5$ [$\theta_{23} < \pi/4$] or $\sin^2\theta_{23} > 0.5$ [$\theta_{23} > \pi/4$]) is also unknown. The value of $\delta_{\rm CP}$ is only poorly constrained. While positive values of $\sin\delta_{\rm CP}$ are disfavored, all $\delta_{\rm CP}$ values between π and 2π, including the CP-conserving values $\delta_{\rm CP} = 0, \pi$, are consistent with the world's neutrino data.[2] That the best fit to the world's data favors large CPV is intriguing, providing further impetus for experimental input to resolve this particular question. It is central to the DUNE mission that all of the questions posed here can be addressed by neutrino oscillation experiments.

Conventional horn-focused beams, where either ν_μ or $\bar{\nu}_\mu$ is the dominant species (depending on horn current polarity), provide access to these questions for experiments at long baselines as in the case of DUNE and the LBNF. By virtue of the near-maximal value of θ_{23}, oscillations are mainly in the mode $\nu_\mu \to \nu_\tau$. For realizable baselines, this channel is best studied by measuring the ν_μ disappearance probability as a function of neutrino energy rather than through direct observation of ν_τ appearance. This is because oscillation maxima occur at energies below the threshold for τ-lepton production in ν_τ CC interactions in the detector. On the other hand, the sub-dominant $\nu_\mu \to \nu_e$ channel is amenable to detailed study through the energy dependence of the ν_e and $\bar{\nu}_e$ appearance probabilities, which is directly sensitive (in a rather complex way) to multiple PMNS matrix parameters, as described below.

Specifically, the oscillation probability of $\nu_\mu \to \nu_e$ through matter in a constant density approximation is, to first order [12]:

$$\begin{aligned} P(\nu_\mu \to \nu_e) \simeq\ & \sin^2\theta_{23}\sin^2 2\theta_{13}\frac{\sin^2(\Delta_{31}-aL)}{(\Delta_{31}-aL)^2}\Delta_{31}^2 \\ & + \sin 2\theta_{23}\sin 2\theta_{13}\sin 2\theta_{12}\frac{\sin(\Delta_{31}-aL)}{(\Delta_{31}-aL)}\Delta_{31}\frac{\sin(aL)}{(aL)}\Delta_{21}\cos(\Delta_{31}+\delta_{\rm CP}) \\ & + \cos^2\theta_{23}\sin^2 2\theta_{12}\frac{\sin^2(aL)}{(aL)^2}\Delta_{21}^2, \end{aligned} \tag{2.6}$$

where $\Delta_{ij} = \Delta m^2_{ij} L/4E_\nu$, $a = G_F N_e/\sqrt{2}$, G_F is the Fermi constant, N_e is the number density of electrons in the Earth, L is the baseline in km, and E_ν is the neutrino energy in GeV. In the equation above, both $\delta_{\rm CP}$ and a switch signs in going from the $\nu_\mu \to \nu_e$ to the $\bar{\nu}_\mu \to \bar{\nu}_e$ channel; i.e., a neutrino-antineutrino asymmetry is introduced both by CPV ($\delta_{\rm CP}$) and the matter effect (a). As is evident from equation (2.6), the matter effect introduces a sensitivity to the sign of Δ_{31}, which specifies the neutrino mass ordering. The origin of the matter effect asymmetry is simply the presence of electrons and absence of positrons in the Earth. In the few-GeV energy range, the asymmetry from the matter effect increases with baseline as the neutrinos pass through more matter; therefore an experiment with a longer baseline will be more sensitive to the neutrino mass ordering. For baselines longer than ~1200 km, the degeneracy between the asymmetries from matter and CPV effects can be resolved [13].

The electron neutrino appearance probability, $P(\nu_\mu \to \nu_e)$, is plotted in figure 2.1 at a baseline of 1300 km as a function of neutrino energy for several values of $\delta_{\rm CP}$. As this figure illustrates, the value of $\delta_{\rm CP}$ affects both the amplitude and phase of the oscillation. The difference in probability amplitude for different values of $\delta_{\rm CP}$ is larger at higher oscillation nodes, which correspond to

[2]It should be noted that recent results from the T2K experiment [11] show only marginal consistency with CP-conserving values of $\delta_{\rm CP}$.

2020 JINST 15 T08008

energies less than 1.5 GeV. Therefore, a broadband experiment, capable of measuring not only the rate of ν_e appearance but of mapping out the spectrum of observed oscillations down to energies of at least 500 MeV, is desirable.

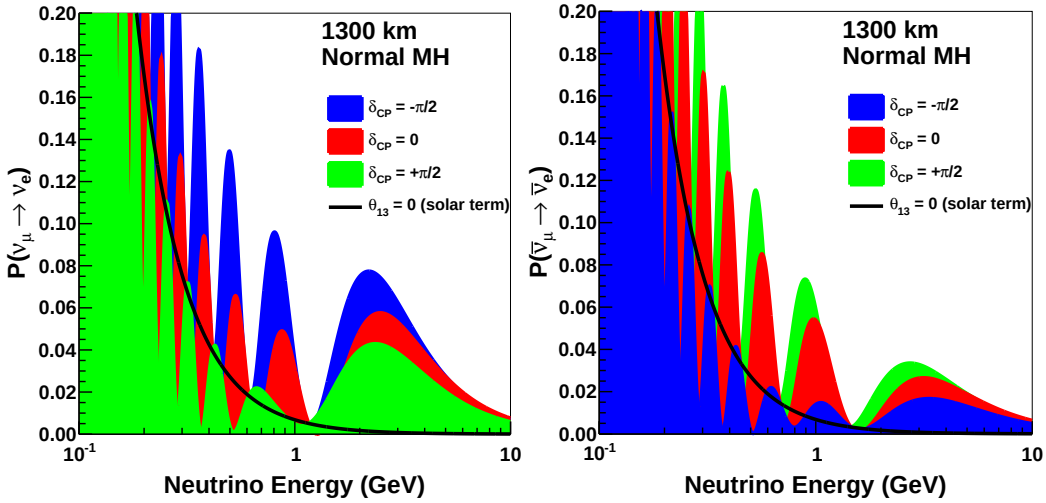

Figure 2.1. The appearance probability at a baseline of 1300 km, as a function of neutrino energy, for δ_{CP} = $-\pi/2$ (blue), 0 (red), and $\pi/2$ (green), for neutrinos (left) and antineutrinos (right), for normal ordering. The black line indicates the oscillation probability if θ_{13} were equal to zero. Note that the DUNE FD will be built at a baseline of 1300 km.

DUNE is designed to address the questions articulated above, to over-constrain the three-flavor paradigm, and to reveal what may potentially lie beyond. Even if consistency is found, the precision measurements obtained by DUNE will have profound implications. As just one example, the discovery of CPV in neutrino oscillations would provide strong circumstantial evidence for the leptogenesis mechanism as the origin of the baryon asymmetry of the universe.

Going further, the patterns defined by the fermion masses and mixing parameters have been the subject of intense theoretical activity for the last several decades. Grand unified theories posit that quarks and leptons are different manifestations of the same fundamental entities, and thus their masses and mixing parameters are related. Different models make different predictions but, in order to compare different possibilities, it is important that lepton mixing parameters be known as precisely as quark mixing parameters. To enable equal-footing comparisons between quark and lepton mixing it is required that the mixing angles be determined at the few percent level while δ_{CP} should be measured at the 10% level or better. Measurements with precision at these levels are expected from DUNE for the mixing angles θ_{23} and θ_{13}, and the CP phase δ_{CP}. These measurements will thus open a new era of flavor physics, with the potential to offer insight on deep questions on which the standard model (SM) is essentially silent.

2.1.2 Baryon number violation

Are protons stable? Few questions within elementary particle physics can be posed as simply and at the same time have implications as immediate. The apparent stability of protons suggests that baryon number is conserved in nature, although no known symmetry requires it to be so. Indeed, baryon

number conservation is implicit in the formulation of the SM Lagrangian, and thus observation of baryon-number violating (BNV) processes such as nucleon decay or neutron-antineutron oscillation would be evidence for physics beyond the SM. On the other hand, continued non-observation of BNV processes will demand an answer to what new symmetry is at play that forbids them.

Especially compelling is that the observation of BNV processes could be the harbinger for grand unified theories, in which strong, weak and electromagnetic forces are unified. Numerous GUT models have been proposed, each with distinct features. Yet, BNV processes are expected on general grounds, and it is a feature of many models that nucleon decay channels can proceed at experimentally accessible rates. This is illustrated for several key nucleon decay channels relevant for DUNE in figure 2.2, along with existing experimental limits.

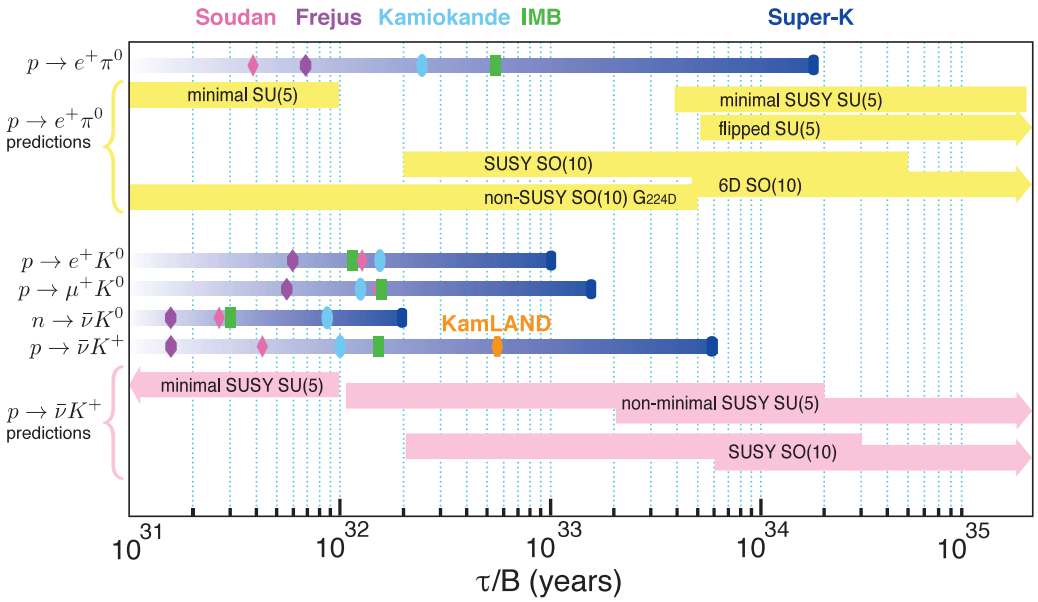

Figure 2.2. Summary of nucleon decay experimental lifetime limits from past or currently running experiments for several modes, and the model predictions for the lifetimes in the two modes $p \to e^+\pi^0$ and $p \to K^+\bar{\nu}$. The limits shown are 90% CL lower limits on the partial lifetimes, τ/B, where τ is the total mean life and B is the branching fraction. Updated from [14].

Given the scale of energy deposition in the few hundred MeV to few GeV range, a detector optimized for neutrino oscillation physics at long baselines is naturally well suited for sensitive searches for nucleon decay and neutron-antineutron oscillations. Thanks to the excellent imaging, calorimetric and particle identification capabilities of the LArTPC, backgrounds can in principle be reduced below the single-event level for key nucleon decay channels at exposures where other detector technologies are no longer background-free. On the other hand, a challenge presented by an argon-based detector is the impact of final-state interactions (FSI) on nucleon decay event reconstruction, which is expected to be more severe than for detectors based on water or liquid scintillator, for example. On balance, however, should nucleon decays occur at rates not far beyond current best limits, a handful of candidate events could be observed by DUNE in a given decay mode. For the case of zero observed candidates, DUNE has the potential to set partial lifetime limits for favorable channels at the 10^{34} year level, as indicated in section 2.3.2.

2020 JINST 15 T08008

2.1.3 Supernova neutrino bursts

The burst of neutrinos [15, 16] from the celebrated core-collapse supernova 1987A in the Large Magellanic Cloud, about 50 kiloparsecs (kpc) from Earth, heralded the era of extragalactic neutrino astronomy. The few dozen recorded $\bar{\nu}_e$ events have confirmed the basic physical picture of core collapse and yielded constraints on a wide range of new physics [17, 18].

Core-collapse supernovae within a few hundred kpc of Earth — within our own galaxy and nearby — are quite rare on a human timescale. They are expected once every few decades in the Milky Way (within about 20 kpc), and with a similar rate in Andromeda, about 700 kpc away. These core collapses should be common enough to have a reasonable chance of occurring during the few-decade long lifetime of a typical large-scale neutrino detector.

It is important that at least one module of the DUNE FD be online at all times to observe this unpredictable and spectacular event, if and when it occurs. The rarity of these events makes it all the more critical for the community to be prepared to capture every last bit of information from them.

The information in a SNB available in principle to be gathered by experimentalists is the *flavor, energy and time structure* of a several-tens-of-second-long, all-flavor, few-tens-of-MeV neutrino burst [19, 20]. Imprinted on the neutrino spectrum as a function of time is information about the progenitor, the collapse, the explosion, and the remnant, as well as information about neutrino parameters and potentially exotic new physics. Neutrino energies and flavor content of the burst can be measured only imperfectly, due to the intrinsic nature of the weak interactions of neutrinos with matter, as well as due to imperfect detection resolution in any real detector. For example, SNB energies are below CC threshold for ν_μ, ν_τ, $\bar{\nu}_\mu$, and $\bar{\nu}_\tau$ (collectively ν_x), which represent two-thirds of the flux; so these flavors are accessible only via NC interactions, which tend to have low cross sections and indistinct detector signatures. These issues make a comprehensive unfolding of neutrino flavor, time and energy structure from the observed interactions a challenging problem.

The core-collapse neutrino signal starts with a short, sharp *neutronization* (or *break-out*) burst primarily composed of ν_e. These neutrinos are messengers of the shock front breaking through the neutrinosphere (the surface of neutrino trapping): when this happens, iron is disintegrated, the neutrino scattering cross section drops, and the lepton number trapped just below the original neutrinosphere is suddenly released. This quick and intense burst is followed by an *accretion phase* lasting some hundreds of milliseconds, depending on the progenitor star mass, as matter falls onto the collapsed core and the shock is stalled at the distance of perhaps $\sim$ 200 km. The gravitational binding energy of the accreting material is powering the neutrino luminosity during this stage. The later *cooling phase* over $\sim$10 seconds represents the main part of the signal, over which the proto-neutron star sheds its trapped energy.

The flavor content and spectra of the neutrinos emitted from the neutrinosphere change throughout these phases, and the supernova's evolution can be followed with the neutrino signal. Some fairly generic features of these emitted neutrino fluxes are illustrated in figure 2.3.

In the world's current supernova neutrino flavor sensitivity portfolio [19, 22], the sensitivity is primarily to electron antineutrino flavor, via inverse beta decay. There is only minor sensitivity to the ν_e component of the flux, which carries with it particularly interesting information content of the burst (e.g., neutronization burst neutrinos are created primarily as ν_e). While there is some

2020 JINST 15 T08008

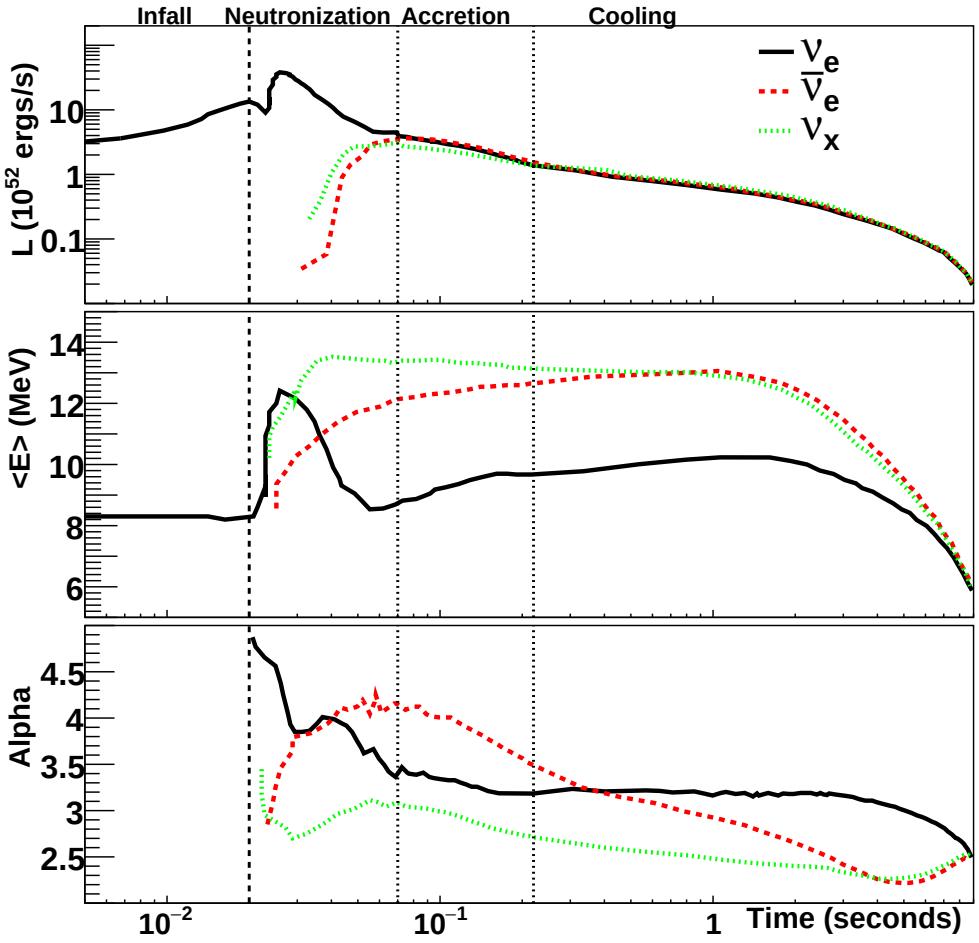

Figure 2.3. Expected time-dependent signal for a specific flux model for an electron-capture supernova [21] at 10 kpc. No oscillations are assumed; the effect of neutrino flavor transitions under different mass ordering assumptions can be dramatic and is described in Volume II Chapter 7. Note that ν_x refers to ν_μ, ν_τ, $\bar{\nu}_\mu$, and $\bar{\nu}_\tau$ collectively. The top plot shows the luminosity as a function of time (ν_x is the sum of all, the second plot shows average neutrino energy, and the third plot shows the α (pinching) parameter. The vertical dashed line at 0.02 seconds indicates the time of core bounce, and the vertical lines indicate different eras in the supernova evolution. The leftmost time interval indicates the infall period. The next interval, from core bounce to 50 ms, is the neutronization burst era, in which the flux is composed primarily of ν_e. The next period, from 50 to 200 ms, is the accretion period. The final era, from 0.2 to 9 seconds, is the proto-neutron-star cooling period. The general features are qualitatively similar for most core-collapse supernovae.

ν_e sensitivity in existing and other planned detectors via elastic scattering on electrons and via subdominant channels on nuclei, statistics are relatively small, and it can be difficult to disentangle the flavor content. It is in this respect that an experiment with an argon target such as DUNE will be especially valuable, since the dominant process in this case is ν_e CC scattering.

2.1.4 Additional Beyond-Standard-Model physics signatures

The capabilities that enable access to the physics program described in the previous sections open a myriad of opportunities to search for evidence of physics beyond the standard model. Below we list

the identified opportunities that we have investigated. Projected sensitivities are shown later in this chapter for only a few of these opportunities; we refer the reader to Volume II, DUNE physics, for a more complete demonstration of the potential impact of DUNE's searches for BSM phenomena, which can justifiably be considered as prominent ancillary elements of the DUNE science program. At the same time, it is important to note that new physics may appear in ways that have not yet been considered: history has repeatedly shown that nature can reward new experimental approaches and sensitive detectors with the appearance of entirely unanticipated phenomena.

Opportunities in BSM physics that have been considered as elements of the DUNE science program include:

Search for active-sterile neutrino mixing: DUNE is sensitive over a broad range of potential sterile neutrino mass splittings by looking for disappearance of CC and NC interactions over the long distance separating the ND and FD, as well as over the short baseline of the ND. With a longer baseline, a more intense beam, and a high-resolution large-mass FD, compared to previous experiments, DUNE provides a unique opportunity to improve significantly on the sensitivities of the existing probes, and greatly enhance the ability to map the extended parameter space if a sterile neutrino is discovered.

Searches for non-unitarity of the PMNS matrix: deviation from unitarity of the 3×3 PMNS matrix due to extra heavy neutrino states may be observable. Parameters characterizing the degree of non-unitarity can become sizable as the masses of the new states decrease.

Searches for nonstandard interactions (NSIs): NSIs affecting neutrino propagation through the Earth can significantly modify the data to be collected by DUNE as long as the new physics parameters are large enough. If the DUNE data are consistent with standard oscillations for three massive neutrinos, interaction effects of order $0.1\ G_F$ can be ruled out at DUNE.

Searches for violation of Lorentz symmetry or charge, parity, and time reversal symmetry (CPT): DUNE can improve the present limits on Lorentz and CPT violation in the neutrino sector by several orders of magnitude, contributing an important experimental test of these fundamental assumptions underlying quantum field theory.

Studies of neutrino trident production: interactions of neutrinos with the Coulomb field of a nucleus can lead to final states with a lepton-pair accompanying the lepton from the neutrino interaction vertex. With a predicted annual rate of over 100 dimuon neutrino trident interactions at the ND, DUNE will be able to measure deviations from the SM rates and test the presence of new gauge symmetries.

Search for light-mass dark matter (LDM): the lack of evidence for weakly-interacting massive particle (WIMP) dark matter (DM) candidates from direct detection and LHC experiments has resulted in a reconsideration of the WIMP paradigm, and has revitalized the effort to search for LDM candidates of around a GeV or below in mass. High-flux neutrino beam experiments, such as DUNE, have been shown to provide coverage of DM+mediator parameter space that cannot be covered by either direct detection or collider experiments. DM particles can be detected in the ND through NC-like interactions either with electrons or nucleons in the detector material and enable DUNE's search for LDM to be competitive and complementary to other experiments.

Search for boosted dark matter (BDM): using its large FD, DUNE will be able to search for BDM. In these models there are several DM particles with different masses and properties concerning their interactions with SM particles. DUNE will search for such particles as generally

produced anywhere in the cosmos or specifically through annihilation in the core of the sun, allowing competitive results for both production scenarios

Search for heavy neutral leptons (HNLs): HNLs in the context of the νMSM model with masses less than 2 GeV can be produced in the beam-dump of the proton beam to generate the DUNE neutrino beam. The ND data can be used to search for HNL decays, and competitive results with other present and proposed facilities can be obtained.

2.2 Summary of assumptions and methods employed

Scientific capabilities are determined assuming that DUNE is configured according to the general parameters described in section 1.1.4. Further assumptions regarding the neutrino beam and detector systems, and their deployment are stated here in sections 2.2.1 and 2.2.2.

Determination of experimental sensitivities relies on the modeling of the underlying physics and background processes, as well as the detector response, including calibration and event reconstruction performance and the utilization of data analysis techniques and tools. Section 2.2.3 gives a brief discussion of the strategies employed.

2.2.1 Beam and detector

Physics sensitivities are based on the optimized design of a 1.2 MW neutrino beam and corresponding protons-on-target per year assumed to be 1.1×10^{21} POT. These numbers assume a combined uptime and efficiency of the Fermilab accelerator complex and the LBNF beamline of 56%.[3]

For the neutrino oscillation physics program, it is assumed that equal exposures (time-integrated beam power times fiducial mass) are obtained with both horn current polarities, and therefore with the corresponding mix of primarily ν_μ and $\bar{\nu}_\mu$ data samples.

It is assumed that the DUNE FD will include some combination of the different 10 kt fiducial volume implementations — SP or DP — of the LArTPC concept for which technical designs have been developed. For much of the science program it is expected that the capabilities of the two proposed FD module implementations will be comparable. As a result of the current state of reconstruction and analysis software development (see section 2.2.3), the physics sensitivity studies reported in this TDR are based on the SP LArTPC implementation, documented in full in Volume IV.

It is also assumed that validation of the DUNE FD designs will come from data and operational experience acquired with the large-scale ProtoDUNE detectors staged at the CERN, including single-particle studies of data obtained in test-beam running.

The ND for DUNE has been under active development, and a CDR is in preparation. Correspondingly, the descriptions in this TDR are consistent with this level of development.

2.2.2 Deployment scenario

Where presented as a function of calendar year, sensitivities are calculated with the following assumed deployment plan, which is based on a technically limited schedule:

[3]This projection, from which one year of LBNF beam operations (live time) can be expressed as 1.7×10^7 seconds, is based on extensive experience with intense neutrino beams at Fermilab, and in particular the NuMI beam line, which incorporates elements like those in the proposed LBNF beamline design and faces similar operating conditions.

- Start of beam run: two FD module volumes for total fiducial mass of 20 kt, 1.2 MW beam;
- After one year: add one FD module volume for total fiducial mass of 30 kt;
- After three years: add one FD module volume for total fiducial mass of 40 kt; and
- After six years: upgrade to 2.4 MW beam.

2.2.3 Simulation, reconstruction, and data analysis tools

The development of algorithms and software infrastructure needed to carry out physics sensitivity studies has been an active effort within DUNE and the associated scientific community. Significant progress has been made: event reconstruction codes can be run on fully simulated neutrino interaction events in DUNE FD modules; the DUNE computing infrastructure allows high-statistics production runs; and end-user interfaces are functioning. Robust end-to-end analyses not previously possible have now been performed and are being reported in this document.

For some aspects — for example, beamline modeling and GeV-scale neutrino interaction simulations — well-developed and validated (with data) software packages have been available throughout much of DUNE's design phase. For others, corresponding tools did not exist and needed to be either developed from scratch or adapted with substantial modifications from other experimental programs. Concurrent with these development efforts, interim descriptions such as parametric detector response modeling, necessarily simple but based on reasonable extrapolation from experience and dedicated studies, were employed to assess physics capabilities. Even for the case of the better-developed tools — again, neutrino interaction modeling is a good example — significant incremental improvements have been made as data from neutrino experiments and other sources have become available and as theoretical understandings have advanced.

As a result of the rapid pace of development as well as practical considerations including human resource availability, different levels of rigor have been applied in the evaluation of physics capabilities for different elements of the program. The strategy adopted for this TDR has been to hold the primary elements of the program to the highest standard of rigor, involving direct analysis of fully simulated data, using actual event reconstruction codes and analysis tools that could be applied to real data from DUNE FD modules. For other elements of the program, sensitivities use realistic beam and physics simulations, but employ parametric detector response models in place of full reconstruction.

The implementation of this strategy comes with caveats and clarifications that are discussed in the corresponding chapters of Volume II. We mention some of these here.

- In the case of the long-baseline oscillation physics program, this approach requires a combination of the full end-to-end analysis of simulated FD data with the concurrent analysis of simulated data from ND systems to capture in a realistic way the level of control over systematic errors. Given the current state of development of the DUNE ND design and corresponding analysis tools, it has been necessary to employ parametric detector response modeling for ND components.
- In the case of the nucleon decay searches, reconstruction and analysis tools dedicated to addressing the particular challenges presented are not as well developed as in the case of the

beam-based oscillation physics program. Effort is ongoing to improve the performance of these tools.

- The SNB program relies on reconstruction of event signatures from LArTPC signals generated by low-energy (MeV-scale) particles (electrons and de-excitation gammas). Full simulation and reconstruction is used for some studies, such as for those demonstrating the supernova pointing capability of DUNE. For other studies, a modified strategy is employed in order to efficiently explore model space: reconstruction metrics (resolution smearing matrices, for example) are derived from analysis of fully simulated and reconstructed low-energy particles and events in the FD, and are applied to understanding the mean detector response over a range of signal predictions.

- For scientific program elements where analysis of fully reconstructed simulated data has not yet been performed, the parametric response models used for the analyses presented here have been well characterized with dedicated studies and incorporation of results from other experiments. The demonstration of sensitivities for the long-baseline oscillation physics program (with full reconstruction) that are comparable to those previously obtained based on parametric response validates this approach.

2.3 Selected results from sensitivity studies

In this section, selected sensitivity projections from the central elements of the DUNE science program are presented. This selection is intended to convey just the headlines from what is an extensive and diverse program of frontier science.

2.3.1 CPV in the neutrino sector and precise oscillation parameter measurements

The key strength of the DUNE design concept is its ability to robustly measure the oscillation patterns of ν_μ and $\bar{\nu}_\mu$ over a range of energies spanning the first and second oscillation maxima.

This is accomplished by a coordinated analysis of the reconstructed ν_μ, $\bar{\nu}_\mu$, ν_e, and $\bar{\nu}_e$ energy spectra in near and far detectors, incorporating data collected with forward (neutrino-dominated) and reverse (antineutrino-dominated) horn current polarities.

The statistical power of DUNE relative to the current generation of long-baseline oscillation experiments is a result of many factors including (1) on-axis operations, (2) the LBNF beam power, (3) long-baseline and correspondingly high energy oscillation maxima and strong separation of normal and inverted neutrino mass ordering scenarios, (4) detector mass, and (5) event reconstruction and selection capabilities. Tables 2.1 and 2.2 give the expected event yields for the appearance (ν_e and $\bar{\nu}_e$) and disappearance (ν_μ and $\bar{\nu}_\mu$) channels, respectively, after seven years of operation. For these estimates, $\delta_{\mathrm{CP}} = 0$ is assumed, and values for other parameters are taken from the NuFIT 4.0 [23, 24] global fit to world neutrino data. (See also [25] and [26] for other recent global fits.) The DUNE ν_e and $\bar{\nu}_e$ event yields represent order-of-magnitude increases relative to those in the current NOvA [27] and T2K [11, 28] data samples, while the corresponding increases are even larger for the ν_μ and $\bar{\nu}_\mu$ channels thanks to DUNE's on-axis exposure to the LBNF beam. Figures 2.4 and 2.5 show the corresponding distributions in reconstructed neutrino energy.

2020 JINST 15 T08008

Table 2.1. ν_e and $\bar{\nu}_e$ appearance yields: integrated yield of selected ν_e CC-like events between 0.5 and 8.0 GeV assuming 3.5-year (staged) exposures in the neutrino-beam and antineutrino-beam modes. The signal yields are shown for both normal mass ordering (NO) and inverted mass ordering (IO), and all the background yields assume normal mass ordering. All the yields assume $\delta_{CP} = 0$, and NuFIT 4.0 [23, 24] values for other parameters.

	Expected Events (3.5 years staged per mode)	
	ν mode	$\bar{\nu}$ mode
ν_e signal NO (IO)	1092 (497)	76 (36)
$\bar{\nu}_e$ signal NO (IO)	18 (31)	224 (470)
Total signal NO (IO)	1110 (528)	300 (506)
Beam $\nu_e + \bar{\nu}_e$ CC background	190	117
NC background	81	38
$\nu_\tau + \bar{\nu}_\tau$ CC background	32	20
$\nu_\mu + \bar{\nu}_\mu$ CC background	14	5
Total background	317	180

Table 2.2. ν_μ and $\bar{\nu}_\mu$ disappearance yields: integrated yield of selected ν_μ CC-like events between 0.5 and 8.0 GeV assuming a 3.5-year (staged) exposure in the neutrino-beam mode and antineutrino-beam mode. The yields are shown for normal mass ordering and $\delta_{CP} = 0$.

	Expected Events (3.5 years staged)
ν mode	
ν_μ Signal	6200
$\bar{\nu}_\mu$ CC background	389
NC background	200
$\nu_\tau + \bar{\nu}_\tau$ CC background	46
$\nu_e + \bar{\nu}_e$ CC background	8
$\bar{\nu}$ mode	
$\bar{\nu}_\mu$ signal	2303
ν_μ CC background	1129
NC background	101
$\nu_\tau + \bar{\nu}_\tau$ CC background	27
$\nu_e + \bar{\nu}_e$ CC background	2

2020 JINST 15 T08008

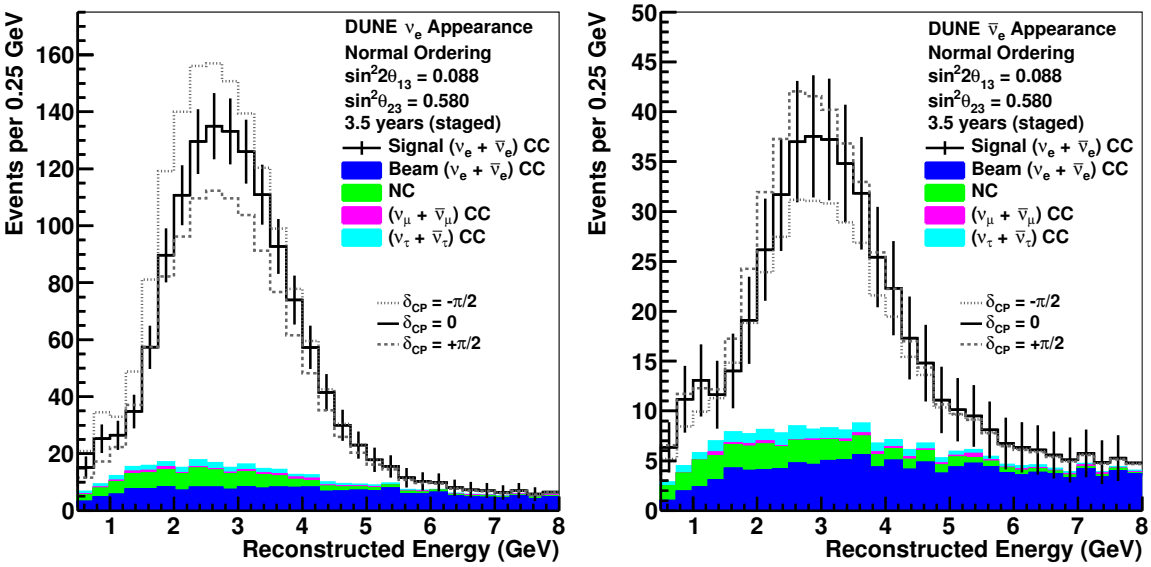

Figure 2.4. ν_e and $\bar{\nu}_e$ appearance spectra: reconstructed energy distribution of selected ν_e CC-like events assuming 3.5 years (staged) running in the neutrino-beam mode (left) and antineutrino-beam mode (right), for a total of seven years (staged) exposure. The plots assume normal mass ordering and include curves for $\delta_{CP} = -\pi/2, 0$, and $\pi/2$.

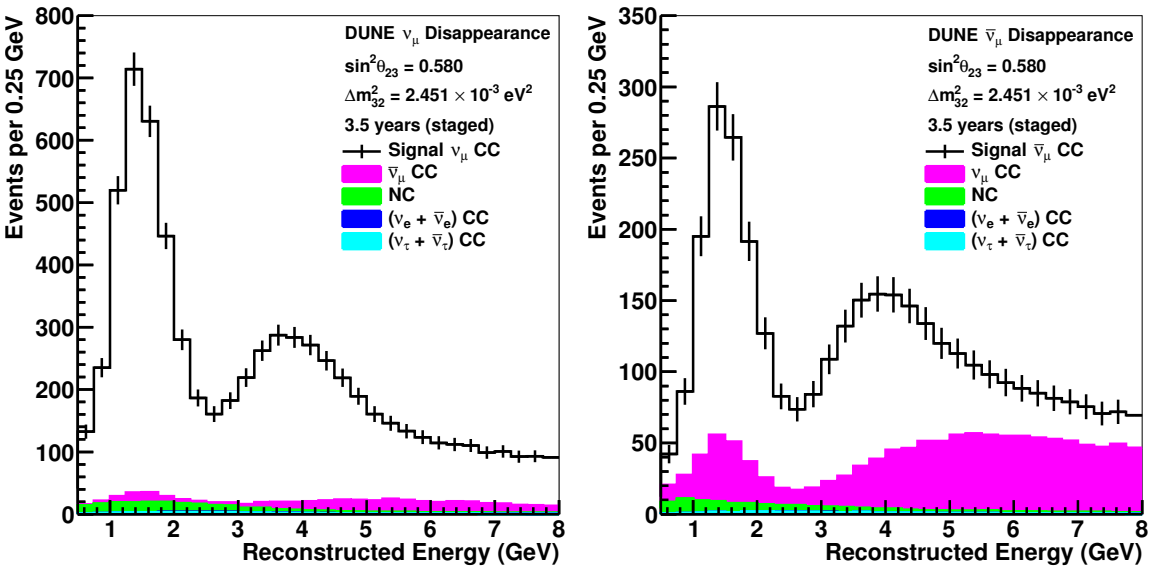

Figure 2.5. ν_μ and $\bar{\nu}_\mu$ disappearance spectra: reconstructed energy distribution of selected ν_μ CC-like events assuming 3.5 years (staged) running in the neutrino-beam mode (left) and antineutrino-beam mode (right), for a total of seven years (staged) exposure. The plots assume normal mass ordering.

Experimental sensitivities were evaluated based on the methodologies described in the preceding section, including incorporation of ND simulations and uncertainties from all known sources of systematic error. Considerable attention and sophistication has been applied to the treatment of systematic errors and the crucial role of the ND, both of which are documented in Volume II, DUNE physics.

A summary of representative sensitivity milestones for neutrino mass ordering and CPV discovery, as well as precision on δ_{CP} and $\sin^2 2\theta_{13}$ is given in table 2.3. The ultimate level of precision that can be obtained on oscillation parameters highlights the point that DUNE will provide crucial input for flavor physics: patterns required by particular symmetries underlying fermion masses and mixing angles may appear. The unitarity of the neutrino mixing matrix can be tested directly through comparisons of $\sin^2 2\theta_{13}$ with the value obtained from reactor experiments. In conjunction with $\sin^2 2\theta_{13}$ and other parameters, the precise value of δ_{CP} can constrain models of leptogenesis that are leading candidates for explanation of the baryon asymmetry of the universe.

Table 2.3. Exposure in years, assuming true normal ordering and equal running in neutrino and antineutrino mode, required to reach selected physics milestones in the nominal analysis, using the NuFIT 4.0 [23, 24] best-fit values for the oscillation parameters. As discussed in Volume II, DUNE physics, chapter 5, there are significant variations in sensitivity with the value of $\sin^2 \theta_{23}$, so the exact values quoted here (using $\sin^2 \theta_{23}$ = 0.580) are strongly dependent on that choice. The staging scenario presented in section 2.2.2 is assumed. Exposures are rounded to the nearest "staged" calendar year. For reference, 30, 100, 200, 336, 624, and 1104 kt · MW · year correspond to 1.2, 3.1, 5.2, 7, 10, and 15 staged years, respectively.

Physics Milestone	Exposure (staged years)
5σ mass ordering (δ_{CP} = -π/2)	1
5σ mass ordering (100% of δ_{CP} values)	2
3σ CPV (δ_{CP} = -π/2)	3
3σ CPV (50% of δ_{CP} values)	5
5σ CPV (δ_{CP} = $-\pi/2$)	7
5σ CPV (50% of δ_{CP} values)	10
3σ CPV (75% of δ_{CP} values)	13
δ_{CP} resolution of 10 degrees (δ_{CP} = 0)	8
δ_{CP} resolution of 20 degrees (δ_{CP} = -π/2)	12
$\sin^2 2\theta_{13}$ resolution of 0.004	15

The milestones presented in table 2.3 form a coarse snapshot of the DUNE program in oscillation physics, demonstrating the prospects for important results throughout the lifetime of the experiment. More detail on the sensitivities for the individual program elements is presented in the sections below.

2.3.1.1 Discovery potential for CPV and neutrino mass ordering

Figure 2.6 illustrates DUNE's ability to distinguish the value of the CP phase $\delta_{\rm CP}$ from CP-conserving values (0 or π) as a function of time in calendar year. These projections incorporate a sophisticated treatment of systematic error, as described in detail in Volume II, DUNE physics, chapter 5. Evidence ($> 3\sigma$) for CPV is obtained for favorable values (half of the phase space) of $\delta_{\rm CP}$ after five years of running, leading to a $> 5\sigma$ observation after ten years.

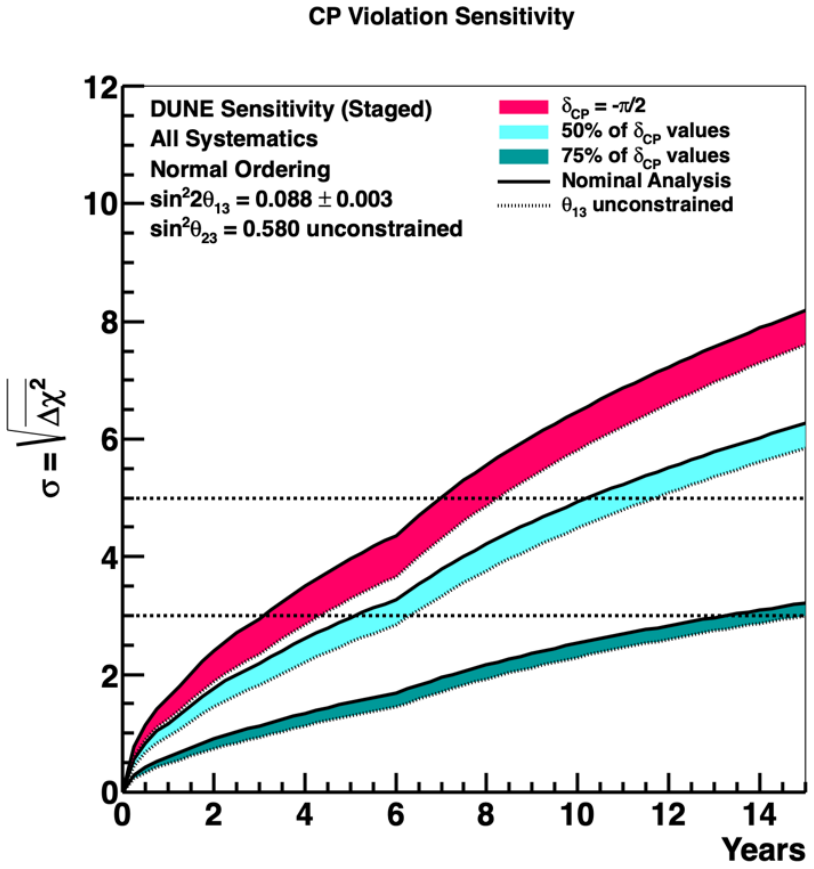

Figure 2.6. Significance of the DUNE determination of CP-violation (i.e.: $\delta_{\rm CP} \neq 0$ or π) for the case when $\delta_{\rm CP} = -\pi/2$, and for 50% and 75% of possible true $\delta_{\rm CP}$ values, as a function of time in calendar years. True normal ordering is assumed. The width of the band shows the impact of applying an external constraint on $\sin^2 2\theta_{13}$.

Figure 2.7 shows the significance with which the neutrino mass ordering can be determined for 100% of δ_{CP} values, and when $\delta_{CP} = -\pi/2$, as a function of exposure in years. The width of the bands show the impact of applying an external constraint on $\sin^2 2\theta_{13}$. As DUNE will be able to establish the neutrino mass ordering at the 5σ level for 100% of δ_{CP} values after 2-3 years, this plot extends only to seven years.

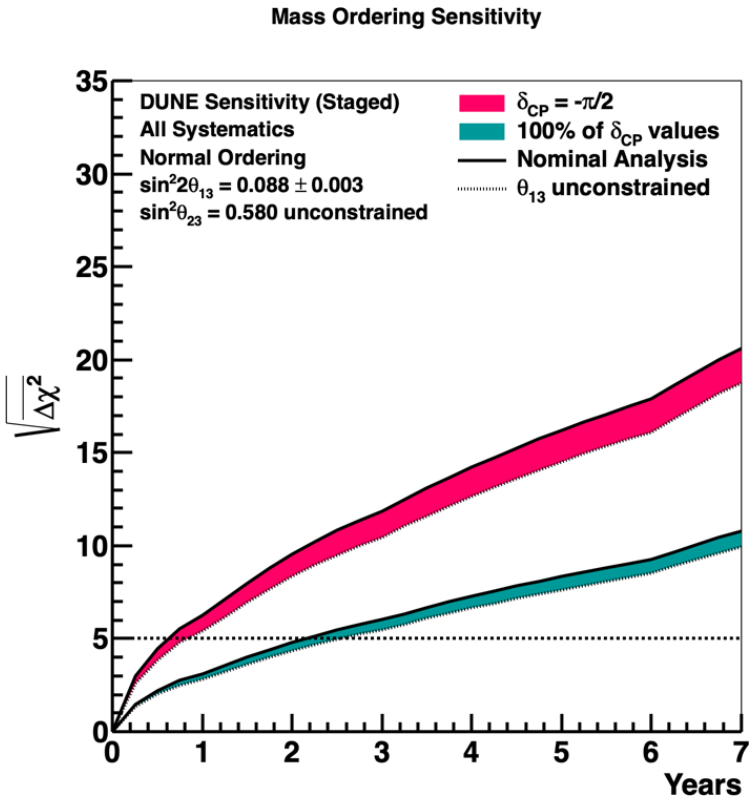

Figure 2.7. Significance of the DUNE determination of the neutrino mass ordering for the case when δ_{CP} $=-\pi/2$, and for 100% of possible true δ_{CP} values, as a function of time in calendar years. True normal ordering is assumed. The width of the band shows the impact of applying an external constraint on $\sin^2 2\theta_{13}$.

2.3.1.2 Precision measurement of mass and mixing parameters

In addition to the discovery potential for neutrino mass ordering and CPV, DUNE will improve the precision on key parameters that govern neutrino oscillations, including: δ_{CP}, $\sin^2 2\theta_{13}$, Δm^2_{31}, $\sin^2 \theta_{23}$, and the octant of θ_{23}.

Figure 2.8 shows the resolution, in degrees, of DUNE's measurement of δ_{CP} as a function of the true value of δ_{CP}. The resolution of this measurement is significantly better near CP-conserving values of δ_{CP}, compared to maximally CP-violating values. For fifteen years of exposure, resolutions between five and fifteen degrees are possible, depending on the true value of δ_{CP}.

Figures 2.9 and 2.10 show the resolution of DUNE's measurements of δ_{CP} and $\sin^2 2\theta_{13}$ and of $\sin^2 2\theta_{23}$ and Δm^2_{32}, respectively, as a function of exposure in kt-MW-years. As seen in figure 2.8, the δ_{CP} resolution varies significantly with the true value of δ_{CP}, but for favorable values, resolutions near five degrees are possible for large exposure. The DUNE measurement of $\sin^2 2\theta_{13}$ approaches

2020 JINST 15 T08008

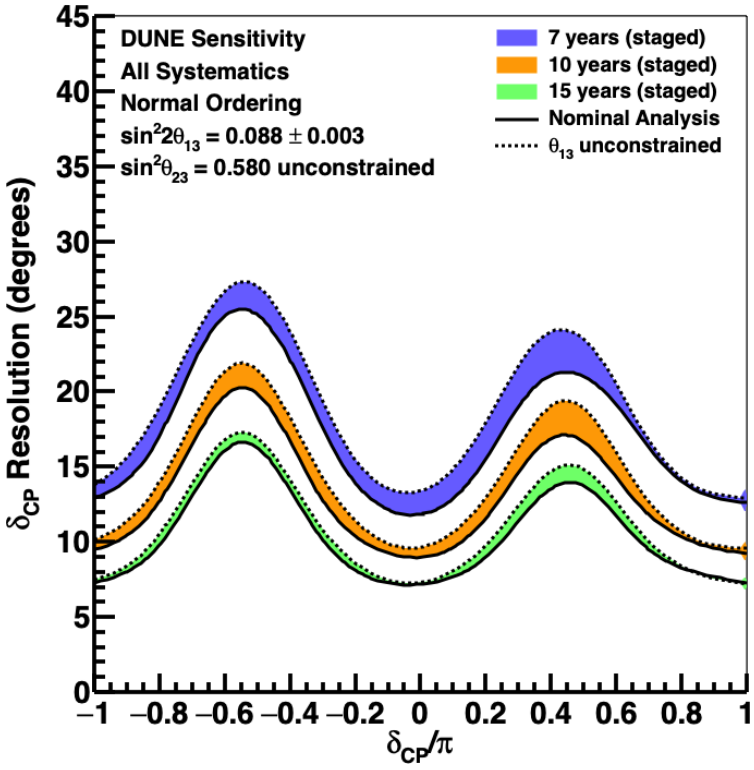

Figure 2.8. Resolution in degrees for the DUNE measurement of δ_{CP}, as a function of the true value of δ_{CP}, for seven (blue), ten (orange), and fifteen (green) years of exposure. True normal ordering is assumed. The width of the band shows the impact of applying an external constraint on $\sin^2 2\theta_{13}$.

the precision of reactor experiments for high exposure, allowing a comparison between the two results, which is of interest as a test of the unitarity of the PMNS matrix.

One of the principal strengths of DUNE is its ability to simultaneously measure all oscillation parameters governing long-baseline neutrino oscillation, without a need for external constraints. As an example, figure 2.11 shows the 90% C.L. allowed regions for $\sin^2 2\theta_{13}$ (left) and $\sin^2 \theta_{23}$ (right) versus δ_{CP} for 7, 10 and 15 years of running, compared to the current measurements from world data.

The measurement of $\nu_\mu \rightarrow \nu_\mu$ oscillations is sensitive to $\sin^2 2\theta_{23}$, whereas the measurement of $\nu_\mu \rightarrow \nu_e$ oscillations is sensitive to $\sin^2 \theta_{23}$. A combination of both ν_e appearance and ν_μ disappearance measurements can probe both maximal mixing and the θ_{23} octant. Figure 2.12 shows the sensitivity to determining the octant as a function of the true value of $\sin^2 \theta_{23}$.

2.3.2 Proton decay and other baryon-number violating processes

By virtue of its deep underground location and large fiducial mass, as well as its excellent event imaging, particle identification and calorimetric capabilities, the DUNE FD will be a powerful instrument to probe baryon-number violation. DUNE will be able to observe signatures of decays of protons and neutrons, as well as the phenomenon of neutron-antineutron mixing, at rates below the limits placed by the current generation of experiments.

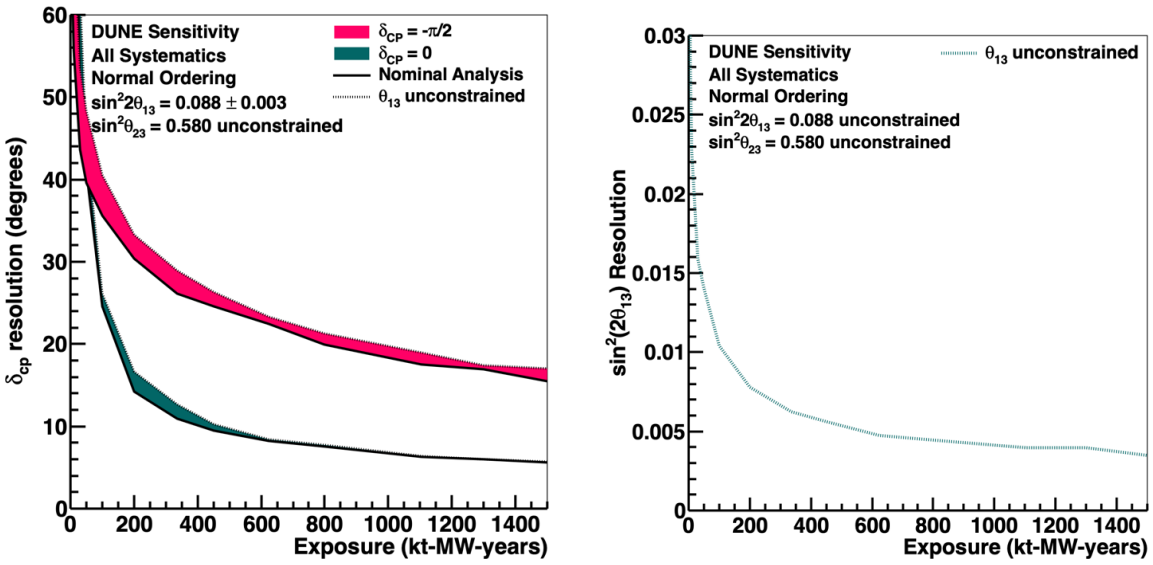

Figure 2.9. Resolution of DUNE measurements of δ_{CP} (left) and $\sin^2 2\theta_{13}$ (right), as a function of exposure in kt-MW-years. As seen in figure 2.8, the δ_{CP} resolution has a significant dependence on the true value of δ_{CP}, so curves for $\delta_{\mathrm{CP}} = -\pi/2$ (red) and $\delta_{\mathrm{CP}} = 0$ (green) are shown. The width of the band shows the impact of applying an external constraint on $\sin^2 2\theta_{13}$. For the $\sin^2 2\theta_{13}$ resolution, an external constraint does not make sense, so only the unconstrained curve is shown. For reference, 336, 624, and 1104 kt · MW · year correspond to 7, 10, and 15 staged years, respectively.

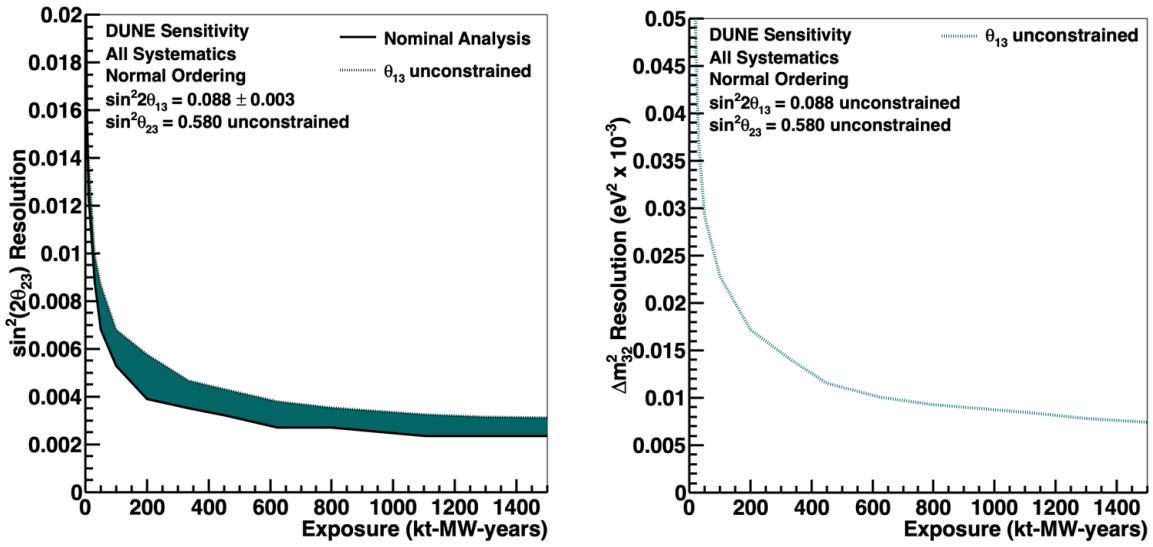

Figure 2.10. Resolution of DUNE measurements of $\sin^2 2\theta_{23}$ (left) and Δm^2_{32} (right), as a function of exposure in kt-MW-years. The width of the band for the $\sin^2 2\theta_{23}$ resolution shows the impact of applying an external constraint on $\sin^2 2\theta_{13}$. For the Δm^2_{32} resolution, an external constraint does not have a significant impact, so only the unconstrained curve is shown. For reference, 336, 624, and 1104 kt · MW · year correspond to 7, 10, and 15 staged years, respectively.

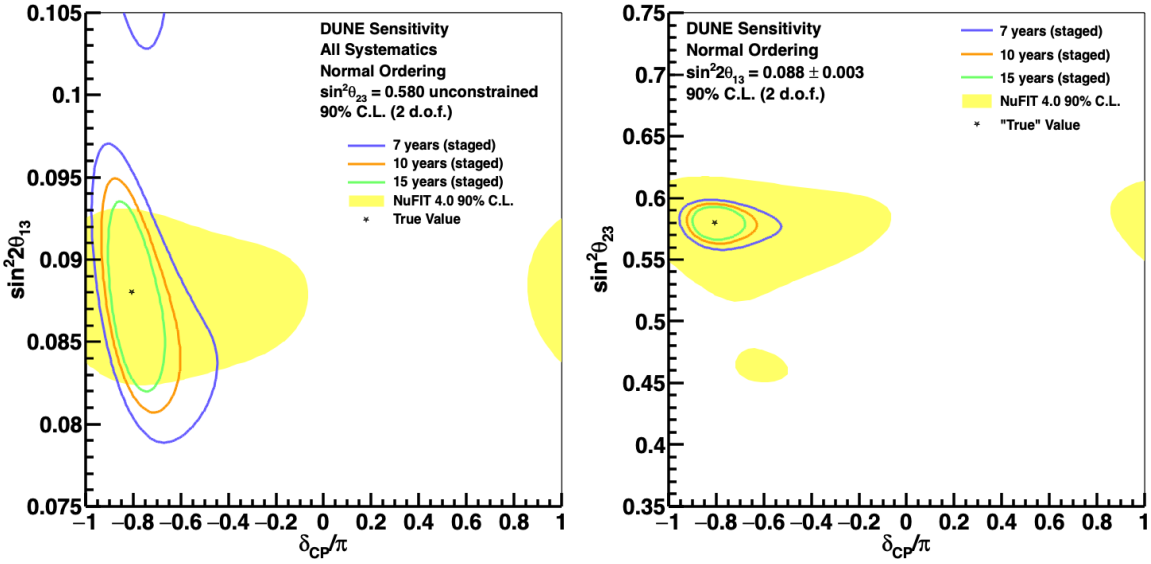

Figure 2.11. Left: two-dimensional 90% C.L. region in $\sin^2 2\theta_{13}$ and δ_{CP}, for 7, 10, and 15 years of exposure, with equal running in neutrino and antineutrino mode. The 90% C. L. region for the NuFIT 4.0 global fit is shown in yellow for comparison. The true values of the oscillation parameters are assumed to be the central values of the NuFIT 4.0 global fit and the oscillation parameters governing long-baseline oscillation are unconstrained. Right: corresponding region in $\sin^2 \theta_{23}$ and δ_{CP}. In this case, $\sin^2 2\theta_{13}$ is constrained by NuFIT 4.0.

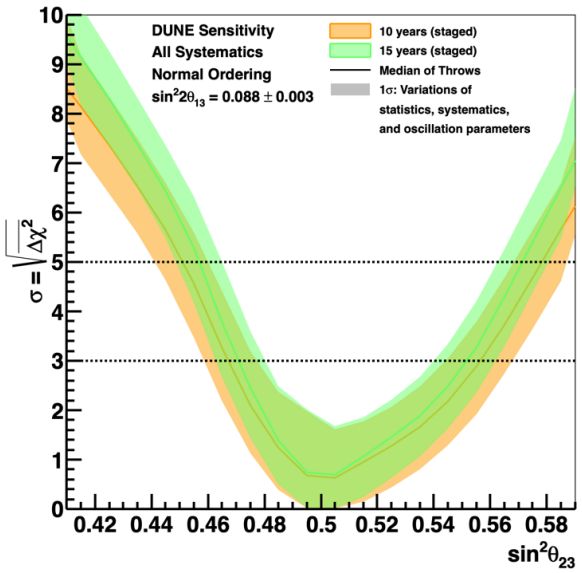

Figure 2.12. Sensitivity to determination of the θ_{23} octant as a function of the true value of $\sin^2 \theta_{23}$, for ten (orange) and fifteen (green) years of exposure. True normal ordering is assumed. The width of the transparent bands cover 68% of fits in which random throws are used to simulate statistical variations and select true values of the oscillation and systematic uncertainty parameters, constrained by pre-fit uncertainties. The solid lines show the median sensitivity.

Many nucleon decay modes are accessible to DUNE. As a benchmark, a particularly compelling discovery channel is the decay of a proton to a positive kaon and a neutrino, $p \rightarrow K^{+}\overline{\nu}$. In this channel, the kaon and its decay products can be imaged, identified, and tested for kinematic consistency with the full decay chain, together with precision sufficient to reject backgrounds due to atmospheric muon and neutrino interactions. Preliminary analysis of single-particle beam and cosmic ray tracks in the ProtoDUNE-SP LArTPC is already demonstrating the particle identification capability of DUNE, as illustrated in figure 2.13. The signature of the kaon track and its observable decay particles is sufficiently rich that a credible claim of evidence for proton decay could be made on the basis of just one or two sufficiently well-imaged events, for the case where background sources are expected to contribute much less than one event.

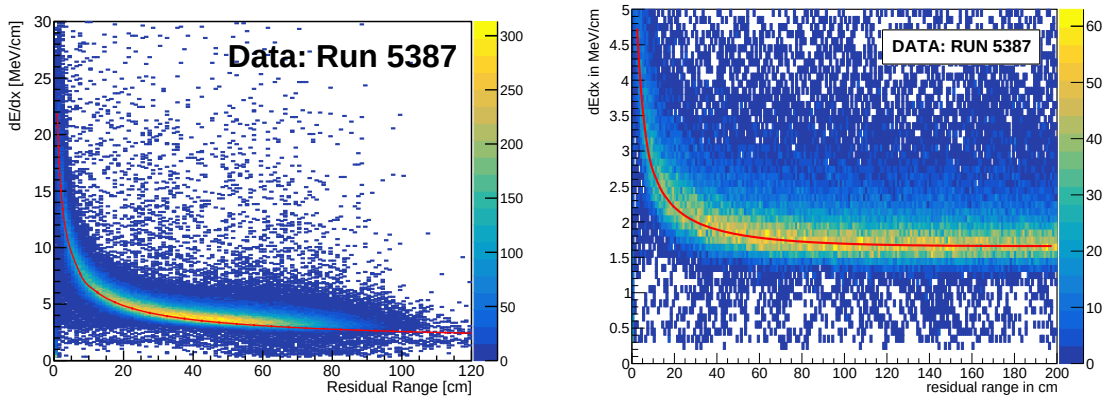

Figure 2.13. Energy loss of protons (left) and muons (right) in 1-GeV running with the ProtoDUNE-SP LArTPC at CERN, as a function of residual range. The protons are beam particles identified from beamline instrumentation; the muons are reconstructed stopping cosmic rays collected concurrently. The red curves represent the mean of the corresponding expected signature. Note the difference in the vertical scale of the two plots. The kaon dE/dx curve will lie between the two curves shown.

Projecting from the current analysis of $p \rightarrow K^{+}\overline{\nu}$ in the DUNE FD, with a detection efficiency of 30% as described in Volume II, DUNE physics, chapter 6, the expected 90% C.L. lower limit on lifetime divided by branching fraction is 1.3×10^{34} years for a 400 kt · year exposure, assuming no candidate events are observed. This is roughly twice the current limit of 5.9×10^{33} years from Super–Kamiokande [29], based on an exposure of 260 kt · year . Thus, should the rate for this decay be at the current Super–Kamiokande limit, five candidate events would be expected in DUNE within ten years of running with four FD modules. Ongoing work is aimed at improving the efficiency in this and other channels.

2.3.3 Galactic supernovae via measurements of neutrino bursts

As has been demonstrated with SN1987a, the observation of neutrinos [15, 16] from a core-collapse supernova can reveal much about these phenomena that is not accessible in its electromagnetic signature. Correspondingly, there is a wide range of predictions from supernova models for even very basic characteristics of the SNBs. Typical models predict that a supernova explosion in the center of the Milky Way will result in several thousand detectable neutrino interactions in the DUNE

2020 JINST 15 T08008

FD occurring over an interval of up to a few tens of seconds. The neutrino energy spectrum peaks around 10 MeV, with appreciable flux up to about 30 MeV.

LAr based detectors are sensitive to the ν_e component of the flux, while water Cherenkov and organic scintillator detectors are most sensitive to the $\bar{\nu}_e$ component. Thus DUNE is uniquely positioned to study the neutronization burst, in which ν_e's are produced during the first few tens of milliseconds. More generally, measurements of the (flavor-dependent) neutrino flux and energy spectrum as a function of time over the entirety of the burst can be sensitive to astrophysical properties of the supernova and its progenitor, and distortions relative to nominal expectations can serve as signatures for phenomena such as shock wave and turbulence effects, or even black hole formation.

Below, we present the results of analyses of DUNE's capabilities for two elements of the SNB program: (1) fits to the reconstructed neutrino energy spectrum and comparison to models in which none of the distortions listed above are present, and (2) neutrino flux direction determination for angular localization of the supernova position.

2.3.3.1 Results from fits to pinched thermal neutrino energy spectrum

The physics of neutrino decoupling and spectra formation is far from trivial, owing to the energy dependence of the cross sections and the roles played by both CC and NC reactions. Detailed transport calculations using methods such as Monte Carlo (MC) or Boltzmann solvers have been employed. It has been observed that spectra coming out of such simulations can typically be parameterized at a given moment in time by the following ansatz (e.g., [30, 31]):

$$\phi(E_\nu) = \mathcal{N} \left(\frac{E_\nu}{\langle E_\nu \rangle} \right)^\alpha \exp \left[-(\alpha + 1) \frac{E_\nu}{\langle E_\nu \rangle} \right], \tag{2.7}$$

where E_ν is the neutrino energy, $\langle E_\nu \rangle$ is the mean neutrino energy, α is a "pinching parameter," and $\mathcal{N}$ is a normalization constant that can be related to the total binding energy release of the supernova, denoted ε in the discussion below. Large α corresponds to a more "pinched" spectrum (suppressed high-energy tail). This parameterization is referred to as a "pinched-thermal" form. The different ν_e, $\overline{\nu}_e$ and ν_x, $x = \mu, \tau$ flavors are expected to have different average energy and α parameters and to evolve differently in time. The primary experimental task is to determine the true neutrino spectrum from the observed supernova event spectrum. Given that the spectrum is well described by the functional form in equation 2.7, this task is approximately equivalent to that of fitting the threepinched-thermal parameters $(\alpha^0, \langle E_\nu \rangle^0, \varepsilon^0)$ that carry the spectral information.

To evaluate DUNE's capabilities, we have developed a forward fitting algorithm requiring a binned reconstructed neutrino energy spectrum expected for a supernova at a given distance generated with a "true" set of these parameters. Figure 2.14 shows an example of a resulting fit, with the approximate parameters for several specific supernova models superimposed to illustrate the potential for discrimination between them.

2.3.3.2 Pointing sensitivity of DUNE

An illustration of another element of the DUNE SNB program is given in figure 2.15, which indicates a pointing resolution of better than 5° that can be obtained by analysis of both subdominant highly-directional ν-e elastic scattering events and dominant weakly-directional ν_e CC events within a SNB,

2020 JINST 15 T08008

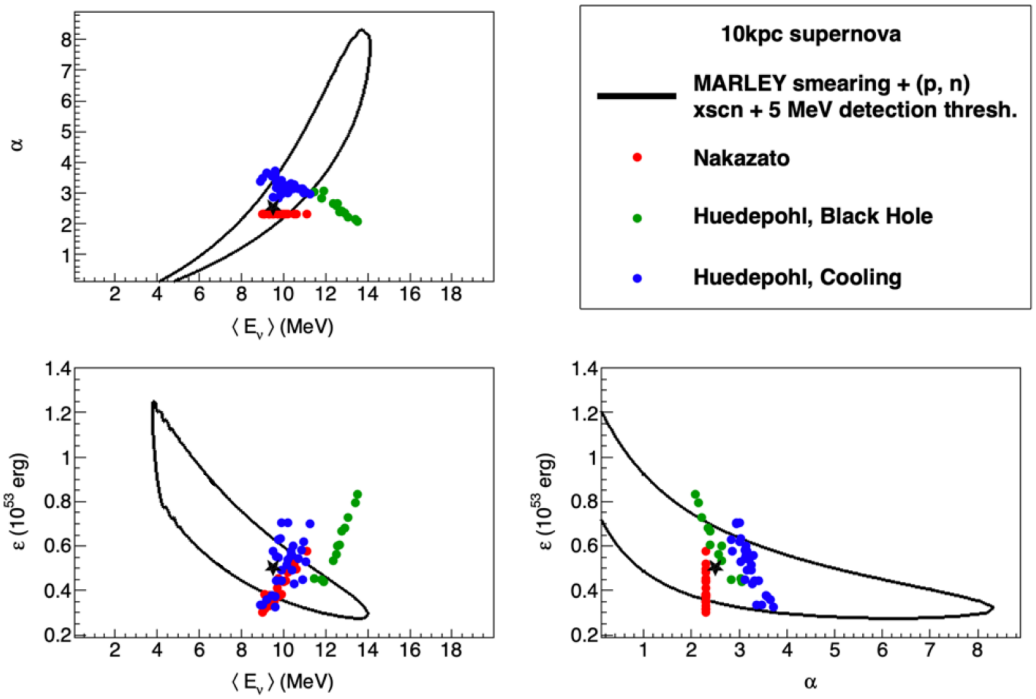

Figure 2.14. Estimated sensitivity regions for DUNE's determination of the three supernova spectra parameters at 90% C.L. given the assumed true value indicated by the black star. The simulated data were generated for a supernova at 10 kpc with a neutrino interaction model appropriate for low energies, realistic detector smearing, and a step efficiency function with a 5 MeV detected energy threshold. To indicate the expected range of possible true flux parameters, superimposed are parameters corresponding to the time-integrated flux for three different sets of models: Nakazato [32], Huedepohl black hole formation models, and Huedepohl cooling models [33]. For the Nakazato parameters (for which there is no explicit pinching, corresponding to $\alpha = 2.3$), the parameters are taken directly from the reference; for the Huedepohl models, they are fit to a time-integrated flux.

based on full reconstruction and analysis. The DUNE results can be combined with corresponding measurements in other neutrino detectors to provide supernova localization from neutrinos alone in real time.

2.3.4 Searches for Beyond-Standard-Model physics

The unique combination of the high-intensity LBNF neutrino beam with DUNE's ND and massive LArTPC FD modules at a 1300 km baseline enables a variety of probes of BSM physics, either novel or with unprecedented sensitivity.

As examples of the potential impact of DUNE, we present results from the analysis of simulated data sets for two BSM scenarios, one with a sterile neutrino species participating in oscillations, and the other with anomalous "neutrino trident" events. From the sterile neutrino analysis, the DUNE sensitivities to the effective mixing angle $\theta_{\mu e}$ (which depends on new mixing angles θ_{14} and θ_{24}), from the appearance and disappearance samples at the ND and FD are shown in figure 2.16.

Considering a neutrino trident analysis in ND data, existing constraints and projected sensitivity to parameters of a Z' boson resulting from the gauging of the difference between muon and tau

2020 JINST 15 T08008

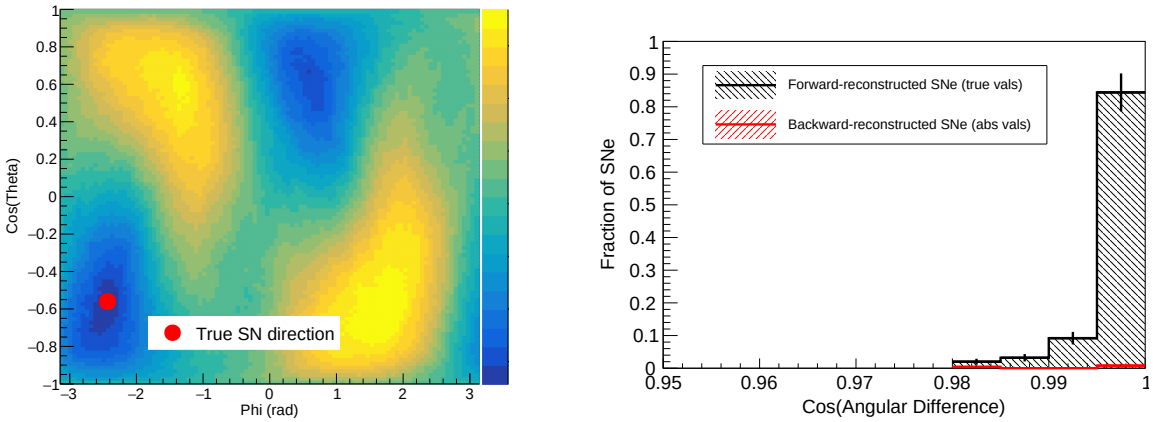

Figure 2.15. Left: log likelihood values as a function of direction for a supernova sample with 260 ν-e elastic scattering (ES) events. Right: distribution of angular differences for directions to 10 kpc supernova using a maximum likelihood method.

lepton numbers, $L_\mu - L_\tau$, are presented in figure 2.17. This plot indicates that DUNE can cover much of parameter space for which this model is able to explain the departure of the present observed muon $g-2$ central value from standard model expectations.

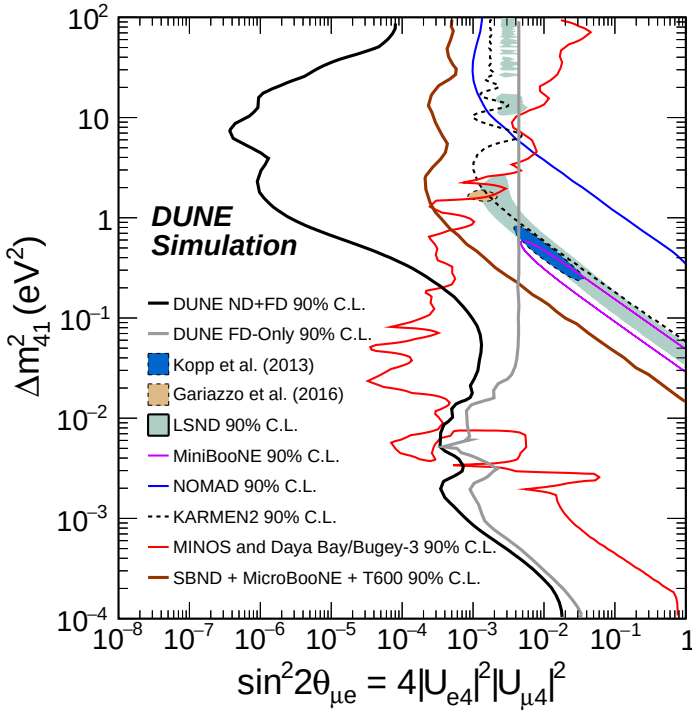

Figure 2.16. DUNE 90% C.L. sensitivities to $\theta_{\mu e}$ from the appearance and disappearance samples at the ND and FD is shown along with a comparison with previous existing experiments and the sensitivity from the future SBN program. Regions to the right of the DUNE contours are excluded.

2020 JINST 15 T08008

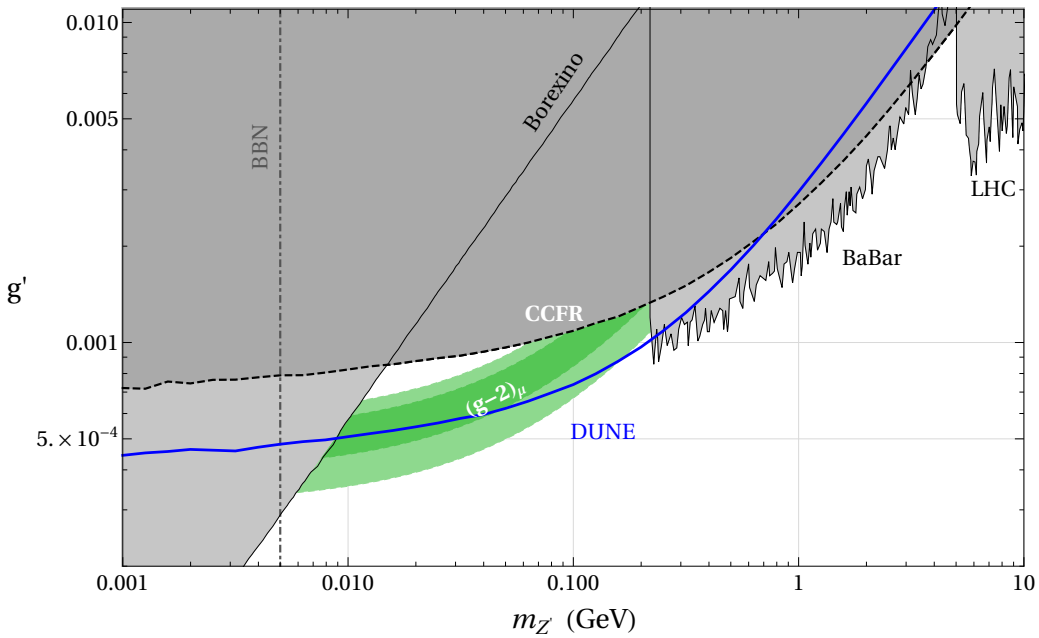

Figure 2.17. Existing constraints and projected DUNE sensitivity in the Z' parameter spaced associated with gauging $L_\mu - L_\tau$. Shown in green is the region where the $(g-2)_\mu$ anomaly can be explained at the 2σ level. The parameter regions already excluded by existing constraints are shaded in gray and correspond to a CMS search for $pp \to \mu^+\mu^- Z' \to \mu^+\mu^-\mu^+\mu^-$ [34] ("LHC"), a BaBar search for $e^+e^- \to \mu^+\mu^- Z' \to \mu^+\mu^-\mu^+\mu^-$ [35] ("BaBar"), a previous measurement of the trident cross section [36, 37] ("CCFR"), a measurement of the scattering rate of solar neutrinos on electrons [38–40] ("Borexino"), and bounds from Big Bang Nucleosynthesis [41, 42] ("BBN"). The DUNE sensitivity shown by the solid blue line assumes a measurement of the trident cross section with 40% precision.

2020 JINST 15 T08008

Chapter 3

Single-phase far detector technology

This chapter provides a brief introduction to the single-phase (SP) far detector technology. The text below closely follows that found in the introductory chapter of Volume IV, The DUNE far detector single-phase technology, where many more details may be found.

3.1 Overview

The overriding physics goals of DUNE are to search for leptonic CPV and for nucleon decay as a signature of a GUT underlying the SM, as well as to observe neutrino bursts from supernovae. Central to achieving this physics program is constructing a detector that combines the many-kiloton fiducial mass necessary for rare event searches with sub-centimeter spatial resolution in its ability to image those events, allowing us to identify the signatures of the physics processes we seek among the many backgrounds. The SP LArTPC [43] allows us to achieve these dual goals, providing a way to read out with sub-centimeter granularity the patterns of ionization in 10 kt volumes of LAr resulting from the $O(1\,\text{MeV})$ interactions of solar and supernova neutrinos up to the $O(1\,\text{GeV})$ interactions of neutrinos from the LBNF beam.

To search for leptonic CPV, we must study ν_e appearance in the LBNF ν_μ beam. This requires the ability to separate electromagnetic activity induced by CC ν_e interactions from similar activity arising from photons, such as photons from π^0 decay. Two signatures allow this. First, photon showers are typically preceded by a gap prior to conversion, characterized by the 18 cm conversion length in LAr. Second, the initial part of a photon shower, where an electron-positron pair is produced, has twice the dE/dx of the initial part of an electron-induced shower. To search for nucleon decay, where the primary channel of interest is $p \rightarrow K^+\overline{\nu}$, we must identify kaon tracks as short as a few centimeters. It is also vital to accurately fiducialize these nucleon-decay events to suppress cosmic-muon-induced backgrounds, and here detecting argon-scintillation photons is important in determining the time of the event. Detecting a SNB poses different challenges: those of dealing with a high data rate and maintaining the high detector up-time required to ensure we do not miss one of these rare events. The signature of an SNB is a collection of MeV-energy electron tracks a few centimeters in length from CC ν_e interactions, spread over the entire detector volume. To fully reconstruct an SNB, the entire detector must be read out, a data-rate of up to 2 TB/s, for 30 s to 100 s, including a $\sim$4 s pre-trigger window.

Figure 1.5 in section 1.3.1 shows a schematic of the general operating principle of a SP LArTPC. A large volume of LAr is subjected to a strong E field of a few hundred volts per centimeter. Charged particles passing through the detector ionize the argon atoms, and the ionization electrons drift in the E field to the anode wall (called an APA array) on a timescale of milliseconds. The SP module APAs consist of layers of active wires strung at angles to each other to form a grid. The relative voltage between the layers is chosen to ensure that all but the final layer are transparent to the drifting electrons, and these first layers produce bipolar induction signals as the electrons pass through them. The final layer collects the drifting electrons, resulting in a monopolar signal.

LAr is also an excellent scintillator, emitting VUV light at a wavelength of 127 nm. This prompt scintillation light, which crosses the detector on a timescale of nanoseconds, is shifted into the visible and collected by PDs. The PDs can provide a t_0 determination for events, indicating when the ionization electrons began to drift. Relative to this t_0, the time at which the ionization electrons reach the anode allows reconstruction of the event topology along the drift direction, which is crucial to fiducialize nucleon-decay events and to apply drift corrections to the ionization charge.

The pattern of current observed on the grid of anode wires provides information for reconstruction in the two coordinates perpendicular to the drift direction. The wire pitch on the wire layers is chosen to optimize considerations of spatial resolution, cost, and S/N of the ionization measurement. S/N is important because the measurement of the ionization collected is a direct measurement of the dE/dx of the charged particles, which is what enables both calorimetry and particle identification (PID).

Figure 1.7 in section 1.3.1.1 shows a 10 kt fiducial mass SP module (17.5 kt total mass); the key parameters of a SP module are listed in table 3.1. Inside a cryostat of outer dimensions 65.8 m (L) by 18.9 m (W) by 17.8 m (H), shown in figure 3.1, four 3.5 m drift volumes are created between five alternating APA and CPA arrays, each of dimensions 58.2 m (L) by 12.0 m (H).

Table 3.1. Key parameters for a 10 kt FD SP module.

Item	Quantity
TPC size	12.0 m × 14.0 m × 58.2 m
Nominal fiducial mass	10 kt
APA size	6 m × 2.3 m
CPA size	1.2 m × 4 m
Number of APAs	150
Number of CPAs	300
Number of X-ARAPUCA PD bars	1500
X-ARAPUCA PD bar size	209 cm × 12 cm × 2 cm
Design voltage	−180 kV
Design drift field	500 V/cm
Drift length	3.5 m
Drift speed	1.6 mm/µs

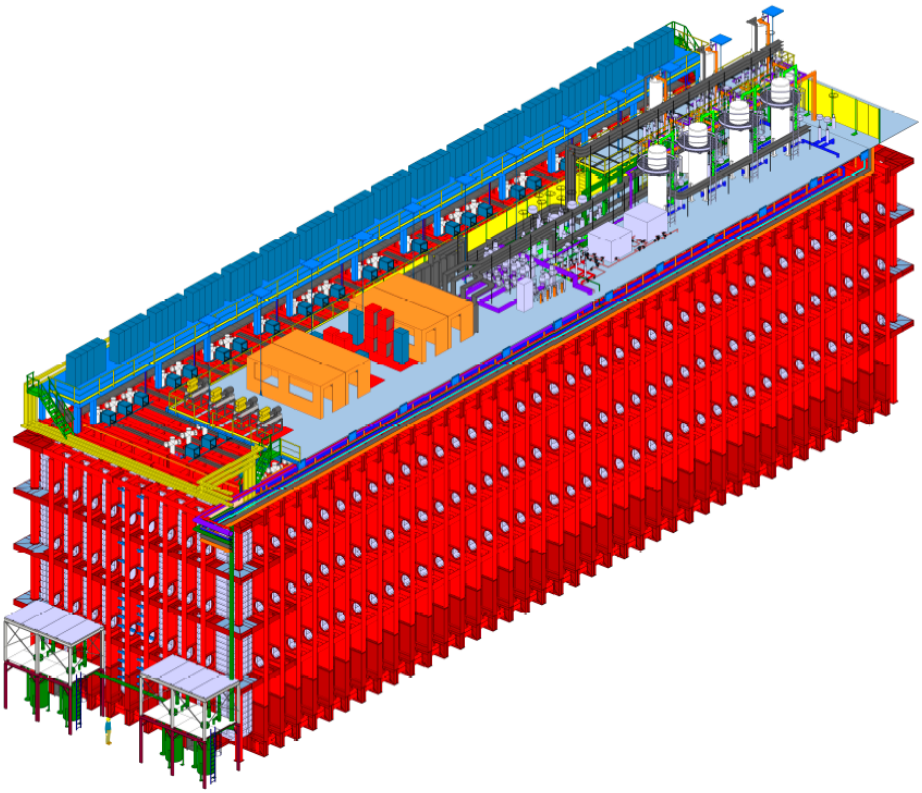

Figure 3.1. A 65.8 m (L) by 18.9 m (W) by 17.8 m (H) outer-dimension cryostat that houses a 10 kt FD module. A mezzanine (light blue) installed 2.3 m above the cryostat supports both detector and cryogenics instrumentation. At lower left, between the LAr recirculation pumps (green) installed on the cavern floor, the figure of a person indicates the scale.

The target purity from electronegative contaminants in the argon is < 100 parts per trillion (ppt) O_2 equivalent, enough to ensure a > 3 ms ionization-electron lifetime at the nominal 500 V/cm drift voltage. This target electron lifetime ensures S/N of > 5 for the induction planes and > 10 for the collection planes, which are necessary to perform pattern recognition and two-track separation.

Nitrogen contamination must be < 25 parts per million (ppm) to ensure we achieve our requirement of at least 0.5 photoelectrons per MeV detected for events in all parts of the detector, which in turn ensures that we can fiducialize nucleon decay events throughout the detector.

3.2 Anode planes

The modular anode walls are each made up of 50 APAs (25 along the module length and two high), each 6 m $\times$ 2.3 m. Figure 3.2 shows a schematic and a photograph. As figure 3.3 shows, the APAs hang vertically. The APAs are two-sided, with three active wire layers and an additional shielding layer, sometimes called a grid layer, wrapped around them. The wire spacing on the layers is ~ 5 mm. The collection layer is called the X layer; the induction layer immediately next to that is called the V layer; the next induction layer is the U layer; and the shielding layer is the G layer. The X and G layer wires run vertically when installed (figure 3.2 shows them horizontal); the U and V layer wires are at $\pm 35.7°$ to the vertical. The wire spacing on each plane defines the spatial

resolution of the APA; it is wide enough to keep readout costs low and S/N high, but small enough to enable reconstruction of short tracks such as few-cm kaon tracks from proton decay events.

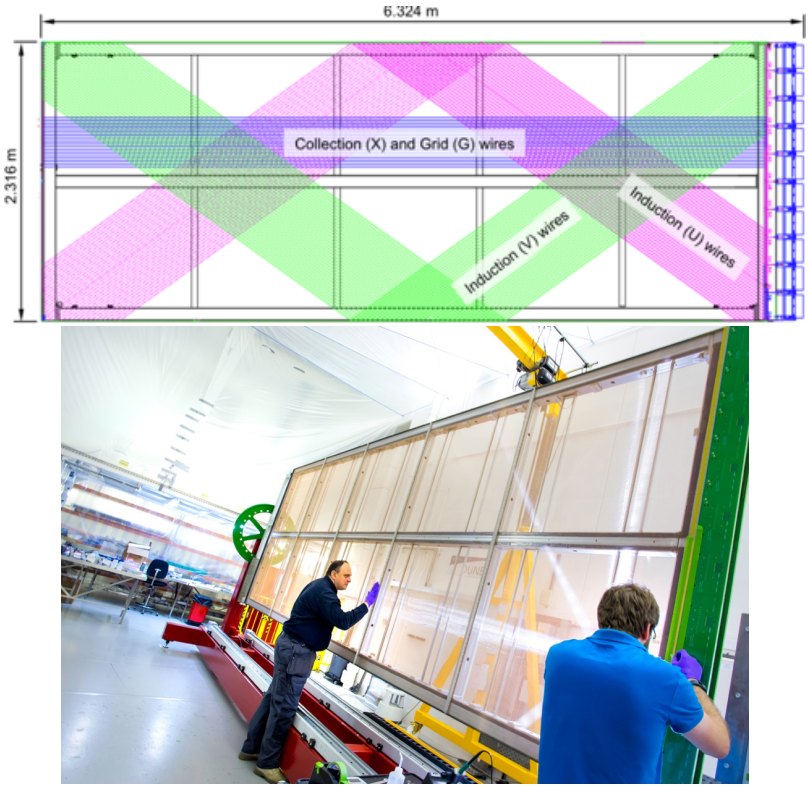

Figure 3.2. Top: a schematic of an APA. The steel APA frame is shown in black. The green and magenta lines indicate the directions of the induction wire layers. The blue lines indicate the directions of the induction and shielding (grid) wire layers. The blue boxes at the right end are the CE. Bottom: a ProtoDUNE-SP APA in a wire-winding machine. The end on the right is the head end, onto which the CE are mounted.

3.3 Cathode planes and high voltage

Each of the module's two cathode plane assembly (CPA) arrays is formed from 150 CPAs (50 along the length, stacked three high), each of which is a 1.2 m × 4 m resistive panel. Each CPA has its own independent HV supply, providing a current of 0.16 mA at −180 kV. With the APA arrays held close to ground, this results in a uniform 500 V/cm E field across the drift volume. A typical minimum ionizing particle (MIP) passing through the argon produces roughly 60k ionization electrons per centimeter that drift toward the anodes at approximately 1.6 mm/µs. The time to cover the full drift distance is about 2.2 ms.

A FC built from field-shaping aluminum profiles surrounds the drift volumes, keeping the E field uniform throughout the active TPC volume to within 1%. The aluminum profiles are connected via a resistive divider chain; between each profile, two 5 GΩ resistors, arranged in parallel, provide 2.5 GΩ resistance to create a nominal 3 kV drop. The FC is illustrated in figure 3.4.

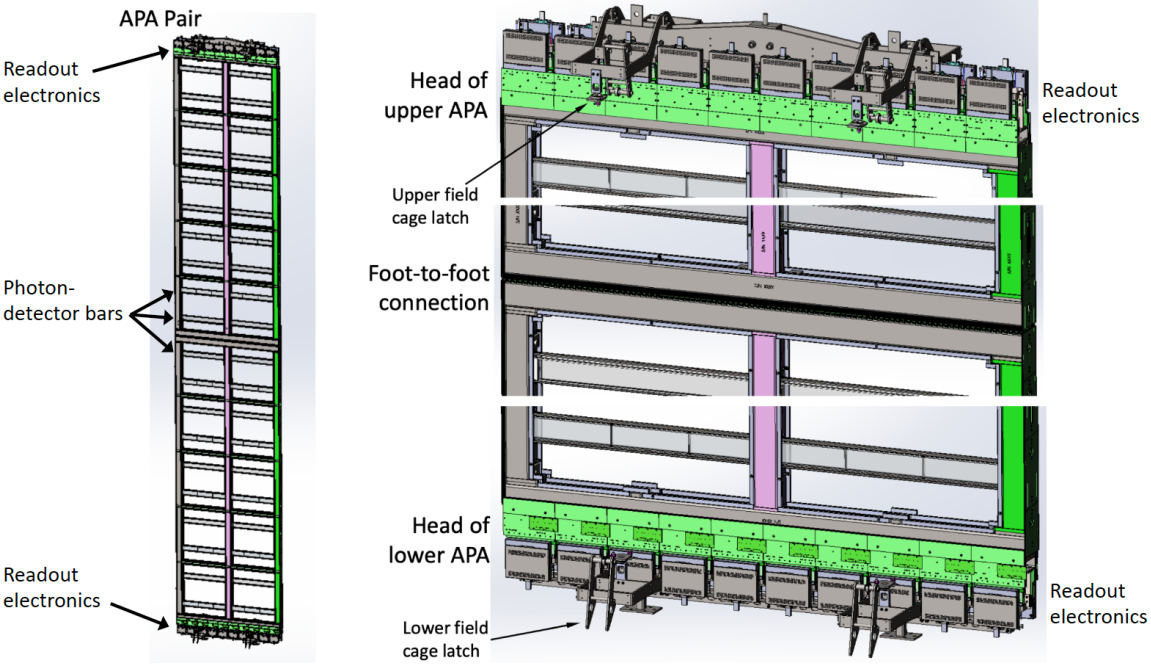

Figure 3.3. Left: two vertically linked APAs form one unit of an APA array. PD bars are installed across the width of the APAs. Right: a zoom into only the top and bottom ends of the APA stack (notice the breaks in white). This shows the readout electronics and the center of the stack where the APAs are connected.

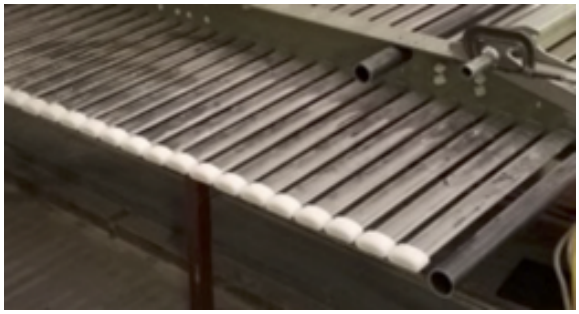

Figure 3.4. A section of the field cage, showing the extruded aluminum field-shaping profiles, with white polyethylene caps on the ends to prevent discharges.

3.4 Electronics

Front-end (FE) readout electronics (in the LAr), called cold electronics (CE), are attached to the top end of the top APA and the bottom end of the bottom APA. Benefitting from a reduction in thermal noise due to the low temperature, the CE shape, amplify, and digitize the signals from the APA induction and collection wires thanks to a series of three different types of ASICs through which all signals pass. Outside the cryostat, signals are passed to warm interface boards (WIBs) that put the signals onto 10 GB optical fibers, ten per APA, which will carry the signals to the upstream DAQ system in the CUC. Each detector module has an independent DAQ system that allows it to run as an independent detector, thereby minimizing any chance of a complete FD outage. Modules can,

however, provide the others with an SNB trigger signal. The DAQ system also provides the detector clock.

To enable observation of low-energy particles, we plan to keep noise below 1000 e^- per channel, which should be compared to the 20k–30k e^- per channel collected from a MIP traveling parallel to the wire plane and perpendicular to the wire orientation. For large signals, we require a linear response up to 500k e^-, which ensures that fewer than 10% of beam events experience saturation. This can be achieved using 12 analog-to-digital converter (ADC) bits. The CE are designed with an FE peaking time of 1 µs, which matches the time for the electrons to drift between wire planes on the APA; this leads to a design sampling frequency of 2 MHz to satisfy the Nyquist criterion.

3.5 Photon detection system

In addition to the ionization, charged particles passing through the argon produce approximately 24,000 scintillation photons per MeV. The scintillation photons are fast, arriving at the photon detectors (PDs) nanoseconds after production. This scintillation light provides a t_0 for each event. Comparison of the arrival time of ionization at the anode with this t_0 enables reconstruction in the drift direction. The SP module implementation enables ~ 1 mm position resolution for 10 MeV SNB events. The PD t_0 is also vital in fiducializing nucleon decay events, which allows us to reject cosmic-muon-induced background events that will occur near the edges of the detector modules.

The photons are collected by devices called X-ARAPUCAs, which are mounted in the APA frames between the sets of wire layers, as shown in figure 3.3. The X-ARAPUCAs consist of layers of dichroic filter and wavelength-shifter, illustrated in figure 3.5, that shift the VUV scintillation light into the visible range trap the visible photons, and transport them to SiPM devices. The signals from these SiPMs are sent along cables that pass through the hollow APA frames, up to feedthroughs in the cryostat roof. The PD and APA-wire data-streams are merged at the DAQ.

PD modules, shown in figure 3.6, are 209 cm × 12 cm × 2 cm bars that each hold 24 X-ARAPUCAs. Ten PD modules are mounted in each APA between the wire layers.

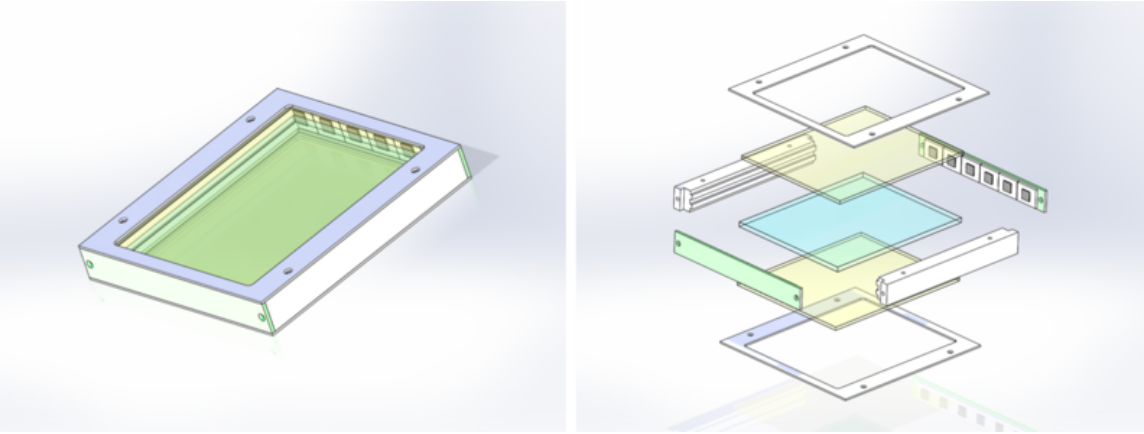

Figure 3.5. Left: an X-ARAPUCA cell. Right: an exploded view of the X-ARAPUCA cell, where the blue sheet is the WLS plate and the yellow sheets are the dichroic filters.

2020 JINST 15 T08008

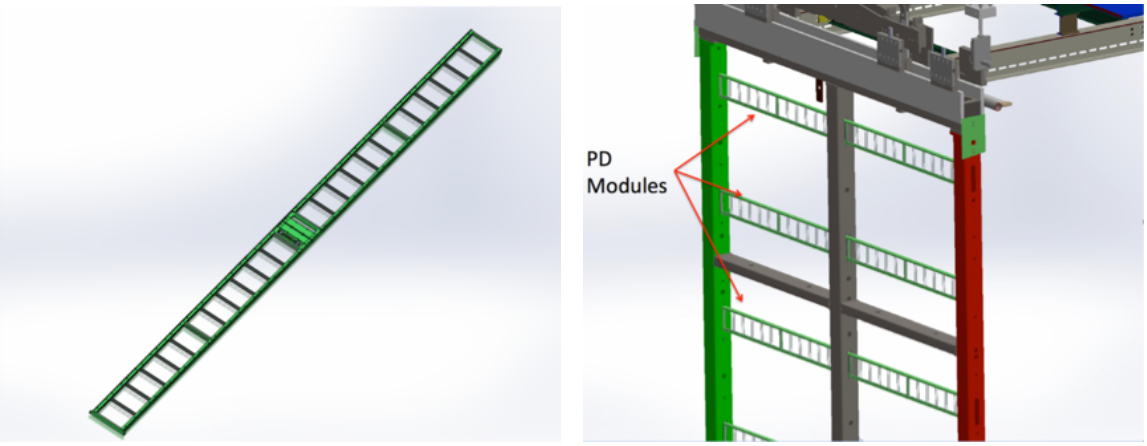

Figure 3.6. Left: an X-ARAPUCA PD module. The 48 SiPMs that detect the light from the 24 cells are along the long edges of the module. Right: X-ARAPUCA PD modules mounted inside an APA.

The 48 SiPMs on each X-ARAPUCA supercell are ganged together, and the signals are collected by FE electronics, mounted on the supercell. The design of the FE electronics is inspired by the system used for the Mu2e cosmic-ray tagger [44], which uses commercial ultrasound ASICs. The FE electronics define the 1 µs timing resolution of the PD system.

3.6 Calibration

The challenge of calibrating the DUNE FD is controlling the response of a huge cryogenic detector over a period of decades, a challenge amplified by the detector's location deep underground and therefore shielded from the cosmic muons that have typically been used as standard candles for LArTPCs. The FD calibration system has been designed jointly for the SP and DP technologies, and uses the same strategies and systems for both.

To achieve our GeV-scale oscillation and nucleon decay physics goals, we must know our fiducial volume to 1–2% and have a similar understanding of the vertex position resolution; understand the ν_e event rate to 2%; and control our lepton energy scales to 1% and hadron energy scales to 3%. At the MeV scale, our physics requirements are driven by our goal of identifying and measuring the spectral structure of an SNB; here, we must achieve a 20–30% energy resolution, understand our event timing to the 1 µs level, and measure our trigger efficiency and levels of radiological background.

The tools available to us for calibration include the LBNF beam, atmospheric neutrinos, atmospheric muons, radiological backgrounds, and dedicated calibration devices installed in the detector. At the lowest energies, we have deployable neutron sources and intrinsic radioactive sources; in particular, the natural ^{39}Ar component of the LAr with its 565 keV end-point, given its pervasive nature across the detector, can be used to measure the spatial and temporal variations in electron lifetime. The possibility of deploying radioactive sources is also under study. In the 10 MeV to 100 MeV energy range, we will use Michel electrons, photons from π^0 decay, stopping protons, and both stopping and through-going muons. We will also have built-in lasers, purity monitors, and thermometers, as well as the ability to inject charge into the readout electronics.

2020 JINST 15 T08008

Finally, data from the ProtoDUNE detectors (section 1.3.2) will be invaluable in understanding the response and particle ID (PID) capabilities of the FD.

Over time, the FD calibration program will evolve as statistics from cosmic rays and the LBNF beam amass and add to the information gained from the calibration hardware systems. These many calibration tools will work alongside the detector monitoring system, the computational fluid dynamics (CFD) models of the argon flow, and ProtoDUNE data to give us a detailed understanding of the FD response across the DUNE physics program.

3.7 Data acquisition

The DAQ systems for the SP and DP technologies have been designed jointly and are identical except for the architecture of the detector readout electronics. The output format of the generated data is common, and both are synchronized to the same global clock signals. The DAQ architecture is based on the Front-End Link eXchange (FELIX) system designed at CERN and used for the LHC experiments.

The DAQ is divided between an upstream section, located underground in the CUC, and a downstream DAQ back-end subsystem (DAQ BE) to be located above ground at the SURF. All trigger decisions are made upstream, and the data is buffered underground until the DAQ BE indicates it is ready to receive data; this controls the rate of data flowing to the surface. An end-goal of the DAQ is to achieve a data rate to tape of no more than 30 PB/year.

For the SP module, the 150 APAs are processed by 75 DAQ readout units (DAQ RUs); each DAQ RU contains one FELIX board. The PDs from the module will have a lower data rate because the PD electronics, unlike the TPC electronics, perform zero-suppression; therefore, the PDs of a module will be processed by six to eight additional DAQ RUs. The DAQ can be partitioned: it will be possible to run multiple instances of the DAQ simultaneously, so most of the detector can be taking physics data while other DAQ instances are doing test runs for development or special runs such as calibration runs.

Two basic triggers will be operating. Beam, cosmic, and nucleon decay events will be triggered using the localized high-energy trigger that will open a readout window of 5.4 ms, enough to read out the full TPC drift around an event. For SNBs, we will use an extended low-energy trigger. This will look for coincident regions of low-energy deposits, below 10 MeV, across an entire module and in a 10 s period. An extended high-energy trigger will open a readout window of 100 s to capture a full SNB.

The DAQ must also provide the system clock that keeps the detector components synchronized and timestamps all data. The timestamp derives from a Global Positioning System (GPS) one-pulse-per-second signal (1PPS signal) fed into the DAQ with 1 µs precision, adequate for beam and SNB events. To provide finer synchronization between detector components, a 10 MHz reference clock drives the module's 62.5 MHz master clock, which is fanned out to all detector components, providing an overall synchronization to a precision of 1 ns.

2020 JINST 15 T08008

3.8 Cryogenics instrumentation and slow controls

DUNE's CISC system is responsible for recognizing and preventing fault conditions that could develop in a detector module over long periods of running. The SP and DP modules will use a CISC system that has been designed jointly.

Cryogenics instrumentation includes purity monitors, various types of temperature monitors, and cameras with their associated light emitting systems. Also included are gas analyzers and LAr level monitors that are directly related to the external cryogenics system, which have substantial interfaces with LBNF.

Cryogenics instrumentation requires significant engineering, physics, and simulation work, such as E field simulations and cryogenics modeling studies using computational fluid dynamics (CFD). E field simulations identify desirable locations for instrumentation devices in the cryostat, away from regions of high E field, so that their presence does not induce large field distortions. CFD simulations help identify expected temperature, impurity, and velocity flow distributions and guide the placement and distribution of instrumentation devices inside the cryostat.

The slow controls portion of CISC consists of three main components: hardware, infrastructure, and software. The slow controls hardware and infrastructure comprises networking hardware, signal processing hardware, computing hardware, and associated rack infrastructure. The slow controls software provides, for every slow control quantity, the central slow controls processing architecture, databases, alarms, archiving, and control room displays.

3.9 Installation

A significant challenge for DUNE is transporting all detector and infrastructure components down the 1500 m Ross shaft and through drifts to a detector cavern. The 150 anode plane assemblies, each 6.0 m high and 2.3 m wide, and weighing 600 kg with 3500 strung sense and shielding wires, must be taken down the shaft as special "slung loads," presenting an extra challenge.

Once the SP module cryostat is ready, a temporary construction opening (TCO) is left open at one end through which the detector components are installed. A cleanroom is built around the TCO to prevent any contamination entering the cryostat during installation. The detector support system (DSS) is then installed into the cryostat, ready to receive the TPC components.

In the cleanroom the APAs are outfitted with PD units and passed through a series of qualification tests. Two APAs are linked into a vertical 12 m high double unit and connected to readout electronics. They are tested in a cold box, then move into the cryostat to be installed at the proper location on the DSS, and have their cabling connected to feedthroughs. The FC, cathode plane assemblies and their HV connections, elements of the CISC, and detector calibration systems are installed in parallel with the APAs.

After twelve months of detector component installation, the TCO closes (the last installation steps occur in a confined space accessed through a narrow human-access port on top of the cryostat). Following leak checks, final electrical connection tests, and installation of the neutron calibration source, the process of filling the cryostat with 17,000,000 kg of LAr begins.

To help plan the installation phase, installation tests will be performed at the NOvA FD site in Ash River, Minnesota, USA. These tests will allow us to develop our procedures, train installation

2020 JINST 15 T08008

workers, and develop our labor planning through time and motion studies. Throughout the project, safety, QA, and quality control (QC) are written into all processes.

Safety of both personnel and detector components is the paramount consideration throughout the installation process and beyond. Once the detectors are taking data, the DUNE detector safety system (DDSS) will be monitoring for argon level drops, water leaks, and smoke. A detailed detector and cavern grounding scheme has been developed that not only guards against ground loops but also ensures that any power faults are safely shunted to the facility ground.

Chapter 4

Dual-phase far detector technology

This chapter provides a brief introduction to the dual-phase far detector technology. The text below closely follows that found in the introductory chapter of Volume V, The DUNE Far Detector Dual-Phase Technology, where many more details may be found.

4.1 Overview

DUNE's rich physics program, with discovery potential for CPV in the neutrino sector and its capability to make significant observations of nucleon decay and astrophysical events is enabled by the exquisite resolution of the LArTPC detector technique, which the DP design further augments relative to the SP design. The operating principle of a DP LArTPC, illustrated in figure 4.1, is very similar to that of the SP design (figure 1.5). Charged particles that traverse the active volume of the LArTPC ionize the medium while also producing scintillation light. In a DP module ionization charges drift vertically in LAr and are transferred into a layer of gas above the liquid where they deposit their charge on a segmented anode. This design allows for a single, fully homogeneous LAr volume, offering a much longer drift length and reducing the quantity of nonactive materials in the LAr. While the longer drift length requires a higher voltage (up to 600 kV) on the cathode, the DP design improves the S/N ratio in the charge readout, reducing the threshold for the smallest observable signals, while also achieving a finer readout granularity. Other advantages of the DP design include accessible readout electronics and fewer detector components, reducing costs and simplifying installation logistics. The precision tracking and calorimetry offered by the DP technology provides excellent capabilities for identifying interactions of interest while mitigating sources of background.

The argon scintillation light, at a wavelength of 127 nm, is deep in the UV spectrum. It is recorded by an array of PMTs located below the cathode at the bottom of the cryostat. The PMTs, coated with a WLS material, shift the light closer to the visible spectrum and record the time and pulse characteristics of the incident light.

Two of the key factors that affect the performance of a LArTPC are argon purity and noise. The DP and SP designs have slightly different purity requirements to cope optimally with the different drift lengths. We express the purity level in terms of electron lifetime: a minimum of 5 ms for DP versus 3 ms for SP. In both cases the levels of electronegative contaminants in the LAr (e.g., oxygen

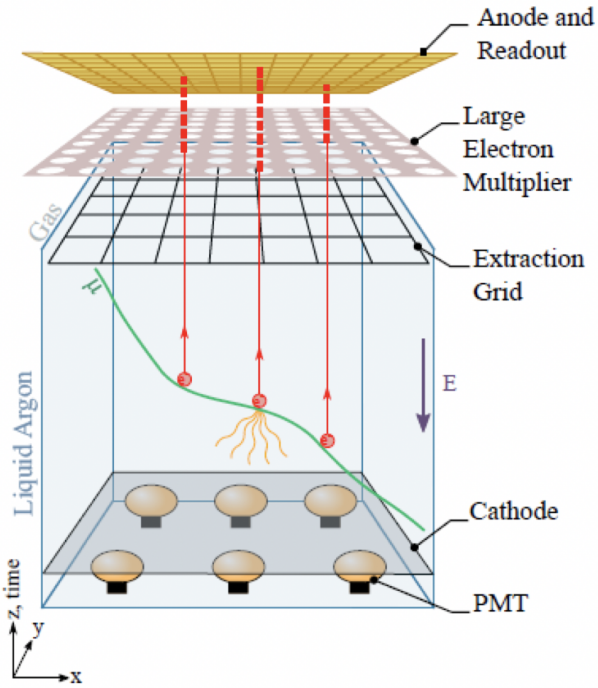

Figure 4.1. Principle of the DP readout.

and water) must remain at ppt levels. To clearly discern the drifting electrons over the baseline of the electronics, the TPC electronic readout noise must be kept very low. This requires use of low-noise cryogenic electronics. Amplification of the electron signal in the gas phase mitigates the potential effect of both factors on the performance.

4.2 Features of the dual-phase design

A DP module, with a 12.1 kt active mass LArTPC and dimensions (LWH) 60.0 m by 12.0 m by 12.0 m, includes all associated cryogenics, electronic readout, computing, and safety systems. The module is built as a single active volume, with the anode at the top in the gas volume, the cathode near the bottom, and an array of PDs underneath the cathode. The active volume (see figure 4.2) is surrounded by a FC. The DP design maximizes the active volume within the confines of the membrane cryostat while minimizing dead regions and the presence of dead materials in the drift region. The detector elements are all modular to facilitate production and to allow for transport underground.

The key differentiating concept of the DP design is the amplification of the ionization signal in an "avalanche" process. Ionization electrons drift upward toward an extraction grid situated just below the liquid-vapor interface. After reaching the grid, an E field stronger than the drift field extracts the electrons from the liquid upward into the ultra-pure argon gas. Once in the gas, the electrons encounter detectors, called LEMs, that have a micro-pattern of high-field regions in which the electrons are greatly amplified (via avalanches caused by Townsend multiplication). The amplified charge is collected on an anode. The use of avalanches to amplify the charges in the gas

phase increases the S/N ratio by at least a factor of ten, with the goal of achieving a gain of about 20, which will significantly improve the event reconstruction quality.

The modular extraction grids, LEMs, and anodes are assembled into three-layered sandwiches with precisely defined inter-stage distances and inter-alignment, which are then connected together horizontally into modular detection units that are 9 m^2. These composite detection units, called CRPs, are discussed in section 4.3. A CRP provides an adjustable charge gain and two independent, orthogonal readout views, each with a pitch of 3.1 mm. It collects the charge projectively, with practically no dead region. Together, the time information (t_0) from the LAr scintillation readout and the 3D track imaging of the CRPs provide dE/dx information.

Slow-control feedthroughs, one per CRP, are used for level meter and temperature probe readout, for pulsing calibration signals, and to apply HV bias on the two sides of the LEMs and on the extraction grid. Calibration and CISC systems for the SP and DP technologies have been designed jointly, and are discussed in sections 3.6 and 3.8, respectively.

Signals in each CRP unit are collected via three SFT chimneys on the roof of the cryostat that house the FE cards with the (replaceable) cryogenic ASIC amplifiers. The only active electronics elements inside the cryostat are the PMT bases. Each SFT chimney is coupled to a Micro Telecommunications Computing Architecture (μTCA) crate to provide signal digitization and DAQ. These crates are connected via optical fiber links to the DAQ back-end. The total number of readout channels per 10 kt module is 153,600.

Figure 4.2 shows the DP module's main components. The number of components and corresponding parameters for a 12.1 kt DP module are summarized in table 4.1.

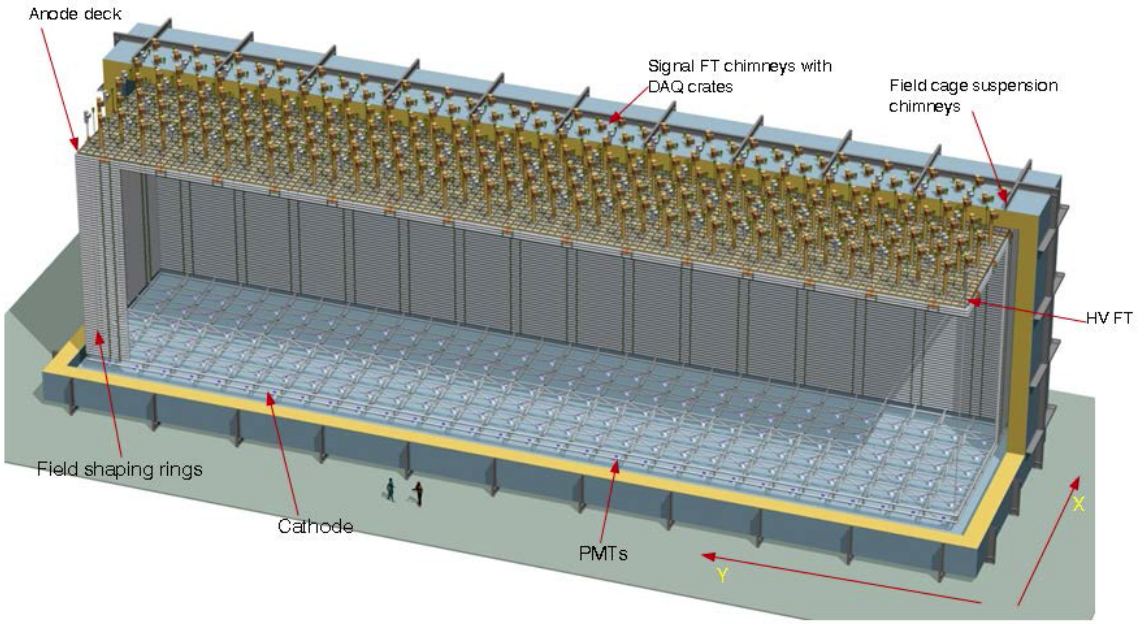

Figure 4.2. A DP module with cathode, PMTs, FC, and anode plane with SFT chimneys.

2020 JINST 15 T08008

Table 4.1. DP module component quantities and parameters.

Component	Value
Anode plane size	W = 12.0 m, L = 60.0 m
CRP unit size	W = 3 m, L = 3 m
CRPs	$4 \times 20 = 80$
CRP channels	153,600
LEM-anode sandwiches per CRP unit	36
LEM-anode sandwiches (total)	2880
SFT chimneys per CRP unit	3
SFT chimneys	240
Charge readout channels per SFT chimney	640
Charge readout channels (total)	153,600
Suspension feedthrough per CRP unit	3
Suspension feedthroughs (total)	240
Slow control feedthroughs (total)	80
HV feedthrough	1
Nominal drift E field	0.5 kV/cm
Nominal/target HV for vertical drift	500 V/cm/600 kV
FC voltage degrader resistive chains	12
FC cathode modules	15
FC rings	199
FC modules (4 m×12 m)	36
PMTs	720 ($1/m^2$)
PMT channels	720

4.3 Charge readout planes

The collection, amplification, and readout components of the TPC are combined into layered modules called CRPs. The charge is collected in a finely segmented readout anode plane at the top of the gas volume and fed to the FE readout electronics. The CRP's amplification components, the LEMs, are horizontally oriented 1 mm-thick printed circuit boards (PCBs) with electrodes on the top and bottom surfaces. The CRP structure also integrates the immersed extraction grid, which is an array of x- and y-oriented stainless steel wires, 0.1 mm in diameter, with a 3.1 mm pitch. Figure 4.3 shows the thicknesses and possible biasing voltages for the different CRP layers.

Each CRP is made up of several independent $0.5 \times 0.5\,m^2$ units, each of which is composed of a LEM-anode "sandwich." The anode is a two-dimensional (2D) PCB with two sets of 3.125 mm-pitch gold-plated copper strips that provide the x and y coordinates (and thus two views) of an event. Both the LEMs and anodes are produced in units of $50 \times 50\,cm^2$. The CRPs are embedded in a mechanically reinforced frame of FR-4 and iron-nickel invar alloy.

2020 JINST 15 T08008

An extraction efficiency of 100 % of the electrons from the liquid to the gas phase is achieved with an E field of the order of 2 kV/cm across the liquid-gas interface, applied between the extraction grid immersed in the liquid and charge amplification devices situated above, in the argon gas.

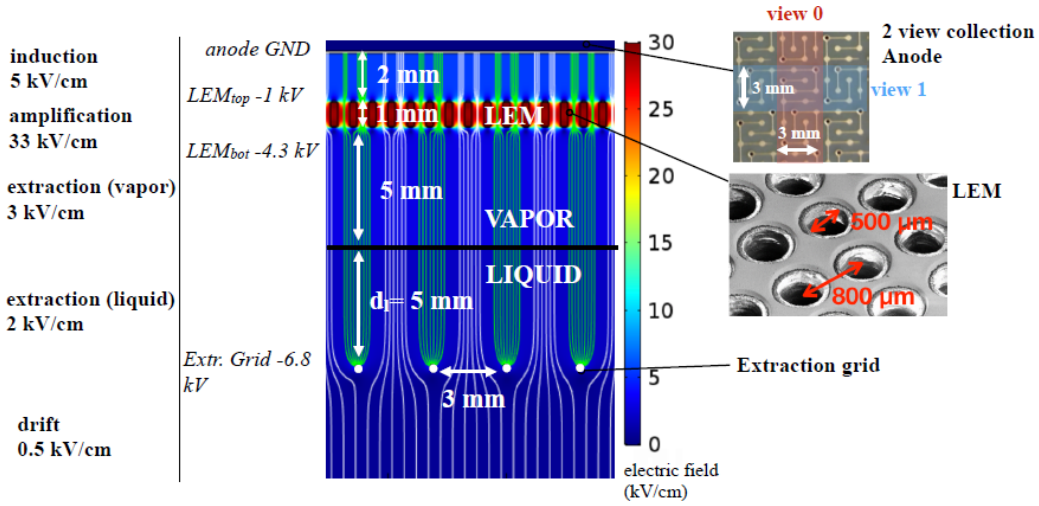

Figure 4.3. Thicknesses and HV values for electron extraction from liquid to gaseous argon, their multiplication by LEMs, and their collection on the *x* and *y* readout anode plane. The HV values are indicated for a drift field of 0.5 kV/cm in LAr.

The LEMs are drilled through with many tiny holes (these are the high-field regions), that collectively form a micro-pattern structure. When a 3 kV potential difference is applied across the a LEM's electrodes, the high E field (30 kV/cm) produces avalanches (via Townsend multiplication) that amplify the ionization electrons.

Each CRP is independently suspended by three stainless-steel ropes linked to the top deck of the cryostat. This suspension system allows adjustment of the CRP height and level such that it remains parallel to the LAr surface and the extraction grid remains immersed.

4.4 Cathode, field cage, and HV system

The drift field (nominal: E $\simeq$ 0.5 kV/cm, minimum: E $\simeq$ 0.25 kV/cm) inside the fully active LAr volume is produced by applying HV to the cathode plane at the bottom of the cryostat and is kept uniform by the FC, a stack of 199 equally spaced, field-shaping electrodes. These electrodes are set to linearly decreasing voltages starting from the cathode voltage at the bottom of the detector module to almost ground potential at the level of the CRP.

The cathode plane is suspended from the FC and hangs near the bottom of the cryostat. It consists of 15 adjacent 4 m $\times$ 12 m modules to span the 60.0 m length of DP module.

As shown in figure 4.4, each cathode module is constructed of two 12 m long trusses made from thin-walled stainless steel tubes with an outer diameter of approximately 50 mm.

A set of 80 3 m $\times$ 3 m ground grid modules, standing on the cryostat floor, are installed to protect the array of PMTs against any electric discharge from the cathode.

The HV for ProtoDUNE-DP was designed for 300 kV, corresponding to a minimal requirement of E field $\simeq$0.25 kV/cm for the DP module. We can test the equivalent of a 12.0 m drift in

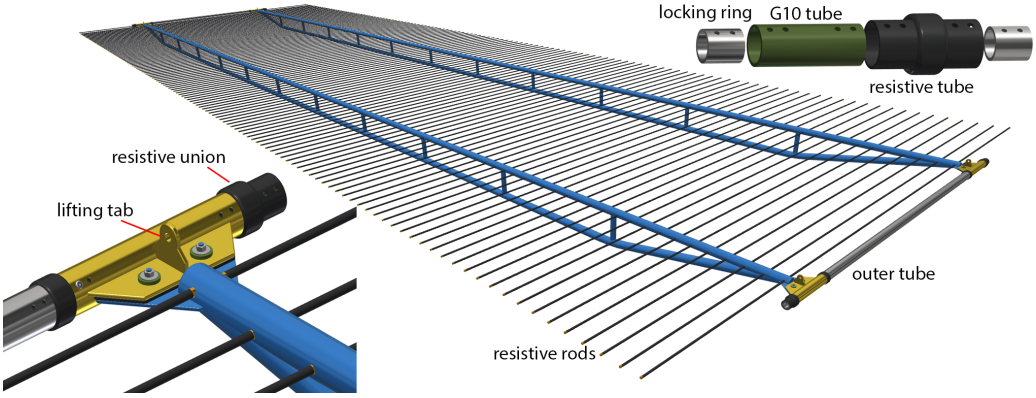

Figure 4.4. Illustration of a DP cathode module. It is constructed using a pair of stainless steel trusses (blue) as the framework with an array of coated FRP rods. The lower-left inset shows the resistive interconnections and the lifting tab on the cathode truss structure. The upper-right inset is shows the resistive union.

ProtoDUNE-DP by further reducing the drift field, and in contradistinction, we expect to test the full 600 kV in a second phase of ProtoDUNE-DP after making some changes to the cathode and the HV feedthrough. Fermilab is also considering building a test setup for 600 kV operation and 12.0 m drift.

4.5 Readout electronics and chimneys

The electrical signals from the collected charges are passed to the outside of the cryostat via a set of dedicated SFT chimneys, tightly-fit pipes that penetrate the top layer of the cryostat insulation, and are therefore exposed to cryogenic temperatures at their lower ends and to room temperature above the cryostat. They are filled with nitrogen gas and closed at the top and bottom by ultra-high-vacuum flanges (warm and cold).

The cryogenic analog FE electronics cards, mounted on 2 m long blades that slide on lateral guides that are integrated into the mechanical structure of the SFT chimney, are installed at the bottom of the chimney and plugged into the top side of the cold flange. This arrangement allows access to and replacement of the cards from the outside. The warm flange connects the analog differential signals to external digitization cards. In the other direction, it distributes the LV and slow control signals to the FE electronics. The chimneys act also as Faraday cages, preventing the analog FE electronics from picking up possible noise from the digital electronics.

The FE cards are based on the analog cryogenic preamplifiers implemented in CMOS ASIC circuits designed for high integration and large-scale affordable production. The ASIC for the DP module circuits have been specially engineered to match the DP module's signal dynamics. Inside the SFT chimneys, the cards are actively cooled to a temperature of approximately 110 K. The bottom sides of the cold flanges connect to CRPs via flat 0.5 m long cables intended to minimize the input capacitance to the preamplifiers. Each SFT chimney collects 640 readout channels.

The digital electronics for the charge digitization system is installed on the cryostat roof. This makes it possible to use common design standards and benefit from commercially supported low-

2020 JINST 15 T08008

cost, high-speed networking technologies, such as μTCA, which is used in the telecommunications industry.

Digitization cards in the advanced mezzanine card (AMC) format read 64 channels per card. Each AMC card can digitize 64 channels at 2.5 MHz and compress and transmit this continuous data stream, without zero-skipping, over a network link operating at 10 Gbit/s. Lossless data compression is particularly effective thanks to the high S/N ratio of DP, which limits noise contributions at the level of one ADC count. Each SFT chimney is coupled to a μTCA crate that holds 10 AMC digitization cards and can therefore read 640 channels. The AMC cards transmit the data to the DAQ back-end. A total of 240 μTCA crates are required for reading the entire detector module.

The light-readout digitization system uses μTCA AMC card design derived from that of the charge readout system, but that implements a circuitry based on the charge and time integrated readout chip (CATIROC) ASIC to trigger the readout.

The timing synchronization is based on the White Rabbit (WR) standard. Specifically developed timing MicroTCA Carrier Hub (MCH) connected to a WR network ensures the distribution of clock, absolute timing, and trigger information on the backplane of the μTCA crates. The White Rabbit μTCA Carrier Hub (WR-MCH) are connected via 1 Gbit/s optical fibers to a system of WR switches that interconnect the WR network. This ensures that the digitization performed by the various AMC cards is completely aligned; it also refers to the absolute UTC time.

4.6 Photon detection system

The PD system is based on an array of PMTs uniformly distributed below the cathode. The PMTs have a tetra-phenyl butadiene (TPB) coating on the photocathode's external glass surface that shifts the scintillation light from deep UV to visible light. The PMTs sit on the corrugated membrane cryostat floor, on mechanical supports that do not interfere with the membrane thermal contraction. Figure 4.5 shows the PMT with its support base attached to the bottom of the ProtoDUNE-DP cryostat (section 1.3.2).

In order to improve the light yield uniformity for signals generated in the top part of the drift volume a system of reflective panels with WLS coating is integrated on the FC walls.

4.7 Data acquisition

The DAQ systems for both the SP and DP technologies have been designed jointly and are identical except for the architecture of the detector readout electronics. The output format of the generated data is common, and both are synchronized to the same global clock signals. The shared DAQ design is introduced in section 3.7.

The DP readout architecture can be organized into 20 regions of interest (ROIs). Triggers are searched on the level-1 event builder machines, interconnecting multiple μTCA crates, on a sliding windows of 10 s contained in the event builder RAM. Figure 4.6 illustrates the DP readout architecture (bottom) and its interface to the DAQ system.

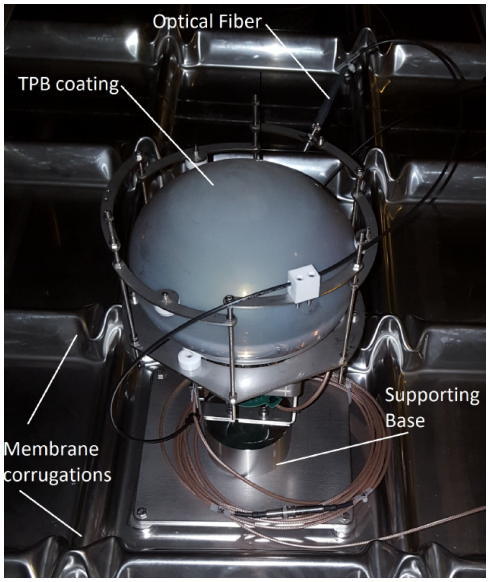

Figure 4.5. Picture of the cryogenic Hamamatsu R5912-MOD20 PMT fixed on the membrane floor of ProtoDUNE-DP. The optical fiber of the calibration system is also visible.

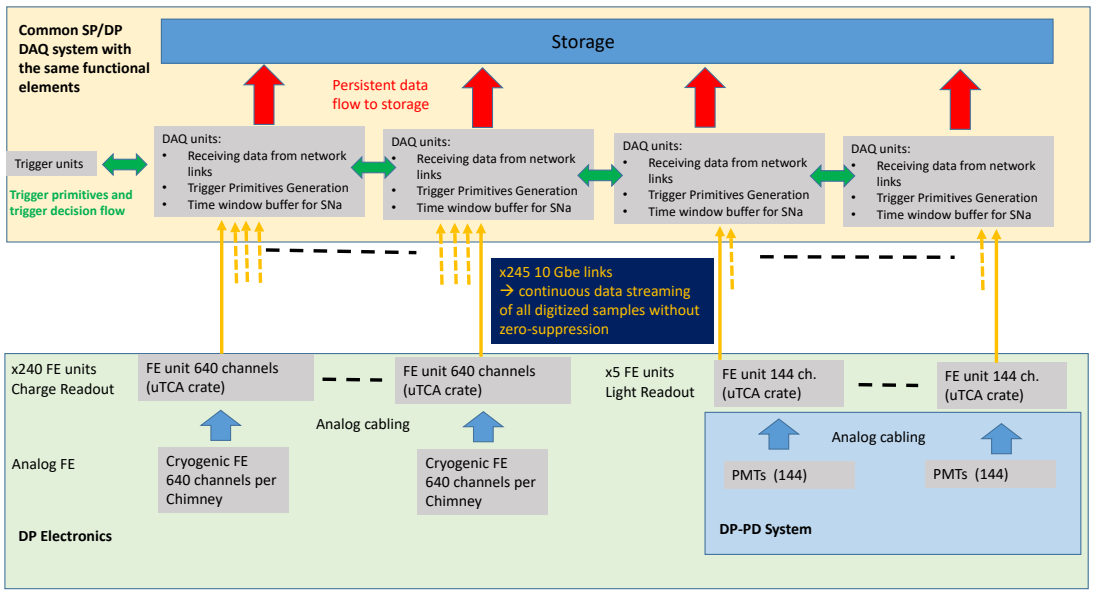

Figure 4.6. Schematic illustration of the interface of DP TPC electronics to DAQ.

2020 JINST 15 T08008

Chapter 5

The DUNE near detector

This chapter briefly introduces the DUNE near detector, emphasizing its role for the DUNE far detector physics program. More details on the near detector may be found in appendices of this TDR volume. DUNE will issue a complete conceptual design report for the near detector in early 2020, with a technical design report to follow.

5.1 Overview of the DUNE near detector

5.1.1 Motivation

The DUNE experiment will measure oscillation probabilities for muon neutrinos or antineutrinos to either remain the same flavor or oscillate into their electron flavor counterparts as a function of the neutrino energy. This will allow the neutrino mass ordering to be definitively determined, as well as enable observation of leptonic CPV for a significant range of δ_{CP} values and precise measurement of neutrino mixing matrix parameters.

The ND will serve as the experiment's control, constraining systematic errors and measuring the initial unoscillated ν_μ and ν_e energy spectra (and that of the corresponding antineutrinos). The energy spectra result from an energy-dependent convolution of flux, cross section, and detector response for each of the four neutrino types (ν_e, ν_μ, $\bar{\nu}_e$, $\bar{\nu}_\mu$). The ND will make measurements that allow the three functions to be independently constrained and partially or fully deconvolved. The constraints will be used to improve the simulation program that is responsible for predicting the energy spectra at the FD for particular choices of the oscillation parameters. This allows the actual oscillation parameters to be estimated from a fit to the FD data.

The ND will also have a physics program of its own, independent of the far detector. This program will include measuring neutrino interactions to explore the two pillars of the standard model: electroweak physics and quantum chromodynamics. The ND physics program will also explore physics beyond the standard model. This includes searches for non-standard interactions, sterile neutrinos, dark photons, and other exotic particles.

5.1.2 Requirements

The components of the ND must address their multiple missions in a complementary fashion. In this section, we list the key overarching requirements driving the ND complex. Section A.7

in appendix A goes into more detail, discussing some thought experiments and case studies that illustrate how different parts of the complex work together. These case studies naturally suggest more detailed capabilities, performance statistics, and technical requirements; we are in the process of tabulating them.

- *Predict the neutrino spectrum at the FD.* The ND must predict the energy spectrum of ν_μ, $\bar{\nu}_\mu$, ν_e and $\bar{\nu}_e$ at the FD. The prediction must be provided as a function of the oscillation parameters, and systematic uncertainties must be small enough to achieve the required CP coverage. This is the primary requirement of the DUNE ND.

- *Measure interactions on argon.* The ND must measure neutrino interactions on argon to reduce uncertainties due to nuclear modeling. The ND must be able to determine the neutrino flavor and measure the full kinematic range of the interactions that will be seen at the FD.

- *Measure the neutrino energy.* The ND must be able to reconstruct the neutrino energy in CC events and control for any biases in energy scale or resolution, keeping them small enough to achieve the required CP coverage. These measurements must also be transferable to the FD.

- *Constrain the cross section model.* The ND must measure neutrino cross sections in order to constrain the cross section model used in the oscillation analysis. In particular, cross section mismodeling that causes incorrect FD predictions as a function of neutrino flavor and true or reconstructed energy must be constrained well enough to achieve the required CP coverage.

- *Measure neutrino fluxes.* The ND must measure neutrino fluxes as a function of flavor and neutrino energy. This allows neutrino cross sections to be measured and constrains the beam model and the extrapolation of neutrino energy spectra from the ND to the FD.

- *Obtain data with different fluxes.* The ND must measure neutrino interactions in different beam fluxes (especially ones with different mean energies) to disentangle flux and cross section, verify the beam model, and guard against systematic uncertainties on the neutrino energy reconstruction.

- *Monitor the neutrino beam.* The ND must monitor the neutrino beam energy spectrum with sufficient statistics to be sensitive to intentional or accidental changes in the beam that could affect the oscillation measurement.

5.1.3 Design

The DUNE ND is formed from three primary detector components and the capability of two of these components to move off the beam axis. The three detector components serve important individual and overlapping functions in the ND mission. Because these components have stand-alone features, the DUNE ND is often discussed as a suite or complex of detectors and capabilities. The movement off-axis provides a valuable extra degree of freedom in the data. The power in the DUNE ND concept lies in the collective set of capabilities.

Table 5.1. High-level breakdown of the three major detector components and the capability of movement for the DUNE ND, along with functions and primary physics goals.

Component	Essential Characteristics	Primary function	Select physics aims
LArTPC (ArgonCube)	Mass	Experimental control for the FD.	$\nu_\mu(\overline{\nu}_\mu)$ CC
	Target nucleus Ar	Unoscillated E_ν spectra measurements.	ν-e$^-$ scattering
	Technology FD-like	Flux determination.	ν_e+$\overline{\nu}_e$ CC Interaction model
Multipurpose detector (MPD)	Magnetic field	Experimental control for the LArTPCs.	$\nu_\mu(\overline{\nu}_\mu)$ CC
	Target nucleus Ar	Momentum-analyze μ's produced in LAr.	ν_e CC, $\overline{\nu}_e$
	Low density	Measure exclusive final states with low momentum threshold.	Interaction model
DUNE-PRISM (capability)	ArgonCube+MPD move off-axis	Change flux spectrum	Deconvolve flux × cross section; Energy response; Provide FD-like energy spectrum at ND; ID mismodeling.
Beam Monitor (SAND)	On-axis	Beam flux monitor	On-axis flux stability
	High-mass polystyrene target	Neutrons	Interaction model;
	KLOE magnet		Atomic number (A) dependence; ν-e$^-$ scattering.

2020 JINST 15 T08008

Figure 1.13 in Chapter 1 shows the DUNE ND in the DUNE ND hall. Table 5.1 provides a high-level overview of the three components of the DUNE ND along with the off-axis capability that is sometimes described as a fourth component.

The core part of the DUNE ND is a LArTPC called ArgonCube. ArgonCube consists of an array of 35 modular TPCs sharing a cryostat. Figure 5.1 is a drawing of a prototype of the modular TPCs. This detector has the same target nucleus as the FD and shares some aspects of form and functionality with it, where the differences are necessitated by the expected intensity of the beam at the ND. This similarity in target nucleus and technology reduces sensitivity to nuclear effects and detector-driven systematic errors in the extraction of the oscillation signal at the FD. The LArTPC is large enough to provide high statistics ($10^8 \nu_\mu$-CC events/year) and its volume is sufficient to provide good hadron containment. The tracking and energy resolution, combined with the mass of the LArTPC, will allow the flux in the beam to be measured using several techniques, including the well understood but rare process of ν_μ-e^- scattering.

The LArTPC acceptance falls off for muons with a measured momentum higher than 0.7 GeV/c due to lack of containment. Since the muon momentum is a critical component of the neutrino energy determination, a magnetic spectrometer is needed downstream of the LArTPC to measure the charge sign and momentum of these muons. The MPD will accomplish this. It consists of a HPgTPC surrounded by an ECAL in a 0.5 T magnetic field (figures 5.2 and 5.3).

The HPgTPC provides a lower-density medium with excellent tracking resolution for the muons from the LArTPC. In addition, with this choice of technology for the tracker, neutrinos interacting on the argon in the gas TPC constitute a sample of ν-Ar events that can be studied with a very low charged-particle tracking threshold, excellent kinematic resolution, and systematic errors that differ from those of the liquid detector. The detector's high pressure will allow us to collect a sample of 2×10^6 ν_μ-CC events/year for these studies, events that will also be valuable for studying the charged particle activity near the interaction vertex since this detector can access lower-momentum protons than the LAr detector and provides better particle identification of charged pions. The relative reduction in secondary interactions in these samples (compared to LAr) will help us to identify the particles produced in the primary interaction and to model secondary interactions in denser detectors, interactions that are known to be important [45]. In addition, using the ECAL we will be able to reconstruct many neutrons produced in neutrino interactions in the gaseous argon via time-of-flight.

The LArTPC and MPD are able to move laterally to take data in positions off the beam axis. This capability is referred to as DUNE-PRISM. As the detectors move off-axis, the incident neutrino flux spectrum changes: the mean energy drops and the spectrum becomes more monochromatic. Although the neutrino interaction rate drops, the intensity of the beam and the size of the LArTPC still combine to yield ample statistics. Figure 5.4 shows a sample of neutrino energy distributions taken at different off-axis angles. Taking data at different off-axis angles allows the deconvolution of the neutrino flux and interaction cross section; it also allows mapping of the reconstructed versus true energy response of the detector. This latter mapping is applicable at the FD to the degree to which the near and far LAr detectors are similar. Stated a different way, it is possible to use information from a linear combination of the different fluxes to create a data sample at the ND with an effective neutrino energy distribution close to the oscillated spectrum at the FD. This data-driven technique will reduce systematic effects coming from differences in the energy spectra of

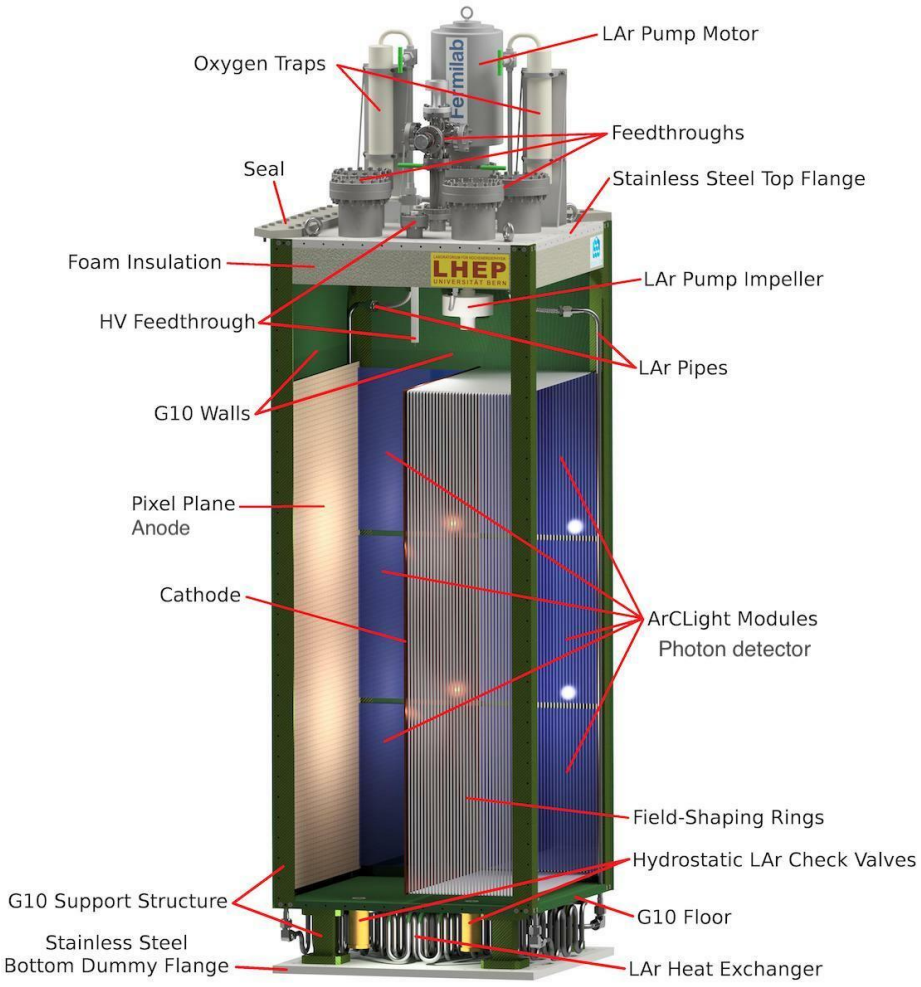

Figure 5.1. Cutaway drawing of a 0.67 m × 0.67 m × 1.81 m ArgonCube prototype module. For illustrative purposes, the drawing shows traditional field-shaping rings instead of a resistive field shell. The G10 walls will completely seal the module, isolating it from the neighboring modules and the outer LAr bath. The modules in this prototype system will not have individual pumps and filters.

the oscillated signal events in the FD and the ND samples used to constrain the interaction model. Finally, the off-axis degree of freedom may enable a sensitivity to some forms of mismodeling in the beam and/or interaction models.

Figure 5.5 shows linear combinations of off-axis fluxes giving FD oscillated spectra for two sets of oscillation parameters. The procedure can model the FD flux well for neutrino energies in the range of 0.6 GeV to 3.6 GeV. The input spectra for the linear combinations, shown in figure 5.4, extend only slightly outside this range; they cannot be combined to model the flux in those extreme ranges while simultaneously fitting the central range well. The modeled range encompasses the range of data of interest for the oscillation program.

The final component of the DUNE ND suite is the beam monitor, called the SAND. The core part of it, the 3D scintillator tracker (3DST), is a plastic scintillator detector made of 1 cm^3 cubes read out along each of three orthogonal dimensions. The design eliminates the typical planar-strip

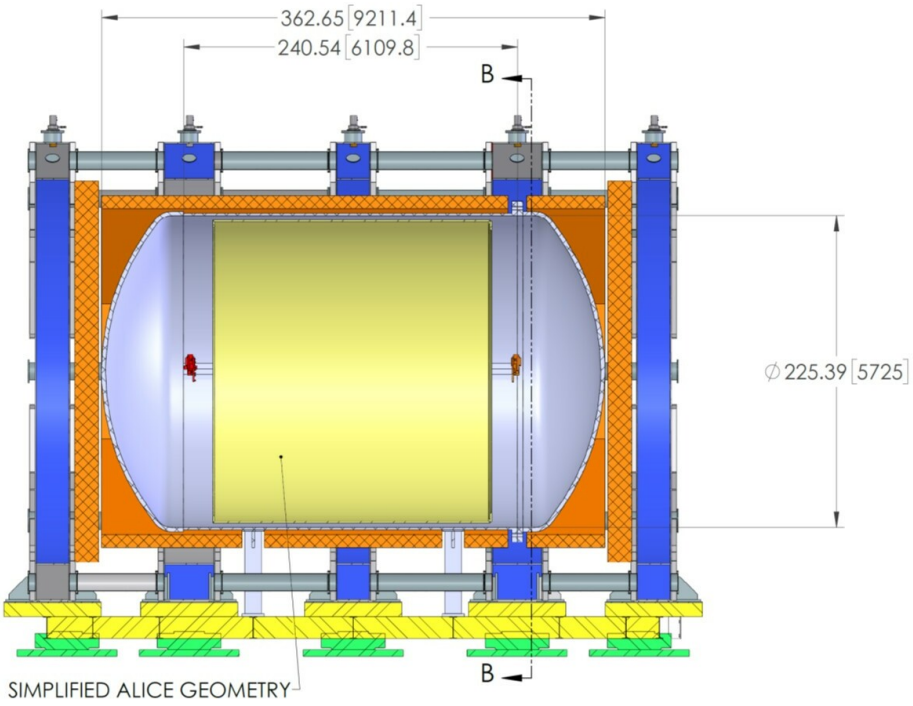

Figure 5.2. The conceptual design of the MPD system for the ND. The TPC is shown in yellow inside the pressure vessel. Outside the pressure vessel, the ECAL is shown in orange, and outside that are the magnet coils and cryostats. The drawing illustrates the five-coil superconducting design.

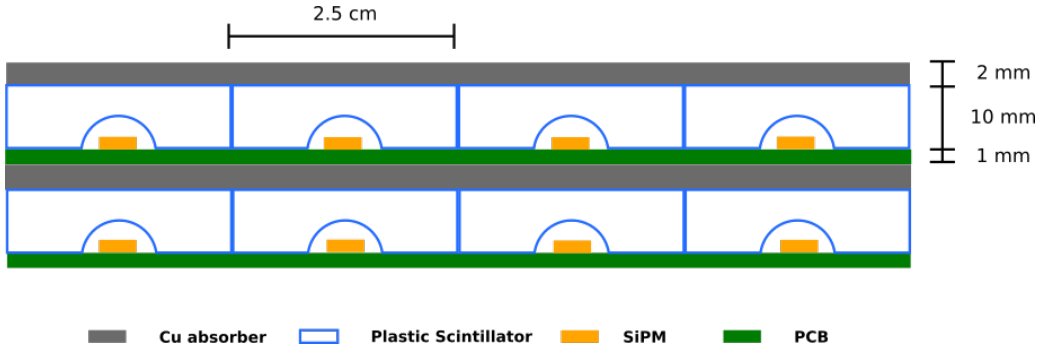

Figure 5.3. Conceptual layout of the calorimeter showing the absorber structure, scintillator tiles, SiPMs, and PCB. The scintillating layers consist of a mix of tiles and cross-strips with embedded wavelength shifting fibers to achieve a comparable effective granularity.

geometry common to scintillator detectors, leading to improved acceptance at large angles relative to the beam direction. It is mounted inside an envelope of high-resolution, normal pressure TPCs and an ECAL, all of which are surrounded by a magnet, as illustrated in figure 5.6. The reference design uses a repurposed magnet and ECAL from the KLOE experiment.

SAND serves as a dedicated neutrino spectrum monitor that never moves off-axis. It also provides an excellent on-axis, neutrino flux determination using many of the methods discussed in section A.4. The neutrino flux determined using this detector, with technologies, targets, and

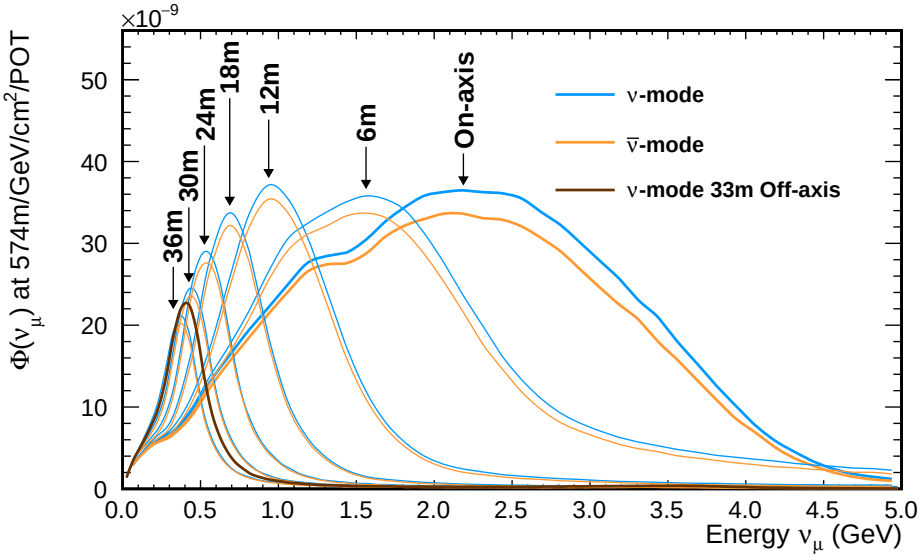

Figure 5.4. The variation in the neutrino energy spectrum shown as a function of detector off-axis position, assuming the nominal ND location 574 m downstream from the production target.

interaction systematic errors that are different from ArgonCube, is an important point of comparison and a systematic cross-check for the flux as determined by ArgonCube.

SAND provides very fast timing and can isolate small energy depositions from neutrons in three dimensions. This provides the capability to incorporate neutrons in the event reconstruction using energy determination via time-of-flight with a high efficiency. This capability should be useful for the low-ν flux determination[1] because it either allows events to be tagged with a significant neutron energy component or provides a way to include that energy in the calculation. Including neutrons in detailed studies of neutrino interactions in SAND using single transverse variables may prove useful in motivating improvements in the neutrino interaction model. Although the target for this device is carbon, not argon, basic insights into components of the interaction model may extend to argon. For example, the multi-nucleon component of the interaction model will be used for argon although it was developed in response to observations made on plastic targets.

5.2 Role of the ND in the DUNE oscillation program

Neutrino oscillation experiments must accomplish three main tasks. First, they must identify the flavor of interacting neutrinos in CC events or identify the events as NC interactions. Second, they must measure the energy of the neutrinos because oscillations occur as a function of baseline length over neutrino energy, L/E. Third, they must compare the observed event spectrum in the FD to predictions based on differing sets of oscillation parameters, subject to constraints from data observed in the ND. That comparison and how it varies with the oscillation parameters allows oscillation parameters to be measured.

[1]The low-ν technique involves measuring the flux for events with low energy transfer because the cross section is approximately constant with energy for this sample. It provides a nice way to measure the shape of the spectrum. This is discussed further in section A.4 of appendix A.

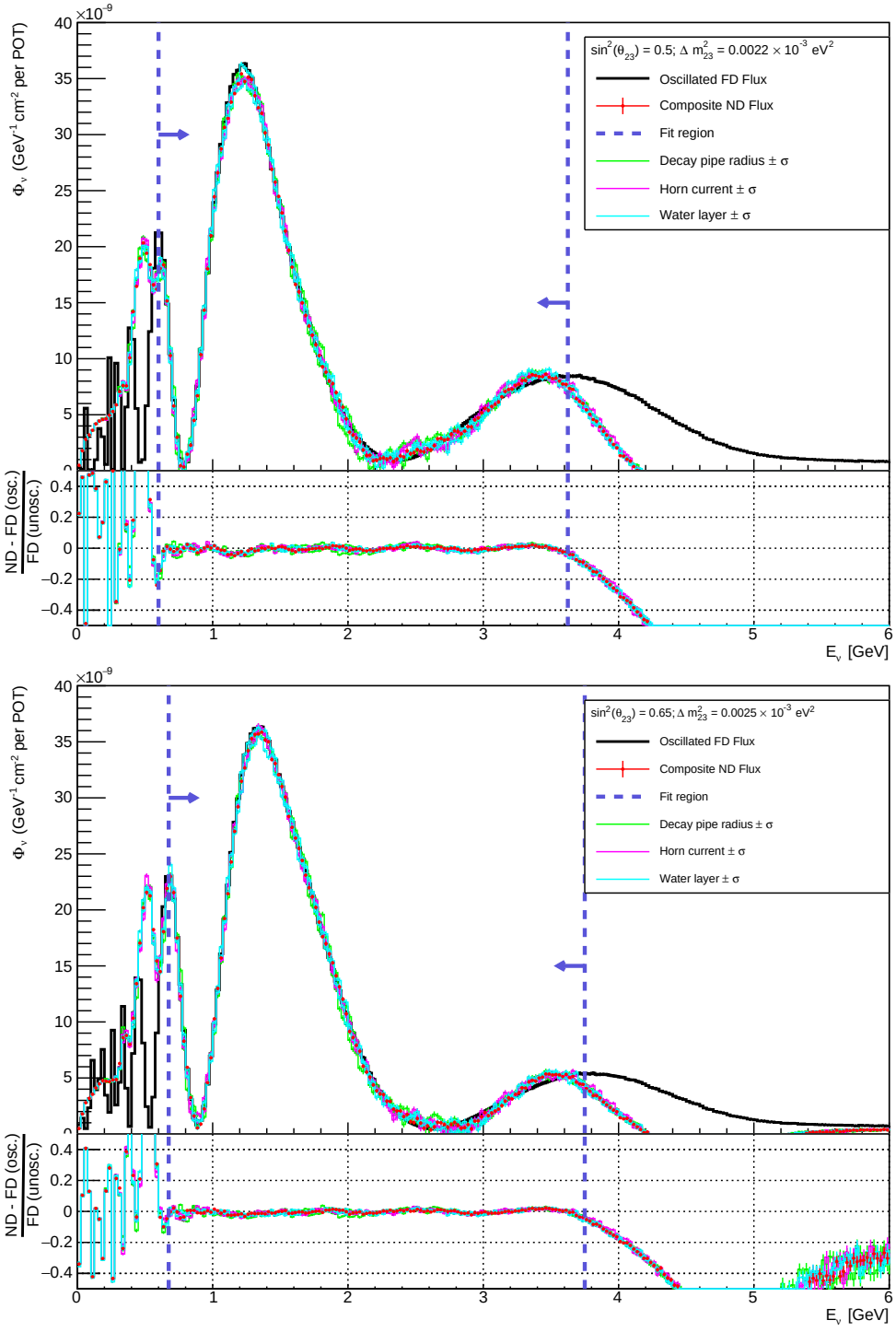

Figure 5.5. Linear combinations of off-axis fluxes giving FD oscillated spectra for a range of oscillation parameters. The FD oscillated flux is shown in black, the target flux is shown in green, and the linearly combined flux obtained with the nominal beam MC is shown in red. Systematic effects due to 1 σ variations of the decay pipe radius (green), horn current (magenta), and horn cooling water layer thickness (teal) are also shown.

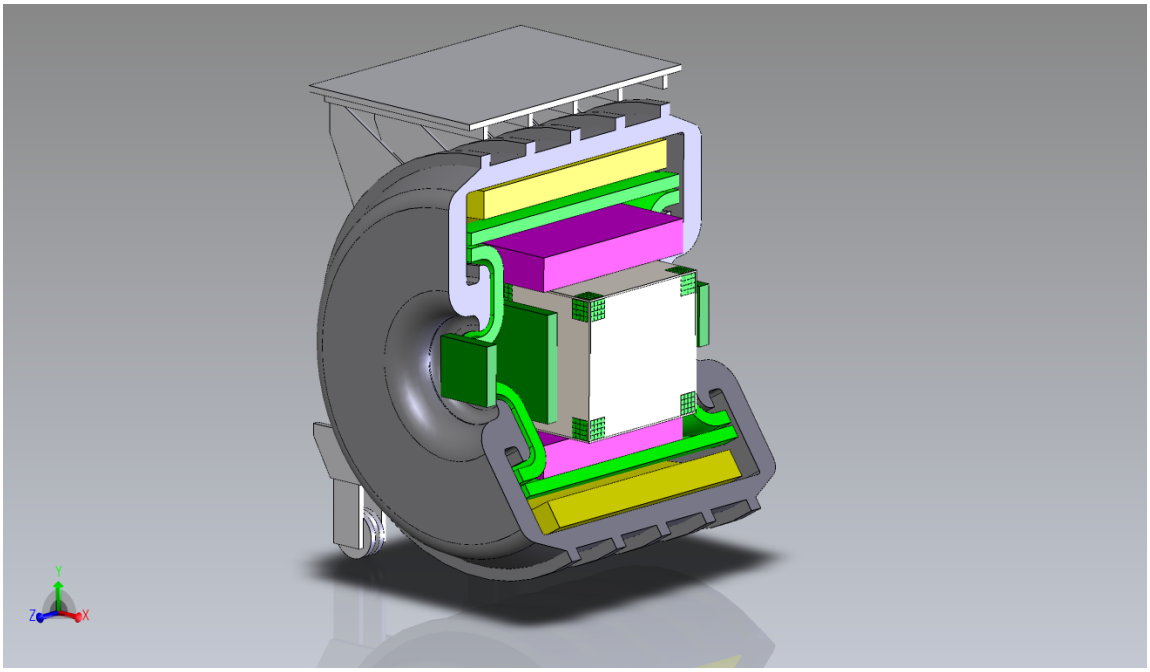

Figure 5.6. The SAND detector configuration with the 3DST inside the KLOE magnet. The drawing shows the 3DST in the center (white), TPCs (magenta), ECAL (green), magnet coil (yellow), and the return yoke (gray).

The connection between the observations in the ND and the FD is made using a simulation that convolves models of the neutrino flux, neutrino interactions, nuclear effects, and detector response. This gives rise to a host of complicating effects that muddy the simple picture. These complications come from two main sources. First, the identification efficiency is not 100 %, and there are some background events (for example, NC interactions with a π^0 present a background to ν_e CC interactions). Both the efficiency and background are imperfectly known. Because the background level tends to be similar in both the FD and ND, it helps if the ND can characterize backgrounds better than the FD.

The second aspect that complicates the simple picture is that the FD (and the similar ND) must use a target material composed of heavy nuclei. The target nucleus affects neutrino interactions in ways that ultimately drive the design of the ND complex. In particular, in heavy nuclei, the nucleons interact with each other and exhibit Fermi motion, providing moving targets for neutrino interactions. The wavelength of an interaction depends on momentum transfer but is often long enough to simultaneously probe multiple nucleons.

Another complication is that neutrino-nucleus scattering models rely on neutrino-nucleus cross sections, but neutrino cross sections on *free nucleons* are not generally well known in the kinematic range of interest to DUNE. Since the ND will enable high-statistics measurements on liquid and gaseous argon, rather than another nucleus, it will reduce nuclear model dependence. A final complication comes about because neutrinos produce hadrons within the nucleus. After production the hadrons undergo FSI and are thereby attenuated as they leave the target nucleus. Section A.2 of appendix A discusses neutrino-nucleus scattering in more detail.

Neutrons can be produced from the struck nucleus, as well as from follow-on interactions of the neutrino's reaction-products with other nuclei. The energy carried away by neutrons is difficult to detect and can bias the reconstructed neutrino energy. The SAND and MPD detectors have capabilities that allow neutron energy to be directly measured. The DUNE-PRISM program constrains the true-to-reconstructed energy relation and is thus also sensitive to energy carried by neutrons.

Heavy nuclei in the detector offer additional complications for particles that have left the struck nucleus, especially in the case where the detector is dense, e.g., in ArgonCube. Particles produced in a neutrino interaction may reinteract inside the detector, creating electromagnetic and hadronic cascades. These cascades, particularly the hadronic ones, confuse the reconstruction program due to overlapping energy and event features. They also cause a degradation of the energy resolution and result in additional energy carried by neutrons that may go missing. Particle identification by dE/dx is less effective for early showering particles, and low-energy particle tracks in a dense detector may be too short to detect. The HPgTPC in the MPD allows us to measure neutrino interactions on argon, but with significantly fewer secondary interactions and much lower-energy tracking thresholds.

Finally, setting aside complications due to heavy nuclei and dense detectors, we note that a significant fraction of the neutrino interactions in DUNE will come from inelastic processes, not the simpler quasi-elastic (QE) scattering. This typically leads to a more complex morphology for events and greater challenges for the detector and the modeling. The DUNE ND acts as a control for the FD and is designed to be more capable than the FD at measuring complicated inelastic events.

These complexities are incorporated imperfectly into the neutrino interaction model. The predicted signal in the ND is a convolution of this interaction model with the beam model and the detector response model. The critical role of the ND is to supply the observations used to tune, or calibrate, this convolved model, thereby reducing the overall uncertainty in the expected signal at the FD, which is used for extracting the oscillation parameters via comparison with the observed signal. And with its high statistics and very capable subsystems, the ND will produce data sets that will provide the raw material for improving the models beyond simple tuning.

5.3 ND hall and construction

Figure 5.7 shows the current design of the underground hall required for the ND construction concept. The hall must house the detector components and enable the required off-axis movement. The layout shows the spaces required for the detector itself, and for safety and egress. This work is in progress.

The overall construction method means the CF must provide a primary access shaft that is large enough for lowering the pressure vessel and the magnet coils. In the figure, ArgonCube is shown in its on-axis construction position, as is the MPD. Because SAND does not move, it is placed in a dedicated alcove downstream of the other detectors.

The DUNE-PRISM design requires that both the MPD and ArgonCube be able to move horizontally to a position off the beam axis. The direction of the motion is to one side of the beam, with a maximum displacement of approximately 30.5 m.

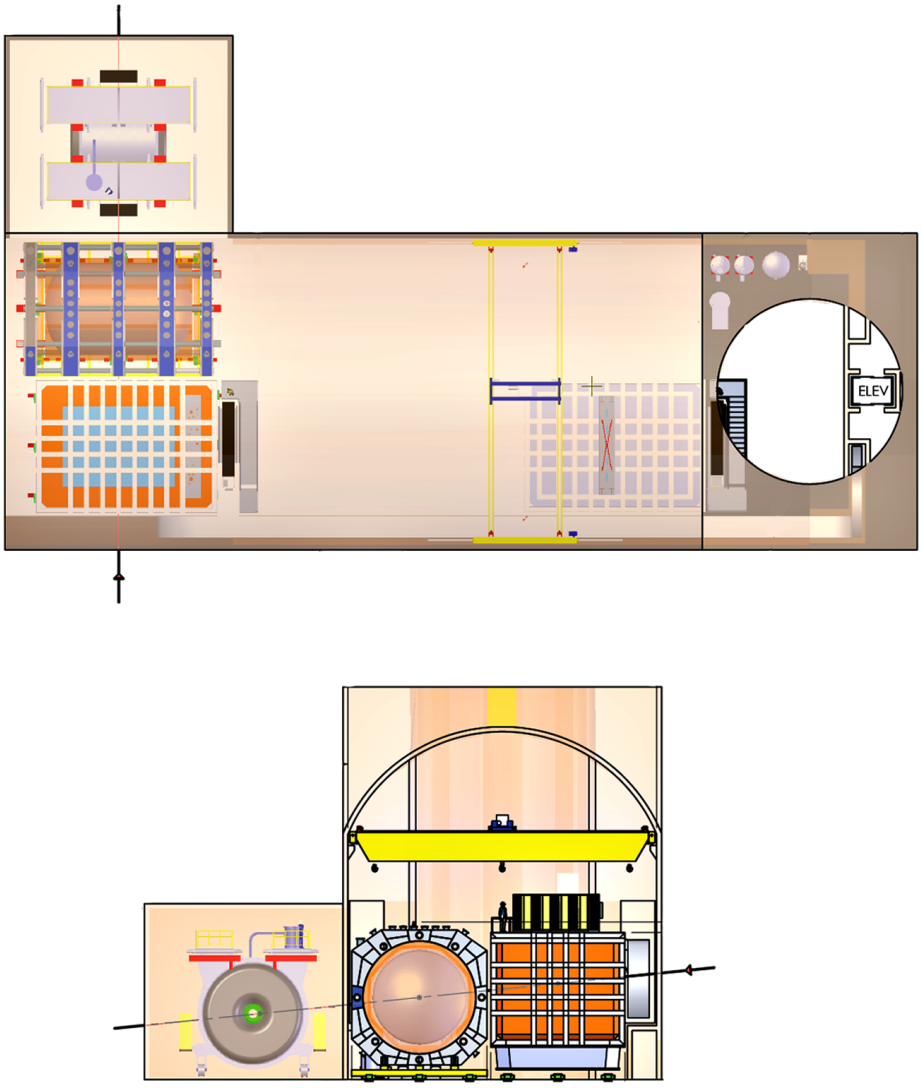

Figure 5.7. DUNE ND hall shown from above (top) and from the side transverse to the beam (bottom). The ArgonCube, MPD, and SAND are shown (in that order, bottom to top, in the upper figure) in position on the beam axis (black arrow) in both drawings.

Chapter 6

Computing in DUNE

This chapter briefly describes the DUNE computing model, which touches on all elements of the ND and FD and their physics programs. More detailed aspects of the model may be found in appendix C. DUNE will produce a complete technical design report for computing over the next two years.

6.1 Overview

The DUNE experiment will commission the first 10 kt fiducial mass FD module between 2024 and 2026 with a long data-taking run, and the remaining three modules between 2026 and 2036. An active prototyping program is ongoing at the CERN, where a short test beam run took place in 2018 with ProtoDUNE-SP, a 700 t, 15,360 channel prototype LArTPC with SP readout. Tests of a DP detector of similar size began in mid-2019. The DUNE experiment has already benefited greatly from these initial tests. The collaboration has recently formed a formal computing and software consortium (CSC), with significant participation of European institutions and interest from groups in Asia, to develop common software and computing, and to formalize resource contributions.

The CSC resource model benefits from the existing Open Science Grid (OSG) and Worldwide LHC Computing Grid (WLCG) infrastructure developed for the LHC and broader HEP community. DUNE is already using global resources to simulate and analyze ProtoDUNE-SP data. Several European institutions are part of this resource pool, making significant contributions to the ProtoDUNE-SP and ProtoDUNE-DP programs. We expect this global computing consortium to grow and evolve as we begin gathering data from the full DUNE detector in the 2020s.

The long-term DUNE science program should produce volumes of raw data similar in scale to the data volumes that current LHC Run-2 experiments have already successfully handled. Baseline predictions for the DUNE data, depending on actual detector performance and noise levels, are ~ 30 PB of raw data per year. These data, with simulations and derived analysis samples, will need to be made available to all collaborating institutions. We anticipate that institutions around the world will both contribute and use storage and CPU resources for DUNE.

The DUNE computing strategy starts with considerable infrastructure in place for international computing collaboration, in part thanks to the LHC program. Additional large non-LHC experiments, such as Large Synoptic Survey Telescope (LSST), the Belle II B-factory experiment, and

2020 JINST 15 T08008

DUNE will begin operation over the next decade and must use and expand upon this model to encourage international cooperation. The broader HEP community is organizing common efforts through the HEP Software Foundation Collaboration (HSC) [46]. The HSC is an organization of interested parties using the extensive knowledge gained over the past two decades to anticipate the needs of experiments over the next two decades, and to develop a sustainable computing landscape for the HEP community. The HSC white papers and roadmaps emphasize common tools and infrastructure as the foundation of this landscape.

The DUNE computing strategy heavily leverages the HSC model of common tools and infrastructure, which encompass data movement and storage, job control and monitoring, accounting, and authentication. DUNE recognizes that other large-scale experiments have similar needs and will encounter complementary issues, thus driving worldwide cooperation on common tools as the most cost-effective way to fulfill the scientific missions of the experiments. DUNE pilot programs already use this model. Most recently in data management and storage, Fermilab, CERN, Rutherford Appleton Laboratory, and other research and academic institutions in the UK are collaborating on adapting and using the Rucio data management systems [47] to serve as the core data management system for DUNE.

This protoculture of international collaboration within DUNE was demonstrated during the 2018 test beam run of the ProtoDUNE-SP detector, which produced raw data at rates of up to 2 GB/s. These data were transferred and stored in the archive facilities at CERN and Fermilab, and replicated at sites in the UK and Czech Republic. In a more recent commissioning test for the ProtoDUNE-DP detector, similar data transmission rates were achieved to CERN, Fermilab, and the CCIN2P3 computer center in Lyon, France.

In total, 1.8 PB of raw data were produced during the ten-week test beam run, mimicking, within a factor of two, expected data rates and volumes from the initial running of the FD complex. The prototype run was used to examine and test the scalability of existing and proposed computing infrastructure and to establish operational experience within the institutions that have expressed interest in developing and constructing the DUNE computing environment. The planning for DUNE is primarily based on the measurements and information gained from the ProtoDUNE experience. These measurements are proofs-of-concept for many of the systems, and their behavior can be reliably extrapolated to the projected levels needed for the complete DUNE experiment.

The ProtoDUNE experience highlights the significant technical challenges that must be overcome by 2024 for DUNE. Among the most significant will be 1) the design of DUNE-specific systems able to integrate the large suite of ancillary data (e.g., configurations, calibrations, shower libraries) with the main TPC data stream; 2) the potentially extreme size of some physics interactions, notably supernova bursts, that could produce enough data to overwhelm conventional processors; and 3) the continuing need for evolution of computing architectures and infrastructure over the next decade. These challenges are unique to DUNE where the limiting factor will be human effort.

In summary, the DUNE computing strategy must be global, working with partners worldwide, and collaborative because many of the computational challenges we face are also faced by other, similar experiments. We are extremely fortunate to have the ProtoDUNE experience and test data to exercise our computing infrastructure and develop algorithms for full DUNE operations, although we know significant and interesting challenges lie ahead.

2020 JINST 15 T08008

6.2 Computing consortium

6.2.1 Overview

The mission of the DUNE CSC is to acquire, process, and analyze both detector data and simulations for the collaboration. This mission must extend over all the primary physics drivers for the experiment and must do so both cost effectively and securely. The CSC provides the bridge between the online systems for DAQ and monitoring and the physics groups who develop high-level algorithms and analysis techniques to perform measurements using the DUNE data and simulations. The CSC works with collaborating institutions to identify and provide computational and storage resources. It provides the software and computing infrastructure in the form of analysis frameworks, data catalogs, data transport systems, database infrastructure, code distribution mechanisms, production systems, and other support services essential for recording and analyzing the data and simulations.

The CSC works with national agencies and major laboratories to negotiate use and allocation of computing resources. This work includes support for near-term R&D efforts such as ProtoDUNE runs, and extends to designing, developing, and deploying the DUNE computing model and its requisite systems. This includes evaluating major software infrastructure systems to determine their usefulness in meeting the DUNE physics requirements. These evaluations should identify opportunities to adopt or adapt existing technologies, and to engage in collaborative ventures with HEP experiments outside of DUNE.

At first glance, the DUNE CPU and storage needs appear modest compared to the corresponding needs for the high-luminosity LHC experiments. However, the beam structure, event sizes, and analysis methodologies make DUNE very unlike collider experiments in event processing needs and projected computational budgets. In particular, the large DUNE event sizes (0.1-10 GB as opposed to 1-10 MB per detector readout) present a novel technical challenge when data processing and analysis are mapped onto current and planned computing facilities. The advent of high-performance computing systems optimized for parallel processing of large data arrays is a great advantage for DUNE. These architectures suit the uniform LArTPC raw data structure very well, in contrast to the more complex data structures and geometries present in conventional heterogeneous HEP data.

DUNE will require significant effort to adapt to emerging global computing resources that likely will be both more heterogeneous in computational capabilities (e.g., featuring CPU, GPU, and other advanced technologies) and more diverse in topological architectures and provisioning models. The DUNE CSC must be ready to fully exploit these global resources after 2026, allowing all collaborators to access the data and meet the scientific mission of the experiment.

6.2.2 Resources and governance

The CSC was formed from an earlier ad hoc DUNE computing and software group. The governance structure for the CSC is described in ref. [48]. The consortium coordinates work across the collaboration, but funding comes from collaborating institutions, laboratories, and national funding agencies.

The CSC has an elected consortium leader who is responsible for subsystem deliverables and represents the consortium in the overall DUNE collaboration. In addition, technical leads act as overall project managers for the CSC. The technical leads report to the overall consortium

2020 JINST 15 T08008

leader. CSC has both a host laboratory technical lead to coordinate between the DUNE project and Fermilab, the host laboratory, and an international technical lead to coordinate with other entities. At least one of the three leadership roles should be held by a scientist from outside the USA. CSC management currently appoints people to other roles, typically after a call for nominations. A more formal structure for institutional contributions and commitments is under consideration.

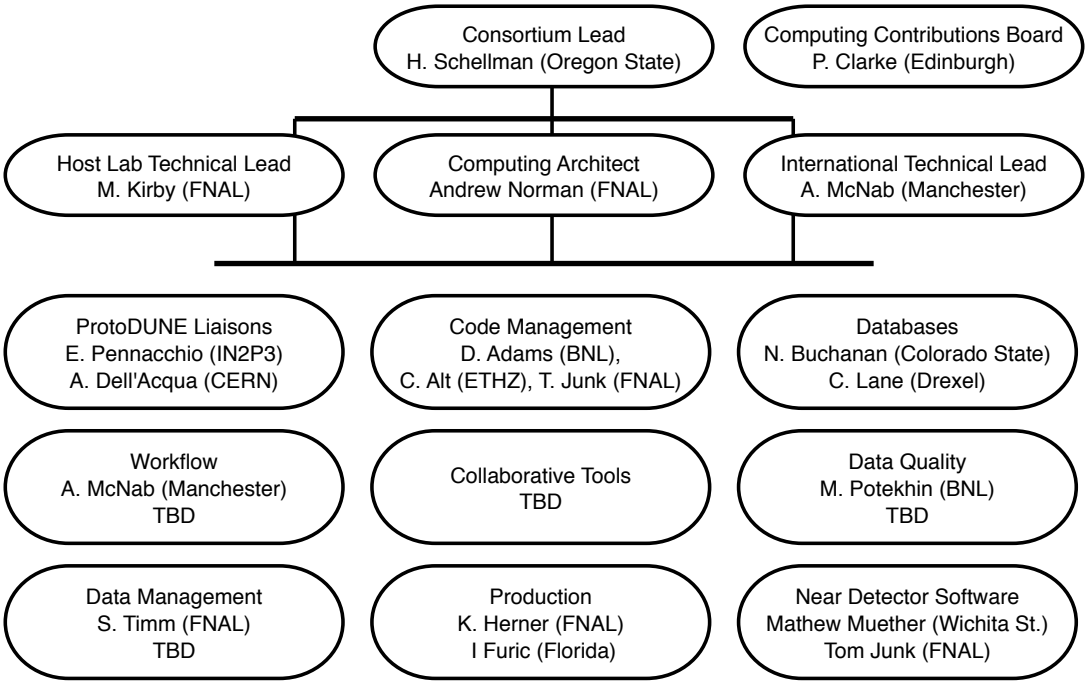

Figure 6.1. Organization chart for current CSC.

6.2.3 Scope of the consortium

The CSC member institutions (table 6.1) focus on the hardware and software infrastructure for offline computing. Responsibility for developing algorithms resides with the physics groups, and online systems at experimental sites are governed by the DAQ and CISC consortia. The CSC defines interfaces, sets coding standards, and provides training. All groups coordinate closely to ensure that the full chain of data acquisition, processing, and analysis functions properly. Formal interfaces with the DAQ and controls groups are described in [49, 50].

The CSC operates at two levels: at the hardware level, where generic resources can be provided as in-kind contributions to the collaboration, and at the human level, where individuals and groups help develop common software infrastructure. The technology for hardware contributions (e.g., grid CPU and storage) exists and was successfully used during the ProtoDUNE-SP data run and its associated simulation and reconstruction. Highlights of that effort are discussed below and in Volume II, DUNE physics, chapter 4.

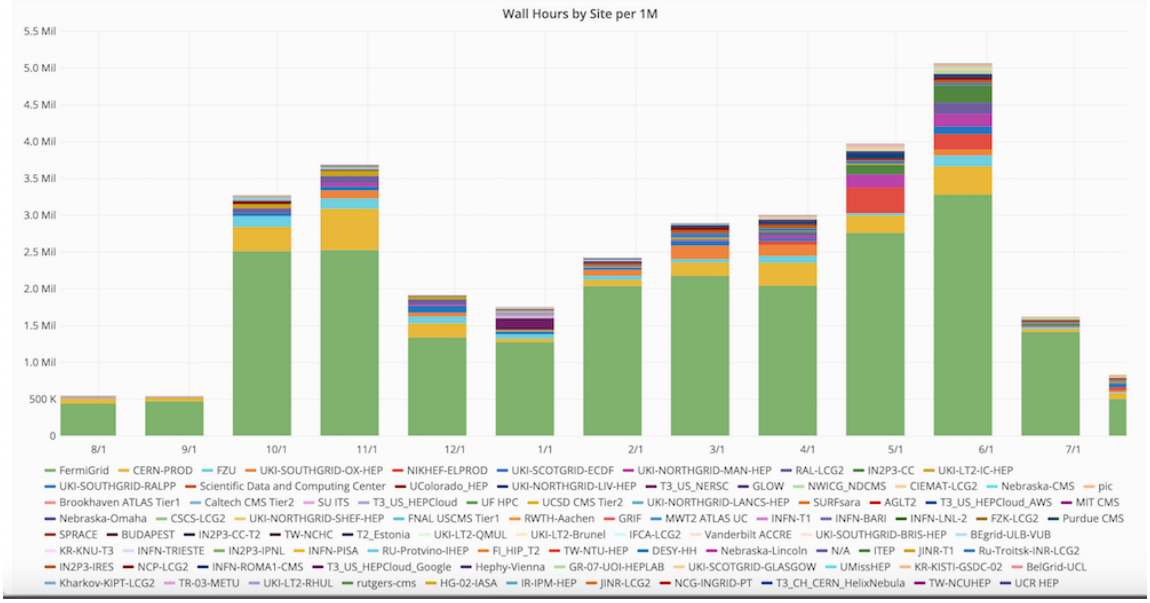

Figure 6.2. CPU wall-time from July 2018 to July 2019, the first peak shows ProtoDUNE-SP reconstruction while the second is dominated by data analysis and ProtoDUNE-DP simulation. A total of 31 million wall-hours were delivered with 24 M-hrs coming from Fermilab.

6.2.4 Hardware resources

As illustrated in figure 6.2, the DUNE collaboration has already used substantial global resources through the WLCG and OSG mechanisms. As the experiment evolves over the next five years, institutions and collaborating nations will be asked to formally pledge resources (both CPU and storage), and those resources will be accounted for and considered in-kind contributions to the collaboration. A computing resources board will be set up to administer this process and serve as liaison to national resource providers.

Several international partners are already contributing substantially to CPU resources, and we continue to integrate additional large national facilities. Most CPU resources are opportunistic, but Fermilab and CERN have committed several thousand processor cores and several PB of data storage. Additionally, DUNE is one of the first beneficiaries of the IRIS project (UK), which provides computing for astronomy and particle physics. We are working with OSG and WLCG to integrate reporting mechanisms for CPU use, so accurate monitoring of hardware contributions will be in place for a second planned ProtoDUNE run in 2021-2022 and the buildup to data taking in the mid 2020's.

6.2.5 Personnel

The advancement of a dedicated DUNE computing team responsible for operations and development of new tools specific to the DUNE experiment is ongoing. Figure 6.1 shows the current CSC organization, where only a few of the listed individuals are full-time on DUNE. Thus, we rely on common tools and techniques shared with other, smaller experiments at CERN and Fermilab. In particular, DUNE operates as one of several intensity frontier experiments at Fermilab where a

Table 6.1. DUNE computing and software consortium members.

Institution	Country
Centro Brasileiro de Pesquisas Físicas	Brazil
Universidade Estadual de Campinas	Brazil
York University	Canada
European Organization for Nuclear Research	CERN
Institute of Physics of the Czech Academy of Sciences	Czech Republic
Laboratoire d'Annecy-le-Vieux de Physique des Particules	France
Tata Institute of Fundamental Research	India
Korean Institute for Science and Technology Information	Korea
Nikhef National Institute of Subatomic Physics	Netherlands
University of Bern	Switzerland
Centro de Investigaciones Energéticas, Medeioambientales y Technólogicas	Spain
University of Edinburgh	UK
The GridPP Collaboration	UK
University of Manchester	UK
Queen Mary University	UK
STFC Rutherford Appleton Laboratory	UK
Argonne National Laboratory	USA
University of California, Berkeley	USA
Brookhaven National Lab	USA
Colorado State University	USA
University of Colorado Boulder	USA
Fermi National Accelerator Laboratory	USA
University of Florida	USA
Lawrence Berkeley National Laboratory	USA
University of Minnesota	USA
Northern Illinois University	USA
University of Notre Dame	USA
Oregon State University	USA
SLAC National Accelerator Laboratory	USA
The University of Texas at Austin	USA
Valley City State University	USA

substantial amount of shared resources can be accessed, but with few personnel assigned specifically to DUNE.

The full DUNE software and computing effort will be much larger than that for ProtoDUNE. The unique DUNE data footprint and anticipated evolution in processor technologies will require a major undertaking to construct and operate the necessary computing infrastructure. This infrastructure must be in place well before detector commissioning begins at SURF.

Two basic design tenets are cooperation with the broader community and reuse of tools. Collaboration scientists will develop much of the high-level algorithms, but a dedicated group of experts with advanced programming and project management skills are needed to build and operate the core software infrastructure for the experiment. Personnel resources are similar to those required for LHCb and Belle II, which are collaborations of a similar size to DUNE. Based on a comparison to those experiments, approximately 20 full-time-equivalent (FTE) workers should be dedicated to ensure primary DUNE software and computing needs are met. This estimate of future personnel requirements follows from an assessment of the LHCb organization structure.

Appendix C.1 describes computing personnel activities in detail. In summary, we will need approximately 20 FTE, with 10 FTE for a software development team that will create and maintain the primary software needed to run DUNE algorithms, and the distributed software infrastructure. Some of these efforts will be completed jointly with other collaborations and HSC/WLCG projects, but in return, DUNE must make substantive contributions to these common efforts. In addition to the software development effort, DUNE computing will require specific operational roles such as data manager, code librarian, and user support. Based on LHCb experience, we have identified ten such roles each requiring an FTE of 0.5 to 2.0. These roles can be filled by experienced DUNE collaborators or computing professionals, and their contributions to the experiment should be properly recognized as equivalent to efforts in construction or operation of the experiment.

The CSC has instituted a series of workshops, which started with two on the topic of "Data Model and Infrastructure" in the summer and fall of 2019, to set the scope of the subprojects to prepare for a formal computing TDR. Table 6.2 gives a draft timeline for the computing project.

6.2.6 Resource contributions

The CSC resource board is developing a formal resource funding model. Currently, we would expect collaborating countries to contribute to computing physical resources and operational duties (e.g., shifts) distributed fairly and developed in consultation with the full DUNE collaboration. The core of the software development effort would mainly come from CSC members. Contributions will be a mix of CPU resources, storage, and personnel, with the mix tailored to the resources and capabilities of each country and institution. To date, these contributions have been voluntary and opportunistic, but will evolve to a more formal model similar to the pledges in the LHC experiments.

6.3 Data types and data volumes

Offline computing for DUNE creates new and considerable challenges because of the experiment's large scale and diverse physics goals. In particular, the advent of LArTPCs with an exquisite resolution and sensitivity, combined with the enormous physical volume of the DUNE far detector and its large number of readout channels, presents challenges in acquiring, storing, reducing, and

Table 6.2. Milestones for DUNE computing development. Data volumes assume 15 PB/year of compressed raw data starting in 2024.

Year	Activity	Integrated data, PB
2018		10
	ProtoDUNE-SP beam run	
2019		19
	ProtoDUNE-SP processing	
	ProtoDUNE-DP commissioning and data taking	
	Develop resource model	
	Develop high level task list	
2020		21
	Continue ProtoDUNE processing/operations Formalize international resource model	
	Build operations team	
	Evaluate data and computing models	
	Database design for hardware	
2021		25
	Produce Computing TDR	
	Framework modifications for HPC	
	Database design for conditions/configuration	
2022		39
	ProtoDUNE second beam run	
	Begin large scale purchases for FD commissioning	
2023		43
	Reconstruct/analyze ProtoDUNE results	
	Continue ProtoDUNE processing/operations	
	Support FD commissioning	
	Conditions and configuration data fully integrated	
	Acquire storage for first year of data from one module	
2024		66
	First real data from one FD module	
	Full operations team in place	
	Data analysis challenges	
2025		88
	Complete provisioning of hardware/storage for first beam run	
2026		111
	First beam run with two modules	

analyzing a prodigious amount of data — orders of magnitude more data than in previous neutrino experiments.

Neutrino experiments operate at low event rates, on the order of 1 Hz even for near detectors. Despite these low event rates, DUNE can generate enormous amounts of data from a single event. This leads to unique challenges in cataloguing, storing and reconstructing data, even though the total volume of data and CPU needs are significantly lower than in large collider experiments. At a collider, each of the billions of triggered beam crossings is reasonably small and effectively independent of the others. In contrast, a single DUNE trigger readout can be many GB in size and, in the case of a supernova candidate, many TB. Maintaining the coherence of such large correlated volumes of data in a distributed computing environment presents a significant challenge.

The rapidly changing computing landscape presents other challenges in this area, as the traditional HEP architecture of individual core processors running single-threaded applications is superseded by applications that efficiently use multiple processors and perhaps even require GPUs. At the same time, despite the rapid development of algorithms for LArTPC reconstruction, they are by no means mature. The ProtoDUNE-SP test at CERN in fall 2018 has contributed greatly to this development by providing a wealth of data that will inform the evolution of future DUNE computing models.

The CSC, SP DAQ, and host laboratory have agreed on a preliminary maximum data transfer rate from the FD to Fermilab of 100 Gbit/s, consistent with projected network bandwidths in the mid 2020s, and a limit of 30 PB/year raw data stored to tape. Calibration for the FD modules (10 PB/year/module to 15 PB/year/module) and beam and cosmic ray interactions in the ND will dominate uncompressed data volumes. With a factor of four for lossless compression, we anticipate a total compressed data volume of 3 PB/year/module to 5 PB/year/module for the full FD; ND rates are not yet established but are likely smaller.

This section describes the make-up and rates of the data to be transfered.

6.3.1 Single-phase technology data estimates

Each of the 150 SP module anode plane assemblies (section 3.2) has 2,560 readout channels, each of which is sampled with 12 bit precision every 500 ns. For a TPC of this size, drift times in the LAr are approximately 2.5 ms and the volume of raw data before compression is approximately 6 GB per 5.4 ms readout window. With no triggering and no zero suppression or compression, the volume of raw data for the four modules would be on the order of 145 exaB/year. Table 6.3 summarizes the relevant parameters for the SP technology. For our calculations of data volume, we assume lossless compression and partial, rather than full, readouts of regions of interest (ROIs) in the FD modules. We do not assume zero-suppression at the level of single channels.

6.3.2 Dual-phase technology data estimates

A DP module will have 153,600 readout channels and a full drift time of 7.5 ms. Given 20,000 samples in an 8 ms readout, the uncompressed event size is 4.2 GB (for one drift window). Gas amplification leads to a high S/N ratio, allowing lossless compression to be applied at the front end with a compression factor of ten; this brings the event size per module to 0.42 GB.

An FD DP module can be treated as twenty smaller detectors, each with a number of readout channels similar to ProtoDUNE-DP running in parallel, and each defining a sub-module ROI. For

Table 6.3. Useful quantities for computing estimates for SP readout.

Quantity	Value	Explanation
Far Detector Beam:		
Single APA readout	41.5 MB	Uncompressed 5.4 ms
APAs per module	150	
Full module readout	6.22 GB	Uncompressed 5.4 ms
Beam rep. rate	0.83 Hz	Untriggered
CPU time/APA	100 sec	from MC/ProtoDUNE
Memory footprint/APA	0.5-1GB	ProtoDUNE experience
Supernova:		
Single channel readout	300 MB	Uncompressed 100 s
Four module readout	450 TB	Uncompressed 100 s
Trigger rate	1 per month	(assumption)

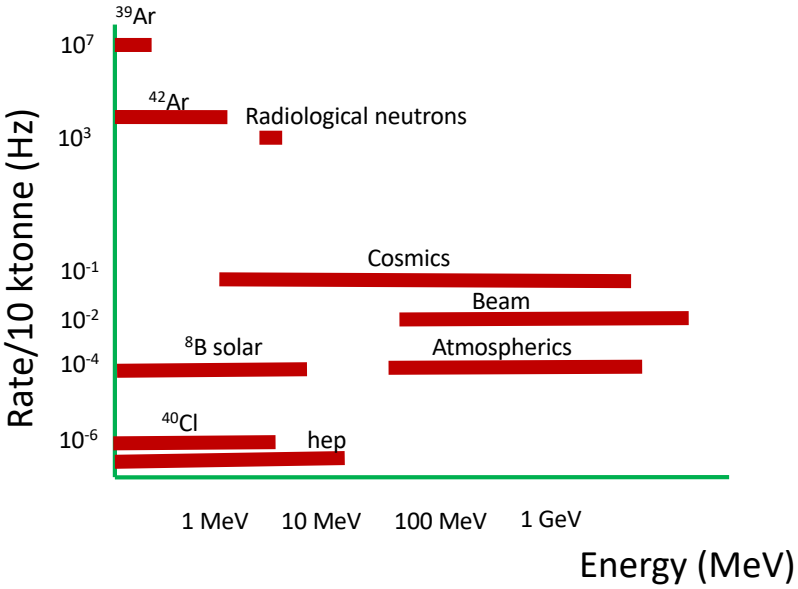

Figure 6.3. Expected physics-related activity rates in a single 10 kt SP module. Figure from Volume IV, The DUNE far detector single-phase technology, chapter 7.

beam or cosmic events, it is possible to record only the interesting ROIs with the compressed size of a single ROI at 22 MB.

6.3.3 Data rates

Figure 6.3 illustrates the raw rates and energy ranges for relevant physical processes in a single DUNE FD module.

Table 6.4. Summary of expected data rates for a single 10 kt SP module (from Volume IV, The DUNE far detector single-phase technology). The rates assume no compression. ^{39}Ar decay candidates are temporarily stored for one to two months at a time. The same applies to fake SNB data. Improved readout algorithms will be developed and evaluated with the initial data and are expected to reduce the data volume by about a factor of ten while retaining efficiency.

Source	Annual Data Volume	Assumptions
Beam interactions	27 TB	10 MeV threshold in coincidence with beam time, including cosmic coincidence; 5.4 ms readout
^{39}Ar, cosmics and atmospheric neutrinos	10 PB	5.4 ms readout
Radiological backgrounds	< 2 PB	< 1 per month fake rate for SNB trigger
Cold electronics calibration	200 TB	
Radioactive source calibration	100 TB	< 10 Hz source rate; single APA readout; 5.4 ms readout
Laser calibration	200 TB	10^6 total laser pulses; half the TPC channels illuminated per pulse; lossy compression (zero-suppression) on all channels
Random triggers	60 TB	45 per day

6.3.3.1 Beam coincident rates

Requiring coincidence with the 10 µs LBNF beam spill would reduce the effective live time from ~ 1.2 s to a 5.4 ms readout window (8 ms for DP), leading to an uncompressed event size of approximately 24 GB for four SP modules (somewhat less for DP) — still too much to record permanently at full rate. Only a few thousand true beam interactions in the FD modules are expected each year. Compression and conservative triggering based on PDs and ionization should reduce the data rate from beam interactions by several orders of magnitude without sacrificing efficiency. Studies discussed in Volume IV, The DUNE far detector single-phase technology, chapter 7 indicate that high trigger efficiencies are achievable at an energy threshold of 10 MeV, leading to event rates for beam-initiated interactions of ~ 6,400/year. Table 6.4, adapted from Volume IV Chapter 7, summarizes expected uncompressed rates from one SP module.

6.3.3.2 Near detector

The ND configuration is not yet fully defined, but we do have substantial experience from T2K and MicroBooNE at lower energies, and MINERvA and NOvA at the DUNE beam energies on cosmic and beam interactions under similar conditions. We expect that the DUNE ND will have ~ 1 beam interaction per m^3 per beam pulse, and non-negligible rates of cosmic rays. Initial estimates indicate that zero-suppressed data rates will be of order 10 MB/s with yearly data volumes less than a PB.

6.3.3.3 Processes not in synchronization with the beam spill

Processes not associated with the beam spill include SNB physics, proton decay, neutron conversion, and atmospheric and solar neutrino interactions. These processes generally have less energy, making triggering more difficult, and they are asynchronous, thus requiring an internal or external trigger. In particular, SNB signals will consist of a large number of low-energy interactions spread throughout the FD volume over a period of 1-100 seconds. Buffering and storing 100 seconds of SNB data would require approximately 20,000 readout windows, or 460 TB for a four-module readout. At a rate of one fake SNB event per month, this would generate 6 PB of uncompressed data per year. Reconstructing and analyzing these data will require substantial evolution in our software frameworks, which were developed to process small (1 MB to 100 MB) events on single processors. Updating the frameworks is a major upcoming task for the DUNE computing R&D.

6.3.3.4 Calibration

The FD modules will require continuous calibration and it is likely that these calibration samples will dominate the data volume. Cosmic-ray muons and atmospheric neutrino interactions will provide a substantial sample for energy and position calibrations. Dedicated runs with radioactive sources and laser calibration will also generate substantial and extremely valuable samples. Table 6.4 includes estimates for the SP module.

Electron lifetime in the detector volume can be monitored via ^{39}Ar decays at rates of ~ 1/kg/sec. As discussed in the appendices for Volume II, DUNE physics, a single 5 ms readout of the full detector would provide 50,000 decays for study. A small number of such readouts per day would provide a global monitor of conditions at the 1% level, but measurements sensitive on meter scales will require a factor of 10^4 more data, and can become a significant fraction of the calibration data stream. In summary, ^{39}Ar cosmic ray and atmospheric neutrino signals collected for calibration make up the bulk of the uncompressed SP data volume at ~ 10 PB/year per module and will dominate the rates from the FD modules.

6.3.3.5 Zero suppression

The data volumes discussed above are for non-zero-suppressed readout of the full FD. A combination of local triggering, zero suppression, and efficient lossless compression mechanisms can substantially reduce the final data volume. However, previous HEPexperience indicates that signal processing must be done carefully and is often done after data-taking, and when the data are well understood. As a result, early running often generates large data volumes while algorithms are being tuned. Experience from the SBN and ProtoDUNE experiments will help us develop these data movement and processing algorithms, but they may be applied later in the processing chain for SP. No zero-suppression is planned for DP.

6.3.4 Simulation

The bulk of data collected with the FD is likely to be background, with real beam interaction events in the FD numbering in the thousands per year, not millions. Thus, the size of beam event simulation samples may be smaller than the unprocessed raw data considered above. Simulation of lower-energy events should reflect the fact that they are very rare; they could be simulated in

sub-volumes of the whole detector. While simulation will be important to the experiment, it is not expected to dominate the data volume as it does in many experiments.

Simulation inputs such as flux files, overlay samples, and shower libraries must be distributed to simulation jobs carefully. Proper simulation requires that these inputs be distributed in unbiased parcels, which from a technical standpoint can be difficult to do efficiently in a widely distributed environment. This will require thoughtful design.

6.3.5 Analysis

We anticipate that most analysis samples will be many times smaller than the raw data, however, since they are distinctive to particular analyses and even users, producing and cataloguing them will require carefully designed tools and substantial oversight. DUNE will need a mix of official samples, produced by physics groups and distributed through a common catalog and through common file transfer mechanisms, as well as small user samples on local disks.

Final oscillation parameter scans with a large number of parameters can be quite CPU-intensive. For example, the NOvA collaboration's recent physics results required tens of millions of high-performance computing (HPC) CPU hours at the NERSC facility at Lawrence Berkeley National Laboratory (LBNL). DUNE collaborators used simpler models but the same techniques to generate some of the results presented in Volume II, DUNE physics. These large-scale analysis projects will require collaboration-wide coordination of resources and will benefit greatly from optimization for specific architectures.

6.3.6 Data storage and retention policies

Some data samples, e.g., real neutrino and cosmic ray interactions in the FD, most of the ND data, and any real SNB events, will be extremely valuable and will require conservative and potentially redundant retention policies. Calibration samples, and possibly fake SNB triggers, may be stored temporarily and discarded after processing.

6.4 ProtoDUNE-SP data

6.4.1 Introduction

ProtoDUNE-SP ran at CERN in the NP04 beamline from September to November of 2018. Before that run, several data challenges at high rate validated the data transfer mechanisms. The run itself has already served as a substantial test of the global computing model, and studies of cosmic rays continue.

This section describes the ProtoDUNE data design and the lessons learned from our experience.

6.4.2 Data challenges

Starting in late 2017, a series of data challenges were performed with ProtoDUNE-SP. Simulated data were passed through the full chain from the event builder machines to tape storage at CERN and Fermilab at rates up to 2 GB/s. These studies allowed optimizing the network and storage elements well before the start of data taking in fall 2018. The full DUNE FD, in writing 30 PB/year, will produce data at rates similar to those in the 2018 data challenges. While accommodating

2020 JINST 15 T08008

the ProtoDUNE-SP data rates was not technically challenging, the integrated data volume from an experiment running 99% of the time over several decades will be.

6.4.3 Commissioning and physics operations

The first phase of operations involved commissioning the detector readout systems while the LAr reached full purity. During this period data were taken with cosmic rays and beam. Once high LAr purity was reached, ProtoDUNE-SP collected physics data with beam through October and half of November 2018. After the beam run, we continued to take cosmic ray data under varying detector conditions, such as modified high voltage and purity, and new readout schemes.

6.4.4 Data volumes

ProtoDUNE-SP comprises a TPC consisting of six APAs, their associated PDs, and a CRT. In addition, the NP04 beamline is instrumented with hodoscopes and Cherenkov counters to generate beam triggers. Random triggers were generated at lower rates to collect unbiased cosmic ray information. During the test beam run, the TPC readout dominated the data volume. The nominal readout window during the beam run was 3 ms as a match to the drift time at full voltage (180 kV), which was maintained for most of the run. The TPC alone produced 138 MB/event without compression, not including headers. The uncompressed event size including all TPC information, CRT, and PD data was 170 MB to 180 MB. Data compression was implemented just before the October beam physics run, reducing this number to 75 MB. In all, 8.1 million beam events produced a total of 572 TB. An additional 2.2 PB of commissioning data and cosmic ray data was also recorded. Table 6.5 summarizes the data volumes recorded in ProtoDUNE-SP from October 2018 to October 2019.

Table 6.5. Data volumes recorded by ProtoDUNE-SP as of October 2019.

Type	Events	Size
Raw Beam	8.1 M	520 TB
Raw Cosmics	19.5 M	1,190 TB
Commissioning	3.86 M	388 TB
Pre-commissioning	13.89 M	641 TB

Events were written out in 8 GB raw data files, each containing approximately 100 events. The beam was live for two 4.5 s spills every 32 s beam cycle, and data were taken at rates up to 50 Hz, exceeding the typical 25 Hz, leading to compressed DC rates of 400 MB/s to 800 MB/s from the detector.

6.4.5 Reconstruction of ProtoDUNE-SP data

Thanks to substantial work by the 35 ton prototype, MicroBooNE, and the LArTPC community, high-quality algorithms were in place to reconstruct the TPC data. As a result, a first pass reconstruction of the ProtoDUNE-SP data with beam triggers was completed in December, 2018, less than a month after data taking ended. Results from that reconstruction are presented in Volume II, DUNE physics, chapter 4 with some highlights summarized here.

2020 JINST 15 T08008

6.4.6 Data preparation

Before pattern recognition begins, data from the ProtoDUNE detector is unpacked and copied to a standard format within the art framework based on ROOT objects. This reformatted raw data includes the waveform for each channel, consisting of 6,000-15,000 12-bit, 0.5 μsec samples. The first step in reconstruction is data preparation, which entails the conversion of each ADC waveform into a calibrated charge waveform with signals proportional to charge. Once the data are prepared, hit-level ROIs are identified, and data outside these regions are discarded, significantly reducing data size. The data preparation process is described more fully in [51].

Figures 6.4 and 6.5 illustrate the transformation of TPC data during data preparation for one wire plane for 3 ms. A full 5.4 ms readout of a single 10 kt module would contain a factor of 750 times more information than this image.

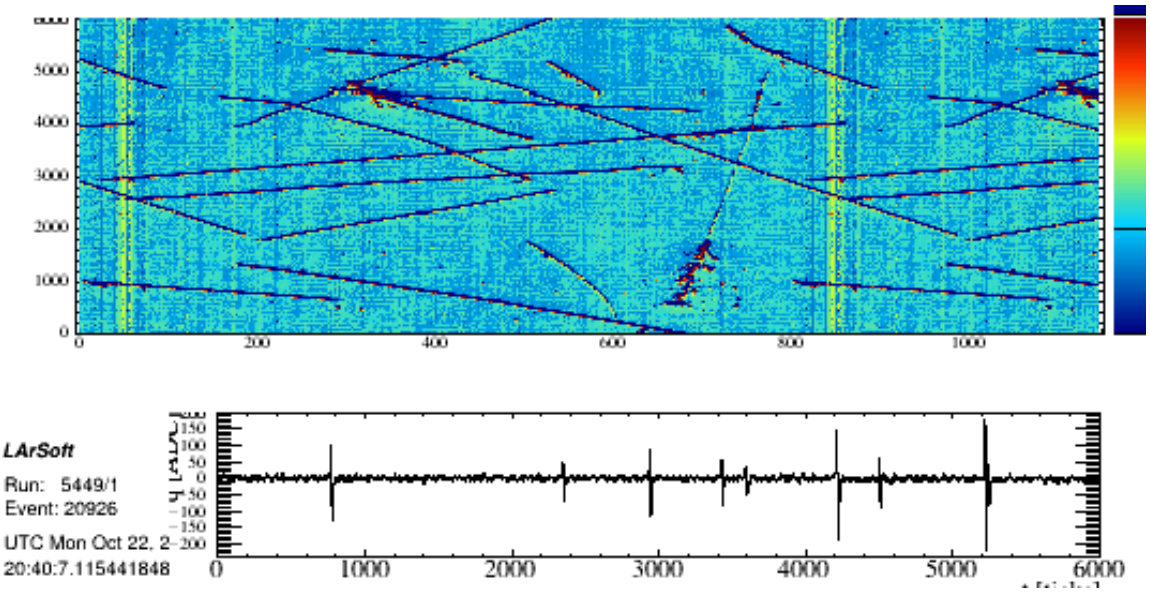

Figure 6.4. Example of pedestal-subtracted data for one ProtoDUNE-SP wire plane. The top pane shows the ADC values in a V (induction) plane (section 3.2) with the x axis as channel number and the y axis as time slice. The bottom pane shows the bipolar pulses induced on one channel.

6.4.7 Computational characteristics of data preparation and deconvolution

Decoding for ProtoDUNE-SP originally stored all six APAs in memory. Each 3 ms of APA readout consists of more than 15 M 16-bit values. Decompressing and converting this information to a floating point format causes substantial memory expansion. Data with a 7.5 ms window were also recorded. The input and output event sizes and reconstruction time scale were found to scale linearly with the readout window and with the number of APAs processed.

Processing each wire plane (three per APA) independently reduces the memory footprint because electrical signals correlate between channels within an APA wire plane but not between planes. However, although subdividing the detector into wire planes reduces the memory footprint for short (beam-related) readouts, this is not a viable solution for the long readouts expected for SNB events. We are still seeking the best strategy for these much larger ($\times$10,000) time windows.

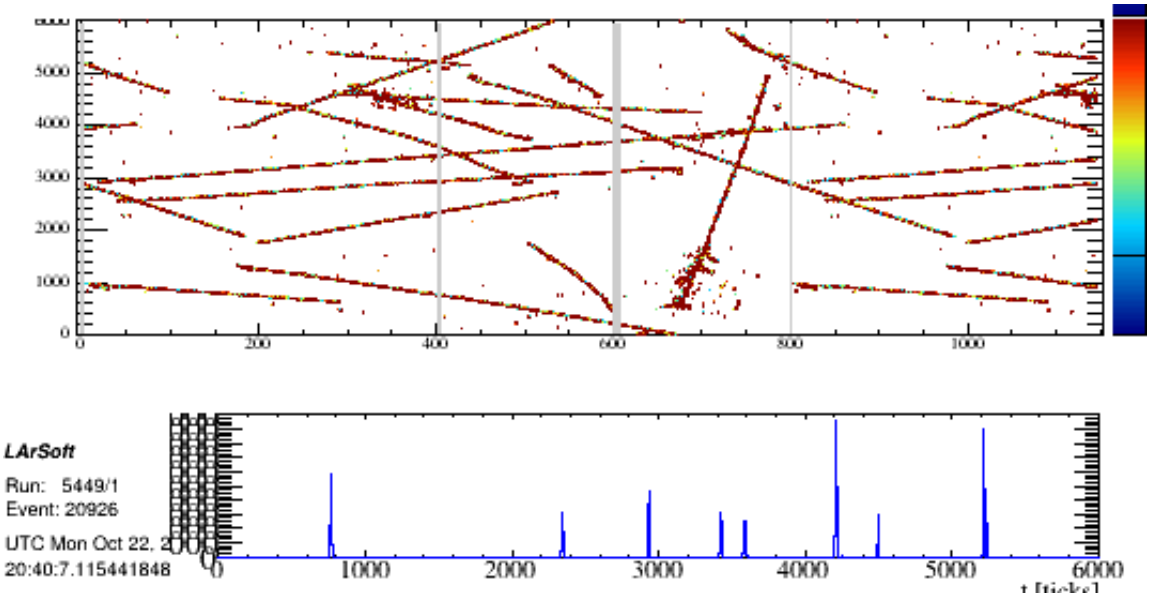

Figure 6.5. Pedestal-subtracted data for one ProtoDUNE-SP wire plane, as in figure 6.4, after calibration, cleanup, deconvolution, and finding ROIs.

The DAQ consortium is exploring methods for segmenting large events (such as SNBs) into smaller ROIs in both time and space for efficient readout. As long as those regions are on the scale of single interactions, the resulting data should fit into a reasonable memory budget at the expense of tracking and collating many distributed interactions.

The operations performed in signal processing require few decisions but do include operations such as fast Fourier transforms and deconvolution. These operations are well suited for GPU and parallel processing. We are actively exploring multi-threaded processing for all data preparation algorithms.

6.4.8 Reconstruction characteristics

Once ROIs have been identified, several 3D reconstruction packages are used. For the first reconstruction pass in November, the Pandora [52], Wire-Cell [53], and Projection Matching Algorithm (PMA) [54] frameworks were used. The results are described in Volume II, DUNE physics. Figure 6.6, taken from that volume, illustrates the measured efficiency for the Pandora algorithm reconstructing a triggered beam particle as a function of momentum for the simulation and data for selected data taking runs. Figure 6.6 demonstrates that the efficiency is already high and reasonably well simulated.

Full reconstruction of these ProtoDUNE-SP interactions, with beam particles and approximately 60 cosmic rays per readout window, took approximately 600 s/event with 200 s each for the signal processing and hit finding stages; the remaining time was divided among three different pattern recognition algorithms. Output event records were substantially smaller (22 MB compressed) but were still dominated by information for TPC hits above threshold.

All these algorithms are run on conventional Linux CPUs using OSG/WLCG grid computing infrastructure. Deep learning techniques based on image pattern recognition algorithms are also

2020 JINST 15 T08008

being developed. Many of these algorithms can be adapted to run on HPC assets, although the optimal architecture for 3D reconstruction likely differs from that for hit finding.

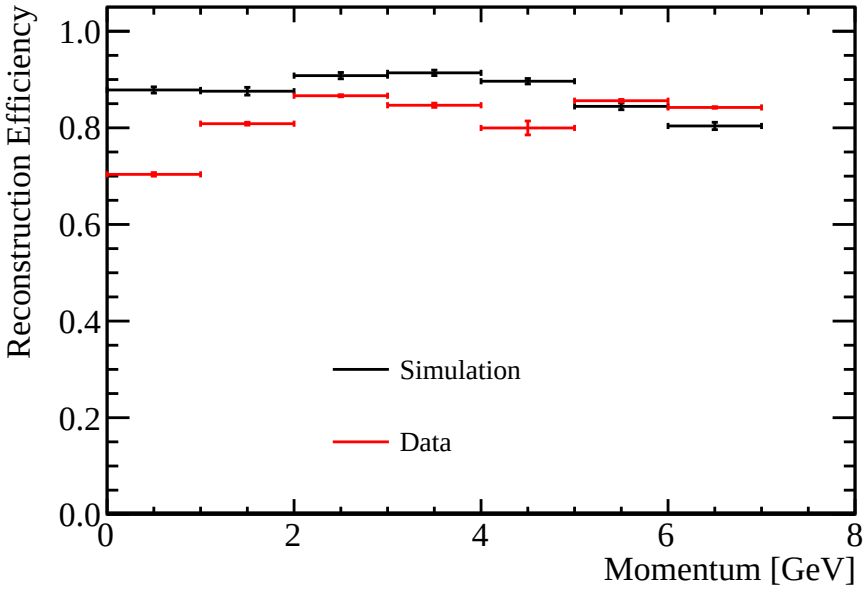

Figure 6.6. The efficiency of reconstruction for the triggered test beam particle as a function of particle momentum in data (red) and simulation (black). (figure 4.30 from Volume II, DUNE physics.)

6.4.9 Lessons learned

The first ProtoDUNE-SP run has given us very valuable information for planning the full DUNE computing model.

- Data and simulation challenges led to a reasonably mature and robust model for acquiring, storing, and cataloging the main data stream at design rates.
- The experiment integrated several existing grid sites and used substantial opportunistic resources. This allowed initial processing of data within one month of the end of the run.
- Prototype infrastructure was in place for provisioning, authentication and authorization, data management, networking, file catalog, and workflow management.
- Reconstruction algorithms were available, permitting immediate studies of detector performance and calibration.
- Beam information was successfully integrated into processing through an IFbeam database.
- Auxiliary information from some systems, e.g., slow controls, was not fully integrated into processing. This led to a manual input of the running conditions by shift personnel, and offline incorporation of that information into the data catalog. This prompted a closer collaboration between the DAQ and CISC groups and the design of robust interfaces for configurations and conditions.

Overall, the ProtoDUNE-SP data taking and processing was a success, despite too much reliance on manual intervention because automated processes were not always in place. Considerable effort must go into integrating detector conditions, data migration, workflow systems, and HPCs with multi-threaded and vectorized software.

Chapter 7

DUNE far site technical coordination

This chapter provides a brief introduction to the DUNE far site technical coordination. The text below closely follows that found in the introductory chapters of Volume III, DUNE far detector technical coordination, where many more details may be found.

7.1 Overview

The DUNE collaboration has responsibility for the design and construction of the DUNE FD. Groups of collaboration institutions, referred to as consortia, assume responsibility for the different detector subsystems. The activities of the consortia are overseen and coordinated through the DUNE technical coordination organization headed by the DUNE TC. The technical coordination organization provides project support functions such as safety coordination, engineering integration, change control, document management, scheduling, risk management, and technical review planning. DUNE technical coordination manages internal, subsystem-to-subsystem interfaces, and is responsible for ensuring the proper integration of the different subsystems.

DUNE technical coordination works closely with the support teams of its LBNF/DUNE partners within the framework of a Joint Project Office (JPO) to ensure coherence in project support functions across the entire global enterprise. To ensure consistency of the DUNE environment, safety and health (ES&H) and QA programs with those across LBNF/DUNE, the LBNF/DUNE ES&H and QA managers, who sit within the JPO, are embedded within the DUNE technical coordination organization.

The LBNF/DUNE integration office under the direction of the project integration director incorporates the on-site team responsible for coordinating integration and installation activities at the SURF. Detector integration and installation activities are supported by the DUNE consortia, which maintain responsibility for ensuring proper installation and commissioning of their subsystems. External DUNE interfaces with the on-site integration and installation activities are managed through the JPO.

2020 JINST 15 T08008

7.2 Global project organization

7.2.1 Global project partners

The LBNF project is responsible for providing both the CF and supporting infrastructure (cryostats and cryogenics systems) that house the DUNE FD modules. The international DUNE collaboration under the direction of its management team is responsible for the detector components. The DUNE FD construction project encompasses all activities required for designing and fabricating the detector elements and incorporates contributions from a number of international partners. The organization of LBNF/DUNE, which encompasses both project elements, is shown in figure 7.1.

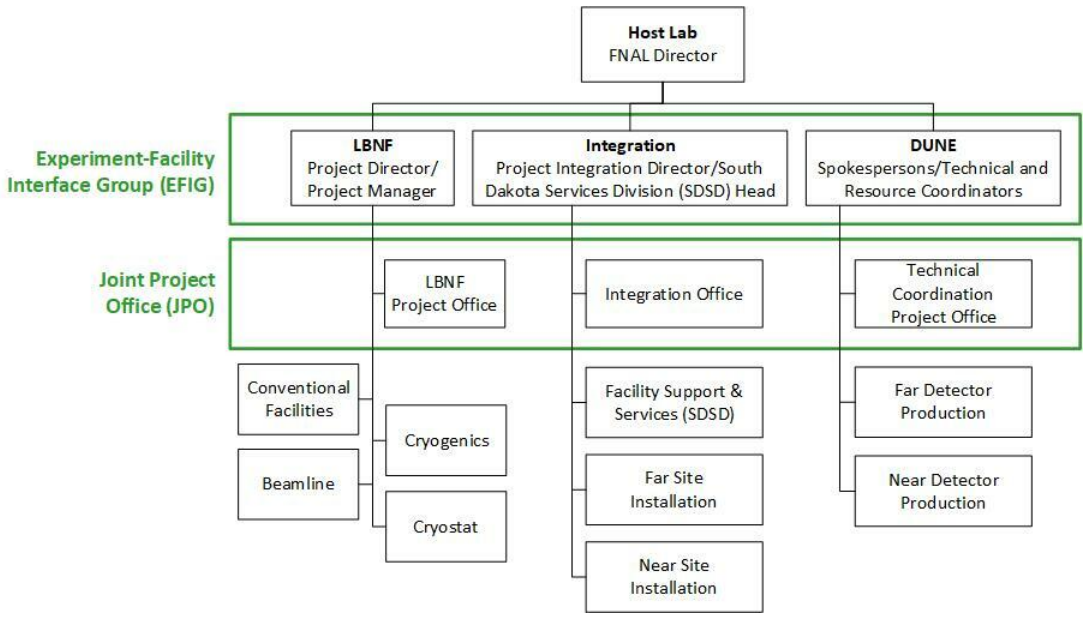

Figure 7.1. The global LBNF/DUNE organization.

The overall coordination of installation activities in the underground caverns is managed as a separate element of LBNF/DUNE under the responsibility of the project integration director, who is appointed by and reports to the Fermilab director. To ensure coordination across all elements of LBNF/DUNE, the project integration director connects to both the facilities and detector construction projects through ex-officio positions on the LBNF project management board and DUNE EB, respectively. The project integration director receives support from the Fermilab South Dakota Services Division (SDSD), a Fermilab division established to provide the necessary supporting infrastructure for installation, commissioning, and operation of the DUNE far detector.

The EFIG is the body responsible for the required high-level coordination between the LBNF and DUNE construction projects. The EFIG is augmented by the JPO that supports both the LBNF and DUNE projects as well as the integration effort that connects the two together. The JPO combines project support functions that exist within the different elements of the global project to ensure proper coordination across the entire LBNF/DUNE enterprise. Project functions coordinated globally through the JPO are shown in figure 7.2 along with the team members currently supporting

these functions within the JPO framework. These team members are drawn from the LBNF project office, DUNE technical coordination, and LBNF/DUNE integration office personnel.

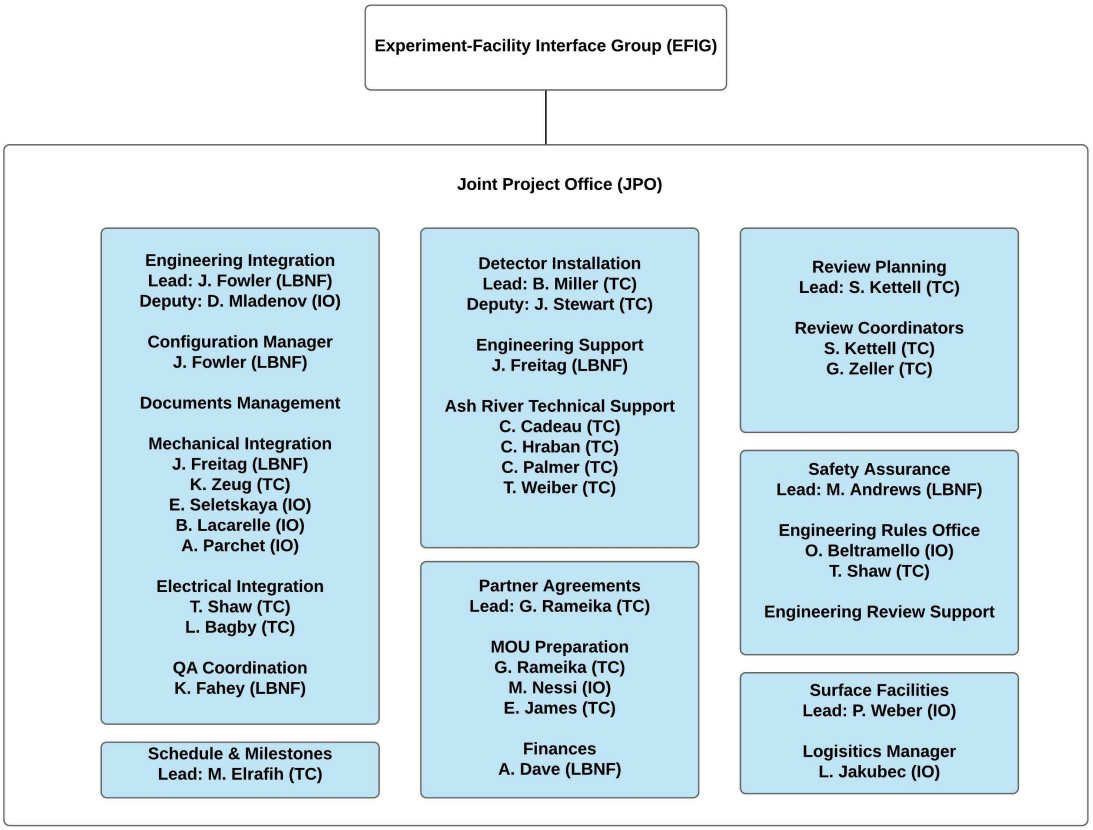

Figure 7.2. JPO global support functions and teams.

7.2.2 Coordinated global project functions

Project support functions requiring JPO coordination include safety, engineering integration, change control and document management, scheduling, review planning and oversight, and development of partner agreements.

Planning activities related to detector installation and the provision of surface facilities are also currently embedded within the framework of the JPO to ensure that all project elements are properly incorporated. At the time when LBNF far site conventional facilities (FSCF) delivers acceptance for use and possession (AUP) of the underground detector caverns at SURF, the coordination of on-site activities associated with detector installation and the operation of surface facilities will be fully embedded within the LBNF/DUNE integration office under the direction of the project integration director.

7.2.3 Coordinated safety program

To ensure a consistent approach to safety across LBNF/DUNE, a single LBNF/DUNE ES&H manager reports to the LBNF project director, the project integration director, and DUNE management

(via the DUNE TC). This individual directs separate safety teams responsible for implementing the LBNF/DUNE ES&H program within the individual LBNF and DUNE projects as well as the coordinated LBNF/DUNE installation activities at SURF. The safety organization is shown in figure 7.3.

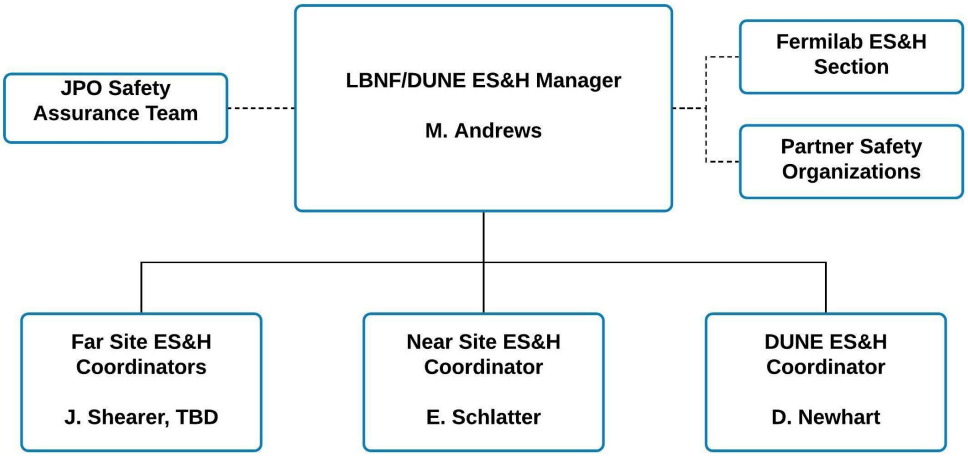

Figure 7.3. High level LBNF/DUNE ES&H organization.

The LBNF/DUNE ES&H manager works with the Fermilab and SURF safety organizations to ensure that all project-related activities comply with the rules and regulations of the host organizations.

The JPO engineering safety assurance team defines a common set of design and construction rules (mechanical and electrical) to ensure consistent application of engineering standards and engineering documentation requirements across LBNF/DUNE. Following lessons learned from the processes used for the ProtoDUNE detectors, an important mandate of the engineering safety assurance team is to ensure that safety issues related to component handling and installation are incorporated within the earliest stages of the design review process.

7.2.4 Detector integration

A central JPO engineering team is responsible for building an integrated model of the detectors within their supporting infrastructure and the FSCF that house them. This team incorporates approved changes as they are received and checks to ensure that no errors or space conflicts are introduced into the model. After receiving the appropriate sign-offs from all parties, the team tags a new frozen release of the model and makes it available to the design teams as the current release against which the next set of design changes will be generated.

Electrical engineers are incorporated within this team to ensure proper integration of the detector electrical components.

The JPO engineering team is also responsible for documenting and controlling the interfaces between the LBNF and DUNE projects as well as the interfaces between these projects and the LBNF/DUNE installation activities at SURF.

The LBNF/DUNE project partners have agreed to adopt the formal change control process developed previously for the LBNF project. The change control process applies to proposed

modifications of requirements, technical designs, schedule, overall project scope, and assigned responsibilities for individual scope items.

7.2.5 Schedule and milestones

The JPO team is responsible for creating a single project schedule for LBNF/DUNE that incorporates all LBNF and DUNE activities together with the installation activities at SURF, incorporating all interdependencies. This schedule will be used to track the status of the global enterprise. DOE activities will be tracked using the formal earned value management system (EVMS) procedures required for the DOE project activities; non-DOE activities will be tracked through regular assessments of progress towards completion by the management teams responsible for those activities.

7.2.6 Partner agreements and financial reporting

Partner contributions to all project elements will be detailed in a series of written agreements. In the case of LBNF, these contributions will be spelled out in bilateral agreements between the DOE and each of the contributing partners. In the case of DUNE, a memorandum of understanding (MoU) will detail the contributions of all participating partners. A series of more technical agreements describing the exact boundaries between partner contributions and the terms and conditions under which they will be delivered will accompany the primary agreements.

7.3 DUNE far detector organization

7.3.1 Detector design and construction

The DUNE FD construction project refers collectively to the activities associated with the design and construction of necessary detector components. DUNE collaboration management is responsible for overseeing this portion of LBNF/DUNE and ensuring its successful execution. The high-level DUNE collaboration management team consisting of the co-spokespersons, TC, and RC is responsible for the management of the construction project.

Construction of the FD modules is carried out by consortia of collaboration institutions who assume responsibility for detector subsystems. Each consortium plans and executes the construction, installation, and commissioning of its subsystem.

Each consortium is managed by an overall consortium leader and a technical lead. The consortium leader chairs an institutional board composed of one representative from each of the institutions contributing to the activities of the consortium. Major consortium decisions such as technology selections and assignment of responsibilities among the institutions pass through its institutional board. These decisions are then passed as recommendations to the DUNE EB for formal collaboration approval.

Because the consortia operate as self-managed entities, a strong technical coordination organization is required to ensure overall integration of the detector elements and successful execution of the detector construction project. Technical coordination areas of responsibility include general project oversight, systems engineering, QA, and safety. Technical coordination also supports the planning and execution of integration and installation activities at SURF. The TC manages the

overall detector construction project through regular technical and project board meetings with the consortium leadership teams and members of the technical coordination organization.

The technical coordination organization, headed by the TC, supports the work of the consortia and has responsibility for a number of major project support functions prior to the delivery of detector components to SURF, including

- ensuring that each consortium has a well defined and complete scope, that interactions between consortia are sufficiently well defined, and that any missing scope outside of the consortia is provided through other sources such as collaboration common funds;
- defining and documenting scope boundaries and technical interfaces both between consortia and with LBNF;
- developing an overall schedule with appropriate dependencies between activities covering all phases of the project;
- ensuring that appropriate engineering and safety standards are developed, understood, and agreed to by all key stakeholders and that these standards are conveyed to and understood by each consortium;
- ensuring that all DUNE requirements on LBNF for FSCF, cryostat, and cryogenics are clearly defined and agreed to by each consortium;
- ensuring that each consortium has well developed and reviewed component designs, construction plans, QC processes, and safety programs; and
- monitoring the overall project schedule and the progress of each consortium towards delivering its assigned scope.

The DUNE technical coordination organizational structure is shown in figure 7.4.

The technical coordination project coordination team incorporates ES&H, QA, and project controls specialists. Overall integration of the detector elements is coordinated through the technical coordination engineering support team headed by the LBNF/DUNE systems engineer and lead DUNE electrical engineer. Planning coordinators for integration and installation activities at SURF (who sit within the LBNF/DUNE integration office) also head the technical coordination installation interfaces team. The dual placement of these individuals facilitates the required coordination of integration and installation planning efforts between the core team directing these activities and the DUNE consortia.

7.3.2 Detector installation and commissioning

The project integration director has responsibility for coordinating the planning and execution of the LBNF/DUNE installation activities, both in the underground detector caverns at SURF and in nearby surface facilities.

The LBNF/DUNE integration office will evolve over time to incorporate the team in South Dakota responsible for the overall coordination of on-site installation activities. In the meantime, the installation planning team within the integration office works with the DUNE consortia and

2020 JINST 15 T08008

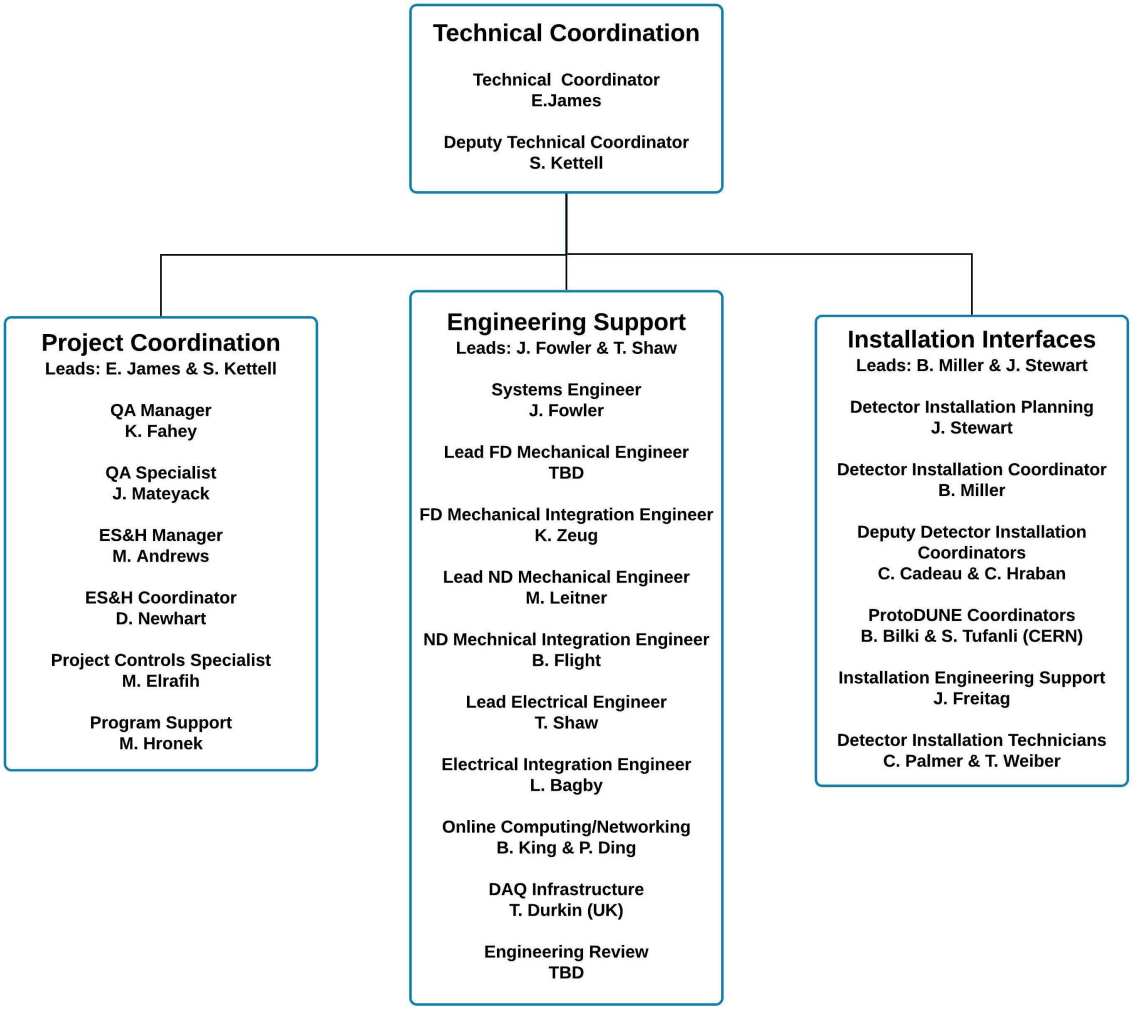

Figure 7.4. DUNE technical coordination organizational chart.

LBNF project team members to plan these activities. This installation team is responsible for specification and procurement of common infrastructure items associated with installation of the detectors. The organization of the on-site team is shown in figure 7.5.

The full on-site integration office team includes rigging teams responsible for moving materials in and out of the shaft, through the underground drifts, and within the detector caverns, and personnel responsible for overseeing safety and logistics planning.

The underground caverns coordinator is responsible for managing all activities in the two underground detector caverns and the CUC. The detector installation teams, distinct from the integration office installation team, incorporate a substantial number of scientific and technical personnel from the DUNE consortia. Integration office coordinators of the detector installation effort are jointly placed within DUNE technical coordination to facilitate consortia involvement in detector installation activities. Any modifications to the facilities occurring after AUP are managed by the underground cavern coordinator under the direction of the project integration director.

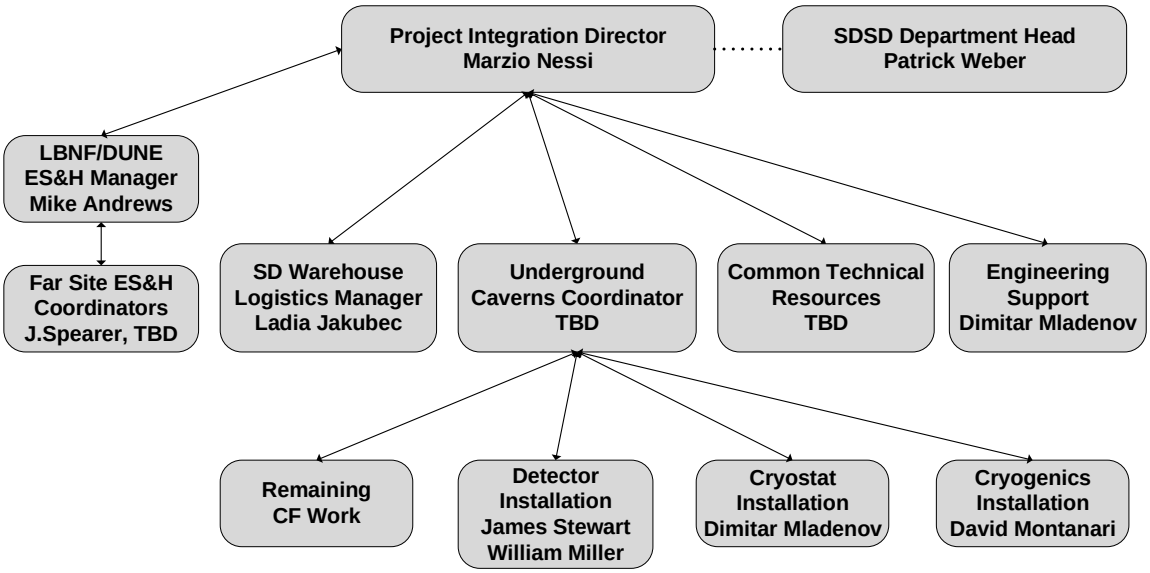

Figure 7.5. Integration office installation team organization chart.

The LBNF/DUNE ES&H manager heads the on-site safety organization and reports to the project integration director to support the execution of this responsibility. The far site ES&H coordinators oversee the day-to-day execution of the installation work.

7.4 Facility description

The DUNE underground campus at the SURF 4850L is shown in figures 1.4 and 7.6. The primary path for both personnel and material access to the underground excavations is through the Ross Shaft.

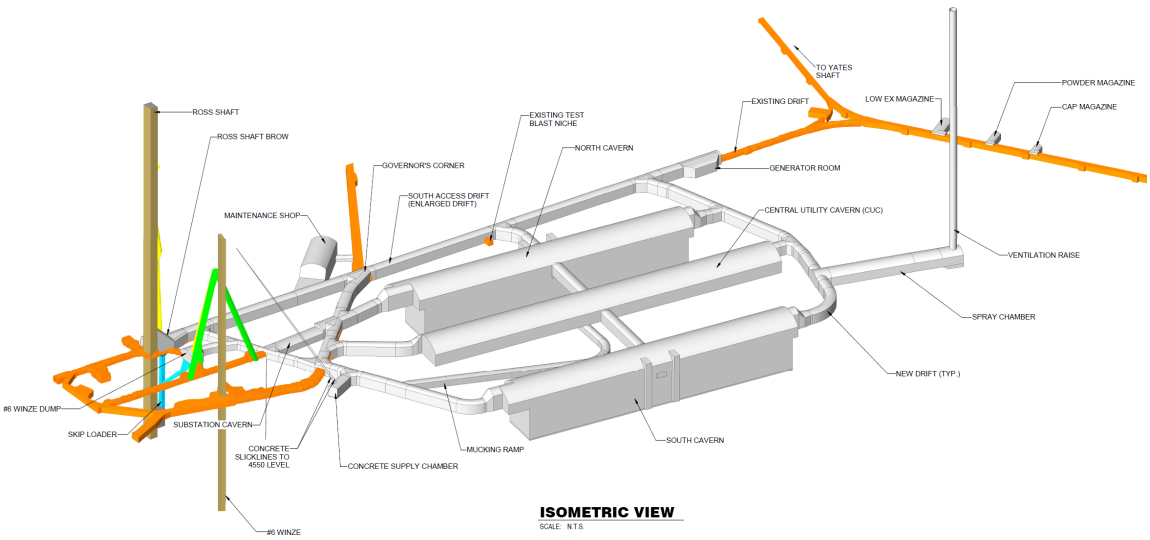

Figure 7.6. Underground campus at the 4850L.

2020 JINST 15 T08008

LBNF will provide facilities and services, on the surface and underground, to support the DUNE FD. This includes logistical, cryogenics, electrical, mechanical, cyber, and environmental facilities and services. All of these facilities are provided for the safe and productive operation of the detector modules.

On the surface, a new compressor building is being constructed adjacent to the Ross headframe. This building will house the cryogenics systems for receiving cryogenic fluids and preparing them for delivery down the Ross Shaft. New piping is being installed down the shaft compartment to transport gaseous argon (GAr) and nitrogen underground where they will be reliquefied.

Two large detector caverns are being excavated. Each of these caverns will support two 17.5 kt-capacity cryostats. The caverns, labeled north and south, are 144.5 m long, 19.8 m wide, and 28.0 m high. The tops of the cryostats are approximately aligned with the 4850L of SURF, with the bottoms resting at the 4910L. A 12 m space between the cryostats will be used for the detector installation process, for placement of cryogenic pumps and valves, and for access to the 4910L. The CUC, between the north and south caverns, is 190 m long, 19.3 m wide, and 10.95 m high.

The South Dakota Warehouse Facility (SDWF) is planned as a leased 5000 m^2 facility, hosted by SDSD, to be located within a maximum one-day roundtrip of SURF. It must be in place for receiving cryostat and detector components approximately six months before AUP of the underground detector caverns is received. Laydown space near the Ross headframe is extremely limited. For this reason, the transportation of materials from the SDWF to the top of the Ross shaft requires careful coordination. The LBNF/DUNE logistics manager works with the construction manager/general contractor (CMGC) through the end of excavation activities and with other members of the integration office team to coordinate transport of materials into the underground areas. Since no detector materials or equipment can be shipped directly to SURF, the SDWF will be used for both short- and long-term storage, as well as for any re-packaging of items required prior to transport into the underground areas.

7.5 Far detector construction management

Eleven FD consortia have been formed to cover the subsystems required for the SP and DP detector technologies (figure 7.7). Three consortia (SP-APA, SP-TPC Electronics and SP-Photon Detection) pursue subsystems specific to the SP design and another three consortia (DP-CRP, DP-TPC Electronics, and DP-Photon Detection) pursue designs for DP-specific subsystems. Five consortia (HV System, DAQ, CISC, Calibration, and Computing) have responsibility for subsystems common to both detector technologies.

The complete scope of the DUNE construction project is captured in a WBS to define and document the distribution of deliverables among the consortia. In combination with interface documentation, the WBS is used to validate that all necessary scope is covered. The WBS is also used as a framework for building DUNE detector cost estimates.

The highest-level layers of the DUNE WBS are summarized in figure 7.8. At level 1 the WBS is broken down into six elements, which correspond to technical coordination (TC in the figure), four FD modules, and a ND. The scope documented in this TDR is fully contained within the elements of level-1 items 1 through 3, the technical coordination, a SP FD module, and a DP FD module.

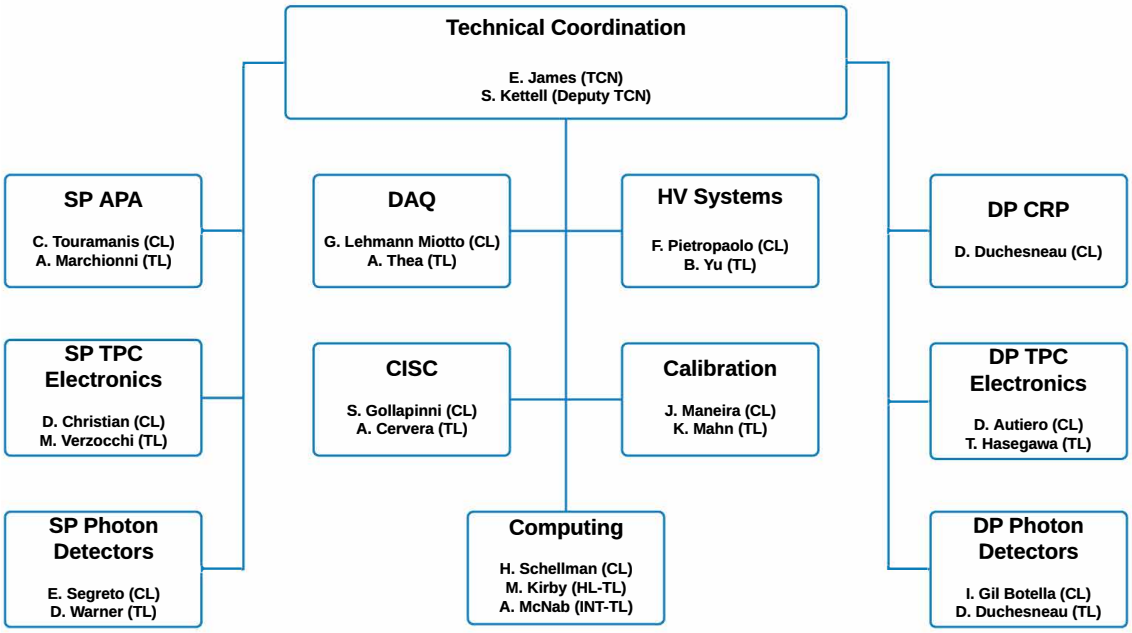

Figure 7.7. Consortia associated with the FD construction effort along with their current leadership teams. CL refers to consortium leader and TL refers to technical lead.

7.6 Integration engineering

Integration engineering for DUNE encompasses three principal focus areas. First, it covers configuration of the mechanical and electrical systems of each detector module and management of the interfaces within them; this includes verifying that subassemblies and their interfaces conform to the approved design of each detector element. A second area is assurance that the detector modules can be integrated and installed into their final configurations. Third, it covers integration of the necessary services provided by FSCF with the detector modules. The overall effort involves the JPO engineering team, who maintains subsystem component documentation for detector configuration management, and the consortia, who provide engineering data for their detector subsystems to the JPO team for incorporation into the global configuration files.

An integration mechanism has been developed to manage and create an overall model of interfaces both within a detector module and between a detector module and facilities. The mechanism defines integration nodes, between which the JPO engineering team carries out and manages interfaces. Figure 7.9 shows the interfaces and nodes between a detector module and the facilities it requires. The JPO engineering team also ensures that the interfaces are appropriately defined and managed for the DAQ room in the CUC and the surface control and network rooms. Interfaces with LBNF are managed at the boundaries of each integration node. Interface documents are developed and maintained to manage the interfaces between consortia and between each consortium and LBNF.

2020 JINST 15 T08008

WBS	WBS name
	DUNE
1	DUNE Technical Coordination (TC)
2	Single Phase Far Detector (DUNE-SP)
2.1	SP Installation (SP-Install)
2.2	SP Anode Plane Assemblies (SP-APA)
2.3	SP TPC Electronics (SP-ELE)
2.4	SP Photon Detection System (SP-PD)
2.8	High Voltage System (SP-HVS)
2.9	DAQ (SP-DAQ)
2.10	Cryogenic Instrumentation & Slow Control (SP-CISC)
2.11	Calibration (SP-CAL)
3	Dual Phase Far Detector (DUNE-DP)
3.1	DP Installation (DP-Install)
3.5	Charge Readout Plane (DP-CRP)
3.6	DP TPC Electronics (DP-ELE)
3.7	DP Photon Detection System (DP-PD)
3.8	High Voltage System (DP-HVS)
3.9	DAQ (DP-DAQ)
3.10	Cryogenic Instrumentation & Slow Control (DP-CISC)
3.11	Calibration (DP-CAL)
4	Reserved for future far detectors
5	Reserved for future far detectors
6	Reserved for near detector

Figure 7.8. High level DUNE WBS to level 2.

7.7 Reviews

The integration office and technical coordination review all stages of detector development and work with each consortium to arrange reviews of the design (conceptual design review, preliminary design review and final design review), production (production readiness review and production progress review), installation (installation readiness review), and operation (operational readiness review) of their system. The reviews are organized by the JPO review office. These reviews provide information to the technical board (TB), EB, and EFIG in evaluating technical decisions.

Review reports are tracked by the JPO review office and technical coordination and provide guidance on key issues that require engineering oversight by the JPO engineering team. The review office maintains a calendar of DUNE reviews.

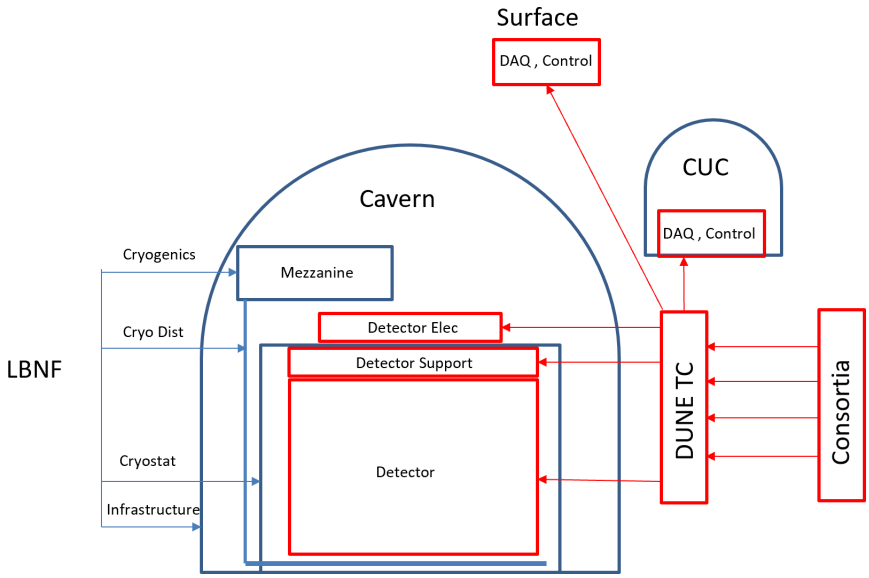

Figure 7.9. Overall integration nodes and interfaces. The items provided by LBNF within the cavern are shown on the left and the items provided by DUNE are on the right.

7.8 Quality assurance

DUNE technical coordination monitors technical contributions from collaborating institutions and provides centralized project coordination functions. One part of this project coordination is standardizing quality assurance (QA)/quality control (QC) practices, a facet of which is to assist consortia in defining and implementing QA/QC plans that maintain uniform, high standards across the entire detector construction effort. Figure 7.10 shows how DUNE technical coordination derives its QA program from the principles of the Fermilab QA program: requirements flow down through the LBNF/DUNE QA program into the QC plans developed for consortium fabrication of detector components and integration and installation of the detector. The QA effort includes design,

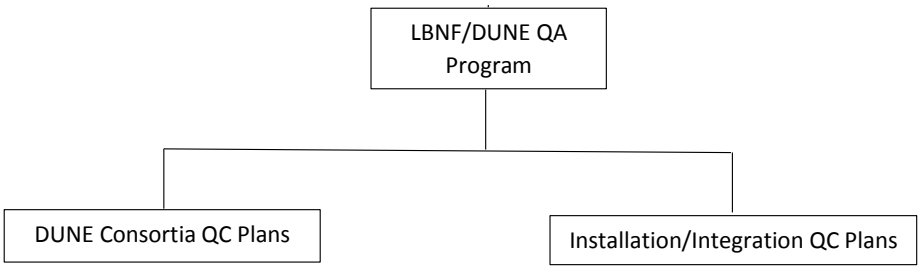

Figure 7.10. Flow-down of Fermilab QA to consortia.

production readiness, and progress reviews as appropriate for the DUNE detector subsystems, as was done for ProtoDUNE-SP under technical coordination oversight.

The primary objective of the LBNF/DUNE QA program is to assure quality in the construction of the LBNF facility and DUNE experiment while providing protection of LBNF/DUNE personnel, the public, and the environment. The QA plan aligns LBNF/DUNE QA activities, which are spread

around the world, with the principles of the Fermilab Quality Assurance Manual. The manual identifies the Fermilab Integrated Quality Assurance Program features that serve as the basis for the LBNF/DUNE QA plan.

A key element of the LBNF/DUNE QA plan is the concept of graded approach; that is, applying a level of analysis, controls, and documentation commensurate with the potential for an environmental, safety, health, or quality impact. To promote continuous improvement, DUNE technical coordination will develop a lessons learned program based on the Fermilab Office of Project Support Services lessons learned program.

The QA plan defines the QA roles and responsibilities of the DUNE project. The DUNE consortium leaders are responsible for identifying the resources to ensure that their team members are adequately trained and qualified to perform their assigned work. All consortium members are responsible for the quality of the work that they do and for using guidance and assistance that is available. All have the authority to stop work and report adverse conditions that affect quality of DUNE products to their respective DUNE consortium leader and the LBNF/DUNE QA manager.

7.9 Environment, safety, and health

LBNF/DUNE is committed to protecting the health and safety of staff, the community, and the environment, as stated in the LBNF/DUNE integrated ES&H plan [55].

The LBNF/DUNE ES&H program complies with applicable standards and local, state, federal, and international legal requirements through the Fermilab Work Smart set of standards and the contract between Fermi Research Alliance (FRA) and the DOE Office of Science (FRA-DOE). Fermilab, as the host laboratory, established the SDSD to provide facility support. SDSD is responsible for support of LBNF/DUNE operations at SURF.

The TC and project integration director have responsibility for implementation of the DUNE ES&H program for the construction and installation activities, respectively. The LBNF/DUNE ES&H manager reports to the TC and project integration director and is responsible for providing ES&H support and oversight for development and implementation of the LBNF/DUNE ES&H program.

The DUNE ES&H coordinator reports to the LBNF/DUNE ES&H manager and has primary responsibility for ES&H support and oversight of the DUNE ES&H program for activities at collaborating institutions. The far and near site ES&H coordinators are responsible for providing daily field support and oversight for all installation activities at the SURF and Fermilab sites.

The LBNF/DUNE ES&H plan defines the ES&H requirements applicable to installation activities at the SURF site. A key element of an effective ES&H program is the hazard identification process. Hazard identification allows production of a list of hazards within a facility, so these hazards can be screened and managed through a suitable set of controls. All work activities are subject to work planning and hazard analysis (HA). All work planning documentation is reviewed and approved by the DUNE ES&H coordinator and the DUNE installation readiness review or operational readiness review committees prior to the start of work activities.

A Safety Data Sheet (SDS) will be available for all chemicals and hazardous materials that are used on-site. All chemicals and hazardous materials brought to the SURF site must be reviewed

and approved by the DUNE ES&H coordinator and the SURF ES&H department before arriving at the site.

South Dakota Science and Technology Authority (SDSTA) will maintain an emergency response incident command system and an emergency response team (ERT) on all shifts that can access the underground sites with normal surface fire department response times. This team provides multiple response capabilities for both surface and underground emergencies.

Fire and life safety requirements for LBNF/DUNE areas were analyzed in the LBNF/DUNE Far Site Fire and Life Safety Assessment. All caverns will be equipped with fire detection and suppression systems, with both visual and audible notification. All fire alarms and system supervisory signals will be monitored in the SURF Incident Command Center. The SURF ERT will respond with additional support from the Lead and Deadwood Fire Departments and the county's emergency management department. The caverns will be equipped with an oxygen deficiency hazard (ODH) monitoring and alarm system, with independent visual and audible notification systems.

All workers on the DUNE project have the authority to stop work in any situation that presents an imminent threat to safety, health, or the environment. Work may not resume until the circumstances are investigated and the deficiencies corrected, including the concurrence of the DUNE project integration director and LBNF/DUNE ES&H manager.

2020 JINST 15 T08008

Appendix A

The near detector purpose and conceptual design

A.1 Overview of the DUNE near detector

A.1.1 Motivation

A primary aim of the DUNE experiment is to measure the oscillation probabilities for muon neutrino and muon antineutrinos to either remain the same flavor or oscillate to electron (anti)neutrinos. Measuring these probabilities as a function of the neutrino energy will allow definitive determination of the neutrino mass ordering, observation of leptonic CP violation for a significant range of δ_{CP} values, and precision measurement of PMNS parameters.

The role of the ND is to serve as the experiment's control. The ND establishes the null hypothesis (i.e., no oscillations) and constrains systematic errors. It measures the initial unoscillated ν_μ and ν_e energy spectra, and that of the corresponding antineutrinos. Of course, neutrino energy is not measured directly. What is seen in the detector is a the convolution of flux, cross section, and detector response to the particles produced in the neutrino interactions, all of which have energy dependence. The neutrino energy is reconstructed from observed quantities.[1]

To first order, a "far/near" ratio (or migration matrix), derived from the simulation, can predict the unoscillated energy spectra at the FD based on the ND measurements. The energy spectra at the FD are then sensitive to the oscillation parameters, which can be extracted via a fit. The ND plays a critical role in establishing what the oscillation signal spectrum should look like in the FD because the expectations for the spectra in both the disappearance and appearance signals are based on the precisely measured spectra for ν_μ and $\overline{\nu}_\mu$ interactions in the ND.

To achieve the precision needed for DUNE, the experiment will have to operate beyond the first-order paradigm. With finite energy resolution and nonzero biases, the reconstructed energy spectrum is an unresolved convolution of cross section, flux, and energy response. The ND must independently constrain each of those components. The ND must provide information that can be used to model well each component. Models of the detector, beam, and interactions fill in holes

[1] In experimental neutrino physics, it is common practice to refer to the neutrino energy (and spectra) when, in fact, it is the reconstructed neutrino energy (spectra) which is meant, along with all of the flux, cross section, and detector response complexities that implies.

2020 JINST 15 T08008

and biases left by imperfect understanding and they are used to estimate the size of many systematic effects. When imperfect models are not able to match observations, the ND must provide the information needed to deal with that and estimate the impact of the imperfect modeling on final measurements. In general, this requires that the ND significantly outperform the FD, which is limited by the need for a large, underground mass. The ND must have multiple methods for measuring neutrino fluxes as independently of cross section uncertainties as possible. With the necessity of relying on models, the ND needs to measure neutrino interactions with much better detail than the FD. This includes having a larger efficiency across the kinematically allowed phase space of all relevant reaction channels, superior identification of charged and neutral particles, better energy reconstruction, and better controls on experimental biases. The ND must also have the ability to measure events in a similar way to the FD, so that it can determine the ramifications of the more limited FD performance, provide corrections, and take advantage of effects canceling to some extent in the near to far extrapolation.

The conceptual design of the ND is based on the collective experience of the many DUNE collaborators who have had significant roles in the current generation of neutrino experiments (MINOS, MiniBooNE, T2K, NOvA, MINERvA, and the SBN program). These programs have provided (and will provide) a wealth of useful data and experience that has led to improved neutrino interaction models, powerful new analyses and reconstruction techniques, a deep appreciation of analysis pitfalls, and a better understanding of the error budget. These experiments, while similar to DUNE, were all done with a lower precision, in a different energy range, or with very different detector technologies. While the existing and projected experience and data from those experiments provide a strong base for DUNE, it is not sufficient to enable DUNE to accomplish its physics goals without a highly performing ND.

The DUNE ND will also have a physics program of its own measuring cross sections, non-standard interactions (NSI), searching for sterile neutrinos, dark photons, and other exotic particles. These are important aims that expand the physics impact of the ND complex. Furthermore, the cross section program is coupled to the oscillation measurement insofar as the cross sections will be useful as input to theory and model development. (Note that many of the ND data samples are incorporated into the oscillation fits directly.)

A.1.2 Design

The DUNE ND is formed from three primary detector components and the capability for two of these components to move off the beam axis. The three detector components serve important individual and overlapping functions with regard to the mission of the ND. Because these components have standalone features, the DUNE ND is often discussed as a suite or complex of detectors and capabilities. The movement off axis provides a valuable extra degree of freedom in the data which is discussed extensively in this report. The power in the DUNE ND concept lies in the collective set of capabilities. It is not unreasonable to think of the component detectors in the DUNE ND as being somewhat analogous to subsystems in a collider experiment, the difference being that, with one important exception (higher momentum muons), individual events are contained within the subsystems. The DUNE ND is shown in the DUNE ND hall in figure 1.13. Table 5.1 provides a high-level overview of the three components of the DUNE ND along with the off-axis capability that is sometimes described as a fourth component.

2020 JINST 15 T08008

The core part of the DUNE ND is a LArTPC called ArgonCube. The particular implementation of the LArTPC technology in this detector is described in section A.5.2 below. This detector has the same target nucleus and shares some aspects of form and functionality with the FD, while the differences are necessitated by the expected intensity of the beam at the ND. This similarity in target nucleus and, to some extent, technology, reduces sensitivity to nuclear effects and detector-driven systematic errors in the extraction of the oscillation signal at the FD. The LArTPC is large enough to provide high statistics ($1 \times 10^8 \nu_\mu$-CC events/year on axis) and a sufficient volume to provide good hadron containment. The tracking and energy resolution, combined with the mass of the LArTPC, will allow for the measurement of the flux in the beam using several techniques, including the rare process of ν-e^- scattering.

The LArTPC begins to lose acceptance for muons above ~0.7 GeV/c due to lack of containment. Because the muon momentum is a critical component of the neutrino energy determination, a magnetic spectrometer is needed downstream of the LArTPC to measure the charge sign and momentum of these muons. In the DUNE ND concept, this function is accomplished by the MPD, which consists of a HPgTPC surrounded by an ECAL in a 0.5 T magnetic field. The HPgTPC provides a lower density medium with excellent tracking resolution for the muons from the LArTPC. In addition, with this choice of technology for the tracker, neutrinos interacting on the argon in the HPgTPC constitute a large (approximately $1 \times 10^6 \nu_\mu$-CC events/year on axis) independent sample of ν-Ar events that can be studied with a very low momentum threshold for tracking charged particles, excellent resolution, and with systematic errors that differ from the liquid detector. These events will be valuable for studying the charged particle activity near the interaction vertex, since this detector can access lower-momentum protons than the LArTPC and has better particle identification of charged pions. Misidentification of pions as knock-out protons (or vice versa) causes a mistake in the reconstructed neutrino energy, moving it away from its true value by the amount of a pion mass. This mistake can become quite significant at the lower-energy second oscillation maximum. The gas detector will play an important role in mitigating this mistake, since pions are rarely misidentified as protons in the HPgTPC. In addition, the relatively low level of secondary interactions in the gas samples will be helpful for identifying the particles produced in the primary interaction and modeling secondary interactions in denser detectors, which are known to be important effects [45]. The high pressure increases the statistics for these studies, improves the particle identification capabilities, and improves the momentum resolution. The MPD is discussed further in section A.5.3.

The LArTPC and MPD can move to take data in positions off the beam axis. This capability is referred to as DUNE-PRISM. As the detectors move off-axis, the incident neutrino flux spectrum changes, with the mean energy dropping and the spectrum becoming somewhat monochromatic. Though the neutrino interaction rate drops off-axis, the intensity of the beam and the size of the LArTPC combine to yield ample statistics even in the off-axis positions. Data taken at different off-axis angles allow deconvolution of the neutrino flux and interaction cross section and the mapping of the reconstructed versus true energy response of the detector. This latter mapping is applicable at the FD up to the level to which the near and far LAr detectors are similar. Stated a different way, it is possible to use information from a linear combination of the different fluxes to create a data sample at the ND with an effective neutrino energy distribution that is close to that of the oscillated spectrum at the FD. This data-driven technique will reduce systematic effects coming

2020 JINST 15 T08008

from differences in the energy spectra of the oscillated signal events in the FD and the ND samples used to constrain the interaction model. Finally, the off-axis degree of freedom provides a sensitivity to some forms of mismodeling in the beam and/or interaction models. The DUNE-PRISM program is discussed further in section A.5.4.

The final component of the DUNE ND suite is the beam monitor, called the SAND. The core part of it, the 3DST, is a plastic scintillator detector made of $1\,\mathrm{cm}^3$ cubes read out along each of three orthogonal dimensions. The design eliminates the typical planar-strip geometry common to scintillator detectors, leading to improved acceptance at large angles relative to the beam direction. It is mounted inside an envelope of high-resolution, normal pressure TPCs and an ECAL, all of which are surrounded by a magnet, as illustrated in figure A.40. The reference design uses a repurposed magnet and ECAL from the KLOE experiment. The 3DST serves as a dedicated neutrino spectrum monitor that never moves off-axis. It also provides an excellent on-axis, neutrino flux determination using many of the methods discussed in section A.4. The neutrino flux determined using this detector, with technologies, targets, and interaction systematic errors that are different from ArgonCube, is an important point of comparison and a systematic cross-check for the flux as determined by ArgonCube.

SAND provides very fast timing and can isolate small energy depositions from neutrons in three dimensions. This provides the capability to incorporate neutrons in the event reconstruction using energy determination via time-of-flight with a high efficiency. This capability is expected to be useful for the low-ν flux determination since it allows for tagging of events with a significant neutron energy component.[2] The inclusion of the neutron reconstruction also provides a handle for improving the neutrino energy reconstruction in $\overline{\nu}_\mu$ CCQE events, which is helpful for the $\overline{\nu}_\mu$ flux determination. The different mass number A of the carbon target relative to argon may prove to be useful for developing models of nuclear effects and building confidence in the interaction model and the size of numerous systematic errors. The addition of the neutron reconstruction capability extends the DUNE ND theme of including regions of phase space in neutrino interactions not seen in previous experiments. This capability may provide insights that foster improvements in the neutrino interaction model on carbon. Though extrapolating such improvements to argon is not straightforward, the development of current generators has benefited from data taken with different nuclear targets, including carbon. The SAND component of the ND is discussed more in section A.6.2.

Table A.1 shows the statistics expected in the different ND components for a few processes that are important for constraining the neutrino flux. Some additional information on constraining the flux is provided in section A.4.

A.2 Role of the ND in the DUNE oscillation program

Oscillation experiments need to accomplish three main tasks. First, they must identify the flavor of interacting neutrinos in CC events, or identify the events as NC interactions. Second, they need to measure the energy of the neutrinos since oscillations occur as a function of baseline length

[2]The low-ν technique involves measuring the flux for events with low energy transfer because the cross section is approximately constant with energy for this sample. It provides a nice way to measure the shape of the spectrum. This is discussed further in section A.4.

2020 JINST 15 T08008

Table A.1. Event rates for processes that can be used to constrain the neutrino flux. The rates are given per year for a 1 ton (FV) HPgTPC, a 25 ton (FV) LArTPC [56], and a 9 t (FV) 3DST. The flux for the HPgTPC and LArTPC is from the simulated "2017 engineered" LBNF beam with a primary momentum of 120 GeV/c and 1.1×10^{21} POT/year. The flux for the 3DST is the 80 GeV, three-horn, optimized beam with 1.46×10^{21} POT/year. The detectors are assumed to be on-axis. Fiducial volumes are analysis dependent and in the case of the LArTPC, it is likely the volume could be made larger by a factor of two for many analyses.

Event class	LArTPC	HPgTPC	3DST
$\nu_\mu + e^-$ elastic ($E_e > 500$ MeV)	3.3×10^3	1.3×10^2	1.1×10^3
ν_μ low-ν ($\nu < 250$ MeV)	5.3×10^6	2.1×10^5	1.48×10^6
ν_μ CC coherent	2.2×10^5	8.8×10^3	
$\bar{\nu}_\mu$ CC coherent	2.1×10^4	8.4×10^2	

over neutrino energy, L/E. Third, they need to compare the observed event spectrum in the FD to predictions based on differing sets of oscillation parameters, subject to constraints from the data observed in the ND. That comparison and how it varies with the oscillation parameters allows for the extraction of the measured oscillation parameters and errors.

The connection between the observations in the ND and the FD is made using a simulation that convolves models of the neutrino flux, neutrino interactions, nuclear effects, and detector response. This gives rise to a host of complicating effects that muddy the simple picture. They come from two main sources. First, the identification efficiency is not 100 % and there is some background (e.g., NC events with a π^0 are a background to ν_e CC interactions). Both the efficiency and the background are imperfectly known. Generally, it is helpful to have a ND that is as similar as feasible to the FD because a bias in the efficiency as a function of energy will cancel between the two detectors. Since the background level tends to be similar between the two detectors, it is helpful if the ND is more capable than the FD at characterizing backgrounds, either due to its technology, or by leveraging the much larger statistics and freedom to take data in alternative beam configuration modes (e.g., different horn currents or movement off the beam axis).

The second major source of complication occurs because the FD (and the similar ND) has to be made of heavy nuclei rather than hydrogen. Neutrino interactions can be idealized as a three stage process: (1) a neutrino impinges on a nucleus with nucleons in some initial state configuration, (2) scattering occurs with one of the nucleons, perhaps creating mesons, and (3) the hadrons reinteract with the remnant nucleus on their way out (so called FSI). The presence of the nucleus impacts all three stages in ways that ultimately drive the design of the ND complex. To better understand this it is useful to consider what would happen if the detectors were made of hydrogen.

In a detector made of hydrogen, the initial state is a proton at rest and there are no FSI. The scattering consists of a variety of processes. The simplest is QE scattering: $\bar{\nu}_\ell p \rightarrow \ell^+ n$. The detector sees a lepton (which establishes the flavor of the neutrino), no mesons, and perhaps a neutron interaction away from the lepton's vertex. Because there are no mesons the kinematics is that of two body scattering and the neutrino energy can be reconstructed from the lepton's angle (with respect to the ν beam) and energy. This is independent of whether the neutron is observed.

2020 JINST 15 T08008

For ν_ℓ interactions on hydrogen there is no QE process. The simplest scattering channel is single pion production $\nu_\ell p \rightarrow \ell^- \pi^{(+,0)}(n,p)$. In that case the neutrino energy may be reconstructed from the energy of the muon and pion, and their angles with respect to the beam.[3] In both cases, the neutrino energy can be measured without bias so long as the detector itself measures lepton and meson momenta and angles without bias. The neutrino energy in complicated scattering channels, such as ones with multiple pions or heavy baryons can be measured in a similar way (at least in principle).

A key simplifying feature offered by a hypothetical hydrogen detector is simply that there are enough constraints to measure the neutrino energy without needing to measure the single nucleon (especially a neutron escaping the detector). Additionally, the cross sections for different scattering channels (particularly the simpler ones) can be expressed in terms of leptonic and hadronic currents. The leptonic current is well understood. The structural elements of the hadronic current are known on general theoretical grounds. The current is often represented by form factors that are constrained by electron scattering experiments, beta decay, and neutrino scattering measurements that the detector can make itself (or take from other experiments).

The situation is significantly more complicated in a detector with heavy nuclei. The nucleons in the initial state of the nucleus are mutually interacting and exhibit Fermi motion. This motion ruins the key momentum conservation constraint available in hydrogen due to the target being at rest. Scattering at lower momentum transfer is suppressed because the nucleon in the final state would have a momentum that is excluded by the Pauli principle.

The nucleon momentum distribution in heavy nuclei is commonly modeled as a Fermi gas with a cutoff momentum $k_F \approx 250\,\mathrm{MeV/c}$ [57]. This picture is overly simplistic. For example, there are nucleons with momenta larger than k_F due to short-range correlated nucleon-nucleon interactions (SRC) [58]. Scattering on a nucleon with $p > k_F$ implies that there is a spectator nucleon recoiling against the target with a significant momentum. SRC have been the subject of much investigation but are not fully understood or fully implemented in neutrino event generators.

Additionally, there is a second multi-body effect. For the few-GeV neutrinos of interest to DUNE, the typical momentum transfer corresponds to a probe that has a wavelength on par with the size of a nucleon. In this case, the scattering can occur on two targets in the nucleus which may be closely correlated (2p2h scattering). Experiments can easily confuse this process for QE scattering since there are no mesons and one or both of the two nucleons may have low energy, evading detection. The presence of two nucleons in the initial and final state again ruins the kinematic constraints available in hydrogen. It is now known that 2p2h scattering is a significant part of the total scattering cross section at DUNE energies [59]. The 2p2h cross section is difficult to compute because it cannot be expressed as the sum over cross sections on individual nucleons. The dependence on atomic number and the fine details of the interaction (e.g., the final energies of the two particles) are also currently unknown. Finally, it is widely expected that there are components of 2p2h and SRC scattering that result in meson production. Event generators do not currently include such processes.

[3]The nucleon does not need to be observed. This is a consequence of having four energy-momentum conservation constraints, which allows E_ν and $\vec{p}_N$ to be computed.

2020 JINST 15 T08008

Neutrino scattering on nuclei is also subject to FSI. FSI collectively refers to the process by which nucleons and mesons produced by the neutrino interaction traverse the remnant nucleus. The hadrons reinteract with a variety of consequences: additional nucleons can be liberated; "thermal" energy can be imparted to the nucleus; pions can be created and absorbed; and pions and nucleons can undergo charge exchange scattering (e.g., $\pi^- p \rightarrow \pi^0 n$). Event generators include phenomenological models for FSI, anchoring to hadron-nucleus scattering data.

The heavy nuclei in a detector also act as targets for the particles that have escaped the struck nucleus. Generally speaking, the denser the detector and the more crudely it samples deposited energy, the more difficult it is to observe low-energy particles. Negatively and positively charged pions leave different signatures in a detector since the former are readily absorbed while the latter are likely to decay. Neutrons can be produced from the struck nucleus, but also from follow-on interactions of the neutrino's reaction products with other nuclei. The energy carried away by neutrons is challenging to detect and can bias the reconstructed neutrino energy.

Finally, it is important to note that a significant fraction of the neutrino interactions in DUNE will come from deep inelastic scattering rather than the simpler QE scattering discussed above. This leads typically to a more complex morphology for events (beyond the heavy nucleus complications) and greater challenges for the detector and the modeling.

A.3 Lessons learned

A.3.1 Current experiments

Neutrino beams are notoriously difficult to model at the precision and accuracy required for modern accelerator-based experiments. Recent long-baseline (LBL) experiments make use of a ND placed close to the beam source, where oscillations are not yet a significant effect. The beam model, the neutrino interaction model, and perhaps the detector response model are tuned, or calibrated, by the data recorded in the ND. The tuned model is used in the extraction of the oscillation signal at the FD. Known effects that are not understood or modeled well must be propagated into the final results as part of the systematic error budget. Unknown effects that manifest as disagreements between the model and observations in the ND also must be propagated into the final results as part of the systematic error budget. These kinds of disagreements have happened historically to every precision accelerator oscillation experiment. When such disagreements arise, some assumption or range of assumptions must be made about the source of the disagreement. Without narrowing down the range of possibilities, this can become a leading systematic error.

Since the final results depend on the comparison of what is seen in the FD to that in the ND, having functionally identical detectors (i.e., the same target nucleus and similar detector response) is helpful. In a similar vein, differences between the neutrino spectrum at the ND and the oscillated spectrum seen at the FD lead to increased sensitivity to systematic effects propagated from the ND to the FD.

The past experience of the neutrino community is a driving force in the design of the DUNE ND complex. The performance of current, state-of-the-art long baseline oscillation experiments provides a practical guide to many of the errors and potential limitations DUNE can expect to encounter, as well as case studies of issues that arose which were unanticipated at the design stage.

2020 JINST 15 T08008

The T2K experiment uses an off-axis neutrino beam that has a narrow energy distribution peaked below 1 GeV. This means, relative to DUNE, interactions in T2K are predominantly CCQE and have relatively simple morphologies. The data sample has little feed-down from higher energy interactions. The T2K ND (plastic scintillator and TPC) technology is very different from its FD (water Cerenkov), though the ND contains embedded water targets that provide samples of interactions on the same target used in the FD. The experiment relies on the flux and neutrino interaction models, as well as the ND and FD response models to extrapolate the constraint from the ND to the FD. In the most recent oscillation results released by T2K, the ND data constraint reduces the flux and interaction model uncertainties at the FD from 11–14% down to 2.5–4% [28]. Inclusion of the water target data was responsible for a factor of two reduction in the systematic uncertainties, highlighting the importance of measuring interactions on the same target nucleus as the FD.[4]

The NOvA experiment uses an off-axis neutrino beam from NuMI that has a narrow energy distribution peaked around 2 GeV. The NOvA ND is functionally identical to its FD. Still, it is significantly smaller than the FD and it sees a different neutrino spectrum due to geometry and oscillations. Even with the functionally identical near and far detectors, NOvA uses a model to subtract NC background and relies on a model-dependent response matrix to translate what is seen in the ND to the "true" spectrum, which is then extrapolated to the FD where it is put through a model again to predict what is seen in the FD [60, 61]. Within the extrapolation, the functional similarity of the near and far detectors reduces but does not eliminate many systematic effects. Uncertainties arising from the neutrino cross section model dominate the NOvA ν_e appearance systematic error budget and are among the larger errors in the ν_μ disappearance results. The ND constraint is significant. For the ν_e appearance signal sample in the latest NOvA results, for example, a measure of the systematic error arising from cross section uncertainties without using the ND extrapolation is 12 % and this drops to 5 % if the ND extrapolation is used [61].

The process of implementing the ND constraint in both T2K and NOvA is less straightforward than the typical description implies. It will not be any more straightforward for DUNE. One issue is that there are unavoidable near and far differences. Even in the case of functionally identical detectors, the beam spectrum and intensity are very different near to far. For DUNE, in particular, ArgonCube is smaller than the FD and is divided into modular, optically isolated regions that have a pixelated readout rather than the wire readout of the FD. Space charge effects will differ near to far. All of this imposes model dependence on the extrapolation from near to far. This is mitigated by collecting data at differing off-axis angles with DUNE-PRISM, where an analysis can be done with an ND flux that is similar to the oscillated FD flux (see section A.5.4). (Data from ProtoDUNE will also be useful to understand the energy-dependent detector response for the FD.) Regardless, near to far differences will persist and must be accounted for through the beam, detector, and neutrino interaction models.

Although long baseline oscillation experiments use the correlation of fluxes at the ND and the FD to reduce sensitivity to flux modeling, the beam model is a critical component in understanding this correlation. Recently, the MINERvA experiment used spectral information in the data to

[4]These numbers are not used directly in the analysis but were extracted to provide an indication of the power of the ND constraint.

2020 JINST 15 T08008

diagnose a discrepancy between the expected and observed neutrino event energy distribution in the NuMI medium energy beam [62]. In investigating this issue, MINERvA compared the observed and simulated neutrino event energy distribution for low-ν events, as shown in figure A.1. Since the cross section is known to be relatively flat as a function of neutrino energy for this sample, the observed disagreement as a function of energy indicated a clear problem in the flux model or reconstruction. MINERvA believes the observed discrepancy between the data and simulation is best described by what is a mismodeling in horn focusing combined with an error in the muon energy reconstruction (using range traversed in the downstream spectrometer). This is notable, in part, because the two identified culprits in this saga would manifest differently in the extrapolation to the far detector in an oscillation experiment. The spectral analysis provided critical information in arriving at the final conclusion. This experience illustrates the importance of good monitoring/measurements of the neutrino beam spectrum.

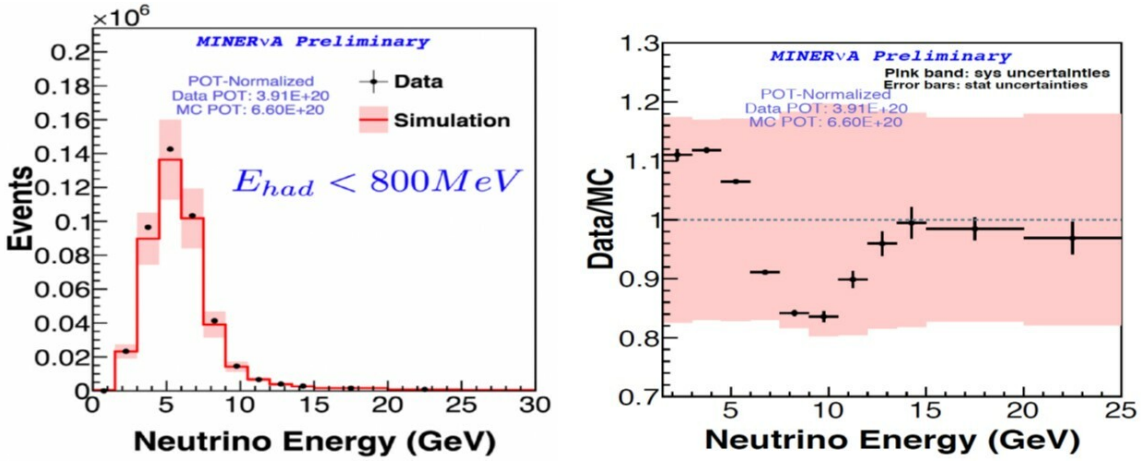

Figure A.1. Reconstructed MINERvA medium energy NuMI neutrino event spectrum for low-energy transfer events compared to simulation (left) and same comparison shown as a ratio (right). From [62].

Another important issue is that the neutrino interaction model is not perfect, regardless of the experiment and implementation. With an underlying model that does not describe reality, even a model tuned to ND data will have residual disagreements with that data. These disagreements must be accounted for in the systematic error budget of the ultimate oscillation measurements. Although the model(s) may improve before DUNE operation, the degree of that improvement cannot be predicted and the DUNE ND complex should have the capability to gather as much information as possible to help improve and tune the model(s) during the lifetime of the experiment. In other words, the ND needs to be capable of narrowing the range of plausible possibilities giving rise to data-model differences at the ND in order to limit the systematic error incurred in the results extracted from the FD.

Recent history provides illustrations of progress and continuing struggles to improve neutrino interaction models. The MiniBooNE collaboration published results in 2010 showing a disagreement between the data and the expected distribution of CCQE events as a function of Q^2 [63, 64]. They brought the model into agreement with the data by increasing the axial mass form factor used in the model. K2K [64] and MINOS [65] made similar measurements. It has since been shown

that the observed disagreement is due to the need to include multi-nucleon processes and that the use of the large effective axial mass form factor used by these experiments to fit the data leads to a misreconstruction of the neutrino energy.

The importance of modeling multi-nucleon (2p2h) processes for oscillation experiments is underscored by the fact that such interactions when reconstructed as a CCQE (1p1h) process lead to a significant low-side tail in the reconstructed neutrino energy [66]. Multi-nucleon processes also change the hadronic calorimetric response. The first NOvA ν_μ disappearance oscillation results had a dominant systematic error driven by the disagreement of their model to the data in their hadronic energy distribution [67]. In more recent work, the inclusion of multi-nucleon processes in the interaction model contributed to a substantial reduction of this disagreement [60].

The MINERvA experiment has compiled a significant catalog of neutrino and antineutrino results and recently developed a model tuned to their QE-like (NuMI low energy) data [59]. The tune is based on a modern neutrino interaction generator (Generates Events for Neutrino Interaction Experiments (GENIE) 2.8.4 [68], using a global Fermi gas model [57] with a Bodek-Ritchie tail [69] and the INTRANUKE-hA FSI model [70]). Even so, MINERvA scales down non-resonance pion production [71], includes a random phase approximation model (RPA) [72, 73], and incorporates a multi-nucleon model [74–76] with an empirical enhancement in the dip region between the QE and Δ region that is determined by a fit to the neutrino data [59]. The same tune as developed on the neutrino data also fits well the MINERvA antineutrino QE-like data (with no additional tuning or ingredient). The required enhancement of the multi-nucleon contribution to the model implies shortcomings in the interaction model, but the decent fit to data for both neutrinos and antineutrinos implies that the tune is effectively making up for some imperfections in the model.

More recent versions of GENIE include some of the modifications incorporated by MINERvA in the tune discussed above [77]. This illustrates the dynamic nature of neutrino interaction modeling and the interplay between the experiments and generator developers. The evolution of the field continues as illustrated with a snapshot of some of the current questions and areas of focus:

- There is a pronounced deficit of pions produced at low Q^2 in CC1π° events as compared to expectations [78–82]. Current models take this into account by tuning to data without any underlying physical explanation for how or why this happens.

- The MINERvA tune that fits both neutrino and antineutrino CCQE data involves a significant enhancement and distortion of the 2p2h contribution to the cross section. The real physical origin of this cross section strength is unknown. Models of multi-nucleon processes disagree significantly in predicted rates.

- Multi-nucleon processes likely contribute to resonance production. This is neither modeled nor well constrained.

- Cross section measurements used for comparison to models are a convolution of what the models view as initial state, hard scattering, and final state physics. Measurements able to deconvolve these contributions are expected to be very useful for model refinements.

- Most neutrino generators make assumptions about the form of form factors and factorize nuclear effects in neutrino interactions into initial and final state effects via the impulse ap-

2020 JINST 15 T08008

proximation. These are likely oversimplifications. The models will evolve and the systematic errors will need to be evaluated in light of that evolution.

- Neutrino detectors are largely blind to neutrons and low-momentum protons and pions (though some π^+ are visible via Michel decay). This leads to smearing in the reconstructed energy and transverse momentum, as well as a reduced ability to accurately identify specific interaction morphologies. The closure of these holes in the reconstructed particle phase space is expected to provide improved handles for model refinement.

- There may be small but significant differences in the ν_μ and ν_e CCQE cross sections which are poorly constrained [83].

Given the critical importance of neutrino interaction models and the likelihood that the process of refining these models will continue through the lifetime of DUNE, it is important the DUNE ND suite be highly capable.

A.3.2 Past experience

The philosophy driving the DUNE ND concept is to provide sufficient redundancy to address areas of known weaknesses in previous experiments and known issues in the interaction modeling insofar as possible, while providing a powerful suite of measurements that is likely to be sensitive to unanticipated issues and useful for continued model improvements. Anything less reduces DUNE's potential to achieve significantly improved systematic errors over previous experiments in the LBL analyses.

The DUNE ND incorporates many elements in response to lessons learned from previous experiments. The massive ND LArTPC has the same target nucleus and a similar technology to the FD. These characteristics reduce the detector and target systematic sensitivity in the extrapolation of flux constraints from this detector to the FD. This detector is capable of providing the primary sample of CC ν_μ interactions to constrain the flux at the FD, along with other important measurements of the flux from processes like ν-e$^-$ scattering and low-ν. Samples taken with this detector at off-axis angles (DUNE-PRISM) will allow the deconvolution of the flux and cross section errors and provide potential sensitivity to mismodeling. The off-axis data can, in addition, be used to map out the detector response function and construct effective ND samples that mimic the energy distribution of the oscillated sample at the FD.

The DUNE ND provides access to particles produced in neutrino interactions that have been largely invisible in previous experiments, such as low-momentum protons and charged pions measured in the HPgTPC and neutrons in the 3DST and ECAL. The HPgTPC provides data on interactions that minimize the effect of secondary interactions on the produced particles. These capabilities improve the experiment's ability to identify specific interaction morphologies, study samples with improved energy resolution, and extract samples potentially useful for improved tuning of model(s) of multi-nucleon processes. The neutron content in neutrino and antineutrino interactions is different and this will lead to differences in the detector response. For an experiment that is measuring CPV, data on neutron production in neutrino interactions is likely to be an important handle in the tuning of the interaction model and the flavor-dependent detector response function model.

2020 JINST 15 T08008

The 3DST provides dedicated beam spectrum monitoring on axis, as well as high statistics samples useful for the on-axis flux determination as a crosscheck on the primary flux determination (which has different detector and target systematic errors). The beam spectrum monitoring is useful for identifying and diagnosing unexpected changes in the beam. This proved useful for NuMI and is likely to be more important for DUNE given the need to associate data taken at different times and off-axis angles.

The large data sets that will be accumulated by the three main detectors in the ND suite will allow for differential studies and the use of transverse kinematic imbalance variables, where each detector brings its unique strengths to the study: the LArTPC has good tracking resolution and containment and massive statistics; the HPgTPC has excellent tracking resolution, very low charged particle tracking thresholds, and unambiguous track charge sign determination; and the 3DST has good containment and can include neutrons on an event-by-event basis. The neutrino interaction samples acquired by this array of detectors will constitute a powerful laboratory for deconvoluting the initial state, hard scattering, and final state physics, which, in turn, will lead to improved modeling and confidence in the final results extracted from the FD.

A.4 Constraining the flux in the ND

The DUNE FD will not measure the neutrino oscillation probability directly. Instead, it will measure the neutrino interaction rate for different neutrino flavors as a function of the reconstructed neutrino energy. It is useful to formalize the measurements that are performed in the near and far detector modules in the following equations:

$$\frac{dN_x^{FD}}{dE_{\rm rec}}(E_{\rm rec}) = \int \Phi_{\nu_\mu}^{FD}(E_\nu) P_{\nu_\mu \to x}(E_\nu) \sigma_x^{Ar}(E_\nu) T_x^{FD,Ar}(E_\nu, E_{\rm rec}) dE_\nu \tag{A.1}$$

$$\frac{dN_x^{ND}}{dE_{\rm rec}}(E_{\rm rec}) = \int \Phi_x^{ND}(E_\nu) \sigma_x^{m}(E_\nu) T_x^{d,m}(E_\nu, E_{\rm rec}) dE_\nu \tag{A.2}$$

with

- $x = \nu_e, \nu_\mu$
- d = detector index(ND,FD)
- m = interaction target/material, (e.g., H, C, or Ar)
- E_ν = true neutrino energy
- $E_{\rm rec}$ = reconstructed neutrino energy
- $T_x^{d,m}(E_\nu, E_{\rm rec})$ = true-to-reconstruction transfer function
- $\sigma_x^m(E_\nu)$ = neutrino interaction cross section
- $\Phi_x^d(E_\mu)$ = un-oscillated neutrino flux
- $\frac{dN_x^d}{dE_{\rm rec}}(E_{\rm rec})$ = measured differential event rate per target (nucleus/electron)

2020 JINST 15 T08008

There are equivalent formulae for antineutrinos. For simplicity, the instrumental backgrounds (wrongly selected events) and the intrinsic beam contaminations (ν_e interactions in case of the appearance measurement) have been ignored. But an important function of the ND is also to quantify and characterize those backgrounds.

It is not possible to constrain the FD neutrino flux directly, but the near-to-far flux ratio is believed to be tightly constrained by existing hadron production data and the beamline optics. As such equation (A.1) can be rewritten as

$$\frac{dN_x^{FD}}{dE_{\text{rec}}}(E_{\text{rec}}) = \int \Phi_{\nu_\mu}^{ND}(E_\nu) R(E_\nu) P_{\nu_\mu \to x}(E_\nu) \sigma_x^{Ar}(E_\nu) T_x^{d,Ar}(E_\nu, E_{\text{rec}}) dE_\nu \tag{A.3}$$

with

$$R(E_\nu) = \frac{\Phi_{\nu_\mu}^{FD}(E_\nu)}{\Phi_{\nu_\mu}^{ND}(E_\nu)} \tag{A.4}$$

taken from the beam simulation. It is not possible to measure only a near-to-far event ratio and extract the oscillation probability since many effects do not cancel trivially. This is due to the non-diagonal true-to-reconstruction matrix, which not only depends on the underlying differential cross section, but also on the detector used to measure a specific reaction.

$$\frac{dN_x^{FD}}{dE_{\text{rec}}}(E_{\text{rec}}) / \frac{dN_{\nu_\mu}^{ND}}{dE_{\text{rec}}}(E_{\text{rec}}) \neq R(E_\nu) P_{\nu_\mu \to x}(E_\nu) \frac{\sigma_x^{Ar}(E_\nu)}{\sigma_{\nu_\mu}^{m}(E_\nu)} \tag{A.5}$$

It is therefore important that the DUNE ND suite constrain as many components as possible.

While the near-to-far flux ratio is tightly constrained to the level of 1 % to 2 %, the same is not true for the absolute flux itself. T2K, using hadron production data obtained from a replica target, can constrain the absolute flux at the ND to 5 % to 6 % in the peak region and to around 10% in most of its energy range. The NuMI beam has been constrained to 8% using a suite of thin target hadron production data. The better the ND flux is known, the easier it is to constrain modeling uncertainties by measuring flux-integrated cross sections. Predicting the event rate at the FD to a few percent will require additional constraints to be placed with the ND or substantial improvements in our understanding of the hadron production and focusing uncertainties.

Several handles to constrain the flux are addressed below. Briefly they offer the following constraints:

- The overall flux normalization and spectrum can be constrained by measuring neutrino scattering off of atomic electrons.
- The energy dependence ("shape") of the ν_μ and $\bar{\nu}_\mu$ flux can be constrained using the "low-ν" scattering process.
- The flux ratio $\bar{\nu}_\mu / \nu_\mu$ can be constrained using CC coherent neutrino scattering.
- The ν_e / ν_μ flux ratio in the energy region where standard oscillations occur is well-constrained by the beam simulation. The experiment can also measure the ν_e / ν_μ interaction ratio and constrain the flux ratio using cross section universality.

A.4.1 Neutrino-electron elastic scattering

Neutrino-electron scattering ($\nu\, e \rightarrow \nu\, e$) is a pure electroweak process with calculable cross section at tree level. The final state consists of a single electron, subject to the kinematic constraint

$$1 - \cos\theta = \frac{m_e(1-y)}{E_e}, \tag{A.6}$$

where θ is the angle between the electron and incoming neutrino, E_e and m_e are the electron mass and total energy, respectively, and $y = T_e/E_\nu$ is the fraction of the neutrino energy transferred to the electron. For DUNE energies, $E_e \gg m_e$, and the angle θ is very small, such that $E_e\theta^2 < 2m_e$.

The overall flux normalization can be determined by counting $\nu\, e \rightarrow \nu\, e$ events. Events can be identified by searching for a single electromagnetic shower with no other visible particles. Backgrounds from ν_e CC scattering can be rejected by looking for large energy deposits near the interaction vertex, which are evidence of nuclear breakup. Photon-induced showers from NC π^0 events can be distinguished from electrons by the energy profile at the start of the track. The dominant background is expected to be ν_e CC scattering at very low Q^2, where final-state hadrons are below threshold, and $E_e\theta^2$ happens to be small. The background rate can be constrained with a control sample at higher $E_e\theta^2$, but the shape extrapolation to $E_e\theta^2 \rightarrow 0$ is uncertain at the 10 % to 20 % level.

For the DUNE flux, approximately 100 events per year per ton of fiducial mass are expected with electron energy above 0.5 GeV. For a LArTPC mass of 25 tons, this corresponds to 3300 events per year. The statistical uncertainty on the flux normalization from this technique is expected to be ~1%. MINERvA has achieved a systematic uncertainty of 2.3% and it seems plausible that DUNE could do at least as well [84]. The 3DST can also do this measurement with significant statistics and with detector and reconstruction systematics largely uncorrelated with ArgonCube. The signal is independent of the atomic number A and the background is small; so, it seems plausible the samples can be combined to good effect.

A.4.2 The low-ν method

The inclusive cross section for CC scattering ($\nu_l + N \rightarrow l^- + X$) does not depend on the neutrino energy in the limit where the energy transferred to the nucleus $\nu = E_\nu - E_l$ is zero [85]. In that limit, the event rate is proportional to the flux, and by measuring the rate as a function of energy, one can get the flux "shape." This measurement has been used in previous experiments and has the potential to provide a constraint in DUNE with a statistical uncertainty < 1%.

In practice, one cannot measure the rate at $\nu = 0$. Instead it is necessary to restrict ν to be less than a few 100 MeV. This introduces a relatively small E_ν dependence into the cross section that must be accounted for to obtain the flux shape. Thus the measurement technique depends on the cross section model but the uncertainty is manageable [86]. This is particularly true if low-energy protons and neutrons produced in the neutrino interaction can be detected.

A.4.3 Coherent neutrino-nucleus scattering

The interactions $\nu_\ell + A \rightarrow \ell^- + \pi^+ + A$ and $\overline{\nu}_\ell + N \rightarrow \ell^+ + \pi^- + N$ occur with very low three momentum transfer to the target nucleus (A). As such, the interactions proceed coherently with the

2020 JINST 15 T08008

entire nucleus, and do not suffer from nuclear effects (though background channels certainly do). These coherent interactions are most useful as a constraint on the $\bar{\nu}_\mu/\nu_\mu$ flux ratio. Identifying with high efficiency and purity requires a detector with excellent momentum and angular resolution.

A.4.4 Beam ν_e content

Electron neutrinos in a wide-band beam come from two primary sources: kaon decays and muon decays. These "beam" ν_e are an irreducible background in $\nu_\mu \rightarrow \nu_e$ oscillation searches. As such, the LBNF beam was optimized to make the ν_e flux as small as possible while maximizing the ν_μ flux. In the energy range relevant for oscillations (0.5 GeV - 4.0 GeV) the predicted ν_e/ν_μ ratio varies between 0.5% and 1.2% as a function of energy. The beam ν_e flux in the same energy range is strongly correlated with the ν_μ flux due to the decay chain $\pi^+ \rightarrow \mu^+\nu_\mu$ followed by $\mu^+ \rightarrow \bar{\nu}_\mu e^+\nu_e$ (and likewise for $\bar{\nu}_e$). As a result, the LBNF beam simulation predicts that the uncertainty on the ν_e/ν_μ ratio varies from 2.0 % to 4.5 %. At the FD, in a 3.5 year run, the statistical uncertainty on the beam ν_e component is expected to be 7% for the ν mode beam and 10% for the $\bar{\nu}$ mode beam. The systematic uncertainty on the beam ν_e flux is therefore subdominant, but not negligible.

A.5 Movable components of the ND and the DUNE-PRISM program

A.5.1 Introduction to DUNE-PRISM

One of the primary challenges for DUNE will be controlling systematic uncertainties from the modeling of neutrino-argon interactions. The relationship between the observable final state particles from a neutrino interaction and the incident neutrino energy is currently not understood with sufficient precision to achieve DUNE physics goals. This is due in part to mismodeling of the outgoing particle composition and kinematics and due to missing energy from undetected particles, such a neutrons and low energy charged pions, and misidentified particles. The latter effects tend to cause a "feed-down" in reconstructed neutrino energy relative to the true energy. Since neutrino energy spectra at the FD and ND have substantially different features due to the presence of oscillations at the FD, these mismodeling and neutrino energy feed-down effects do not cancel in a far-to-near ratio as a function of neutrino energy, and lead to biases in the measured oscillation parameters.

Understanding ND constraints on neutrino-nucleus interaction uncertainties is challenging, since no complete model of neutrino-argon interactions is available. If it were possible to construct a model that was known to be correct, even with a large number of unknown parameters, then the task of a ND would much simpler: to build a detector that can constrain the unknown parameters of the model. However, in the absence of such a model, this procedure will be subject to unknown biases due to the interaction model itself, which are difficult to quantify or constrain.

The DUNE-PRISM ND program consists of a mobile ND that can perform measurements over a range of angles off-axis from the neutrino beam direction in order to sample many different neutrino energy distributions, as shown in figure A.2. By measuring the neutrino-interaction final state observables over these continuously varying incident neutrino energy spectra, it is possible to experimentally determine the relationship between neutrino energy and what is measured in the detector (i.e., some observable such as reconstructed energy).

In the DUNE ND, the movable components of the detector that are used in the DUNE-PRISM program are ArgonCube and the MPD. These components of the ND will take data both on the

2020 JINST 15 T08008

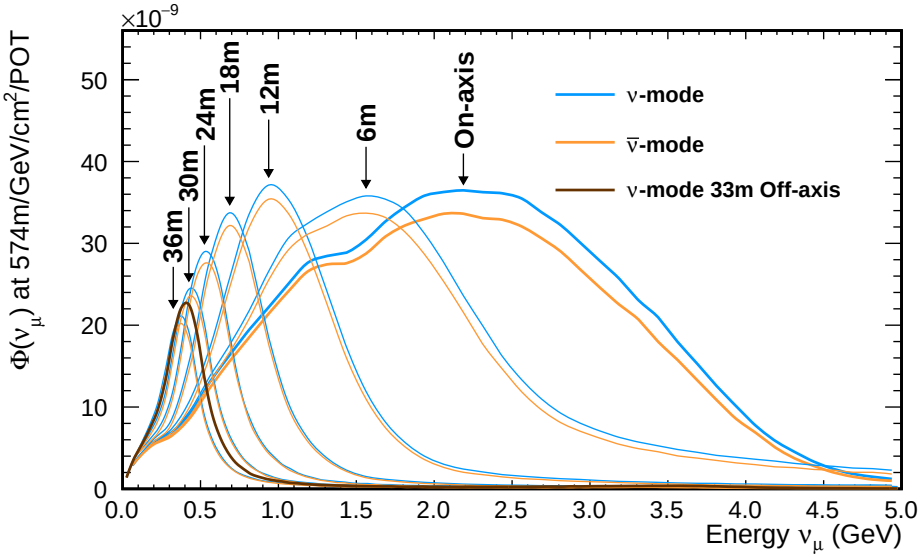

Figure A.2. The variation in the neutrino energy spectrum is shown as a function of detector off-axis position, assuming the nominal ND location 574 m downstream from the production target.

beam axis and off-axis. In the following sections, ArgonCube and the MPD will be described in some detail and then the DUNE-PRISM program will be described in more detail.

A.5.2 LArTPC component in the DUNE ND: ArgonCube

As the DUNE FDs have LAr targets, there needs to be a major LAr component in the DUNE ND complex in order to reduce cross section and detector systematic uncertainties for oscillation analyses [87, 88]. However, the intense neutrino flux and high event rate at the ND makes traditional, monolithic, projective wire readout TPCs unsuitable. This has motivated a program of R&D into a new LArTPC design, suitable for such a high-rate environment, known as ArgonCube [89]. ArgonCube utilizes detector modularization to improve drift field stability, reducing HV and the LAr purity requirements; pixelized charge readout [90, 91], which provides unambiguous 3D imaging of particle interactions, drastically simplifying the reconstruction; and new dielectric light detection techniques with ArCLight [92], which can be placed inside the FC to increase light yield, and improve the localization of light signals. Additionally, ArgonCube uses a resistive field shell, instead of traditional field shaping rings, to maximize the active volume, and to minimize the power release in the event of a breakdown [93].

The program of ArgonCube R&D has been very successful to date, working on small component prototypes and is summarized in references [8, 90–96]. With the various technological developments demonstrated with small-scale TPCs, the next step in the ArgonCube program is to demonstrate the scalability of the pixelized charge readout and light detection systems, and to show that information from separate modules can be combined to produce high-quality event reconstruction for particle interactions. To that end, a mid-scale (1.4 m × 1.4 m × 1.2 m) modular TPC, dubbed the ArgonCube 2×2 demonstrator, with four independent LArTPC modules arranged in a 2×2 grid has been designed, and is currently under construction.

After a period of testing at the University of Bern, the ArgonCube 2×2 demonstrator will be placed in the MINOS ND hall at Fermilab where it will form the core of a prototype DUNE ND, ProtoDUNE-ND [97]. As part of ProtoDUNE ND, the ArgonCube concept can be studied and operated in an intense, few-GeV neutrino beam. This program aims to demonstrate stable operation and the ability to handle backgrounds, relate energy associated with a single event across ArgonCube modules, and connect tracks to detector elements outside of ArgonCube. The ArgonCube 2×2 demonstrator is described below in some detail since the DUNE ND modules are anticipated to be very similar.

A.5.2.1 ArgonCube in ProtoDUNE-ND

The ArgonCube concept is a detector made of self-contained TPC modules sharing a common cryostat. Each module is made of a rectangular box with a square footprint and a height optimized to meet the physics goals and/or sensitivity constraints. The ArgonCube 2×2 demonstrator module will be housed within an existing LN_2-cooled and vacuum-insulated cryostat, which is ~2.2 m in diameter and ~2.8 m deep, for a total volume of ~10.6 m^3. The size of the cryostat sets the dimensions of the modules for the demonstrator. The square base of each module will be 0.67 m × 0.67 m, and the height will be 1.81 m. This makes the modules comparable in size to, but slightly smaller than, the proposed ArgonCube DUNE ND modules, which will have a base of 1 m × 1 m and a 3.5 m height.

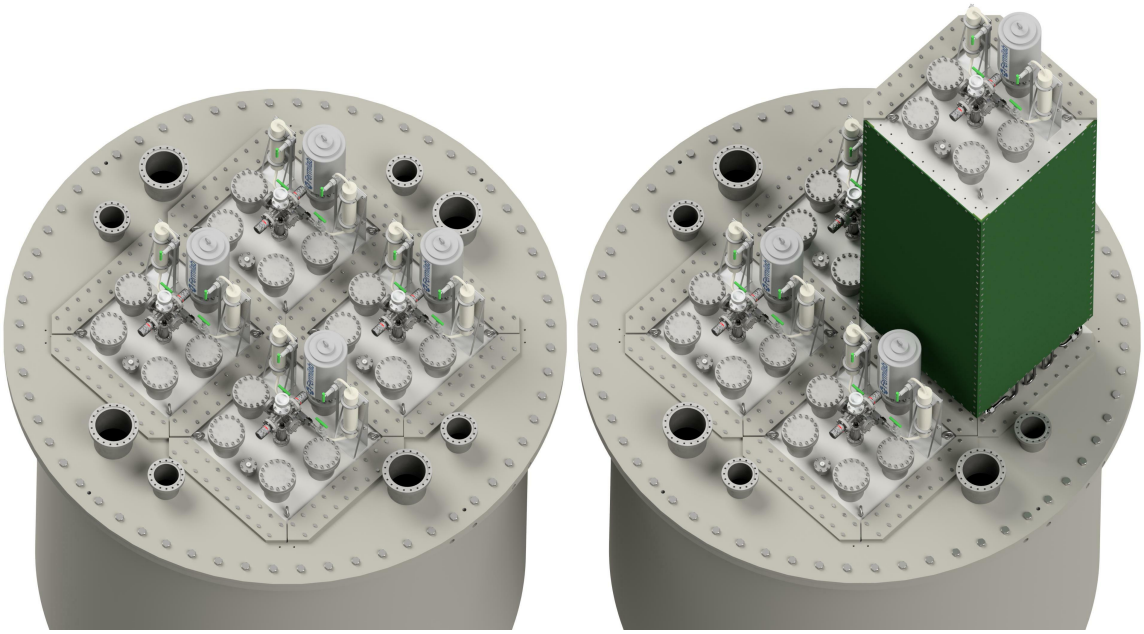

Figure A.3. Illustration of the ArgonCube 2×2 demonstrator module. The four modules are visible, with one of them partly extracted, on the right. This figure has been reproduced from ref. [89].

Individual modules can be extracted or reinserted into a common LAr bath as needed, as is illustrated in figure A.3. This feature will be demonstrated during a commissioning run at the University of Bern, but is not intended to be part of the detector engineering studies in the MINOS-ND hall. The pressure inside the modules is kept close to the bath pressure, putting almost no

2020 JINST 15 T08008

hydrostatic force on the module walls. This allows the walls to be thin, minimizing the quantity of inactive material in the walls. The purity of the LAr is maintained within the modules, independent of the bath, as will be described below. The argon surrounding the modules need not meet as stringent purity requirements as the argon inside. Under normal operating conditions, all modules are inserted with clearance distances of only 1.5 mm between modules. Cooling power to the bath is supplied by liquid nitrogen circulated through lines on the outer surface of the inner cryostat vessel.

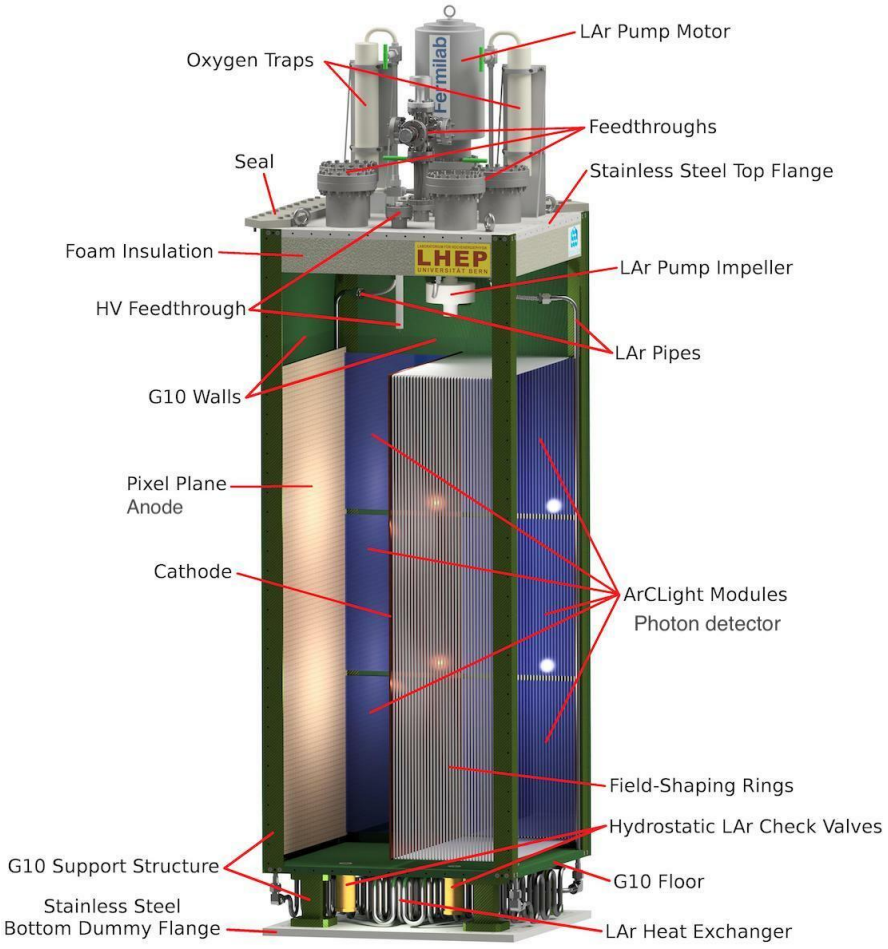

Figure A.4. Cutaway drawing of a 0.67 m × 0.67 m × 1.81 m ArgonCube module for the 2×2 demonstrator module. For illustrative purposes the drawing shows traditional field-shaping rings instead of a resistive field shell. The G10 walls will completely seal the module, isolating it from the neighboring modules and the outer LAr bath. The 2×2 modules will not have individual pumps and filters.

A cutaway drawing of an individual 2×2 module is shown in figure A.4. The side walls of each module are made from 1 cm G10 sheets, to which the resistive field shell is laminated. The G10 radiation length (X_0 = 19.4 cm) and hadronic interaction length (λ_{int} = 53.1 cm) [10] are both comparable to LAr (14.0 cm and 83.7 cm respectively). G10 provides a strong dielectric, capable of 200 kV · cm^{-1} when 1 cm thick [98]. This dielectric shielding eliminates the need for a clearance volume between the TPCs and the cryostat, while also shielding the TPC from field breakdowns in a neighboring module.

Each module is split into two TPCs by a central cathode made of an additional resistive layer on a G10 substrate. The segmented drift length does not require a high cathode voltage, and minimizes stored energy. For the 2×2 module footprint of 0.67 m × 0.67 m, and an E field of 1 kV · cm^{-1}, a cathode potential of only 33 kV is required. Operating a LArTPC at this voltage is feasible without a prohibitive loss of active volume [95]. The high field is helpful for reducing drift time and the potential for pileup, minimizing the slow component of the scintillation light, reducing space charge effects, and providing robustness against loss of LAr purity.

The detector is oriented such that the cathodes are parallel to the beam. This minimizes the load on the readout electronics by spreading the event over more channels and reducing the required digitization rate for hit channels. In turn, this reduces the heat load generated at the charge readout and prevents localized boiling.

During filling and emptying of the cryostat, the argon flow is controlled by hydrostatic check valves located at the lower flange of the module, which require a minimal differential pressure of 15 mbar to open. The purity inside each module is maintained by means of continuous LAr recirculation through oxygen traps. Dirty argon is extracted from the base of the module, and is then pushed through oxygen traps outside the cryostat, clean argon then re-enters the module above the active volume. For optimal heat transport, the argon flow is directed along the cold electronics. To prevent dirty argon from the bath entering the modules, their interior is held at a slight over-pressure. For the 2×2, the dirty argon from all four modules is extracted by a single pump at the base of the cryostat with a four-to-one line, and after being filtered and cooled, the clean argon is pumped back in the module via a one-to-four line. A more extensive version of the same scheme is envisaged for the DUNE ND.

ArgonCube offers true 3D tracking information using the LArPix cryogenic ASIC [91] pixelated charge readout. LArPix ASICs amplify and digitize the charge collected at single-pixels in the cold to mitigate the need for analogue signal multiplexing, and thus produce unambiguous 3D information. Sixty-four pixels can be connected to a single LArPix ASIC. The baseline design for the 2×2 is a 4 mm pixel pitch, corresponding to 62.5k pixels m^{-2}. Pixelated anode planes are located on the two module walls parallel to the cathode; each plane is 1.28 m^2 × 0.64 m^2. The total area across all four modules is 6.6 m^2, which corresponds to 410k pixels. The readout electronics utilize two field programmable gate array (FPGA) boards per module, connected to a single Ethernet switch. It should be noted that the pixel pitch may be reduced as prototypes develop, but this can be accommodated in the readout design.

The charge readout window (drift time) of 137 µs is long compared to the 10 µs [99] beam spill length in the NuMI and LBNF beams. For a 1 MW beam intensity, the expected rate of neutrino interactions at the DUNE ND is roughly 0.5 per spill per ArgonCube module. With LArPix, reconstruction issues are greatly simplified compared to a projective readout TPC. Tracks and connected energy deposits will frequently overlap in any 2D projection, but can be resolved easily with the full 3D readout. However, disconnected energy deposits, such as those from photon conversions or neutron interactions in the detector, cannot be associated easily to a specific neutrino interaction. This problem can be solved by incorporating fast timing information from the prompt scintillation light emitted in LAr. The module's opaque cathode and walls contain scintillation light within each TPC (half module), improving the detection efficiency of the prompt component of the scintillation light. Furthermore, attenuation due to Rayleigh scattering, characterized by an

2020 JINST 15 T08008

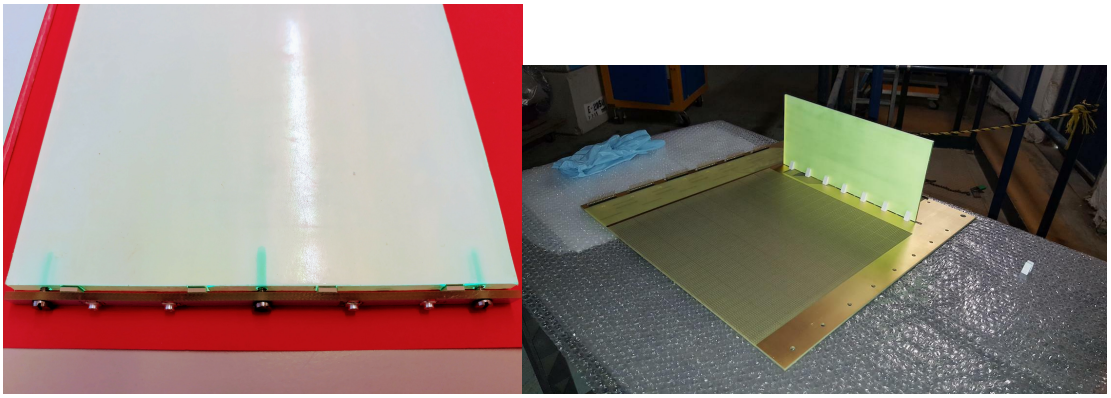

(a) ArCLight paddle (b) ArCLight mounted on a pixel readout PCB

Figure A.5. (a) A prototype ArgonCube light readout paddle. The paddle is 50 cm long and 10 cm, with four SiPMs coupled to one end. Reproduced from ref. [89]. (b) ArCLight paddle mounted on the PixLAr pixelated charge readout plane, as used in test beam studies at Fermilab.

attenuation length of 0.66 m in LAr [100], is mitigated by the maximum photon propagation length of 0.3 m. It is desirable to have a large area PD system to maximize the utility of scintillation light signals in the detector. To minimize any dead material within the active volume, it is also desirable that the light detection be as compact as possible. The solution pursued for the ArgonCube effort is ArCLight [92], which is a very compact dielectric light trap that allows for light collection from a large area, inside high E fields. An example ArCLight sheet is shown in figure A.5. These sheets are mounted on the walls of the module, inside the field shell, aligned with the drift direction, between the anode and the cathode. The additional 5 mm deep dead volume is similar to the one caused by the charge readout in the perpendicular direction.

A.5.2.2 Dimensions of the ArgonCube component of the DUNE ND

Since it is unrealistic to build a 25 m long LArTPC in order to contain a 5 GeV muon, the LArTPC dimensions have instead been optimized for hadronic shower containment [101], relying on a downstream spectrometer to analyze crossing muons. Hadronic showers are defined as contained if a reasonable efficiency across a wide range of kinematics is maintained, and there is no phase space with zero acceptance. The specific metric used is that >95% of hadronic energy has to be contained for interactions in the FV, excluding neutrons and their descendants.

To assess the efficiency, detector volumes of varying sizes were simulated in a neutrino beam. This provides a good measure of the efficiency of a given volume to contain different events, but it is not necessarily a good quantity to assess the required detector size. Many events are not contained because of their specific location and/or orientation. Cross section coverage remedies this deficiency by looking at the actual extent of the event, instead of its containment, at a random position inside a realistic detector volume. However, events extending through the full detector will very likely never be contained in a real detector due to the low probability of such an event happening in exactly the right location (e.g., at the upstream edge of the detector). Therefore, the maximum event size needs to be smaller than the full detector size. For the ND simulation this buffer was chosen to be 0.5 m in all directions. In this way, this measure of cross section coverage allows us to look for phase-space regions which are inaccessible to particular detector volume configurations.

2020 JINST 15 T08008

To find the optimal detector size in each dimension, two are held constant at their nominal values, while the third dimension is varied and the cross section coverage is plotted as a function of neutrino energy. This is shown for the dimension along the beam direction in figure A.6. In this case, figure A.6 shows us that 4.5 m would be sufficient, but to avoid model dependencies, 5 m has been selected. Increasing the length beyond 5 m does little to improve cross section coverage, but reducing to 4 m begins to limit coverage at higher energies. Note that 1 minus the cross section coverage gives the fraction of events that cannot be well reconstructed no matter where their vertex is, or how they are rotated within the FV. The optimized dimensions found using this technique were 3 m tall, 4 m wide, and 5 m along the beam direction. There is also a need to measure large angle muons that do not go into the HPgTPC. Widening the detector to 7 m accomplishes that goal without the added complication of a side muon detector.

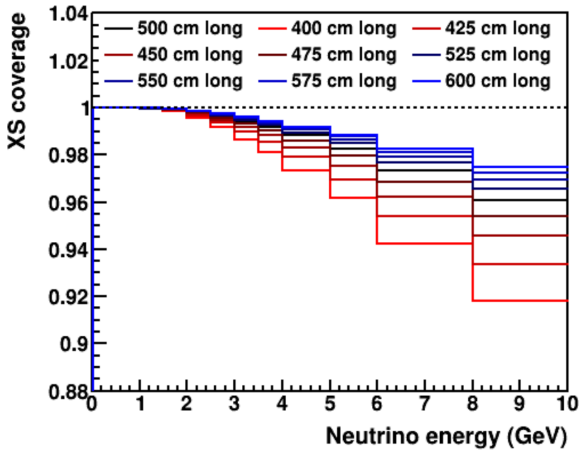

Figure A.6. Influence of the LArTPC size on hadron containment, expressed in terms of cross section coverage as a function of neutrino energy. Two dimensions are held constant at their nominal values, while the third is varied, in this case the height is held at 2.5 m and the width at 4 m. The optimal length is found to be 5 m. See text for explanation of cross section coverage [101].

A.5.2.3 ArgonCube module dimensions

The DUNE ND ArgonCube module dimensions are set to maintain a high drift field, $1\,\mathrm{kV}\cdot\mathrm{cm}^{-1}$, with minimal bias voltage, and to allow for the detection of prompt scintillation light while mitigating the effects of diffusion on drifting electrons. The prompt scintillation light, τ <6.2 ns [102], can be efficiently measured with a dielectric light readout with $O(1)$ ns timing resolution, such as ArCLight [92]. To reduce attenuation and smearing due to Rayleigh scattering, the optical path must be kept below the 0.66 m [100] scattering length. Additionally, the slow scintillation component can be further suppressed by operating at higher E fields [103], effectively reducing the ionization density [104] required to produce excited states.

A module with a 1 m × 1 m footprint split into two TPCs with drift lengths of 50 cm requires only a 50 kV bias. With ArCLight mounted either side of the 1 m wide TPC, the maximal optical path is only 50 cm. For a nonzero drift field, diffusion needs to be split into longitudinal and transverse components. Gushchin [105] report a transverse diffusion of $13\,\mathrm{cm}^2\cdot\mathrm{s}^{-1}$ at $1\,\mathrm{kV}\cdot\mathrm{cm}^{-1}$. This results [106] in a transverse spread of 0.8 mm for the drift time of 250 µs, well below the

proposed pixel pitch of 3 mm. The longitudinal component is smaller than the transverse [106], and is therefore negligible.

A.5.2.4 ND dimensions

Though the acceptance study discussed in section A.5.2.2 indicated a width of 4 m is sufficient to contain the hadronic component of most events of interest, the width has been increased to 7 m in order to mitigate the need for a side-going muon spectrometer. Figure A.7 shows the overall dimensions of the planned ArgonCube deployment in the DUNE ND. With an active volume of 1 m × 1 m × 3 m per module, the full ArgonCube detector corresponds to seven modules transverse to the beam direction, and five modules along it. It should be noted that the cryostat design is currently based on ProtoDUNE [9], and will be optimized for the ND pending a full engineering study.

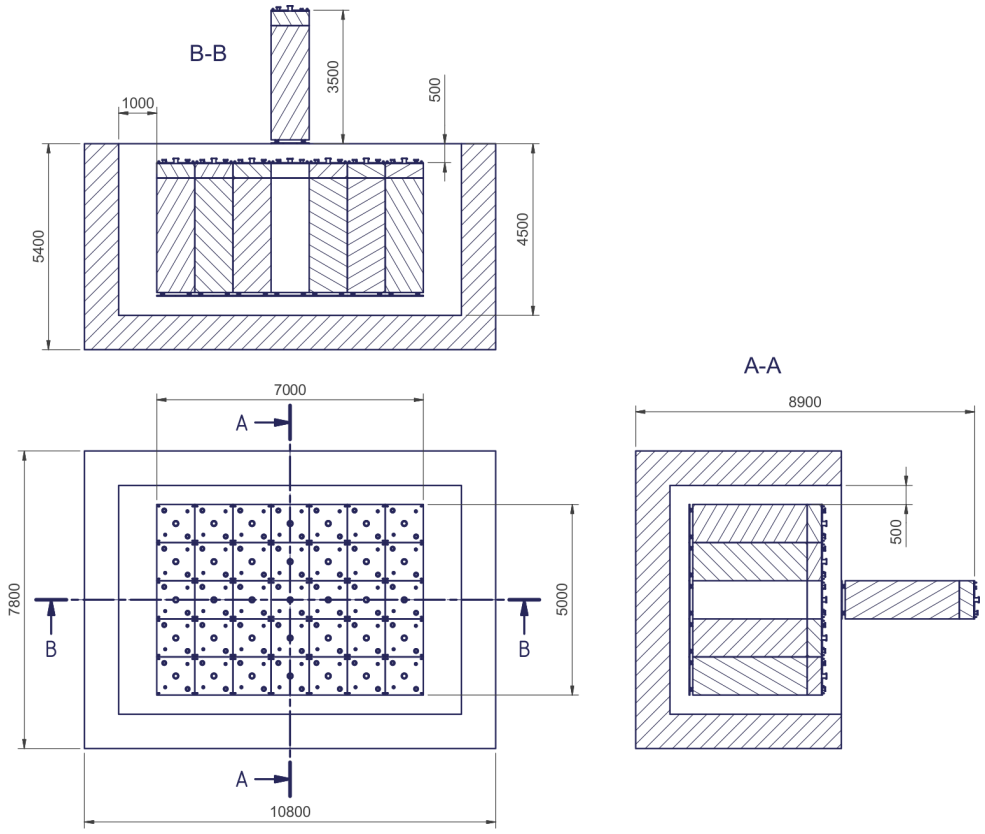

Figure A.7. The current ArgonCube Dimensions for the DUNE ND. The cryostat is based on ProtoDUNE [9], and yet to be optimized for the DUNE ND.

A.5.2.4.1 Statistics in fiducial volume

Figure A.8 shows 37 million total CC ν_μ neutrino events per year within a 25 t FV in FHC mode at 1.07 MW (on-axis). Figure A.9 shows only the event rate for events where the visible hadronic system is fully contained, for the same FV and beam configuration. Note that for the visible hadronic

system to be contained, all energy not associated with the outgoing lepton, or outgoing neutrons, was required to be contained.

For hadronic containment, there is a 30 cm veto region upstream and on all sides of the active volume, and 50 cm veto region downstream. The FV is then defined as 50 cm from all edges, with 150 cm downstream. Within the 25 t FV in FHC mode at 1.07 MW the number of fully reconstructed (contained or matched muon, discussed below, plus contained hadrons) CC ν_μ events per year is 14 million.

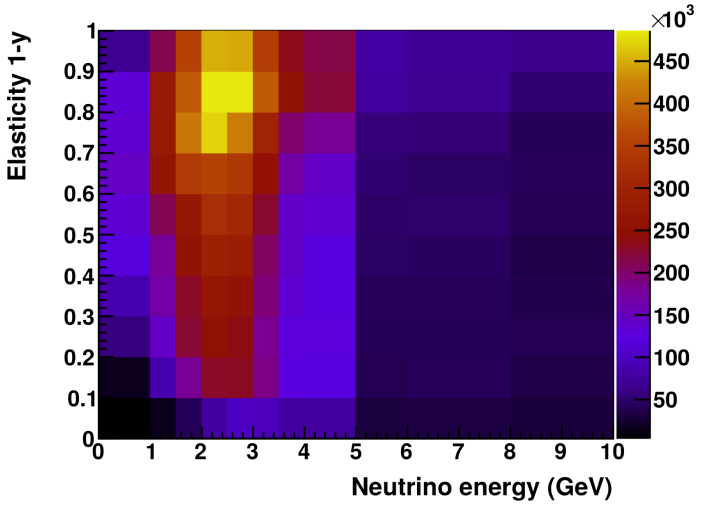

Figure A.8. All neutrino events in the nominal 25 t FV, in FHC at 1.07 MW, per year, rates are per bin. The elasticity is the fraction of the original neutrino energy carried by the outgoing lepton.

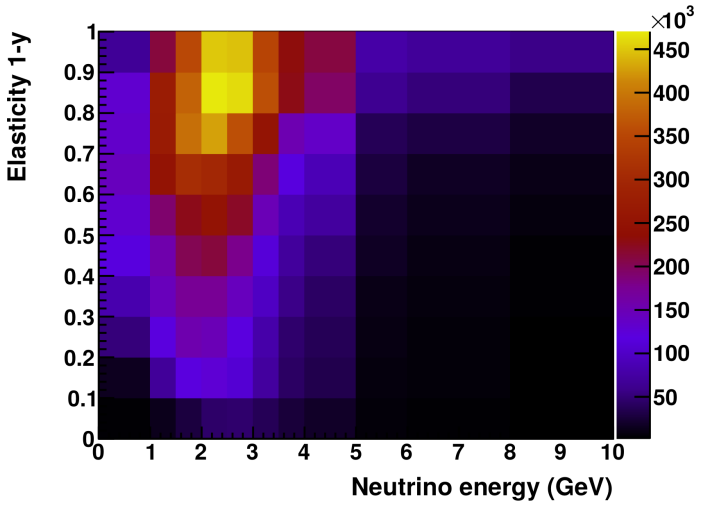

Figure A.9. Events where the visible hadronic system is contained within the nominal 25 t FV, in FHC at 1.07 MW, per year, rates are per bin. The elasticity is the fraction of the original neutrino energy that is carried by the outgoing lepton.

A.5.2.4.2 Muon acceptance

Muons are considered as useful for physics if they stop in the active region of ArgonCube or if they leave the LAr detector and are reconstructed in a magnetic spectrometer downstream. Under the assumption that the downstream magnetic spectrometer is the multipurpose detector described in section A.5.3, figure A.10 shows the muon acceptance as a function of true neutrino energy (on the left) and muon energy (on the right). The acceptance dip at 1 GeV in muon energy is from muons that exit ArgonCube and are not reconstructed in the MPD downstream. This dip can be reduced by minimizing the passive material between the liquid argon and high pressure gaseous argon detectors.

ICARUS and MicroBooNE have used multiple Coulomb scattering to determine muon momentum [107]. This technique may prove to be useful for muons in ArgonCube and could mitigate somewhat the size of the dip in figure A.10.

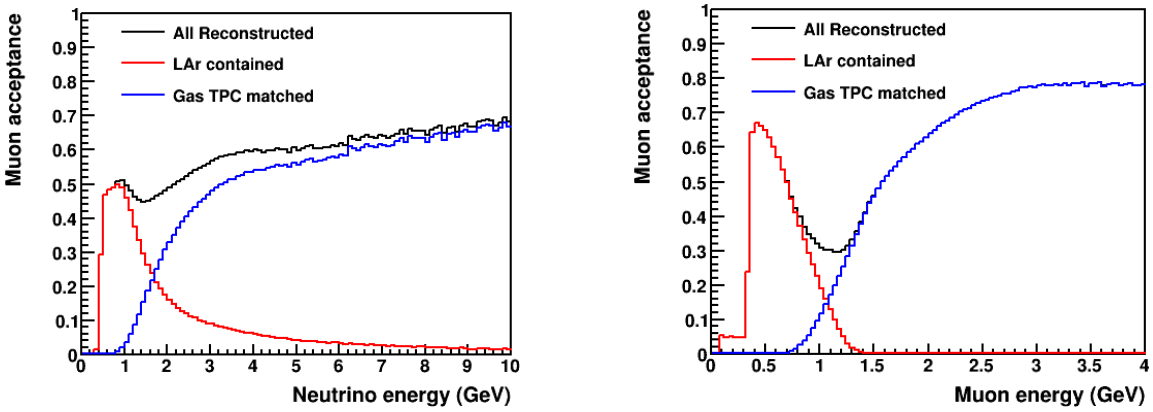

Figure A.10. Muon acceptance shown as a function of true neutrino energy (left) and true muon energy (right). The acceptance for muons that stop in ArgonCube is shown in red and that for muons reconstructed in the downstream magnetic spectrometer is shown in blue.

A.5.2.5 Acceptance vs. energy and momentum transfer

The acceptance of ArgonCube with the MPD acting as a downstream spectrometer can be studied in a more nuanced way by looking at it as a function of the energy q_0 and three-momentum q_3 transferred to the target nucleus. The energy transfer is simply $q_0 = E_\nu - E_\mu$. The three-momentum transfer is related to the four-momentum transfer Q and q_0 by $q_3 = \sqrt{Q^2 + q_0^2}$. These variables have long been used to study nuclear structure in electron scattering experiments.

Figure A.11 shows the event rate (left figures) and acceptance (right figures) in bins of (q_3, q_0). The rows correspond to two neutrino energy bins. The top row is for E_ν between 1.0-2.0 GeV and it covers the first oscillation maximum. The second bin is for E_ν between 4.0-5.0 GeV. The rate histograms have "islands" corresponding to hadronic systems with fixed invariant mass. The islands are smeared by Fermi motion and decay width. The lower island in (q_3, q_0) corresponds to the quasi-elastic peak while the upper corresponds to the Δ resonance. One should note that the axes in the lower row cover a larger range of kinematic space than those in the upper row.

2020 JINST 15 T08008

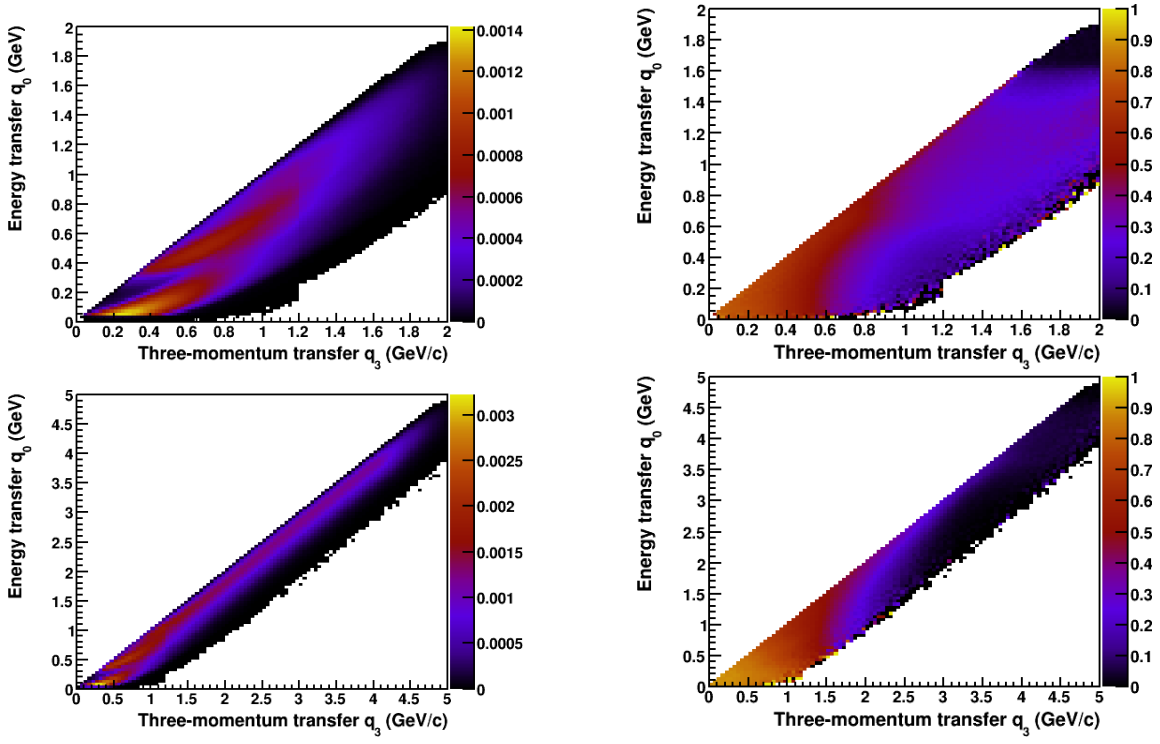

Figure A.11. Neutrino acceptance shown as a function of energy transfer and momentum transfer (q_0 and q_3) to the target nucleus. The units for q_0 and q_3 are GeV and GeV/c, respectively. The figures show the event rate (left) and the acceptance (right) for reconstructing the muon and containing the hadronic system. The top row was made for neutrinos with true neutrino energy between 1.0 and 2.0 GeV and the bottom was made for neutrinos between 4.0 and 5.0 GeV.

The acceptance is generally very good in the kinematic region where the vast majority of the events occur but is nowhere perfect. This is not necessarily a problem because the loss is chiefly geometrical. Losses typically occur in events with a vertex near one boundary of the detector where the muon, or hadronic system exits out that boundary. However for each lost event there is generally a set of symmetric events that are accepted because the final state is rotated by some angle about the neutrino beam axis (ϕ symmetry) or is closer to the center of the fiducial volume (x,y symmetry).

Regions where the acceptance is zero are problematic because they will introduce model dependence into the prediction of the rate at the far detector (which has a nearly 4π acceptance). Acceptances of even a few % in some kinematic regions are not necessarily a problem as long as the event rate is large enough to accumulate a statistically significant number of events. There is a potential danger if the acceptance varies quickly as a function of the kinematic variables because a small mismodeling of the detector boundaries or neutrino cross-sections could translate into a large mismodeling in the number of accepted events.

The size of the accepted event set decreases as a function of both q_0 and q_3 (and therefore E_ν) due to more energetic hadronic systems and larger angle muons. This can clearly be seen in the transition from the colored region to the black region in the $4.0 < E_\nu < 5.0$ GeV acceptance histogram shown in the lower right-hand corner of figure A.11. The transition is smooth and gradual.

2020 JINST 15 T08008

The acceptance for $1.0 < E_\nu < 2.0$ GeV (shown in the upper right-hand corner of figure A.11) is larger than 10% except in a small region at high q_0 and q_3. Events in that region have a low-energy muon and are misidentified as neutral-current according to the simple event selection applied in the study. The fraction of events in that region is quite small, as can be seen in the upper left-hand plot of figure A.11.

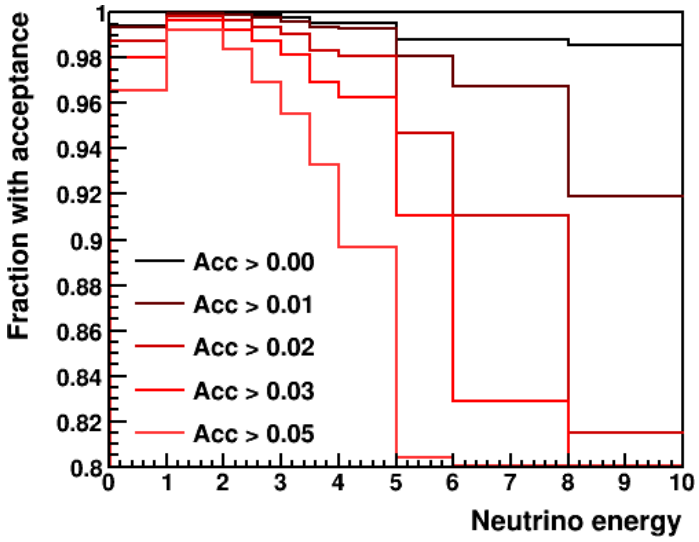

Figure A.12. This figure summarizes the neutrino acceptance in the (q_3, q_0) plane, as shown in figure A.11, for all bins of neutrino energy (plotted in GeV). Here the quantity on the vertical axis is the fraction of events that come from bins in (q_3, q_0) with an acceptance greater than A_{cc}. As an example we consider the 4.0-5.0 GeV neutrino energy bin. The $A_{cc} > 0.03$ curve in that neutrino energy bin indicates that 96% of events come from (q_3, q_0) bins that have an acceptance greater than 3%.

Figure A.12 summarizes the neutrino acceptance in the (q_3, q_0) plane as function of neutrino energy. The y axis shows the fraction of events coming from (q_3, q_0) bins with an acceptance greater than A_{cc}. The $A_{cc} > 0.00$ curve shows the fraction of events for which there is nonzero acceptance. For $E_\nu < 5.0$ GeV (the oscillation region) that fraction is greater than 99%. So, there are no significant acceptance holes. In the same energy region, more than 96% of events come from regions where the acceptance is greater than 3%.

A.5.2.6 Muon and electron momentum resolution and scale error

For muons stopping in the LAr and for those with momentum measured in the downstream tracker (MPD), the energy scale uncertainty from ArgonCube is driven by the material model of the LAr and passive materials. This is expected to be known to <1%. Note that the B field in the MPD is expected to be known to about 0.5% from simulation and field maps made with Hall and NMR probes.

For electrons, the energy will be measured calorimetrically, rather than by range. The MIP energy scale (charge/MeV) will be set by rock muons. The scaling to more dense deposits from EM showers can give rise to uncertainties, i.e., recombination could be different. Such uncertainties can be reduced by taking data with ArgonCube modules in a test beam. Outside of this, a useful

calibration sample of electrons up to 50 MeV comes from Michel electrons from stopping rock muons. The π^0 invariant mass peak is another good standard candle.

A.5.2.7 Tagging fast neutrons

Studies have shown that contained prompt scintillation light provides an important handle for neutron tagging, allowing for the association of detached energy deposits to the correct neutrino interaction using timing information. Such neutron tagging is important for minimizing the uncertainty on neutrino energy reconstruction, both for neutrons generated at a neutrino vertex and for hadronic showers that fluctuate to neutrons.

Figure A.13 shows a simulated beam spill in the 5 m × 4 m × 3 m LAr component of the DUNE ND.[5] It highlights the problem of associating fast-neutron induced energy deposits to a neutrino vertex using only collected charge.

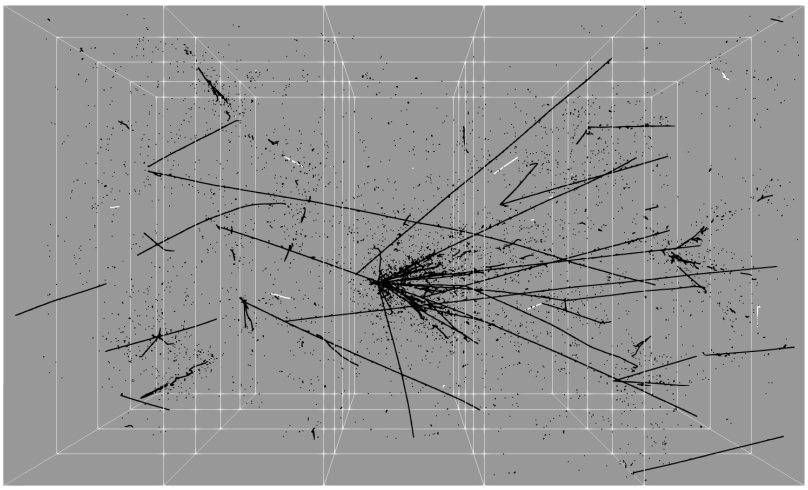

Figure A.13. A beam spill in the LAr component of the DUNE ND. The detector volume is 5 m × 4 m × 3 m. Fast-neutron induced recoiling proton tracks, with an energy threshold greater than ~ 10 MeV, are shown in white. The black tracks are all other energy deposits sufficient to cause charge collected at the pixel planes.

By containing scintillation light, prompt light signals can be used to associate fast-neutron induced deposits back to a neutrino vertex anywhere within the detector. Figure A.14 shows the temporal distribution of neutrino vertices within a representative, randomly selected, beam spill. The mean separation of neutrino vertices is 279 ns, with all fast-neutron induced energy deposits occurring <10 ns after each neutrino interaction.

A.5.2.8 Neutrino-electron elastic scattering

Neutrino scattering on atomic shell electrons, $\nu_l(\overline{\nu}_l) + e^- \rightarrow \nu_l(\overline{\nu}_l) + e^-$, is a purely electroweak process with a known cross section as function of neutrino energy, E_ν, in which all neutrino flavors participate, albeit with different cross sections. This process is not affected by nuclear interactions and has a clean signal of a single very forward-going electron. MINERvA [108] has used this technique to characterize the NuMI beam flux normalization (running in the NuMI low-energy

[5]Note that this study was performed before the detector width was increased to 7 m, as described in section A.5.2.4.

2020 JINST 15 T08008

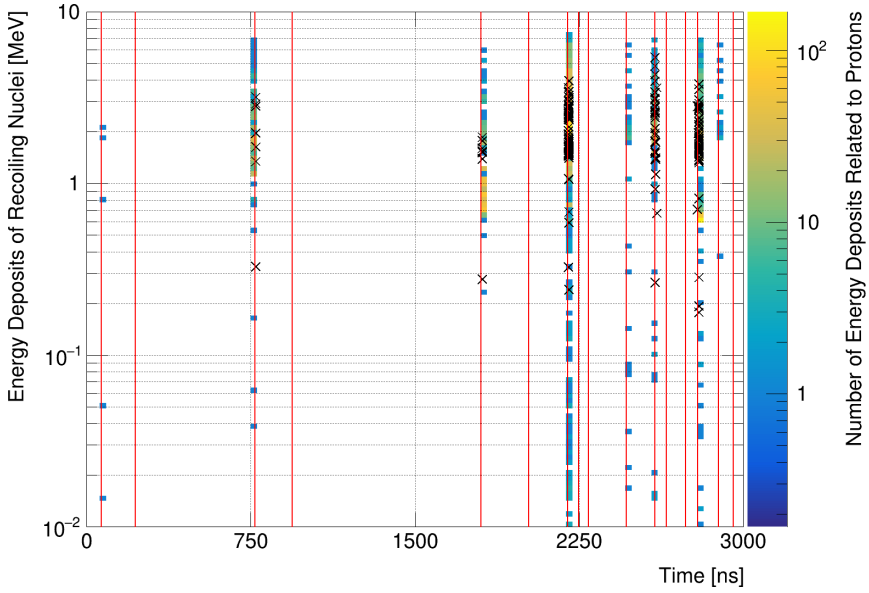

Figure A.14. The temporal distribution of neutrino vertices (red lines) within a beam spill in the LAr component of DUNE ND. The mean separation of neutrino vertices is 279 ns. The filled bins show the number of hits due to recoiling protons, crosses indicate a hit due to a recoiling ^{2}H, ^{3}H, ^{2}He or ^{3}He nucleus. All fast-neutron induced energy deposits occur <10 ns after each neutrino interaction.

mode), although the rate and detector resolution were insufficient to make a shape constraint. It has been investigated as a cross section model-independent way to constrain the neutrino flux at the DUNE ND.

For a neutrino-electron sample, E_ν could, in principle, be reconstructed event-by-event in an ideal detector using the formula

$$E_\nu = \frac{E_e}{1 - \frac{E_e(1-\cos\theta_e)}{m_e}}, \tag{A.7}$$

where m_e and E_e are the electron mass and outgoing energy, and θ_e is the angle between the outgoing electron and the incoming neutrino direction. The initial energy of the electrons are low enough to be safely neglected (~10 keV). It is clear from equation (A.7) that the ability to constrain the shape of the flux is critically dependent on the energy- and, in particular, angular-resolution of electrons. For a realistic detector, the granularity of the E_ν shape constraint (the binning) depends on its performance. Additionally, the divergence of the beam (few mrad) at the DUNE ND site is a limiting factor to how well the incoming neutrino direction is known.

In work described in ref. [109], the ability for various proposed DUNE ND components to constrain the DUNE flux is shown using the latest three-horn optimized flux and including full flavor and correlation information. This was used to determine what is achievable relative to the best performance expected from hadron production target models. When producing the input flux covariance matrix, it was assumed that an NA61 [110] style replica-target experiment was already used to provide a strong prior shape constraint. Detector reconstruction effects and potential background processes are included, and a constrained flux-covariance is produced following the method used in ref. [108].

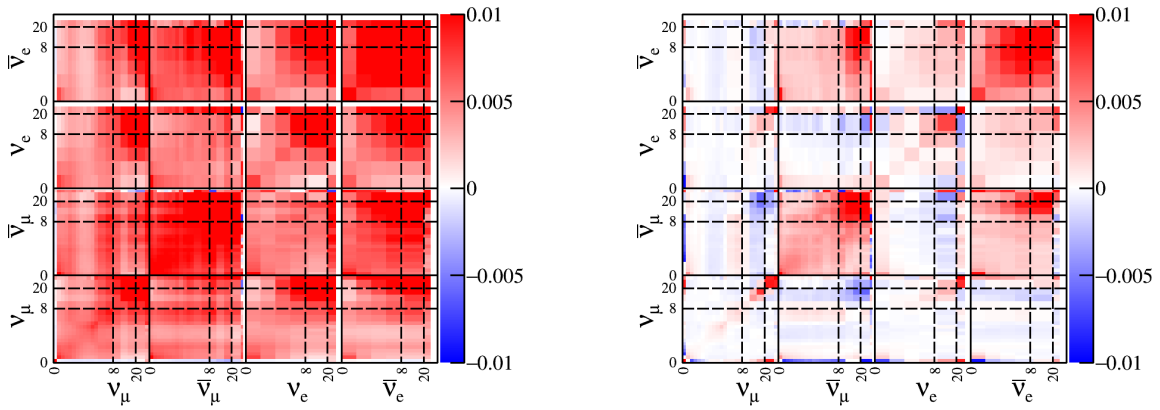

(a) FHC pre-fit

(b) FHC post-fit

Figure A.15. Pre- and post-fit FHC flux covariance matrices for the nominal 35 t ArgonCube LAr detector using a five-year exposure.

The impact of the neutrino-electron scattering constraint on the flux covariance is shown in figure A.15 for FHC and a five year exposure of the nominal 35 t ArgonCube LAr detector (corresponding to ~22k neutrino-electron events). It is clear that the overall uncertainty on the flux has decreased dramatically, although, as expected, an anticorrelated component has been introduced between flavors (as it is not possible to tell what flavor contributed to the signal on an event-by-event basis). Similar constraints are obtained for RHC running.

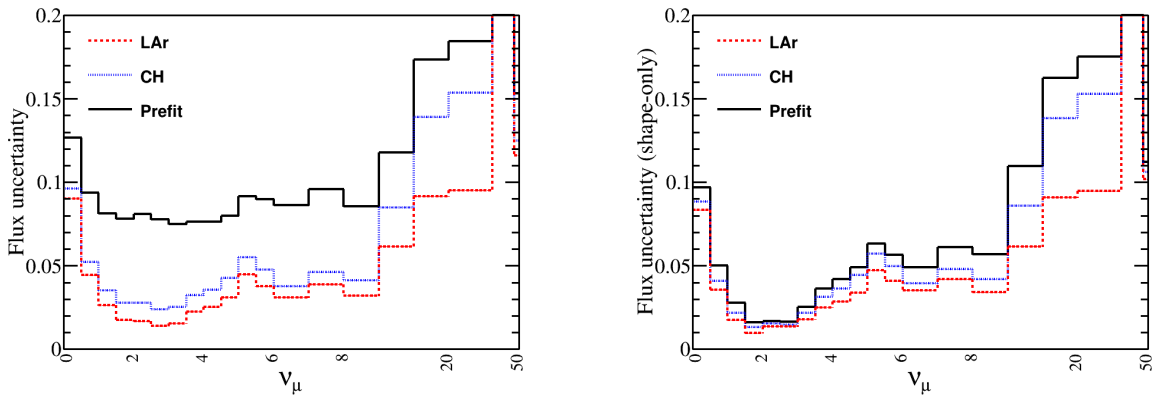

(a) Rate+shape

(b) Shape-only

Figure A.16. Rate+shape and shape-only bin-by-bin flux uncertainties as a function of neutrino energy for a five year exposure with various detector options, compared with the input flux covariance matrix before constraint.

Figure A.16 shows the flux uncertainty as a function of E_ν for the ν_μ-FHC flux, for a variety of ND options. In each case, the constraint on the full covariance matrix is calculated (as in figure A.15), but only the diagonal of the ν_μ portion is shown. In the flux peak of ~2.5 GeV, the total flux uncertainty can be constrained to ~2% for the nominal LAr scenario, and the constraint from other detector types is largely dictated by the detector mass. Clearly the neutrino-electron

2020 JINST 15 T08008

scattering sample at the DUNE ND will be a powerful flux constraint. However, it is also clear that the ability to constrain the shape of the flux is not a drastic improvement on the existing flux covariance matrix, and none of the possible detectors investigated added a significantly stronger constraint. That said, the neutrino-electron sample is able to make in situ measurements of the flux prediction, and is able to diagnose problems with the flux prediction in a unique way.

A.5.3 Multipurpose detector

The multipurpose detector (MPD) extends and enhances the capabilities of the LArTPC. It does this by providing a system that will measure the momentum and sign of charged particles exiting the LArTPC and, for neutrino interactions taking place in the MPD, it will extend charged particle measurement capabilities to lower energies than achievable in the far or near LArTPCs. This capability enables further constraints of systematic uncertainties for the LBL oscillation analysis. The MPD is a magnetized system consisting of a high-pressure gaseous argon time projection chamber (HPgTPC) and a surrounding ECAL. The detector design will be discussed in more detail in a later section.

MPD goals.

- Measure particles that leave the LAr ND component and enter the MPD

  The LAr component of the DUNE ND will not fully contain high-energy muons or measure lepton charge. A downstream MPD will be able to determine the charge sign and measure the momenta of the muons that enter its acceptance, using the curvature of the associated track in the magnetic field.

- Constrain neutrino-nucleus interaction systematic uncertainties

  In its 1-ton gaseous argon FV, the MPD will collect 1.5×10^6 CC muon neutrino interactions per year (plus 5×10^5 NC muon neutrino interactions). The very low energy threshold for reconstruction of tracks in the HPgTPC gives it a view of interactions that is more detailed than what is seen in the LAr, and on the same target nucleus. The associated ECAL provides excellent ability to detect neutral pions, enabling the MPD to measure this important component of the total event energy while also tagging the presence of these pions for interaction model studies.

  The ability to constrain "known unknowns" is a high priority of the MPD. One example is nucleon-nucleon correlation effects and meson exchange currents in neutrino-nucleus scattering. Although a few theoretical models that account for these effects are available in neutrino event generators, no model reproduces well the observed data in NOvA, MINERvA, or T2K. These experiments therefore use empirical models tuned to the limited observables in their detector data. Tuning results in better agreement between simulation and data, although still not perfect. In addition, this type of empirical tuning leaves some large uncertainties, such as the four-momentum transfer response, the neutrino energy dependence of the cross sections (where models disagree, and a "model spread" is typically used for the uncertainty), and the relative fractions of final state nucleon pairs (*pp* vs. *np*).

2020 JINST 15 T08008

Another example of a "known unknown" for which the MPD will provide a more stringent cross section constraint than the LArTPC is the case of single and multiple pion production in CC neutrino interactions. An MPD-based measurement of these processes will be implemented in the DUNE LBL oscillation analysis in the near future, making use of the high-purity samples of CC-0π, CC-1π, and CC-multi-π events in the gaseous argon, separated into π^+ and π^- subsamples and binned in neutrino energy and other variables of interest. Figure A.17 illustrates two simple differences among the HPgTPC CC-1π subsamples; it is still to be determined which variables will be the most useful in the LBL oscillation analysis.

The relative lack of secondary interactions for particles formed in neutrino interactions in the gaseous argon FV will provide samples with a less model dependent connection to the particles produced in the primary interaction. These secondary interactions are a significant effect in denser detectors [45] and this crosscheck/validation of the reinteraction model is likely to be useful in understanding the full energy response of the liquid detectors.

The MPD will measure ratios of inclusive, semi-exclusive, and exclusive cross sections as functions of neutrino energy, where the flux cancels in the ratio. These ratios will be measured separately for NC and CC events, and the NC to CC ratio itself will be measured precisely with the MPD. The ratios of cross sections for different pion, proton, and kaon multiplicity will help constrain interaction models used in the near and far liquid detectors.

The HPgTPC will have better capability than the LArTPC to distinguish among particle species at low momentum using dE/dx measurements. Some muon/pion separation is possible via dE/dx for very low momenta, and protons are very easily distinguished from pions, muons, and kaons for momenta below 2 GeV/c, as shown in figure A.29. At higher momenta, the magnet makes it possible to easily distinguish π^+ from μ^- (or π^- from μ^+), as has been done in T2K near-detector fits for oscillation analyses. The fact that pions will interact hadronically far less often in the gas than in the liquid will give another important handle for constraining uncertainties in the LArTPC. These aspects give the MPD a significant complementarity to the LArTPC, which is not magnetized. Since the target nucleus in the MPD is the same as that in the near and far LArTPCs this information feeds directly into the interaction model constraints without complicating nuclear physics concerns.

Finally, having a ND that can see one level deeper than the far detector keeps open the possibility to investigate "unknown unknowns" as well. Since the MPD will identify and measure interactions more accurately than can be done in the LArTPC, it will provide the ability to investigate more deeply our observations in the liquid argon, and the flexibility to address other unexpected things we may encounter.

- **Precisely and accurately measure all components of the neutrino flux**

  The magnetic field of the MPD enables the precise determination of momenta of charged particles escaping the upstream LArTPC. Because the ND is necessarily smaller than the FD, near-far differences arising from the different containment fractions are compensated by the fact that the ND has a magnetic spectrometer. Also, higher-energy particles from the neutrino interaction will be measured better in the MPD than in the liquid ND or FD (for example, non-contained muons), constraining the effects of energy feed-down in the liquid detectors.

2020 JINST 15 T08008

The ability to separate charge signs will allow the MPD to measure the relative contributions of ν_μ and $\bar{\nu}_\mu$ in both the neutrino beam and the antineutrino beam, as well as distinguishing ν_e from $\bar{\nu}_e$ components. These components are important to anchor the oscillation fit. Otherwise, reliance on the beam modeling is needed to predict the small but uncertain fractions of wrong-sign neutrinos in the beams. Stopping muons' Michel signatures can be used on a statistical basis in the far detector, as the decay rates differ for μ^+ and μ^-, but that is after oscillation has distorted the spectrum. No corresponding test is present for ν_e.

- **Constrain π^0 backgrounds to ν_e events**

  An accurate measurement of backgrounds to the ν_e appearance measurement is a critical input for far detector oscillation analyses. In the LArTPC, the largest background to ν_e's is NC-π^0 interactions in which one photon is not detected and the other is mistakenly identified as an electron. The HPgTPC and ECAL together provide a unique capability to constrain NC-π^0 backgrounds that are misidentified as ν_e CC in the LArTPC. The HPgTPC will collect a reduced background sample of ~ 20k ν_e CC events per year. The LArTPC detector measures ν_e+ mis-ID'ed π^0 events, while the MPD measures ν_e CC events alone (by rejecting all π^0 events using the ECAL). The MPD sample will reduce backgrounds from NC-π^0 events because the photon conversion length in gas is much greater than that in the liquid, and photons from π^0 decays will not often convert in the gas volume of the HPgTPC in such a way as to fake $e^\pm$ from ν_e interactions. The ECAL, however, will have excellent ability to detect the π^0 decays, enabling the MPD to reject π^0 events as background to ν_e's.

  The MPD measurement of ν_e CC events can be scaled to the LArTPC density and volume and corrected to the same acceptance as the LArTPC in order to provide a constraint on the π^0-misID. The difference of the two: (ν_e^{LAr} + mis-ID'ed π^0) – ($\nu_e^{\text{GAr-scaled-to-LAr}}$) yields the π^0-misID rate in LArTPC. This measurement of the backgrounds to ν_e's would not be possible at all if the MPD were replaced by a simple muon range detector. It would also not be easy to extrapolate to the LArTPC if the target material of the MPD were not argon.

- **Measure energetic neutrons from ν-Ar interactions via time-of-flight with the ECAL**

  Neutron production in neutrino and antineutrino interactions is highly uncertain, and is a large source of neutrino energy misreconstruction. In the HPgTPC+ECAL system, a preliminary study of the time-of-flight from the HPgTPC neutrino interaction point to hits in the ECAL is encouraging, indicating that ToF can be used to detect and correctly identify neutrons. With the current ECAL design, an average neutron detection efficiency of 60% is achieved by selecting events in which an ECAL cell has one hit with more than 3 MeV. This is still very preliminary work, and further studies to understand the impact of backgrounds and ECAL optimization (strip vs. tile, overall thickness) are underway.

- **Reconstruct neutrino energy via spectrometry and calorimetry**

  Although all neutral particles from an event must be measured with the ECAL in the MPD, the HPgTPC will be able to make very precise momentum measurements of charged particle tracks with a larger acceptance than the upstream LArTPC, including tracks created by high-momentum exiting particles, which allows the measurement of the entire neutrino spectrum.

2020 JINST 15 T08008

In addition, short and/or stopping tracks will be measured via dE/dx. The sum of this capability provides a complementary event sample to that obtained in the LAr, whose much higher density leads to many secondary interactions for charged particles. The two methods of measurement in the MPD will help in understanding the LAr energy resolution.

- **Constrain LArTPC detector response and selection efficiency**

  The MPD will collect large amounts of data in each of the exclusive neutrino interaction channels, with the exception of $\nu - e$ elastic scattering, where the HPgTPC sample will be too small to be useful. The high statistics ν-Ar interaction samples will make it possible to directly crosscheck every kinematic distribution that will be used to constrain the fluxes and cross sections. Typically these checks will be over an extended range of that variable. The high purity of the MPD samples and low detection threshold for final state particles in the HPgTPC will give a benchmark or constraint on LArTPC detector response and selection efficiencies for each of the interaction channels.

  Using the events collected in the HPgTPC (where selection and energy reconstruction are easy), the performance of LAr event selection and energy reconstruction metrics can be tested by simulating the well-measured HPgTPC four-vectors in the LArTPC. This allows the validation of the LArTPC reconstruction performance on these events. This process is expected to reduce the errors in the LArTPC detector energy response model.

MPD strengths. The strengths of the MPD enable it to reach the goals above and to augment the capabilities of the LArTPC. Below are a few examples of its strengths relative to the LArTPC:

- High-fidelity particle charge determination via magnetic curvature. This is the only detector that can measure electron and positron charge.

- Precise and independent measurement of particle momentum, via magnetic curvature, will allow the measurement of the momentum of higher-energy charged particles without requiring containment. This extends the utility of the ND, especially for the high-energy beam tune. The absolute momentum scale is easily calibrated in the magnetic spectrometer and provides a cross-check on energy loss through ionization measurements. Calibration strategies for the magnetic tracking include pre-assembly field maps, *in situ* NMR probes, and K^0_s and Λ^0 reconstruction.

- Particle identification through dE/dx. The gaseous argon TPC has better separation power of particle species by dE/dx than the liquid because the momentum can be measured along with energy loss.

- High-resolution imaging of particles emerging from the ν-Ar vertex (including nucleons). The reconstruction threshold in the gas phase is much lower than the threshold in liquid because particles travel further in the low density medium, e.g., a proton requires only 3.7 MeV kinetic energy to make a 2 cm track in 10 atmospheres of gaseous argon, while a 3.7 MeV proton in liquid can only travel 0.02 cm. Figure A.18 demonstrates the difference in the thresholds for reconstructing protons in the HPgTPC and the LArTPC in light of the energy spectra of final state protons from a selection of types of neutrino interactions at the

2020 JINST 15 T08008

DUNE ND. The LArTPC threshold is what has been achieved in MicroBooNE up to now, and the HPgTPC threshold is what has been achieved with the tools discussed in section A.5.3.2.3.

- Separation of tracks and showers for less-ambiguous reconstruction. Particle tracks are locally helical and tend to bend away from each other in the magnetic field as they travel from a dense vertex. Electromagnetic showers do not occur in the gas, but in the physically separate ECAL. By contrast, in a LArTPC tracks and showers frequently overlap. The measurement resolution scales are comparable between the liquid and the gas, but the distance scales on which interactions occur are much longer in the gas, allowing particles to be identified and measured separately more easily.

- The measurement of energetic neutrons through time-of-flight with ECAL is a potential game-changer for validating energy reconstruction. Preliminary studies of the HPgTPC+ECAL system indicate that an average neutron detection efficiency of 60% can be achieved via a time-of-flight analysis. A study of the impact of backgrounds is underway, but initial studies are encouraging.

- The HPgTPC is able to measure the momentum of particles over almost the full solid angle. Particles that are emitted at a large angle with respect to the beam have a high probability of exiting the LAr without leaving a matching track in the MPD. However, events collected in the HPgTPC, with its $\simeq 4\pi$ coverage, can be used in the regions of phase space where the exiting fraction is high in the liquid argon to ensure that the events are accurately modeled in all directions in the FD.

- The MPD neutrino event sample, while smaller than the LArTPC sample, is a statistically independent sample. Moreover, the systematic uncertainties of the MPD will be very different than the LArTPC and likely smaller in many cases. This will allow the MPD to act as a systematics constraint for the LArTPC.

A.5.3.1 MPD technical details

A.5.3.1.1 High-pressure gaseous argon TPC

The basic geometry of the HPgTPC is a gas-filled cylinder with a HV electrode at its mid-plane, providing the drift field for ionization electrons. It is oriented inside the magnet such that the magnetic and E fields are parallel, reducing transverse diffusion to give better point resolution. Primary ionization electrons drift to the end plates of the cylinder, which are instrumented with multi-wire proportional chambers to initiate avalanches (gas gain) at the anode wires. Signals proportional to the avalanches are induced on cathode pads situated behind the wires; readout of the induced pad signals provides the hit coordinates in two dimensions. The drift time provides the third coordinate of the hit.

The details of the HPgTPC design will be based closely on the design of the ALICE detector [111] shown in figure A.19. Two readout planes sandwich a central HV electrode (25 μm of aluminized mylar) at HV that generates the drift field, which is parallel to a 0.5 T magnetic field. On each side of the electrode, primary ionization electrons drift up to 2.5 m to reach the endplates,

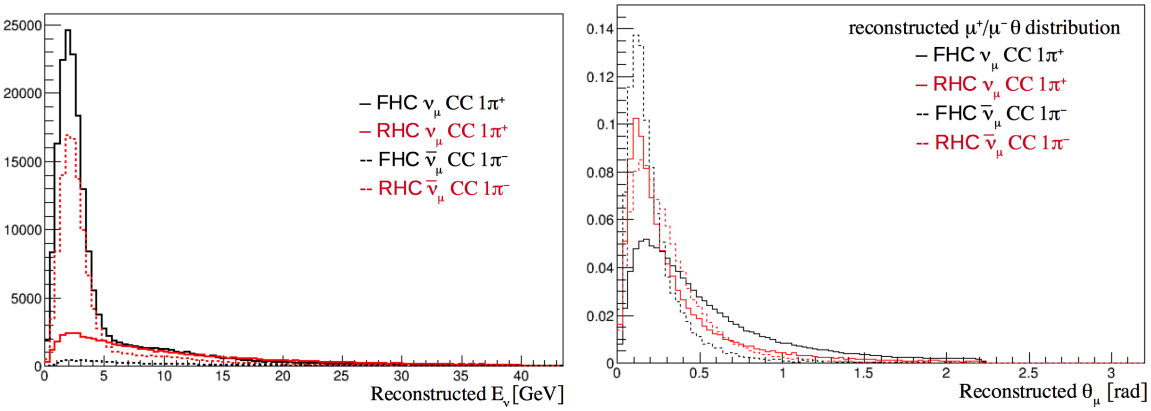

Figure A.17. Representative differences among subsamples of CC ν_μ interactions with one π^+ (solid lines) and CC $\bar{\nu}_\mu$ interactions with one π^- (dashed lines). The forward- and reverse- horn current samples are shown in black and red, respectively. Left: reconstructed neutrino energy spectra, normalized to the same number of protons on target. Right: angle of outgoing muon relative to neutrino direction, normalized to unit area for shape comparison.

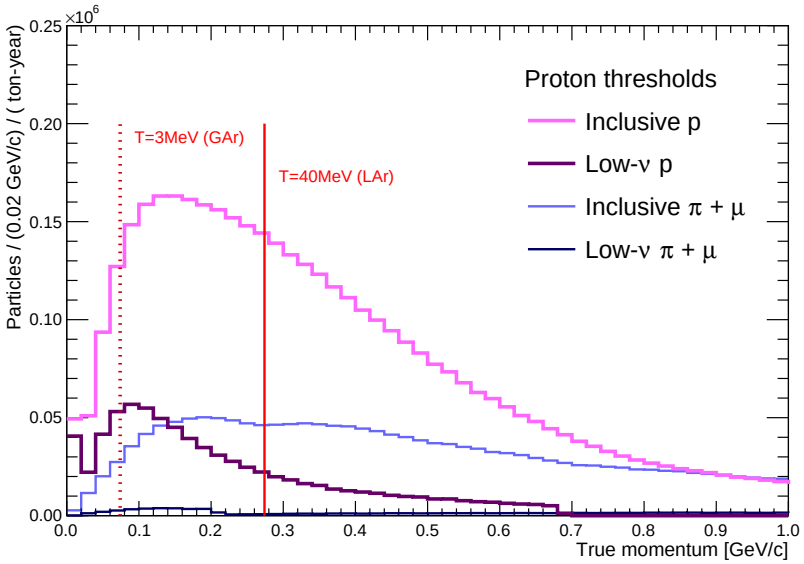

Figure A.18. The momentum spectra of protons ejected from neutrino interactions in argon, for several categories of interaction types. The vertical lines indicate the lowest momentum protons that have been reconstructed using existing automated reconstruction tools, where the dotted line is the HPgTPC threshold, and the solid line is the LArTPC threshold (from MicroBooNE).

which are segmented azimuthally into 18 trapezoidal regions instrumented with readout chambers (ROCs) that consist of MWPC amplification regions and cathode pad planes to read out the signals. A cross sectional view of an ALICE MWPC-based ROC is shown in figure A.20. The ROCs are built in two sizes: a smaller inner readout chamber (IROC) and a larger outer readout chamber (OROC). The trapezoidal segments of the endplates are divided radially into inner and outer sections, and the IROCs and OROCs are installed in those sections. The existing IROCs and OROCs will become available in 2019, when they are scheduled to be replaced by new GEM-based ROCs for upgraded pileup capability in the high rate environment of the LHC. For the DUNE HPgTPC, the existing ROCs are more than capable of providing the necessary performance in a neutrino beam.

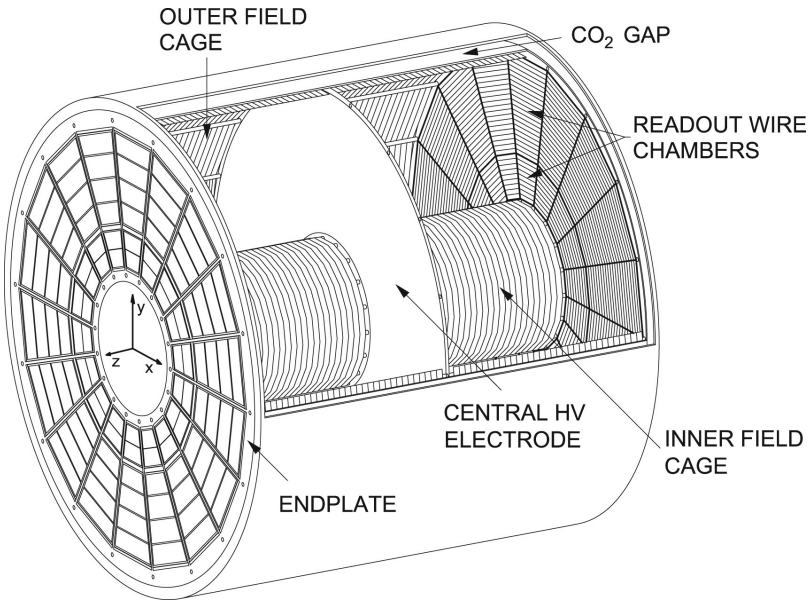

Figure A.19. Diagram of the ALICE TPC, from ref. [112]. The drift HV cathode is located at the center of the TPC, defining two drift volumes, each with 2.5 m of drift along the axis of the cylinder toward the endplate. The endplates are divided into 18 sectors, and each endplate holds 36 readout chambers.

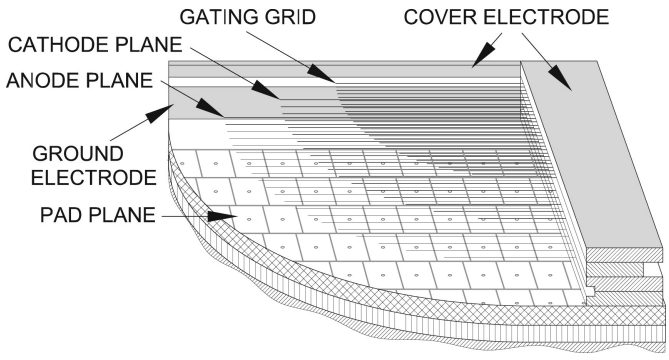

Figure A.20. Schematic diagram of the ALICE MWPC-based ROC with pad plane readout, from ref. [112].

2020 JINST 15 T08008

In the ALICE design, the innermost barrel region was isolated from the TPC and instrumented with a silicon-based inner tracker; for the DUNE HPgTPC, the inner field cage labeled in figure A.19 will be removed, and the entire inner region will be combined to make a single gas volume for the TPC. New ROCs will be built to fill in the central uninstrumented region, which is 1.6 m in diameter, left by reusing the existing ALICE chambers. The active dimensions of the HPgTPC will be 5.2 m in diameter and 5 m long, which yields an active mass of $\simeq$ 1.8 t.

MPD pressure vessel. The preliminary design of the pressure vessel, presented in figure A.21, accounts for the additional volume needed to accommodate the TPC field cage, the ROC support structure, FE electronics, and possibly part of the ECAL.

The pressure vessel can be fabricated from aluminum or stainless steel, has a cylindrical section that is 6 m in diameter and 6 m long and utilizes two semi-elliptical end pieces with flanges. The walls of the cylinder barrel section are $\simeq 1.6X_0$ in thickness in the case of stainless steel or $\simeq 0.3X_0$ in the case of Al 5083. Further reduction of the thickness in radiation lengths can be accomplished with the addition of stiffening rings. This preliminary design includes two flanged endcaps. However, these large flanges are the cost driver for the pressure vessel and, therefore, vessel designs with a single flange will also be considered. As an example, DOE/NETL-2002/1169 (Process Equipment Cost Estimation Final Report) indicates that a horizontal pressure vessel of the size indicated here and rated at 1034 kPag (150 psig) (approximately 10 atmospheres) is costed at \$150k ($\simeq$ \$210k in 2019 dollars). The budgetary estimate for a vessel with two flanges was \$1.2M with the flanges driving the cost. DOE/NETL-2002/1169 also indicates that pressure is not a significant cost driver. Reducing the pressure from 1034 kPag to 103 kPag (15 psig) only reduces the basic (\$150k) vessel cost by a factor of two.

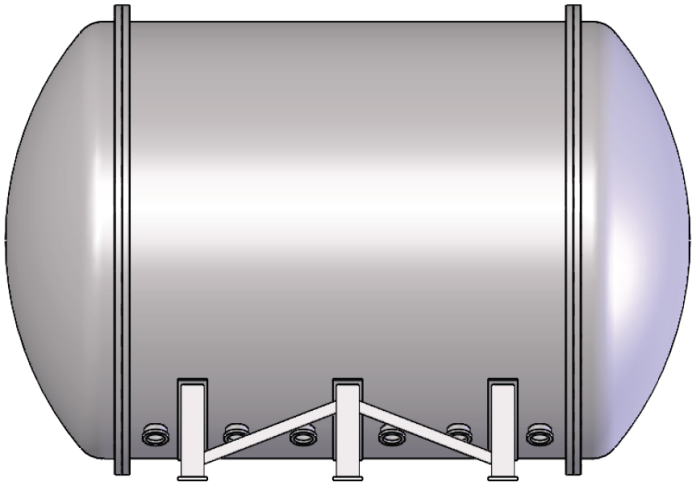

Figure A.21. Pressure vessel preliminary design.

A.5.3.1.2 Electromagnetic calorimeter (ECAL)

The MPD ECAL concept is based on a high granularity calorimeter to provide direction information in addition to the energy measurement of electromagnetic showers and an efficient rejection of

2020 JINST 15 T08008

background. The principal role of the ECAL is to reconstruct photons directly produced in neutrino interactions and originating from π^0 decays, providing a measurement of the photon's energy and direction to enable the association of photons to interactions observed in the HPgTPC and the determination of the decay vertex of the π^0s. In the case of ν_e measurements in the HPgTPC, the ECAL will play an important role in rejecting events with π^0 decays, which represent a background to ν_e interactions in the LArTPC. The ECAL can also be used to reject external backgrounds, such as rock neutrons and muons, providing a sub-nanosecond timestamp [113] for each hit in the detector. As the ECAL uses hydrogen-rich scintillator, it is assumed to have capabilities to provide neutron detection, and studies are underway to determine the performance of neutron detection.

ECAL design. The ECAL design is inspired by the design of the CALICE analog hadron calorimeter (AHCAL) [114].

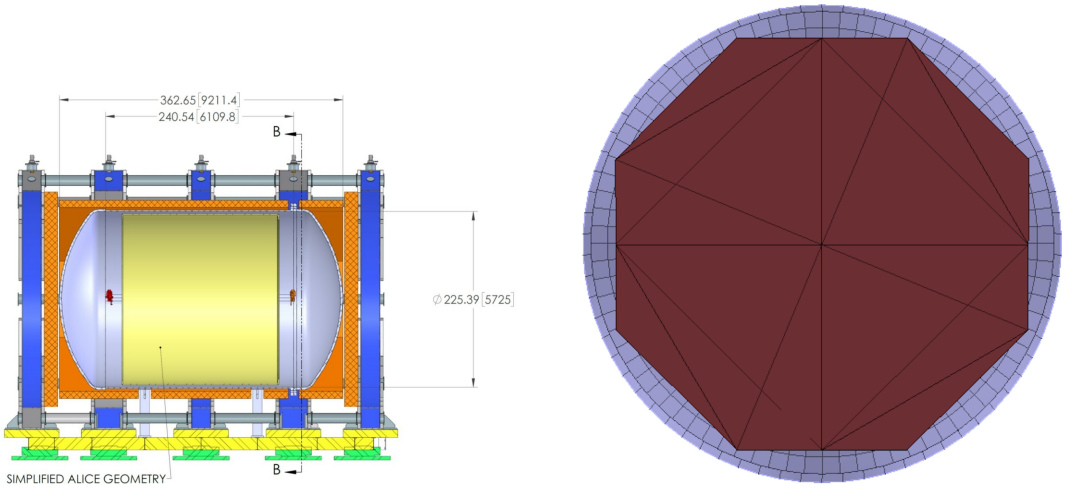

Figure A.22. On the left, the conceptual design of the MPD system for the ND. The ECAL (orange) is located outside the HPgTPC pressure vessel. On the right, a conceptual design of the ECAL endcap system.

The ECAL is shown in figure A.22. The barrel has an octagonal shape with each quadrant composed of several trapezoidal modules. The ECAL endcap has a similar design providing hermeticity and a large solid-angle coverage. Each module consists of scintillating layers of polystyrene as active material read out by SiPMs, sandwiched between absorber sheets. The scintillating layers consist of a mix of tiles with dimensions between 2×2 cm^2 to 3×3 cm^2 (see figure A.23) and cross-strips with embedded wavelength shifting fibers to achieve a comparable effective granularity. The high-granularity layers are concentrated in the front part of the detector, since that has been shown to be the most relevant factor for the angular resolution [115]. With the current design, the number of channels is of the order 2.5 to 3 million. A first design of the ECAL and the simulated performance has already been studied in [115].

In the preliminary design, it was assumed that the full ECAL barrel is outside the pressure vessel. The thickness of the pressure vessel has an impact on the calorimeter energy resolution [115], and more recent designs of the pressure vessel have reduced its thickness. Currently, the ECAL design is undergoing a detailed design study in order to further optimize the detector design, cost, and performance.

2020 JINST 15 T08008

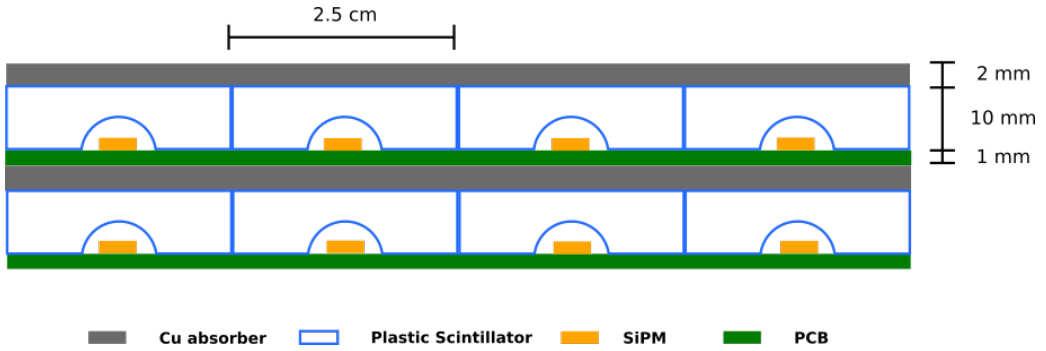

Figure A.23. Conceptual layout of the ECAL showing the absorber structure, scintillator tiles, SiPMs and PCB.

A.5.3.1.3 Magnet

Two magnet designs are under consideration to house the HPgTPC and the ECAL. One is a UA1-type conventional electromagnet, the other is based on a superconducting Helmholtz-coil-like design. The common requirement is a central magnetic field of 0.5 T with ±20% uniformity over the TPC volume (5 m long and 5 m in diameter). With the current design of the access shaft (11.8 m diameter), the clear diameter is about 7.8 m. Recent studies for the construction of an electromagnet similar to the UA1 magnet predict that the cost of the design, procurement, infrastructure (power and cooling) and assembly will be in excess of $20 million, with operation costs of approximately $1.6M per year of running. Because of this, the main focus has been on the superconducting design.

Superconducting magnet. The SC magnet design is a Helmholtz-coil-like configuration, air core, five coil magnet system. Three central coils produce the analyzing field and two outer shielding coils help contain stray field. The advantage of this design is that little or no iron is used for field containment or shaping. This eliminates background coming from neutrino interactions in the iron, which for the normal-conducting magnet case is the largest component of the background. Figure A.24 shows the magnet concept indicating the five-coil arrangement and support structure.

All five coils have the same inner radius of 3.5 m. The center and shielding coils are identical with the same number of ampere-turns. The side coils are placed at 2.5 m, the shielding coils at 6 m from the magnet center along z. The case where the shielding coils are at 5 m from the magnet center so that the magnet system would be the same width as the LAr detector is also being examined. The magnet system will have a stored energy of about 110 MJ, using a conventional NbTi superconducting cable design, a SSC-type Rutherford cable soldered in a copper channel with a 50% margin. All coils should be wired in series to reduce imbalanced forces during a possible quench. Small transverse centering force components are possible due to coil de-centering from mechanical errors. Shown in figure A.25 is the field along the z-axis at different radii. The peak field in the coils is 2.14 T (center), 5 T (side) and 2.03 T (shield). The resulting forces are only along the z-axis, F_z is 0.0 MN (center), −6.81 MN (side) and 2.2 MN (shield). The fringe field at the shielding coil is rather large but can be reduced further; more studies will be needed. There is a preliminary mechanical support design. A first glimpse at the radiative heat load assumes a coil and support surface of 180 m^2, resulting in a load of 5.4 W from 77 K to 4.5 K. The coil support

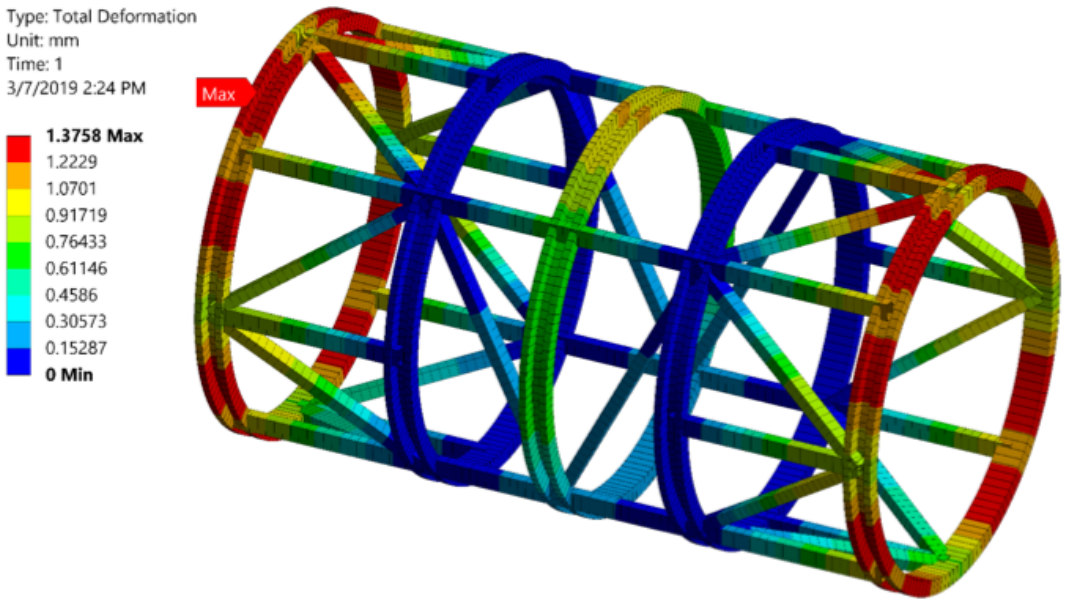

Figure A.24. Helmholz coil arrangement for MPD superconducting magnet.

and leads will likely have a much larger contribution (power leads usually have 15 W for 10 kA). With a mass of 42 t the magnets are in some aspects similar to the Mu2e solenoids.

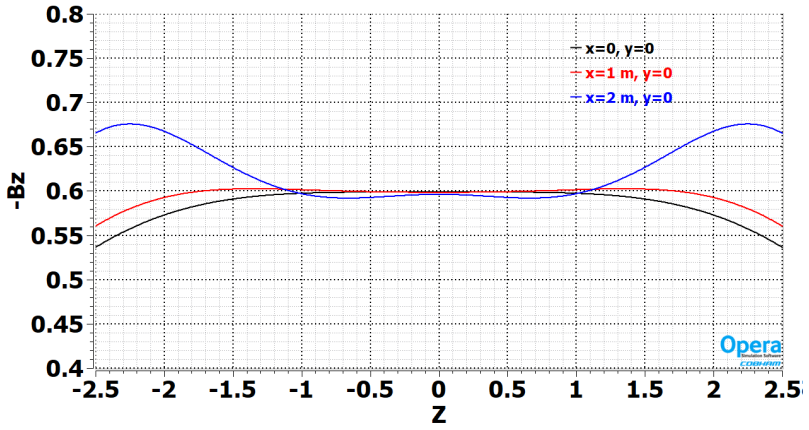

Figure A.25. Field map of the superconducting magnet along the z axis. The colors represent different radii from the center line.

Normal conducting magnet. Although the SC magnet design is the favored option, the normal conducting magnet design produced for the LBNE CDR is also being revised and studied. Due to the cylindrical geometry imposed by the HPgTPC, a cylindrical coil design for the normal conducting magnet is the baseline. The cooling requirement of the coil is approximately 3.5 MW and involves a substantial cooling water flow. A thermal shield between the coils and the detector volume is required in order to minimize heat flow to the HPgTPC and the ECAL. The coil thickness becomes excessive (in order to maintain a maximum 5° C temperature in the coil) if the thermal

2020 JINST 15 T08008

shield is not used. The shield does take up space in the magnet volume, however. Note: the iron end-walls will most likely not be needed. The estimated magnet weight is well over 1 kt, and this mass provides a significant source of background for the high pressure gas TPC and, perhaps, the LAr. There is a significant amount of material between the LArTPC and the HPgTPC in the MPD in this configuration, which will affect the acceptance for muons emanating from events in the LAr. This option will continue to be studied as part of the optimization process.

A.5.3.1.4 Size optimization

The process of optimizing the design of the MPD is in progress. One of the more critical issues is the size of the MPD. This is an important factor in the angular acceptance of particles exiting the upstream LArTPC. A preliminary study of geometries shows that reducing the HPgTPC diameter by more than 1 meter, or reducing the length by more than 1.5 meters would have significant consequences on the acceptance. Reducing the HPgTPC diameter from its nominal 5 meters to a slightly smaller 4.5 meters while increasing its length in the direction transverse to the neutrino beam improves acceptance, since the HPgTPC would better match the 7-meter width of the LArTPC in the transverse direction. It should be noted, however, that reducing the diameter may actually result in a higher-cost MPD, since the ALICE TPC readout chambers would not be used in the configuration for which they were designed. Increasing the length of the HPgTPC is feasible, but will require additional studies of high voltage stability in the gas, since HV breakdown in gas is proportional to the pressure (in the absence of field enhancements). The HPgTPC operating pressure will be nominally 10 times that of ALICE, so extending the drift distance from 2.5 meters to 3 meters while keeping the same drift velocity will require raising the drift HV by approximately 20 kV.

A.5.3.2 MPD performance

The expected performance of the MPD is summarized in table A.2. Details of the HPgTPC performance are based upon experience from operation of the PEP-4 [116–118] and ALICE [119] time projection chambers. Performance of the ECAL is based on experience from operation of similar ECALs and on simulations.

A.5.3.2.1 Track reconstruction and particle identification

The combination of very high resolution magnetic analysis and superb particle identification from the HPgTPC, coupled with a high-performance ECAL will lead to excellent event reconstruction capabilities and potent tools to use in neutrino event analysis. As an example of this capability, the top panel of figure A.26 shows a $\nu_e + {}^{(N)}Ar \rightarrow e^- + \pi^+ + n + {}^{(N-1)}Ar$ in the HPgTPC with automatically-reconstructed tracks. The same event was simulated in a FD SP module, and is shown in the bottom panel of figure A.26.

Since important components of the hardware and design for the HPgTPC are taken from or duplicated from the ALICE detector, the ALICE reconstruction is a useful point of reference in this discussion. Track reconstruction in ALICE is achieved by combining hits recorded on the ROC pads into tracks following a trajectory that a charged particle traveled through the TPC drift volume. The HPgTPC is oriented so that the neutrino beam is perpendicular to the magnetic field, which

2020 JINST 15 T08008

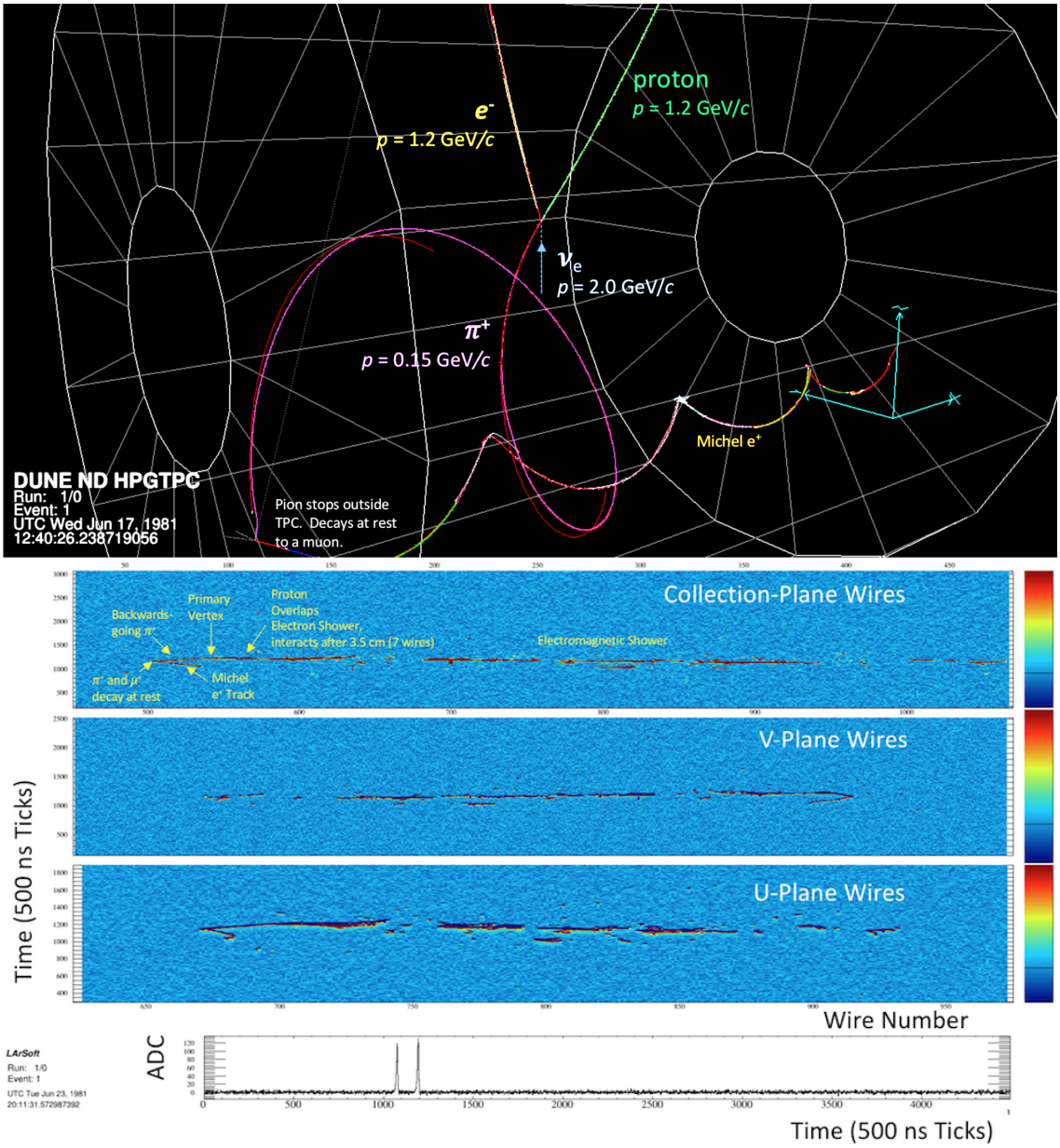

Figure A.26. (Top) Track-reconstructed ν_e CC event in the HPgTPC, simulated and reconstructed with GArSoft. The annotations are from MC truth. (Bottom) The same ν_e CC event, but simulated in a SP module using LArSoft. The topmost blue panel shows the collection-plane view, the middle blue panel shows the V view, and the bottom blue panel shows the U view. Wire number increases on the horizontal axes and sample time along the vertical axes. The wire number in the collection view is labeled on the top of the panel, while the V and U wire numbers are below their respective panels. Simulated ADC values are indicated by the colors. The curve in the bottom-most panel is a simulated waveform from a collection-plane wire. The annotations are from MC truth.

2020 JINST 15 T08008

Table A.2. Expected MPD performance, extrapolated from ALICE.

Parameter	Value	units
σ_x	250	μm
σ_y	250	μm
σ_z	1500	μm
$\sigma_{r\phi}$	<1000	μm
Two-track separation	1	cm
Angular resolution	2-4	mrad
$\sigma(dE/dx)$	5	%
σ_{pT}/p_T	0.7	% (10-1 GeV/c)
σ_{pT}/p_T	1-2	% (1 GeV/c to 0.1 GeV/c)
Energy scale uncertainty	$\lesssim 1$	% (dominated by δ_p/p)
Charged particle detection thresh.	5	MeV (K.E.)
ECAL energy resolution	$5\text{-}7/\sqrt{E/\text{GeV}}$	%
ECAL pointing resolution	$\simeq 6$ at 500 MeV	degrees

is the most favorable orientation for measuring charged particles traveling along the neutrino beam direction.

The GArSoft simulation and reconstruction package borrows heavily from LArTPC, and is based on the *art* event processing framework and `GEANT4`. It is designed to be able to reconstruct tracks with a full 4π acceptance. GArSoft simulates a 10 atmosphere gaseous argon detector with readout chambers filling in the central holes in the ALICE geometry. GArSoft's tracking efficiency has been evaluated in a large sample of GENIE ν_μ events interacting in the TPC gas at least 40 cm from the edges, generated using the optimized LBNF forward horn current beam spectra. The efficiency for reconstructing tracks associated with pions and muons as a function of track momentum p is shown in figure A.27. The efficiency is above 90% for tracks with $p > 40\,\text{MeV}/c$, and it steadily rises with increasing momentum.

Also shown is the efficiency for reconstructing all charged particles with $p > 200\,\text{MeV}/\text{c}$ as a function of λ, the track angle with respect to the center plane. The tracking efficiency for protons is shown in figure A.28 as a function of kinetic energy, T_p. Currently, the tracking works well down to $T_p \simeq 20\,\text{MeV}$. For $T_p < 20\,\text{MeV}$, a machine-learning algorithm is in development, targeting short tracks near the primary vertex. This algorithm, although currently in a very early stage of development, is already showing good performance, and efficiency improvements are expected with more development. The machine learning algorithm is described in section A.5.3.2.3.

The ALICE detector, as it runs at the LHC, typically operates with particle densities ranging from 2000 to 8000 charged particles per unit rapidity (dN/dy) for central Pb-Pb interactions [120]. The expected particle densities in the DUNE neutrino beam will be much lower and less of a challenge for the reconstruction.

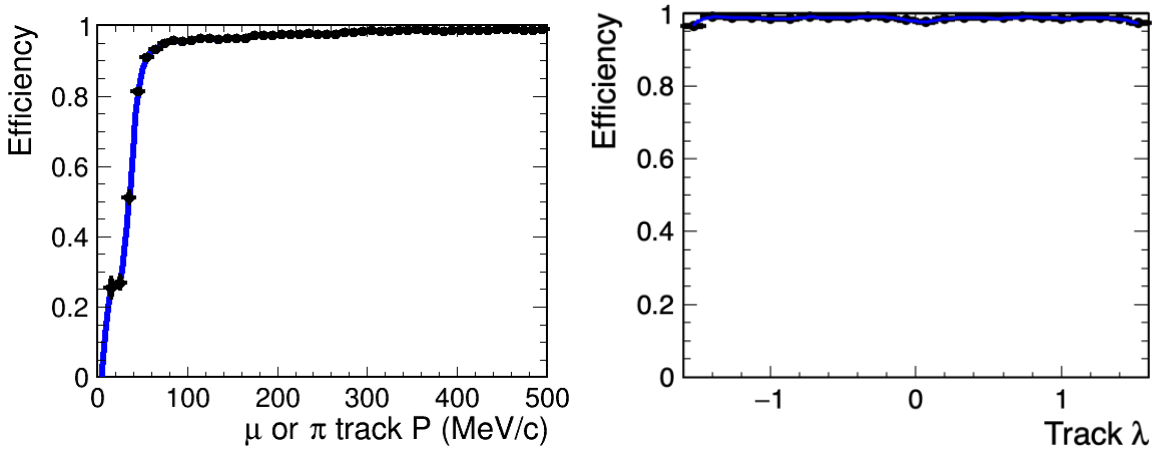

Figure A.27. (Left) The efficiency to find tracks in the HPgTPC as a function of momentum, p, for tracks in a sample of GENIE events simulating 2 GeV and ν_μ interactions in the gas, using GArSoft. (Right) The efficiency to find tracks as a function of λ, the angle with respect to the center plane, for tracks with $p > 200\,\mathrm{MeV}/c$.

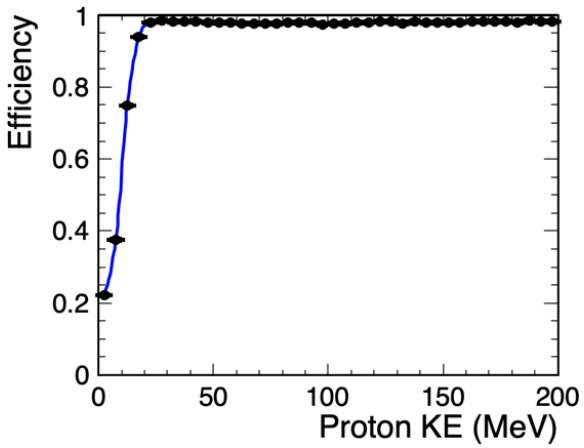

Figure A.28. Tracking efficiency for protons in the HPgTPC as a function of kinetic energy.

ALICE chose to use neon, rather than argon, for the primary gas in their first run; the decision was driven by a number of factors, but two-track separation capability was one of the primary motivations due to the extremely high track multiplicities in the experiment. Neon performs better than argon in this regard. A better comparison for the HPgTPC's operation in DUNE is the two-track separation that was obtained in PEP4 [117]. PEP4 ran an 80-20 mixture of Ar-CH_4 at 8.5 atmospheres, yielding a two-track separation performance of 1 cm.

In ALICE, the ionization produced by charged particle tracks is sampled by the TPC pad rows (there are 159 pad rows in the TPC) and a truncated mean is used for the calculation of the PID signal. Figure A.29 (left) shows the ionization signals of charged particle tracks in ALICE for pp collisions at $\sqrt{s} = 7\,\mathrm{TeV}$. The different characteristic bands for various particles are clearly visible and distinct at momenta below a few GeV. When repurposing ALICE as the HPgTPC component of the MPD, better performance is expected for particles leaving the active volume,

since the detector will be operating at higher pressure (10 atmospheres vs. the nominal ALICE 1 atmosphere operation), resulting in ten times more ionization per unit track length available for collection. Figure A.29 (right) shows the charged particle identification for PEP-4/9 [121], a higher pressure gas TPC that operated at 8.5 atmospheres, which is very close to the baseline argon gas mixture and pressure of the DUNE HPgTPC.

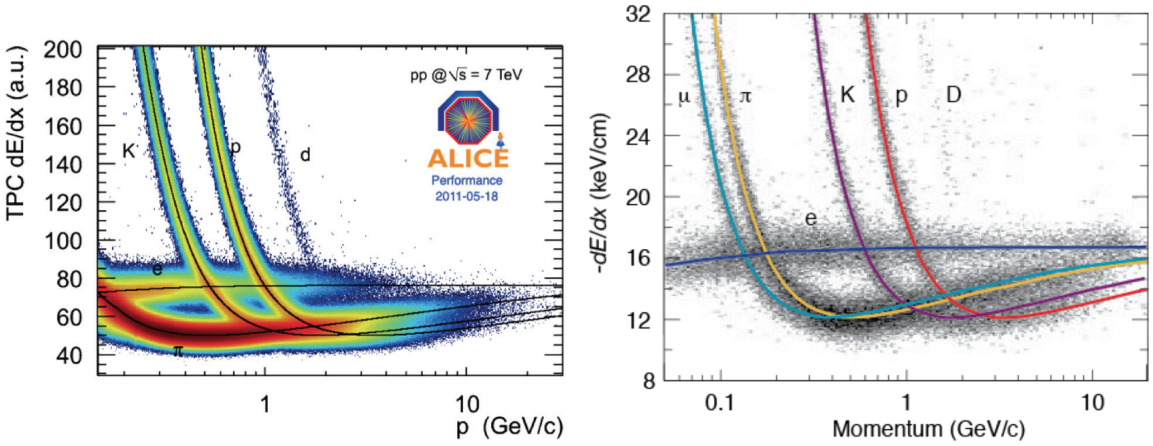

Figure A.29. Left: ALICE TPC dE/dx-based particle identification as a function of momentum (from [122]). Right: PEP-4/9 TPC (80:20 Ar-CH4, operated at 8.5 Atm, from [121]) dE/dx-based particle identification.

A.5.3.2.2 Momentum and angular resolution for charged particles

The ability to determine the sign of the charge of a particle in the HPgTPC tracking volume is limited by the spatial resolution of the measured drift points in the plane perpendicular to the magnetic field, as well as multiple Coulomb scattering (MCS) in the gas. For a fixed detector configuration, the visibility of the curvature depends on the particle's p_{T}, its track length in the plane perpendicular to the field, and the number and proximity of nearby tracks. Because primary vertices are distributed throughout the tracking volume, the distribution of the lengths of charged-particle tracks is expected to start at very short tracks, unless sufficient FV cuts are made to ensure enough active volume remains to determine particle's track sign. The kinetic energies of particles that leave short tracks and stop in the detector will be better measured from their tracks' lengths than from their curvatures. Protons generally stop before their tracks curl around, but low-energy electrons loop many times before coming to rest in the gas.

Within the FV of the HPgTPC, charged particles can be tracked over the full 4π solid angle. Even near the central electrode, tracking performance will not be degraded due to the very thin (25 μm of mylar) nature of the central electrode. Indeed, tracks crossing the cathode provide an independent measurement of the event time, since the portions of the track on either side of the cathode will only line up with a correct event time assumed when computing drift distances. The 4π coverage is true for all charged particles. ALICE ran with a central field of 0.5 T and their momentum resolution from p–Pb data [123] is shown in figure A.30.

The momentum resolution of muons in neutrino scatters using the GArSoft simulation and reconstruction package is shown in figure A.31, using a sample of 2 GeV ν_μ CC events. This

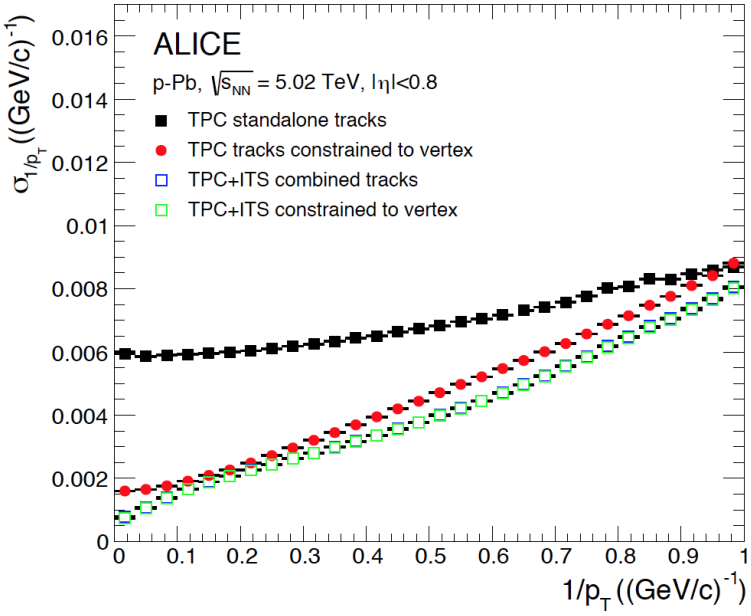

Figure A.30. The black squares show the TPC stand-alone p_T resolution in ALICE for p–Pb collisions. From ref. [123].

resolution differs from ALICE's achieved resolution due to the higher pressure, the heavier argon nucleus compared with neon, the non-centrality of muons produced throughout the detector, and the fact that the GArSoft simulation and reconstruction tools have yet to be fully optimized. The momentum resolution achieved for muons is $\Delta p/p = 4.2\%$, and is expected to improve with optimization of the simulation and reconstruction tools. The 3D angular resolution of muons is approximately 0.8 degrees, as shown in figure A.31.

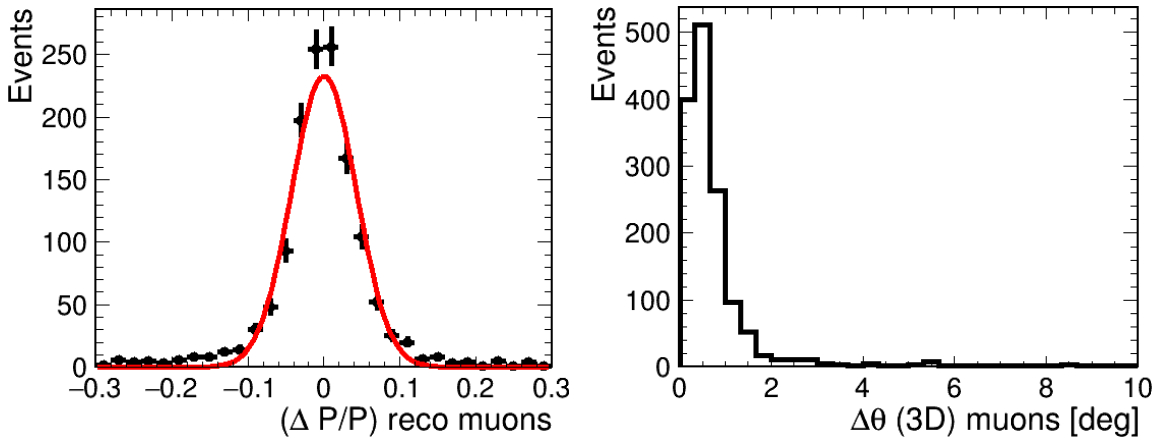

Figure A.31. Left: the momentum resolution for reconstructed muons in GArSoft, in a sample of 2 GeV ν_μ CC events simulated with GENIE. The Gaussian fit to the $\Delta p/p$ distribution has a width of 4.2%. Right: the 3D angular resolution for the same sample of muons in GArSoft.

A.5.3.2.3 Machine learning for low energy protons

As a complement to the existing reconstruction, an initial exploration of several machine learning methods has been performed. The main goal of this effort has been to attempt to reconstruct very low energy protons and pions where traditional tracking methods might struggle. While this study is still in very early stages, there has been success so far in using a fully connected multi-layer perceptron (MLP) to both regress the kinetic energy of and classify between protons and pions. Additionally a Random Sample Consensus (RANSAC) based clustering algorithm has been developed to group hits into short tracks for events where there are multiple particles. Together, these two algorithms can be used to measure the kinetic energy of multiple particles in a single event.

As a demonstration, a test sample of multiple proton events was generated where each event has:

- 0-4 protons, number determined randomly with equal probabilities
- all protons share a common starting point (vertex) whose position in the TPC is randomly determined
- each proton is assigned independently and randomly:
  - a direction in space (isotropically distributed)
  - a scalar momentum between 0 and 200 MeV/c (flat distributed)

The RANSAC-based clustering algorithm assigns individual hits to proton candidate sets of hits which are passed to a MLP that was trained on a set of individual proton events in the TPC to predict kinetic energy. Figure A.32 shows the kinetic energy residuals, the reconstruction efficiency, and a 2D scatter plot of the measured kinetic energy versus the true kinetic energy for each individual proton with kinetic energy between 3 and 15 MeV in the test sample. Additionally, the residual for the total kinetic energy in each multi-proton event is given.

A.5.3.2.4 ECAL performance

The expected performance of the calorimeter was studied with Geant4-based [124] simulations and GArSoft [125]. In the following, a first scenario referred to as scenario A (shown by the red curve in the figures below) in which the ECAL is located inside the pressure vessel is considered. The barrel geometry consists of 55 layers with the following layout:

- 8 layers of 2 mm copper + 10 mm of 2.5×2.5 cm^2 tiles + 1 mm FR4
- 47 layers of 4 mm copper + 10 mm of cross-strips 4 cm wide

For the present studies, copper has been chosen as absorber material as initial studies have shown that this material provides a good compromise between calorimeter compactness, energy resolution, and angular resolution. However, the choice of absorber material is still under study. The choice of granularity, scintillator thickness, and the arrangement of tiles and strips is still under optimization in order to reduce the number of readout channels while keeping the calorimeter performance. Two alternative scenarios are shown below: scenario B (black curve) has a different arrangement of the tile and strip layers, and scenario C (blue curve) has thinner absorbers in the front layers.

2020 JINST 15 T08008

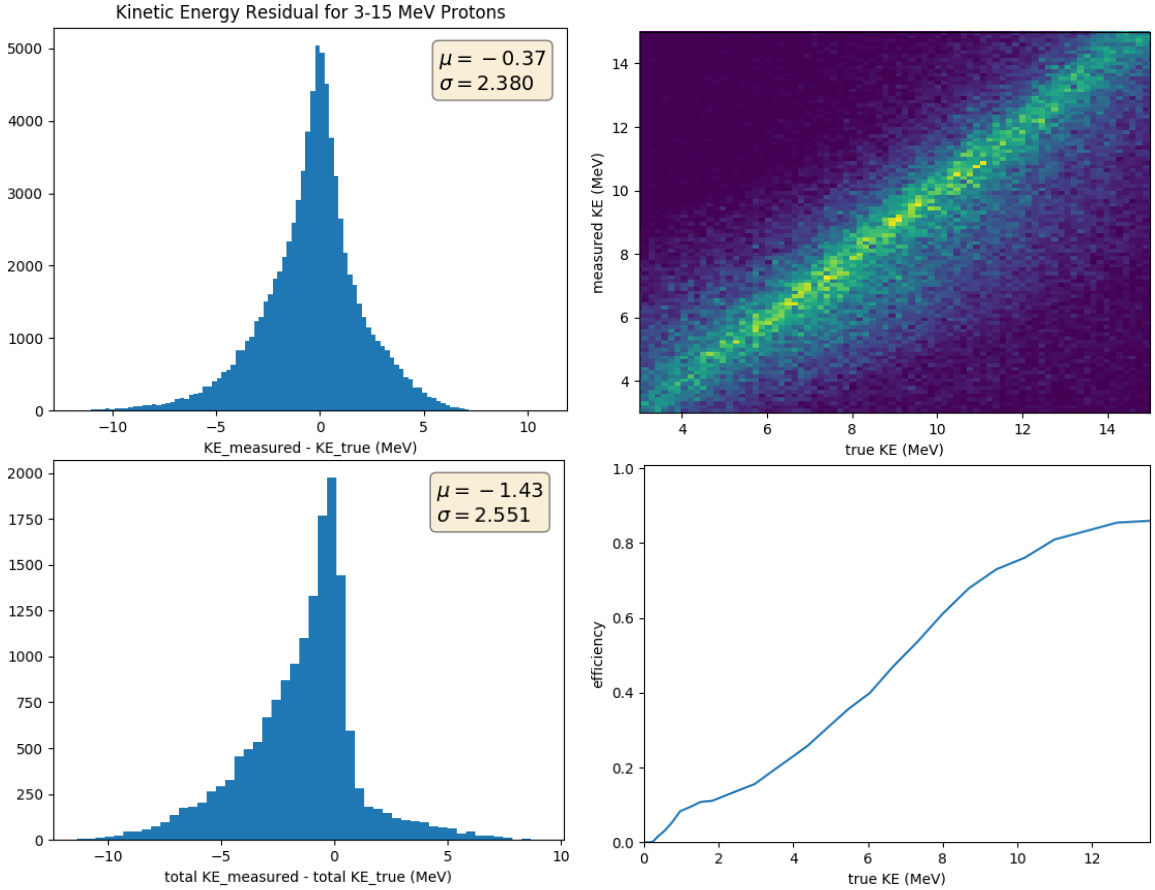

Figure A.32. (Top left) Kinetic energy residual, (Top right) measured KE vs. true KE, and (Bottom right) reconstruction efficiency for individual protons with 3 MeV to 15 MeV KE in the test set. (Bottom left) Residual of the total kinetic energy of all protons in each event in the test sample.

Digitization effects are accounted for by introducing an energy threshold of 0.25 MIPs (~200 keV) for each detector cell/strip, a Gaussian smearing of 0.1 MeV for the electronic noise, SiPM saturation effects, and single photon statistics.

Energy resolution. The energy resolution is determined by fitting the visible energy with a Gaussian. Converted photons are rejected based on Monte-Carlo information. A fit function of the form $\frac{\sigma_E}{E} = \frac{A}{\sqrt{E}} \oplus \frac{B}{E} \oplus C$ is used, where A denotes the stochastic term, B the noise term, C the constant term, and E is in GeV. Figure A.33 shows the energy resolution as a function of the photon energy. For scenario A, shown in red, the energy resolution is around $\frac{6.7\%}{\sqrt{E}}$. With further optimization, it is believed that an energy resolution of (or below) $\frac{6\%}{\sqrt{E}}$ is achievable. It should be noted that due to the lack of non-uniformities, dead cells, and other effects in the simulation, the energy resolution is slightly optimistic.

Angular resolution. The angular resolution of the calorimeter has been determined using a principal component analysis (PCA) of all reconstructed calorimeter hits. The direction is taken as the first eigenvector (main axis) of all the reconstructed hits. The angular resolution is determined

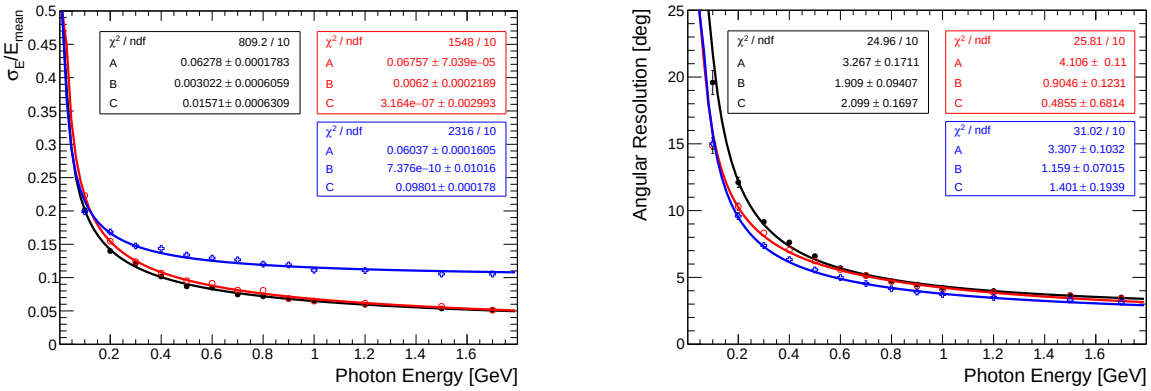

Figure A.33. Left: energy resolution in the barrel as a function of the photon energy for three ECAL scenarios. The energy resolution is determined by a Gaussian fit to the visible energy. Right: the angular resolution in the barrel as a function of the photon energy for the three ECAL scenarios. The angular resolution is determined by a Gaussian fit to the 68% quantile distribution. For both figures, the scenario A is shown by the red curve, scenario B by the black curve and scenario C by the blue curve. The fit function is of the form $\frac{\sigma_E}{E} = \frac{A}{\sqrt{E}} \oplus \frac{B}{E} \oplus C$.

by taking the 68% quantile of the reconstructed angle distribution and fitting a Gaussian distribution. The mean of the Gaussian is taken as the angular resolution and the error as its variance. Figure A.33 shows the angular resolution as a function of the photon energy. In scenario A, shown in red, an angular resolution of $\frac{3.85°}{\sqrt{E}} \oplus 2.12°$ can be achieved. This can potentially be further improved with a different arrangement of the tile and strip layers, an optimization of the absorber thickness, and an improved reconstruction method. However, the requirements will be further refined and will impact the detector optimization. The angular resolution is mainly driven by the energy deposits in the first layers of the ECAL. Using an absorber with a large X_0 creates an elongated shower that helps in determining the direction of the shower. In general, high granularity leads to a better angular resolution, however, studies have shown that there is no additional benefit to having cell sizes below 2×2 cm^2 [115].

Neutron detection. The ECAL is sensitive to neutrons due to the scintillator containing hydrogen. Previous simulation studies showed that a detection efficiency above 60% can be achieved for neutron energies greater than 50 MeV. However, the energy measurement is not very accurate (around 50-60% below 600 MeV) [115]. Other methods of detection such as time of flight (ToF) could be used to improve the neutron energy measurement by measuring precisely the hit time of the neutron and its travel distance in the calorimeter. This is currently under study.

π^0 reconstruction. For identification of neutral pions, both the energy and angular resolution are relevant. In an initial study, the position of the neutral pion is determined by using a χ^2-minimization procedure taking into account the reconstructed energy of the two photons and the reconstructed direction of the photon showers [115]. The location of the decay vertex of the neutral pion can be determined with an accuracy between 10 cm to 40 cm, depending on the distance from the downstream calorimeter and the π^0 kinetic energy. This is sufficient to associate the π^0 to an interaction in the HPgTPC, since the gas will have less than one neutrino interaction per beam spill.

2020 JINST 15 T08008

The pointing accuracy to the pion decay vertex may be further improved by a more sophisticated analysis technique and by using precision timing information, and is a subject of current study.

A.5.4 The DUNE-PRISM program

The goals of the off-axis measurements are twofold:

- **To identify problems in the cross section modeling.** By comparing ND data to MC at many off-axis locations with different energy spectra, the neutrino interaction model will be more tightly constrained than it would be with only on-axis measurements, and the potential for biases in the measured oscillation parameters can be identified, i.e., the off-axis data might be sensitive to mismodelings that are degenerate or indeterminate with only on-axis measurements.

- **To overcome problems in the cross section modeling.** The most important novel feature of a DUNE-PRISM detector is that measurements at different off-axis positions can be linearly combined to determine any set of observables for any user-defined neutrino energy spectrum. In particular, it is possible to predict the expected distribution of an observable, such as the reconstructed neutrino energy, for a neutrino flux with oscillations using linear combinations of ND off-axis spectra. This will greatly reduce the dependence on neutrino interaction modeling within the oscillation analysis.

A.5.4.1 Impact of cross section modeling on neutrino oscillations

One strategy to understand the potential impact of using imperfect neutrino interaction models is to extract oscillation parameters from a "fake" data set that is different from the model used in the analysis. This fake data set represents a reality that includes effects unknown to or not accounted for properly by the model used in the analysis to fit the data. In this way, it is possible to understand potential biases in the measured oscillation parameter values extracted from a full near+far detector fit due to the use of an incorrect cross section model in the fit.

The fake data set considered here assumes that 20% of the kinetic energy that the interaction model originally assigned to protons was instead carried away by neutrons. The resulting model is then further modified by adjusting the differential cross section in proton energy as a function of true neutrino energy until the measured kinematic distributions in the on-axis ND match the prediction from the default model. This procedure is similar to actions that are routinely taken in actual neutrino oscillation experiments to resolved discrepancies between ND data and the Monte Carlo simulation. There are many potential modifications to the cross section model that can be chosen to resolve such disagreements. Incorrect choices can lead to biased oscillation parameter measurements because the associated incorrect particle composition and cross section model can lead to an incorrect relation between reconstructed and true energy.

The resulting fake data is analyzed as though it were the actual data taken by the experiment. The ND and FD data are fit simultaneously to constrain nuisance parameters in the flux and cross section models, and to extract the measured value of the neutrino oscillation parameters. The results of this fit are shown in figure A.34. The fit to the fake data shows a clear bias in the measured oscillation parameter values that lie outside the 95% confidence limit contours.

2020 JINST 15 T08008

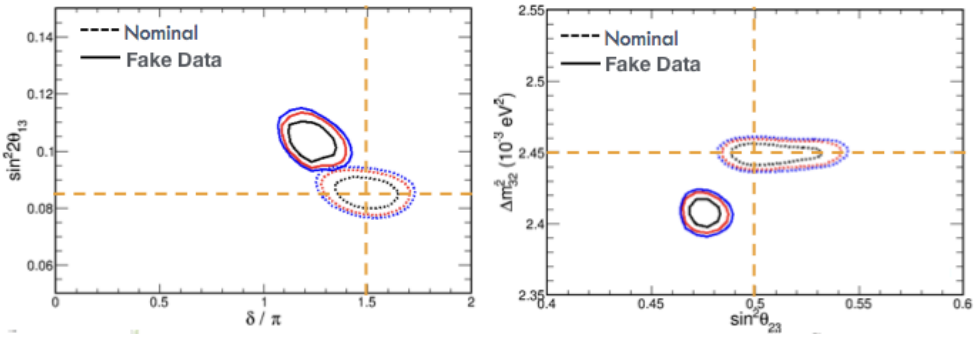

Figure A.34. The results of a full two-flavor, antineutrino+neutrino, near+far oscillation fit are shown for a fit to the nominal MC (dashed) and a fit to the fake data set (solid). The true values of the oscillation parameters in each of the data sets are indicated by the dashed yellow lines. Clear biases can be see in all oscillation parameters that are well outside the 1σ (black), 2σ (red), and 3σ (blue) contours.

A comparison of the fake data and the nominal Monte Carlo reconstruction energy distributions is shown in figure A.35. In the on-axis location, good agreement is seen, as was intended in the construction of the fake data samples. This good agreement is assured since the model is tuned to the on-axis data. Conversely, clear disagreement is seen between these samples when moving off-axis. As the off-axis location is varied, this comparison can be made across a wide range of neutrino energy distributions.

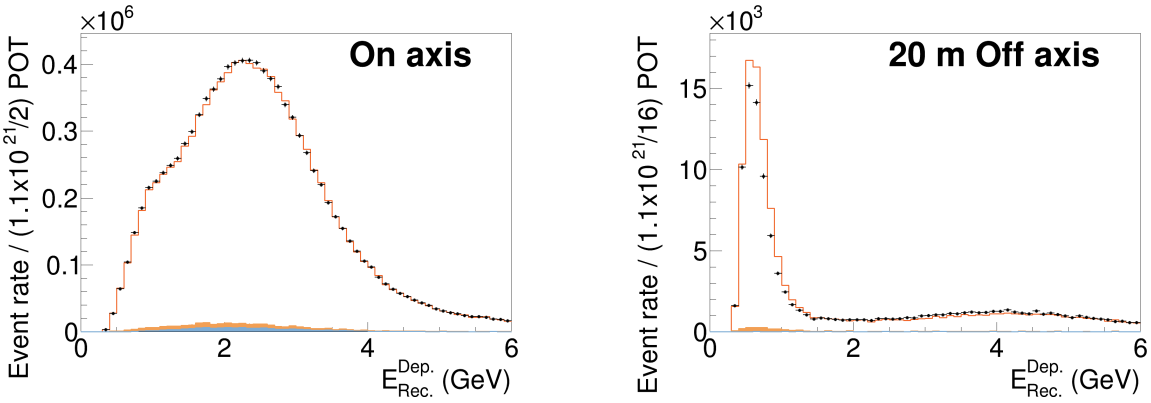

Figure A.35. A comparison between the fake data (green) and nominal Monte Carlo (red) reconstructed neutrino energy distributions are shown for the on-axis ND location (left) and a position 18 m off-axis (right).

A.5.4.2 DUNE-PRISM linear combination analysis

In addition to identifying problems in cross section modeling, DUNE-PRISM measurements provide a mechanism for creating FD predictions directly from the ND data that is largely independent of neutrino interaction modeling. By constructing linear combinations of measurements taken under exposure to different neutrino fluxes, it is possible to determine the distribution of any observable (e.g. reconstructed neutrino energy) for a different neutrino flux of interest. This means, for example, from the ND data alone it is possible to create a distribution of the expected reconstructed neutrino energy distribution at the FD in the event of oscillations with a specific set of parameters. This

distribution, created using this data-driven technique, can then be compared to that seen in the FD with a reduced dependence on the flux and neutrino interaction models and their associated uncertainties.

A few example fits of the off-axis ND muon neutrino spectra to an oscillated FD muon neutrino energy spectrum are shown in figure A.36. Good agreement is seen near the first and second oscillation maxima at 2.5 GeV and 0.7 GeV, respectively. The ability to fit the FD spectrum breaks down outside the central range of energy because the constituent off-axis spectra used in the fit extend only slightly outside this range and cannot duplicate the spectrum in any combination. This does not pose a significant problem for the oscillation analysis because the fit is good for the bulk of the events and in the region that drives the CP sensitivity. This technique can also be applied to match the off-axis muon neutrino spectra to the ND intrinsic electron neutrino spectrum, in order to make a precise measurement of $\sigma(\nu_e)/\sigma(\nu_\mu)$ with a common flux, or to the FD oscillated electron neutrino energy spectra for the measurement of δ_{CP}.

A.6 Fixed on-axis component of the DUNE ND

A.6.1 Motivation and introduction

In spite of tremendous efforts to ensure stable operation, neutrino beams are dynamic in nature. Experiments must track changes in the beam as a function of time in order to understand and model the neutrino flux spectrum well enough to achieve their physics goals. In addition, neutrino interactions observed by experiments in the beam, if taken at a sufficient rate with good energy and spatial resolutions, can provide unique and invaluable information as a beam diagnostic. The issue of beam stability is particularly important for DUNE because the wide-band beam is sensitive to a large range of beamline changes and the DUNE-PRISM program makes use of spectral shifts induced by off-axis translation which must be distinguished from time-dependent neutrino spectral changes intrinsic to the beam. On-axis beam monitoring, in particular, is critical because the DUNE far detector sees that beam. The on-axis spectrum must be modeled and used for the extraction of the oscillation parameters at the far detector.

There are many valuable lessons for DUNE/LBNF in the NuMI experience. One of those lessons is that unexpected things happen to neutrino beamline elements that can take them well outside the typical error tolerance. One example of this at NuMI was degradation in the target due to broken upstream target fins. This was observed and diagnosed prior to target autopsy by the change in the observed near detector neutrino event spectrum [126]. Figure A.37 shows MINOS near detector data in bins of reconstructed neutrino event energy. Within each bin are points representing successive periods of the data taking run. A time-dependent shift in the three peak bins, i.e., a change in the spectral shape, is obvious in the plot. Another example of a significant and noticeable change in the beam spectra at NuMI was caused by magnetic horn tilt due to degradation of a supporting washer [127]. Yet another significant wiggle in the beam spectral shape has been observed in the MINERvA and NOvA medium energy run [62]. Notably, this wiggle is not as significant in the off-axis data taken by the NOvA near detector as it is for on-axis MINERvA. MINERvA studies indicate the observed spectral shift is best modeled by a shifted horn position or a slight change in the inner horn radius relative to the expected value.

2020 JINST 15 T08008

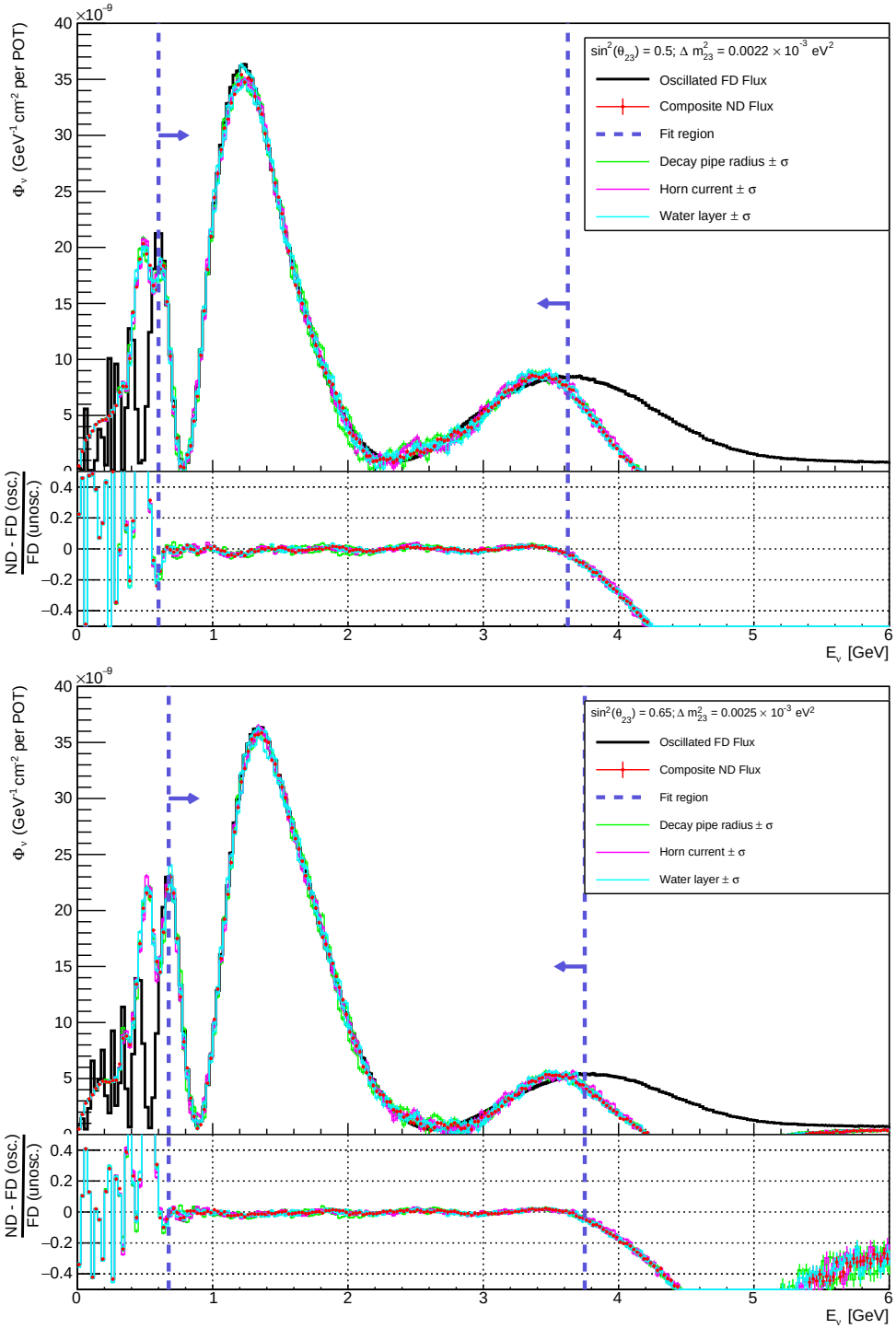

Figure A.36. Linear combinations of off-axis fluxes giving far-detector oscillated spectra for a range of oscillation parameters. The FD oscillated flux is shown in black, the target flux is shown in green, and the linearly combined flux obtained with the nominal beam MC is shown in red. Systematic effects due to 1 σ variations of the decay pipe radius (green), horn current (magenta) and horn cooling water layer thickness (teal) are shown.

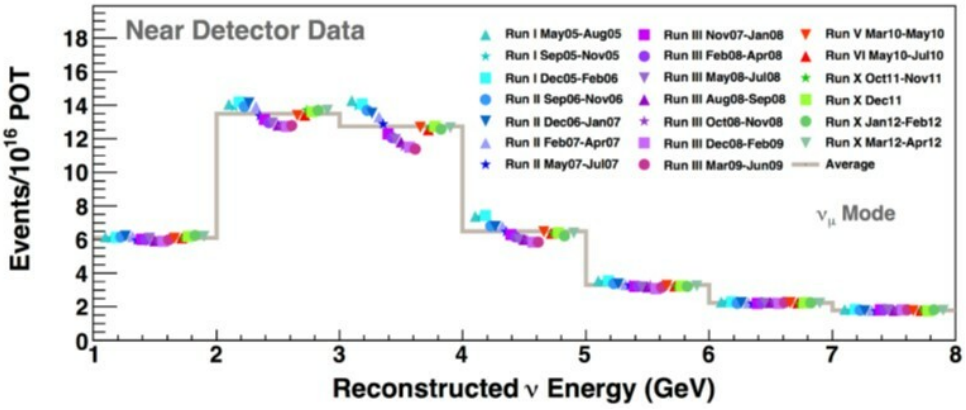

Figure A.37. The low energy run MINOS event rate as a function of neutrino energy broken down in time. From [126].

Given the past experience from NuMI, it is thought to be critically important that the DUNE ND monitor and track the beam spectrum over time. ArgonCube and the MPD will make on-axis neutrino beam spectrum measurements when they are located on-axis. There are two broadly different concepts under discussion for how to monitor the on-axis beam when ArgonCube and the MPD move off-axis as required by the DUNE-PRISM program. One concept is to have a dedicated on-axis beam monitor that is capable of measuring the neutrino beam spectrum as a function of time. Such a capability would require target mass and a magnet or range stack with tracking to measure the momentum of muons arising from CC ν_μ interactions. The other concept assumes a dedicated on-axis neutrino interaction rate monitor. Both the on-axis rate monitor and the off-axis spectrometer would each track beam stability. In the case of an observed instability of either the rate or the off-axis spectrum, ArgonCube and the MPD would move back on-axis to make a spectrum measurement. It is likely the DUNE-PRISM run plan would include intermittent on-axis measurements as well regardless of observed instabilities. Since the first concept involves a magnet or large range stack, it is likely to be more expensive to implement than the option that makes use of the dedicated rate monitor on-axis. On the other hand, the latter option with intermittent on-axis spectral measurements involves additional movements of the large, DUNE-PRISM detectors, precision comparison of spectral measurements separated in time with detectors that have moved in the interim, and accepting the risk that rate and off-axis spectral monitoring are both less sensitive to some changes in the beam than on-axis spectral monitoring. Figure A.38 provides an illustration, for a small subset of relevant beam parameters, of the differing sensitivities of integrated rate monitoring as compared to spectral monitoring of the beam. Additional studies are in progress.

The reference design described below in section A.6.2 assumes the beam monitoring is done with a dedicated on-axis magnetic spectrometer. The device described is a capable beam monitor in that it has the required mass and muon momentum resolution as will be shown in section A.6.2.4. In addition, the on-axis spectrometer described below has capabilities that go beyond beam monitoring, which are useful for building confidence in the flux model and providing information that is potentially useful for the evolution of the neutrino interaction model. Other concepts, including one that utilizes an on-axis rate monitor, are under consideration.

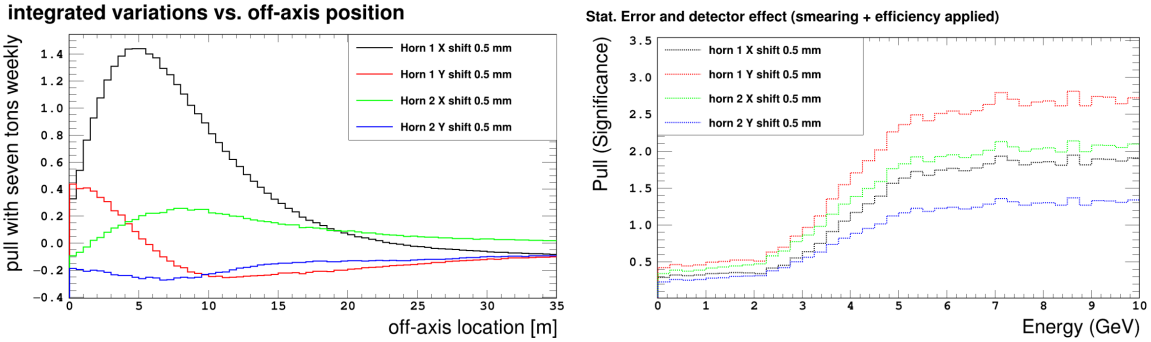

Figure A.38. Comparison of rate monitoring and spectral monitoring of the neutrino beam for 1-sigma shifts of the horn positions. On the left is shown the significance of the variation in the observed rate for one week of running with a seven ton fiducial mass detector. It is shown as a function of off-axis angle (including zero, i.e., on-axis). On the right is shown the significance of the shape change as a function of energy for one week of running with an 8.7 ton fiducial mass on-axis spectrometer.

A.6.2 Three-dimensional projection scintillator tracker spectrometer

SAND consists of an active target core of scintillator called the 3DST surrounded by TPCs and an ECAL in a 0.5 T magnetic field. This system has two main goals in the context of the larger ND complex. First, SAND functions as an on-axis, high mass target and muon spectrometer that is capable of producing a statistically significant neutrino beam spectrum measurement in a short period. This dedicated, on-axis beam monitoring will be important in light of the movement of ArgonCube and the MPD within the context of the DUNE-PRISM program. Second, the 3DST can measure neutrons on an event-by-event basis, including those at a lower neutron kinetic energy than those seen by the other components of the ND. The inclusion of neutrons in the event reconstruction on an event-by-event basis is a powerful new tool that can be used for flux measurements and to probe neutrino interaction physics and modeling.

The 3DST is a fully active plastic scintillator detector made up of optically isolated 1 cm^3 cubes [128]. The cubes are read out by wavelength shifting (WLS) fibers along 3 orthogonal axes providing three two-dimensional projections that yield effective three-dimensional reconstruction.

The 3DST is dense enough to provide a large statistics sample with reasonable containment of hadrons and photons from neutrino interactions. The high statistics and granularity of the 3DST will allow for timely beam monitoring, flux determination via different methods (with charge separation), and the study of many different neutrino interaction morphologies. The sub-ns timing resolution provides the capability to include neutrons in the event reconstruction via Time-of-Flight (ToF) with a reasonably high efficiency.

To date, neutrino experiments have been largely blind to neutrons on an event-by-event basis. This is not ideal, in part because the neutron content of neutrino and antineutrino interactions differ, and in part because neutrons can carry a significant part of the outgoing energy and momentum of a neutrino interaction which compromises the reconstruction of events with missing neutrons. Preliminary studies show the 3DST is likely to be able to measure neutrons to a lower neutron KE (KE_n) than the other component detectors of the ND and pursue event-by-event analysis with fully reconstructed final state particles, including neutrons. The addition of neutrons in event

reconstruction will open the avenue to improved single transverse variable analyses that are expected to yield an improved neutrino energy resolution for flux (particularly antineutrinos) determination and for studies that may aid the evolution of the neutrino interaction model.

The 3DST uses the same technology as the SuperFGD detector that is being constructed for the T2K ND upgrade [129]. The two detectors are functionally identical, though somewhat different in size. The SuperFGD will be installed 2021 and will act effectively as a prototype for the larger 3DST in the DUNE ND.

A.6.2.1 Detector configuration

The 3DST detector concept is shown in figure A.39. The scintillator composition is polystyrene doped with 1.5% of paraterphenyl (PTP) and 0.01% of POPOP. After fabrication, the scintillator surface of the cubes is etched with a chemical agent that results in the formation of a white, reflecting polystyrene micro-pore deposit over the scintillator. Three orthogonal through holes of 1.5 mm diameter are drilled in the cubes to accommodate WLS fibers. This novel geometry provides full angular coverage for particle produced in neutrino interactions. The momentum threshold for protons is about 300 MeV/c (if at least three hits are requested).

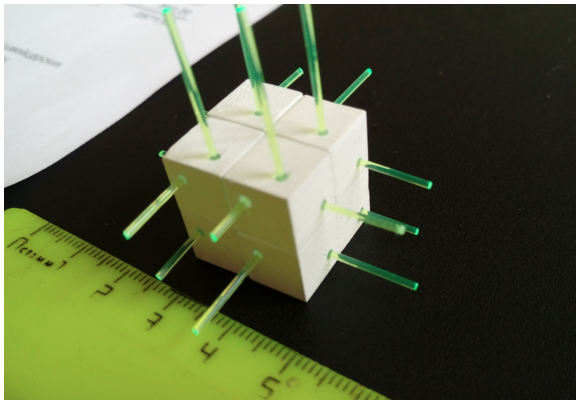

Figure A.39. A few plastic scintillator cubes assembled with WLS fibers.

The 3DST and surrounding elements are shown in figure A.40. The size of the 3DST detector is under discussion. Detectors of size 2.4×2.4×2.0 m^3, 3.0×2.0×2.0 m^3, and 2.0×2.0×2.0 m^3 have been used in different studies. The primary considerations that drive the size are space, statistics, and neutron containment.

The 3DST is surrounded by low mass trackers to measure the kinematics of charged particles produced but not stopping in 3DST, and an ECAL to identify and reconstruct photons and electrons exiting the 3DST. The trackers are TPCs in the reference design. Straw tube trackers are also under consideration. All the detectors will be immersed in a 0.5 T magnetic field provided by the KLOE magnet. The TPCs are envisioned to be similar to those being constructed for the T2K ND280 detector upgrade, described in [129]. They are approximately 80 cm thick and use a gas mixture of Ar-CF4-iC4H10 (95% - 3% - 2%).

The KLOE magnet and ECAL already exist and have been used successfully for many years in a running experiment. The work and infrastructure necessary to transport the devices to Fermilab, as well as to install and operate them in the ND hall are under study.

2020 JINST 15 T08008

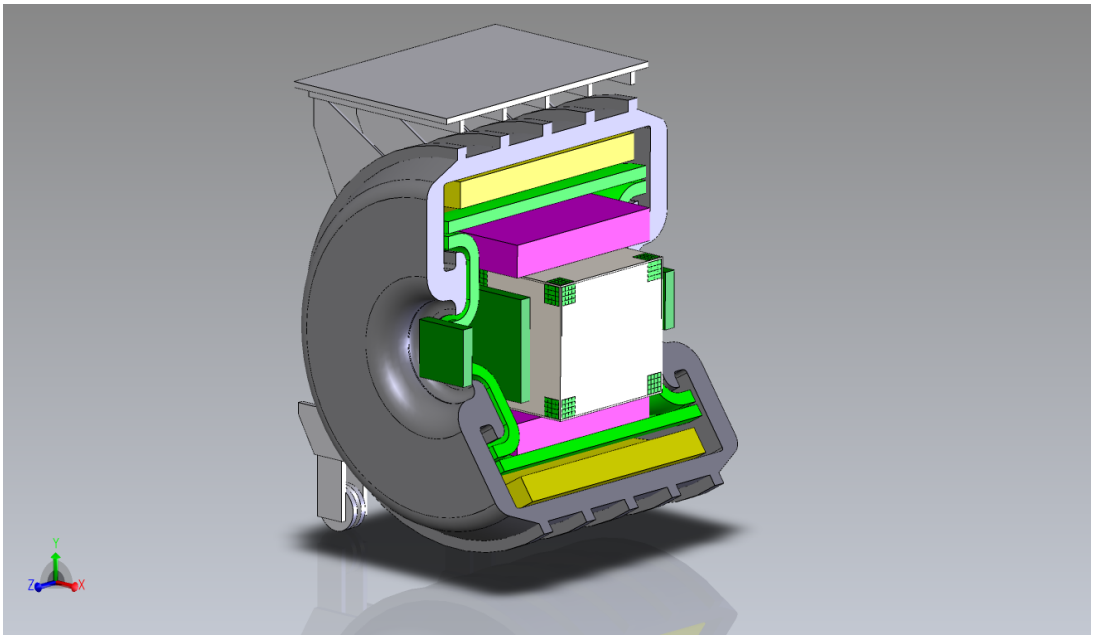

Figure A.40. The 3DST inside the KLOE magnet. The drawing shows the 3DST in the center (white), TPCs (orange), ECAL (green), magnet coil (yellow), and the return yoke (gray).

A.6.2.2 3DST detector performance

The performance of devices built on the 3DST concept have been tested in several test beams at CERN [130]. A small prototype of $5 \times 5 \times 5$ cubes collected data in the T10 test-beam area at CERN in 2017, with the goal of characterizing the response of the plastic scintillator cubes. The detector was instrumented with 75 WLS fibers (1 mm diameter Y11(200) Kuraray S-type of 1.3 m length). One end of the fiber was attached to a photosensor while the other end was covered by a reflective Al-based paint (Silvershine). The photosensors in the beam test were Hamamatsu MPPCs 12571-025C with a 1×1 mm^2 active area and 1600 pixels. The data were collected with a 16-channel CAEN digitizer DT5742 with 5 GHz sampling rate and 12-bit resolution.

The average light yield was about 40 p.e./MIP in a single fiber, and the total light yield from two fibers in the same cube was measured on an event-by-event basis to be about 80 p.e., as expected. The light cross-talk probability between a cube fired by a charged particle and a neighboring cube was studied. The light measured in the neighboring cube was about 3.4% of the light collected from the fired cube. The timing resolution for a single fiber was measured to be ~0.95 ns. If the light of a cube is read out by two WLS fibers, the timing resolution becomes better than 0.7 ns and would improve further if the light collected by all the three WLS fibers is taken into account. In figure A.41 the light yield and the time spectra obtained from two fibers reading out the light in the same cube are shown.

In the summer of 2018, a prototype made of 9,216 cubes with a size of 8×24×48 cm^3 collected data in the CERN T9 test-beam line. A different electronic readout was used, which was based on the CITIROC chip used in the Baby MIND experiment. Preliminary results confirmed the light yield performances of the 2017 test-beam data. A more detailed analysis of the data is currently ongoing. Some event displays are shown in figure A.42.

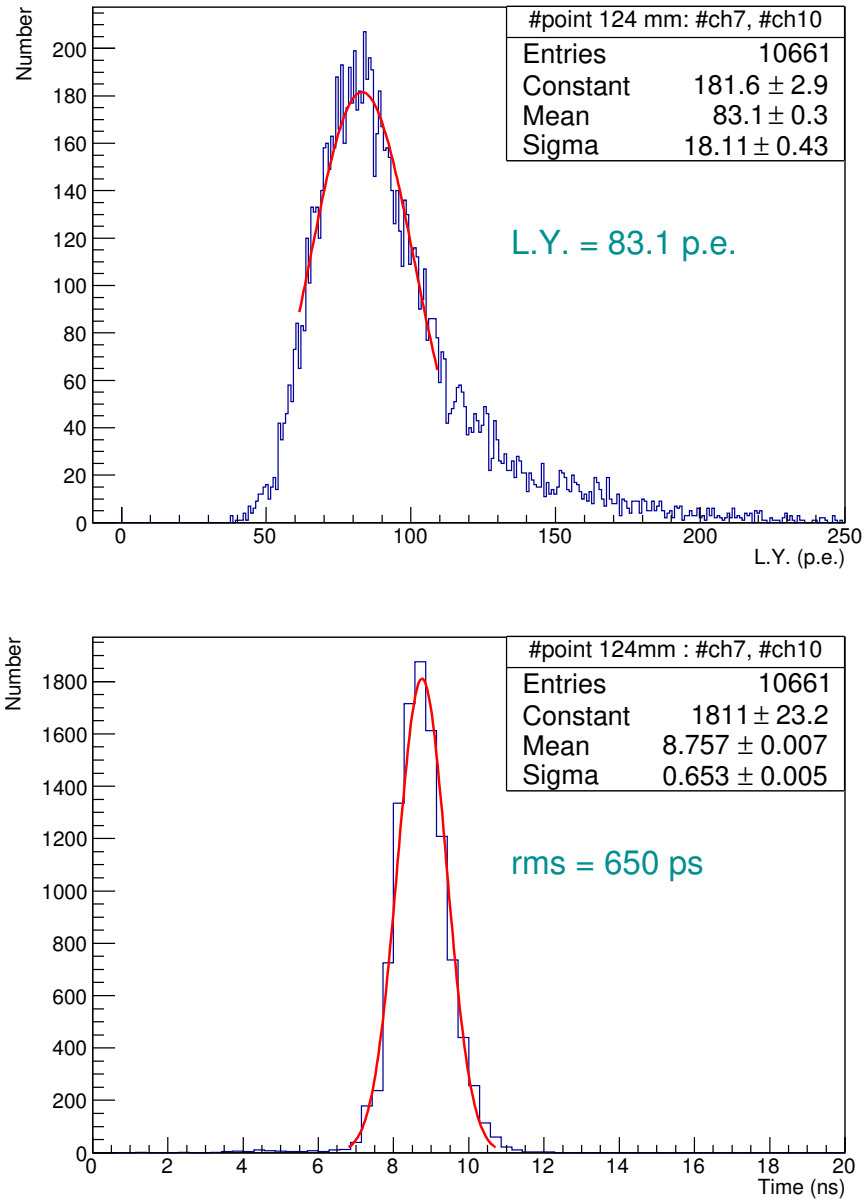

Figure A.41. Charge and time spectra for a single 3DST cube. Charge signal is a sum from two fibers, the time is an average time between two fibers.

A.6.2.3 Expected statistics

The default size of the 3DST, 2.4×2.4×2.0 m^3, gives a total target mass of 12 metric tons. Implementing a generic veto region around each side of the detector of 10 cm, gives a fiducial mass of 8.7 tons. Table A.3 gives the number of events expected per year in the FV of such a 3DST detector. The numbers given in the table are assuming the 80 GeV, 3 horn, optimized LBNF beam flux and 1.46×10^{21} POT/year.

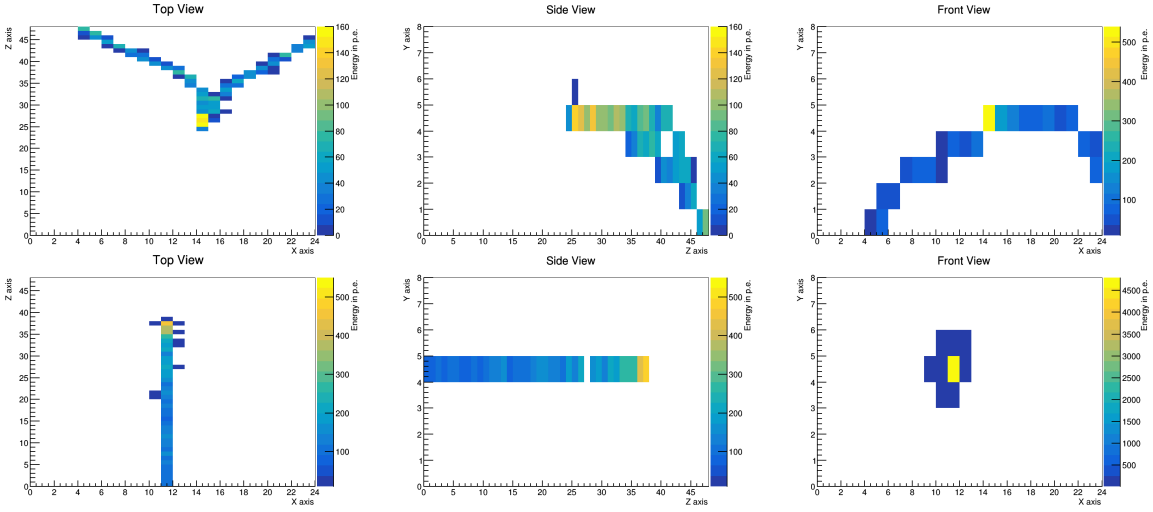

Figure A.42. Event displays showing the three two-dimensional projections of energy from a photon conversion (top) and a stopping proton (bottom). From data collected at the 2018 test beams at the CERN T9 area.

Table A.3. This table summarizes the projected event rates per year for a 2.4 m × 2.4 m × 2.0 m 3DST detector, assuming the 80 GeV, three horn, optimized LBNF beam. A 10 cm veto region at each side was required.

Channel	ν mode	$\bar{\nu}$ mode
ν_μ CC inclusive	13.6×10^6	5.1×10^6
CCQE	2.9×10^6	1.6×10^6
CC π° inclusive	3.8×10^6	0.97×10^6
NC total	4.9×10^6	2.1×10^6
ν_μ-e$^-$ scattering	1067	1008
ν_e CC inclusive	2.5×10^5	0.56×10^5

A.6.2.4 Beam monitoring

SAND is a capable on-axis beam monitor. The plot in figure A.43 shows the number of events seen in 2.5 days of nominal running across the face of the 3DST. The beam center can be measured to 11 cm in that time. The right plot of figure A.38, previously shown, shows the significance of the change in the reconstructed neutrino energy spectra as a function of reconstructed energy for one week of nominal running for 1σ shifts in the transverse position of horns 1 and 2. The leptonic and hadronic energies were smeared with a parameterization appropriate for SAND.

A.6.2.5 Neutron detection performance

The MINERvA experiment demonstrated the ability of measuring neutrons produced in neutrino interactions with a plastic scintillator detector [131]. The 3DST should be able to do this far better than MINERvA because of its high granularity and exquisite timing resolution (both much better than MINERvA).

2020 JINST 15 T08008

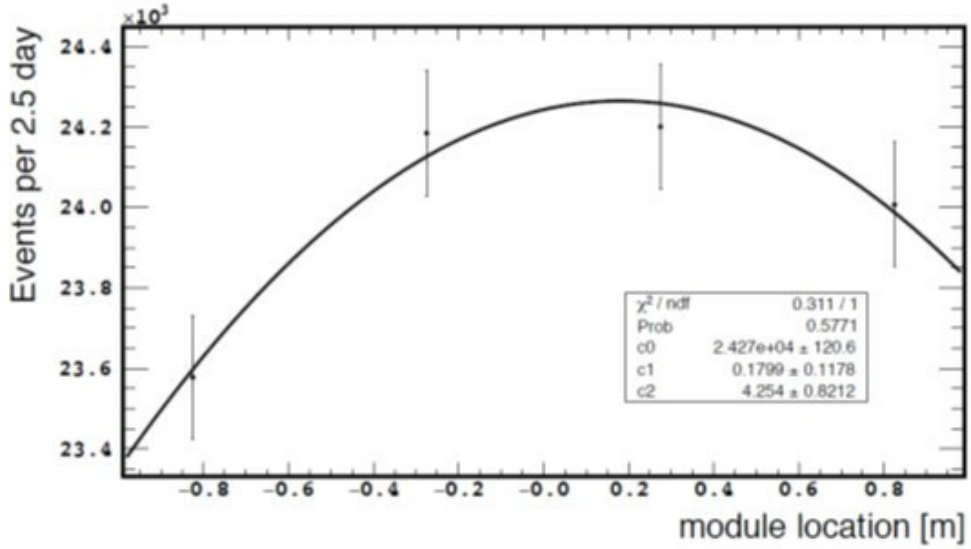

Figure A.43. Beam center determination after 2.5 days of running with SAND.

Neutron scattering can be seen clearly in 3DST simulations. Figure A.44 shows an example of an $\overline{\nu}_\mu$ CC single charged pion interaction. The neutron-induced energy deposition due to proton recoil can be seen apart from the vertex region. Inspired by MINERvA, recent studies (described below) have shown that the 3DST can tag the presence of neutrons as well as determine the neutron energy via time-of-flight. This capability is likely to be helpful for improving both neutrino and antineutrino interaction models, and of potential use when faced with "unknown unknown" sources of systematic uncertainties. The argon-based detectors in the ND complex are expected to have some ability to detect neutrons, but studies indicate the sensitivity will be limited to regions of relatively high neutron kinetic energy (due to backgrounds and event confusion that arise at lower neutron kinetic energy where the considered event time window must be larger). The 3DST will be sensitive to neutrons down to significantly lower kinetic energy.

The neutron measurements in the 3DST are on carbon and likely will have limited direct bearing on tuning the neutron model for argon. However, the analysis of events including neutrons on an event-by-event basis may lead to improvements in the neutrino interaction model for carbon. Insights and neutrino interaction model improvements on carbon may inform the model used for argon. A notable example of this from the recent past is the 2p2h process, which is included in many current interaction models for argon even though the evidence for multi-nucleon processes was extracted from data taken on hydrocarbon targets.

Since work to date has focused on establishing the ability and quality of the neutron detection in the 3DST (as shown below), detailed studies making use of the neutron reconstruction in simulated analyses are in an early stage. Simulations show the selection of $\overline{\nu}_\mu$ CCQE events with small missing transverse momentum, using a technique described in [132], yields a sample with a substantially improved energy resolution. This sample consists of events with relatively small nuclear effects which is useful for flux determination and studies of nuclear effects in neutrino interactions. It is also expected that neutron multiplicity can be used as an indication that multi-nucleon interactions

or large FSI effects are present, which may be helpful for selecting events particularly useful for exploration of the interaction model.

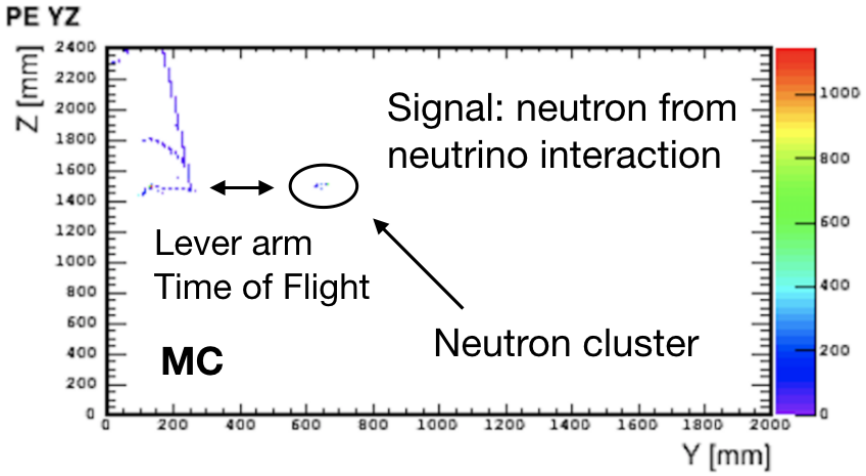

Figure A.44. An example of the antineutrino interaction in a 2.4×2.4×2.0 m^3 3DST. The number of photoelectrons (PE) is plotted. An isolated cluster of hits corresponds to a neutron indirect signature produced by the antineutrino interaction.

With a 2.4×2.4×2.0 m^3 3DST detector, figure A.45 shows the reconstructed neutron energy residual for 100 MeV kinetic energy neutron using time-of-flight with a lever arm (distance between neutron hit and neutrino vertex) larger than 0.5 m and smaller than 1 m. This study was conducted with a neutron particle gun simulation. The tail is due to both the timing resolution as well as the mis-reconstructed neutron flight distance due to non-visible interactions like elastic scattering with carbon. The neutron energy resolution is about 18%.

Neutrons produced by neutrino interactions happening outside the 3DST FV (out-FV), such as in the ECAL, Magnet, front detector, and rock can act as a background to the neutron signal from neutrino interactions. A simulation study was performed to understand the significance of background. In this study, the SAND detector was place in an underground alcove and significant dead material was placed upstream. The FV was taken to be an inner core of 1.0×1.0×1.0 m^3 of scintillator inside a 3DST of size 2.0×2.0×2.0 m^3. Neutrino beam spills of separation 1.3 s were used. Within each spill, the neutrinos were distributed uniformly in time. For each neutrino interaction occurring inside the FV, the earliest neutron-induced hit leaving an energy greater than 0.5 MeV in one cube was recorded. This threshold is thought to be conservative for the 3DST system because of the large light yield expected. If that hit was from the neutrino interaction vertex, it was considered a signal neutron-induced hit. On the other hand, if that hit was created by a particle from outside the FV, it was considered a background neutron-induced hit. Figure A.46 shows the time difference between the neutrino interaction vertex time (t_{vtx}) and the following earliest neutron-induced hit time (t_{neutron}). Note that a pure signal neutron sample can be obtained by cutting on ($t_{\text{neutron}} - t_{vtx}$).

2020 JINST 15 T08008

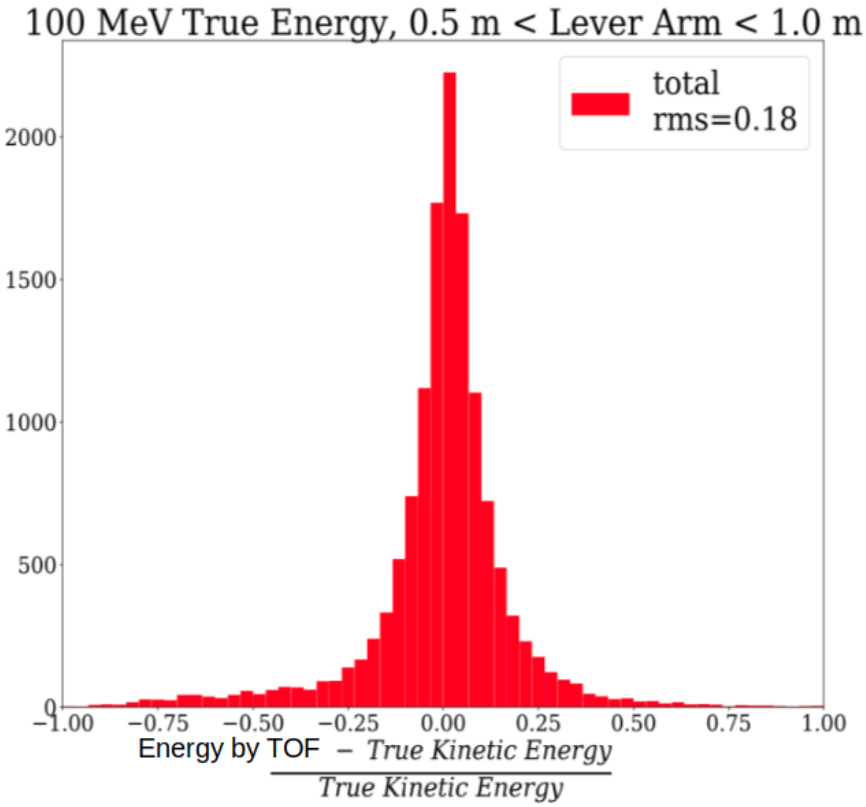

Figure A.45. Reconstructed neutron energy residual with lever arm larger than 0.5 m and smaller than 1 m for 100 MeV for a 2.4×2.4×2.0 m^3 3DST detector.

It is likely to be possible to veto CC and NC interactions with pions in the materials surrounding the 3DST. Such a veto would reduce backgrounds from neutrons generated by these out-FV events. In this study, such a veto was not used. This will be investigated in the future.

To quantify the background, the purity is defined as the ratio of events where the first neutron-induced hit by time is from the signal vertex to all events which have a neutron-induced hit in the FV. Figure A.47 shows the purity in time - lever arm space. Lines indicate regions populated by neutrons with different kinetic energies.

The reconstructed energy resolution in the same (time, lever arm) 2D space was studied. For this work, the time was smeared by 0.58 ns, corresponding to a per fiber time resolution of 1 ns (the documented performance in the CERN test beam is 0.9 ns). Though higher light yield can help improve the time resolution, this effect has not been taken into account. Figure A.48 shows the reconstructed-by-ToF neutron energy resolution. In general, ∼ 20% energy resolution can be reached with most of the lever arm and time windows, in the region selected by the background cut.

A.7 Meeting the near detector requirements

As discussed in sections A.2 and A.1, the DUNE ND complex has many missions, and the components of the ND address these missions in a complementary fashion. In this section we first discuss the key overarching requirements driving the ND complex. We then discuss some thought

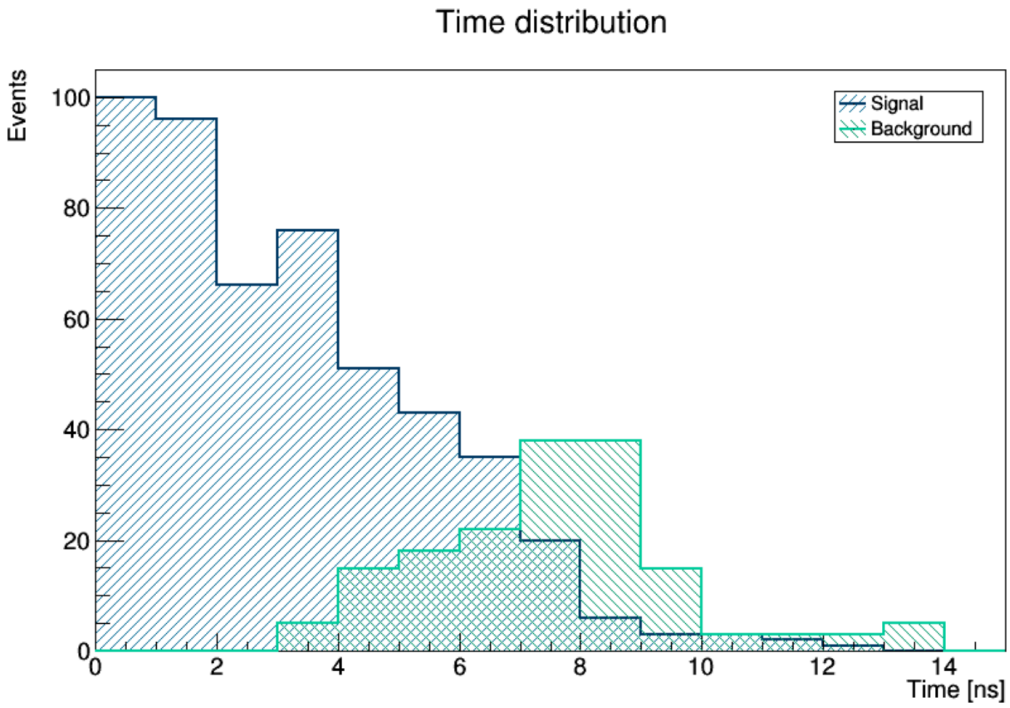

Figure A.46. Time difference between the neutrino interaction vertex time inside the 1.0×1.0×1.0 m^3 FV core of the 3DST and the earliest neutron-induced hit time. The neutron-induced hit leaves at least 0.5 MeV in a single cube. The neutron-induced background hits arise from neutrons produced in neutrino interactions outside the FV.

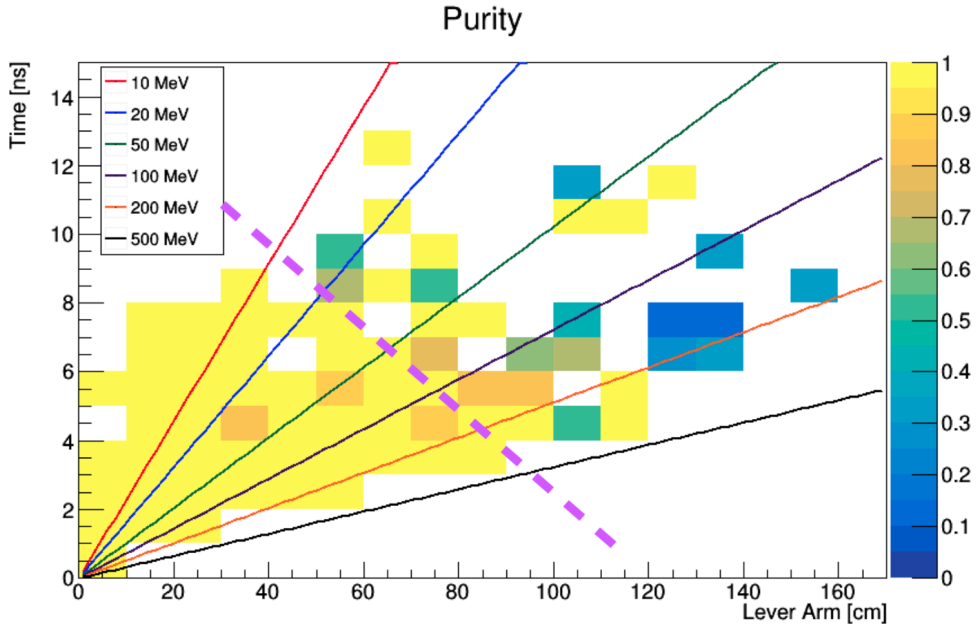

Figure A.47. Purity of the neutron-induced hit in the (time, lever arm) space. The dashed line corresponds to the cut required to select an almost 100% pure sample of signal neutrons. The solid lines are theoretical curves for neutrons with different kinetic energies. Note that this study was performed with a total volume of 2×2×2 m^3. See text for details.

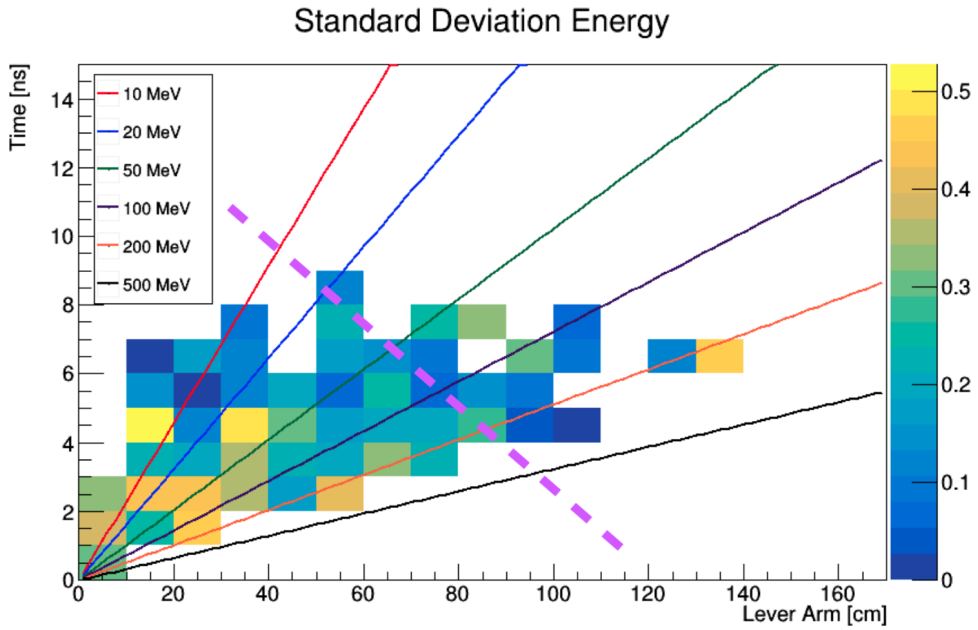

Figure A.48. Energy resolution of the neutron candidates in the (time, lever arm) space. The dashed line corresponds to the cut required to select an almost 100% pure sample of signal neutrons. The solid lines are theoretical curves for neutrons with different kinetic energies. Note that this study was performed with a total volume of 2.0×2.0×2.0 m^3. See text for details.

experiments and case studies that illustrate how different parts of the complex work together. These case studies naturally suggest more detailed capabilities, performance statistics, and technical requirements that we are in the process of tabulating. Most of these require additional studies before numerical values can be tabulated.

A.7.1 Overarching requirements

- **Predict the neutrino spectrum at the FD:** the ND must provide a prediction for the energy spectrum of ν_μ, $\bar{\nu}_\mu$, ν_e and $\bar{\nu}_e$ at the FD. The prediction must be provided as a function of the oscillation parameters and systematic uncertainties must be small enough to achieve the required CP coverage. This is the primary requirement of the DUNE ND.

- **Measure interactions on argon:** the ND must measure neutrino interactions on argon to reduce uncertainties due to nuclear modeling. The ND must be able to determine the neutrino flavor and measure the full kinematic range of the interactions that will be seen at the FD.

- **Measure the neutrino energy:** the ND must be able to reconstruct the neutrino energy in CC events and control for any biases in energy scale or resolution, keeping them small enough to achieve the required CP coverage. These measurements must also be transferable to the FD.

- **Constrain the cross-section model:** the ND must measure neutrino cross-sections in order to constrain the cross-section model used in the oscillation analysis. In particular, cross-section mismodeling that causes incorrect FD predictions as a function of neutrino flavor and true or reconstructed energy must be constrained well enough to achieve the required CP coverage.

2020 JINST 15 T08008

- **Measure neutrino fluxes:** the ND must measure neutrino fluxes as a function of flavor and neutrino energy. This allows for neutrino cross section measurements to be made and constrains the beam model and the extrapolation of neutrino energy spectra from the ND to the FD.
- **Obtain data with different fluxes:** the ND must measure neutrino interactions in different beam fluxes (especially ones with different mean energies) to deconvolve flux and cross section, verify the beam model, and guard against systematic uncertainties on the neutrino energy reconstruction.
- **Monitor the neutrino beam:** the ND must monitor the neutrino beam energy spectrum with sufficient statistics to be sensitive to intentional or accidental changes in the beam that could affect the oscillation measurement.

A.7.2 Event rate and flux measurements

The three most straightforward flux measurements are described here. Other powerful but more complex techniques are described in section A.4.

A.7.2.1 CC ν_μ and $\overline{\nu}_\mu$ interactions

Each core component of the ND complex will have large data samples with which to constrain the flux model: ArgonCube will accumulate 3.7×10^7 CC ν_μ events per year (on axis, less when off axis); the 3DST will see 1.4×10^7 CC ν_μ per year on axis; and the HPgTPC will see 1.6×10^6 CC ν_μ events per year (on axis, less when off axis).

A.7.2.2 Intrinsic electron neutrino and antineutrino fluxes

The intrinsic ν_e and $\overline{\nu}_e$ component of the beam is discussed in section A.4.4. This is an important component to quantify in the ND since it represents an irreducible background for the appearance oscillation analysis at the FD. The number of CC ν_e events expected in the ND per year (on axis) are 6.7×10^5, 2.5×10^5, and 2.5×10^4 for ArgonCube, the 3DST, and the HPgTPC, respectively. The primary background comes from NCπ° production. The systematics are dominated by the flux model and the interaction model (which enters in the background subtraction). In the past, statistics has been a limitation. That will not be the case for DUNE ND. With large samples, ArgonCube and the 3DST each will measure this component of the beam fairly quickly with somewhat different systematic errors. Although accumulating statistics more slowly, the HPgTPC will provide the best overall measurements the ν_e and $\overline{\nu}_e$ components of the beam. Photons mostly do not convert in the gas. This eliminates the primary background to electron (anti)neutrino identification and the accompanying interaction model uncertainty in the background subtraction. In addition, the HPgTPC has a magnetic field that allows for the sign separation of ν_e and $\overline{\nu}_e$.

A.7.2.3 Neutrino-electron scattering

This process and estimates of the ND performance measuring the flux using this technique is discussed in sections A.4.1 and A.5.2.8. Measuring the flux using this process is a critical ND mission because it is independent of nuclear effects. This is a rare process that can be used by

2020 JINST 15 T08008

both ArgonCube and SAND components of the ND to measure the neutrino flux. The target nucleus is irrelevant for neutrino-electron scattering. The measurement places a premium on the overall target mass (for statistics) as well as electron energy and angular resolutions. The primary backgrounds are CC interactions of intrinsic beam ν_e and NCπ° interactions. ArgonCube will do this measurement well as indicated by the results of a study shown in figure A.16. Also, that study shows a MINERvA-like scintillator detector can do the measurement fairly well. SAND will have better angular resolution than the detector used in the study. Note that the detector and reconstruction systematic errors will be different for the two very different detectors. For such an important measurement, the duplication is good, and with many uncorrelated errors it may be possible to combine the ArgonCube data set with that from SAND for a somewhat improved constraint.

A.7.3 Control of systematic errors

A.7.3.1 PRISM program

The PRISM program of on- and off-axis measurements is an essential component of the ND complex and plays a key role in reducing systematic uncertainties on neutrino cross-sections and reconstructed energy. PRISM is described in section A.5.4.

A.7.3.2 Absolute muon energy scale

The ND complex must provide knowledge of the absolute muon energy scale in the LAr ND with sufficient accuracy to meet the oscillation physics requirement and the ancillary low-nu capability. The complex will utilize MPD magnetic field survey information, as well as K_s and Λ decays to charged hadrons within the MPD, to establish the charged particle momentum scale in the MPD. The measurement will be translated to the LAr ND by tracking and momentum analyzing, in the MPD, cosmic ray muons going through the MPD into the LAr ND. The LAr ND will then measure the momentum of the muons (particularly stopping muons) by range and multiple coulomb scattering (MCS) to establish its muon momentum scale and verify the reconstruction and detector simulation.

The momentum scale will be translated to the FD by measuring and comparing the range and MCS of stopping tracks in the data and the simulation.

A.7.3.3 Hadronic energy scale; hadronic response of the LArTPC

The ND complex must calibrate the response (energy measured vs true energy) of the LAr ND and FD to the hadronic system in neutrino interactions with an accuracy to meet the oscillation physics goals. The complex will utilize a simulation benchmarked against the single particle response measured in ProtoDUNE as a baseline. It is expected that the response will differ for different particle species and will not be constant as a function of energy. Additional calibration is needed due to the imperfectly known particle spectra in neutrino interactions, and the confusion that the LAr ND and FD will experience in identifying the composition of particles in the final state. The ND complex will accomplish the calibration by first observing ν_μ-CC interactions in the MPD. The MPD will identify the protons, charged pions and photons in the final state, and precisely reconstruct their energy via curvature in the magnetic field and, for photons, energy deposition in

2020 JINST 15 T08008

the calorimeter. The MPD will also observe, statistically, the energy going into neutrons using time of flight.

The muon kinematics will then be used to select one or more semi-inclusive set of events occurring in the LAr ND and MPD that have identical hadronic final states. A comparison of the reconstructed hadronic energy in the LAr ND with the precisely measured MPD calibrates the response and establishes the hadronic energy scale in LAr. It will also be possible to take the reconstructed data events from the MPD and simulate them in the LAr to compare to the actual events in the LAr. This will serve as a cross-check and as a way of studying the response. For example, one could drop any primary neutron information from the MPD reconstructed events and simulate the rest in LAr ND to compare to the LAr ND data as a way of understanding the amount of neutron energy seen by the LAr ND.

A.7.3.4 Beam monitoring

Previous experience with the NUMI, JPARC, and Booster neutrino beams has shown that DUNE must prepare for changes in the beam that occur on timescales as short as a few days but that are not readily detected by primary and secondary beam monitors. Sudden changes in the beam have the potential of polluting the PRISM program if they occur when the LAr ND and MPD are taking data at off-axis locations. The ND complex addresses this problem with the SAND detector which will continuously measure the ν_μ and $\bar{\nu}_\mu$ energy spectrum on-axis.

A.7.3.5 LArTPC energy resolution

The PRISM measurement program demands that the energy resolution of the LAr ND and FD be as similar as possible, and that any differences can be understood and corrected for.[6] The resolution can be constrained using a similar approach as followed for the hadronic response.

A.7.3.6 LAr ND acceptance

Neutrino flavor change due to oscillation occurs over a broad energy range which demands that the ND complex is able to achieve a broad energy coverage. The LAr ND has acceptance limits (relative to the FD) at large muon angle ($\theta > 25$ deg) and high hadronic energy due to its limited size. Moreover, there is a strongly energy dependent and deep acceptance dip for $1.0 < E_\mu < 1.5\,GeV/c$ due to dead material between the active portions of the LAr ND and MPD TPC. The experiment must understand these features of the LAr ND event sample in order to use it to make predictions for the FD.

To address this shortcoming the MPD must have a nearly 4π acceptance for charged tracks and photons, a high tracking efficiency, and the ability to reconstruct events with high E_ν. A comparison of MPD and LAr ND event rates as a function of kinematic variables will verify the LAr ND acceptance model.

A.7.3.7 LAr detection thresholds

The energy threshold for detecting charged particles in LAr will be verified using the MPD in a way that is similar to the more general LAr ND acceptance study described above.

[6] In fact this is true if the experiment only makes on-axis measurements.

A.7.3.8 Managing pile-up

At the location of the ND, the LBNF beam is expected to generate approximately 1 neutrino interaction per 10 tons per 10 μs spill. Each of the core detectors in the ND complex can eliminate most of the pile-up background with timing from optical elements. For ArgonCube, it is estimated that there will be approximately 0.5 neutrino interactions per spill per ArgonCube module. Prompt scintillation light from the argon detected in ArCLight detectors or something similar is used to provide t_o and separate events (both connected and disconnected parts of the event). For the HPgTPC, an estimate based on a significantly (15×) more massive magnet than the superconducting option presented in section A.5.3.1.3 suggests there will be approximately 75 tracks per 10 μs spill from interactions in surrounding materials passing through the TPC. The excellent <10 ns timing resolution of the ECAL surrounding the TPC will be used to provide a t_o and to define a time window for pileup rejection. Similarly the exquisite (sub-ns) time resolution of the cubes in the 3DST can be used to generate a narrow window in time around neutrino interactions and limit the potential for overlapping events.

A.7.3.9 Energy carried by neutrons

The ND complex must measure or otherwise account for the neutrino energy that goes into neutrons because much of that energy ends up being undetectable by a LArTPC. The fraction of hadronic energy carried by neutrons is sizable and it also differs between ν_μ and $\bar{\nu}_\mu$: 20% vs 40% for the flux peak. To meet the oscillation physics goals these fractions must be known sufficiently well.

The complex will approach this challenge in multiple ways. First, the PRISM measurement program is required to map the relationship between true and reconstructed energy using inclusive CC scattering. These measurements are sensitive to cumulative mismodelings but may have trouble pinning down their origin. To augment the PRISM program, the MPD and SAND are required to measure the energy carried by neutrons using calorimetry and time of flight. The MPD has the advantage of measuring neutron production off of an Ar target, but the disadvantage of doing so with lower statistics than SAND. The MPD measurement is also challenging due to the interaction rate in its calorimeter and the composition of the calorimeter driven by its multi-role nature. The advantage of SAND is in finer granularity and a better ability to reconstruct neutron energy on an event by event basis.

A.7.3.10 ν_e-CC rate and π^0/γ background

Neutral current events with a final state π^0, or a single γ, are a potentially problematic background to the ν_e and $\bar{\nu}_e$ appearance measurements. The ND complex will address this background by using the MPD to precisely measure the rate of ν_e (and $\bar{\nu}_e$) CC interactions as a function of energy and other kinematic variables. The measurement will have relatively small π^0 and γ backgrounds because photons have a low conversion probability in the MPD TPC. The LAr ND will make a similar measurement. The efficiency and background of that measurement will benchmarked using the data from the MPD.

Appendix B

ND hall and construction

Figure B.1 shows the current design of the underground hall as required for the ND construction concept. The underground hall must house the detector components and allow for the required movement. The layout shows the space required for the detector, safety, and egress. This is work in progress.

The overall construction method places requirements on the conventional facilities. The primary access shaft is large enough for lowering the pressure vessel and the magnet coils. The LAr cryostat is shown in its construction position near the main shaft. The multipurpose detector and the LAr detector are also shown in the on-axis position. Since the 3DST detector does not need to move for DUNE-PRISM, it is shown in a dedicated alcove downstream of the LAr and multipurpose detectors.

The overall method of detector construction must be consistent with the construction concepts of each of the elements as outlined in previous sections. The construction method must also allow for parallel activities on major components and reduce demand on individual facilities. The underground hall will be the last facility to be completed. Therefore, insofar as possible, components must be constructed elsewhere and lowered as large assemblies.

The current assumptions for the overall construction involving the major components are listed below. Only the major components are considered, as they place the main constraints on the conventional facilities.

- The primary access shaft diameter is sufficient to accommodate the lowering of the pressure vessel and magnet coils separately. The coils and pressure vessel are constructed on the surface and lowered. This allows for remote and parallel construction.
- Two transport frames and moving systems are built in the cavern. These frames will be used to support and move the multipurpose detector and the LAr detector.
- Articulated carriers are built to carry services supporting the moving detectors.
- The components of SAND are constructed remotely and assembled in the underground alcove cavern.

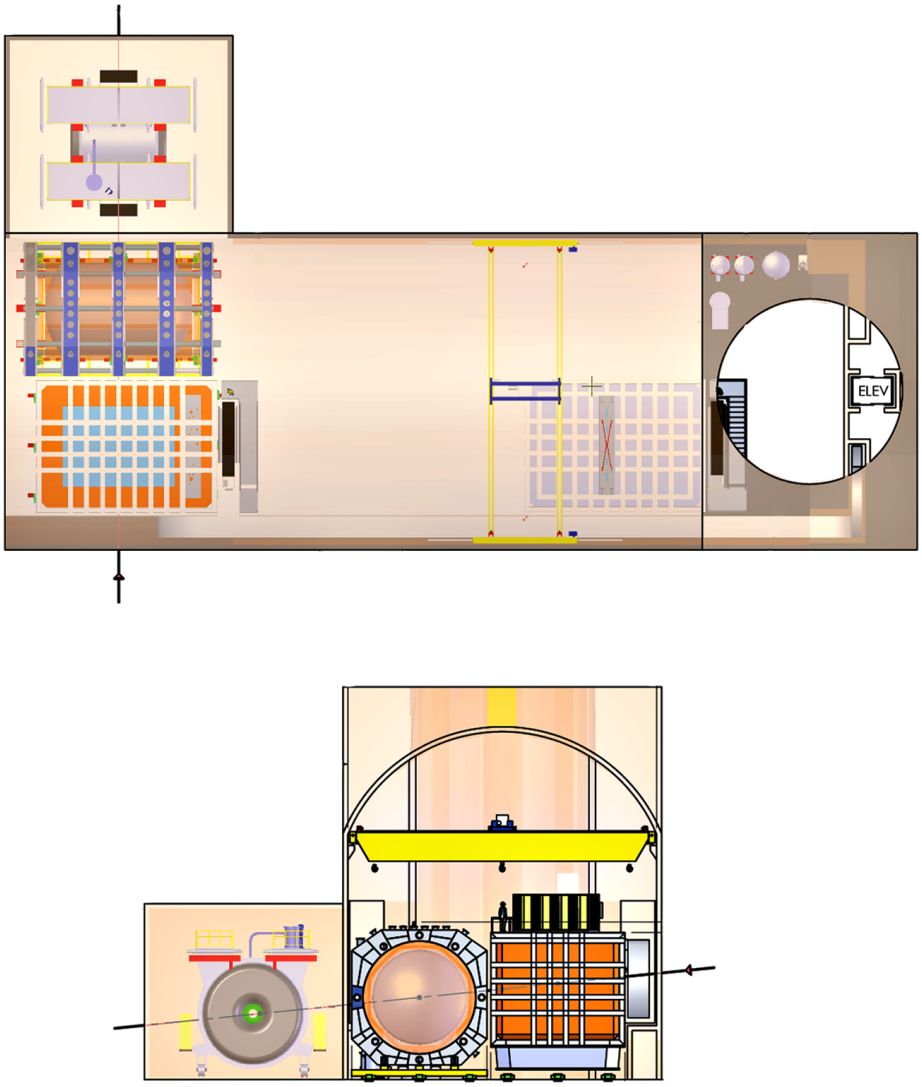

Figure B.1. DUNE ND hall shown from above (top) and from the side transverse to the beam (bottom). The LArTPC, MPD, and 3DST detectors are shown in position on the beam axis in both drawings.

- The five magnet coils are constructed and integrated with cryostats remotely. The magnet coils and cryostats are lowered into the ND hall and assembled together to form the magnet system on one of the transport frames.
- The pressure vessel is fabricated remotely and transported to the ND hall surface building. The TPC and some of the ECAL components are constructed in the surface building and installed in the pressure vessel. The pressure vessel must be fabricated and certified by a qualified fabricator.
- The LAr cryostat is constructed in the cavern on the second transport frame near the main shaft. The construction of the cryostat starts by erecting and assembling the warm exoskeleton from pre-fabricated structural steel members. The warm membrane is then installed and welded in situ. Insulation is then installed inside the warm vessel. The cold membrane is the last

2020 JINST 15 T08008

component and is welded in situ to form the final containment vessel for the LAr. A thin window is installed on the side facing the multipurpose detector.

- The LAr modules are constructed remotely and lowered down the shaft and installed in the cryostat. The modules are inserted/extracted from the top of the cryostat using an overhead lifting device.
- The LAr services are installed.
- The HPgTPC inside the pressure vessel is lowered in the hall and then mounted inside the magnet system.
- The ECAL segments are lowered into the hall and mounted around the pressure vessel.
- Services are installed.

The basic requirement for DUNE-PRISM is that both the MPD and ArgonCube can move horizontally to a position off the beam axis. The direction of the motion is to one side of the beam and the total motion is approximately 30.5 m.

Though the MPD and ArgonCube will be moved together to different positions for operations, they will be able to move independently for engineering, construction, and maintenance reasons. The specific method of movement is not yet determined. However, it is anticipated that tracks and rollers will be used in a fashion similar to what has been done for other large particle physics detectors. The driving mechanism may be a rack and pinion drive, or a similar system, which also allows for continuous motion. It is planned that the speed of movement will allow for the entire motion to be completed in one 8-hour shift. This requires a speed of approximately 6 cm/min. If it is desired that data can be taken during the movement, a slower speed may be used. If moved at a speed of about 0.6 cm/min, an entire round trip would take about one week.

Services for both the MPD and ArgonCube will need to remain connected while moving, or be disconnected and reconnected at intermediate positions. Ideally, the former will be possible, and articulated service carriers will maintain the connections during movement. In the case of ArgonCube this presents particular challenges and will require flexible conduits.

2020 JINST 15 T08008

Appendix C

Computing roles and collaborative projects

C.1 Roles

This appendix lists computing roles for DUNE derived from a comparison with existing similar roles on the LHCb experiment at CERN. LHCb is similar in size and data volumes to DUNE.

Distributed Computing Development and Maintenance - 5.0 FTE

This role includes oversight of all software engineering and development activities for packages needed to operate on distributed computing resources. The role requires a good understanding of the distributed computing infrastructure used by DUNE as well as the DUNE computing model.

Software and Computing Infrastructure Development and Maintenance - 6.0 FTE

This role includes software engineering, development, and maintenance for central services operated by DUNE to support software and computing activities of the project.

Database Design and Maintenance - 0.5 FTE

This role includes designing, maintaining, and scaling databases for tasks within DUNE.

Data Preservation Development - 0.5 FTE

This role includes activities related to reproducibility of analysis as well as data preservation, which requires expert knowledge of analysis and the computing model.

Application Managers and Librarians - 2.0 FTE

Application managers handle software applications for data processing, simulation, and analysis, and also coordinate activites in the areas of development, release preparation, and deployment of software package releases needed by DUNE. Librarians organize the overall setup of software packages needed for releases.

Central Services Manager and Operators - 1.5 FTE

2020 JINST 15 T08008

The site manager and operators are responsible for the central infrastructure and services of the DUNE distributed computing infrastructure. This includes coordination with the host laboratory for services provided to DUNE.

Distributed Production Manager - 0.5 FTE

Distributed production managers are responsible for the setup, launch, monitoring, and completion of processing campaigns executed on distributed computing resources for the experiment. These include data processing, MC simulation, and working group productions.

Distributed Data Manager - 0.5 FTE

The distributed data manager is responsible for operational interactions with distributed computing disk and tape resources. The role includes but is not limited to helping to establish new storage areas and data replication, deletion, and movement.

Distributed Workload Manager - 0.5 FTE

The distributed workload manager is responsible for operational interactions with distributed computing resources. The role includes activities such as helping to establish grid and cloud sites.

Computing Shift Leaders - 1.4 FTE

The shift leader is responsible for the experiment's distributed computing operations for a week-long period starting on a Monday to the following Sunday. Shift leaders chair regular operations meetings during their week and attend general DUNE operations meetings as appropriate.

Distributed Computing Resource Contacts - 0.5 FTE

Distributed computing resource contacts are the primary contacts for the DUNE distributed computing operations team and for the operators of large (Tier-1) sites and regional federations. They interact directly with the computing shift leaders at operations meetings.

User Support - 1.0 FTE

User support (software infrastructure, applications, and distributed computing) underpins all user activities of the DUNE computing project. User support personnel respond to questions from users on mailing lists, Slack-style chat systems, and/or ticketing systems, and are responsible for documenting solutions in knowledge bases and wikis.

Resource Board Chair - 0.1 FTE

This role is responsible for chairing quarterly meetings of the Computing Resource Board, which includes representatives from the various national funding agencies that support DUNE, to discuss funding for and delivery of the computing resources required for successful processing and exploitation of DUNE data.

Computing Coordination - 2.0 FTE

Coordinators oversee management of the computing project.

C.2 Specific collaborative computing projects

The HEP computing community has come together to form a HSC [46] that, through working groups, workshops, and white papers, guides the next generation of shared HEP software. The DUNE experiment's time scale, particularly the planning and evaluation phase, is almost ideal for allowing the HSC to develop effective contributions. Our overall strategy for computing infrastructure is to carefully evaluate existing and proposed field-wide solutions, to participate in useful designs, and to build our own solutions only where common solutions do not fit and additional joint development is not feasible. This section describes some of these common activities.

C.2.1 LArSoft for event reconstruction

Several neutrino experiments using the LArTPC technology share the LArSoft [133] reconstruction package. MicroBooNE, SBND, DUNE, and others share in developing a common core software framework that can be customized for each experiment. This software suite and earlier efforts in other experiments made the rapid reconstruction of the ProtoDUNE-SP data possible. DUNE will contribute heavily to the future evolution of this package, in particular, by introducing full multi-threading to allow parallel reconstruction of parts of large events, thus anticipating the very large events expected from the full detector.

C.2.2 WLCG/OSG and the HEP Software Foundation

The WLCG organization [134], which combines the resource and infrastructure missions of the LHC experiments, has proposed a governance structure called Scientific Computing Infrastructure (SCI) that splits out dedicated resources for LHC experiments from the general middleware infrastructure used to access those resources. In a white paper submitted to the European Strategy Group in December 2018 [135], a formal SCI organization is proposed. Many other experiments worldwide are already using this structure. As part of the formal transition to SCI, the DUNE collaboration was provisionally invited to join the WLCG management board as observers and to participate in the Grid Deployment Board and task forces. Our participation allows us to contribute to the technical decisions on global computing infrastructure while also contributing to that infrastructure. Many of these contributions involve the broader HEP Software Foundation efforts.

Areas of collaboration are described in the following sections.

C.2.2.1 Rucio development and extension

Rucio [47] is a data management system originally developed by the ATLAS collaboration and is now an open-source project. DUNE has chosen to use Rucio for large-scale data movement. Over the short term, it is combined with the sequential access via metadata (SAM) data catalog used by Fermilab experiments. DUNE collaborators at Fermilab and in the UK are actively collaborating on the Rucio project, adding value for both DUNE and the wider community.

Besides DUNE, the global Rucio team now includes Fermilab and Brookhaven National Laboratory (BNL) staff, CMS collaborators, and the core developers on ATLAS who initially wrote Rucio. DUNE CSC members have begun collaborating on several projects: (1) making object stores (such as Amazon S3 and compatible utilities) work with Rucio (a large object store in the UK exists for which DUNE has a sizable allocation); (2) monitoring and administering the Rucio system, and

2020 JINST 15 T08008

leveraging the landscape system at Fermilab; and (3) designing a data description engine that can be used to replace the SAM system we now use.

Rucio has already proved to be a powerful and useful tool for moving defined datasets from point A to point B. Rucio appears to offer a good solution for file localization but it lacks the detailed tools for data description and granular dataset definition available in the SAM system. The rapidly varying conditions in the test beam have shown that we need a sophisticated data description database interfaced to Rucio's location functions.

Efficient integration of caching into the Rucio model will be an important component for DUNE unless we can afford to have most data on disk to avoid staging. The dCache model, a caching front end for a tape store, is used in most Fermilab experiments. In contrast, LHC experiments such as ATLAS and CMS work with disk storage and tape storage that are independent of each other.

C.2.2.2 Testing new storage technologies and interfaces

The larger HEP community [136] currently has a data organization, management, and access (DOMA) task force in which several DUNE collaborators participate. It includes groups working on authorization, caching, third party copy, hierarchical storage, and quality of service. All are of interest to DUNE because they will determine the long-term standards for common computing infrastructure in the field. Authorization is of particular interest; they are covered in section C.2.2.4.

C.2.2.3 Data management and retention policy development

A data life cycle is built into the DUNE data model. Obsolete samples (old simulations and histograms and old commissioning data) need not be maintained indefinitely. We are organizing the structure of lower storage to store the various retention types separately for easy deletion when necessary.

C.2.2.4 Authentication and authorization security and interoperability

Within the next few years, we expect the global HEP community to change significantly the methods of authentication and authorization of computing and storage. Over that period, DUNE must collaborate with the USA and European HEP computing communities on improved authentication methods that will allow secure but transparent access to storage and other resources such as logbooks and code repositories. The current model requires individuals to be authenticated through different mechanisms for access to USA and European resources. Current efforts to expand the trust realm between CERN and Fermilab should allow a single sign-on for access to the two laboratories.

C.2.3 Evaluations of other important infrastructure

The DUNE CSC is still evaluating some major infrastructure components, notably databases, and workflow management systems.

The Fermilab *conditions* database is being used for the first run of ProtoDUNE, but the Belle II [137] system supported by BNL is being considered for subsequent runs [138].

We are evaluating DIRAC [139] as a workflow management tool and plan to investigate PANDA [140], as well, to compare against the current GlideInWMS, HT Condor, and POMS solution that was successfully used for the 2018 ProtoDUNE campaigns. Both DIRAC and PANDA are being integrated with Rucio and several LHC and non-LHC experiments use them.

Acknowledgments

This document was prepared by the DUNE collaboration using the resources of the Fermi National Accelerator Laboratory (Fermilab), a U.S. Department of Energy, Office of Science, HEP User Facility. Fermilab is managed by Fermi Research Alliance, LLC (FRA), acting under Contract No. DE-AC02-07CH11359.

The DUNE collaboration also acknowledges the international, national, and regional funding agencies supporting the institutions who have contributed to completing this Technical Design Report.

Glossary

Micro Telecommunications Computing Architecture (μTCA) The computer architecture specification followed by the crates that house charge and light readout electronics in the DP module. 59, 63, 184, 196

S/N signal-to-noise ratio. 187

one-pulse-per-second signal (1PPS signal) An electrical signal with a fast rise time and that arrives in real time with a precise period of one second. 54, 188

2p2h two particle, two hole. 113, 117

35 ton prototype A prototype cryostat and SP detector built at Fermilab before the ProtoDUNE detectors. 89

3D scintillator tracker (3DST) The core part of the 3D projection scintillator tracker spectrometer in the near detector conceptual design. 69, 73, 111, 112, 118, 119, 121, 162–170, 172, 175–177

4850L The depth in feet (1480 m) of the top of the cryostats underground at SURF; used more generally to refer to the DUNE underground area. Called the "4850 level" or "4850L". 7, 8, 101, 102

analog-to-digital converter (ADC) A sampling of a voltage resulting in a discrete integer count corresponding in some way to the input. 52, 63, 90, 149, 188

ALICE A Large Ion Collider Experiment, at CERN. 150

advanced mezzanine card (AMC) Holds digitizing electronics and lives in μTCA crates. 63, 196

anode plane assembly (APA) A unit of the SP detector module containing the elements sensitive to ionization in the LAr. It contains two faces each of three planes of wires, and interfaces to the cold electronics and photon detection system. 10, 11, 13, 14, 20, 48–55, 84, 89, 90

ARAPUCA A PD system design that consists of a light trap that captures wavelength-shifted photons inside boxes with highly reflective internal surfaces until they are eventually detected by SiPM detectors or are lost. 11, 14, 196

ArCLight a light detector ArgonCube effort. 123, 127, 128, 175

ArgonCube The name of the core part of the DUNE ND, a LArTPC. 15, 17, 68, 69, 71, 74, 75, 110, 111, 115, 121–129, 131, 133, 136, 161, 162, 172, 173, 175, 178, 184

ArgoNeuT The ArgoNeuT test-beam experiment and LArTPC prototype at Fermilab. 10

art A software framework implementing an event-based execution paradigm. 90

Ash River The Ash River, Minnesota, USA NOvA experiment far site, used as an assembly test site for DUNE. 55

2020 JINST 15 T08008

ASIC application-specific integrated circuit. 51, 53, 59, 62, 63, 126, 188, 190

ATLAS One of two general-purpose detectors at the LHC. It investigates a wide range of physics, from the search for the Higgs boson to extra dimensions and particles that could make up DM. 181, 182, 193

acceptance for use and possession (AUP) Required for beneficial occupancy of the underground areas at SURF for LBNF and DUNE. 96, 100, 102

baryon number A quantity expressing the total number of baryons in a system minus the number of antibaryons. 185

boosted dark matter (BDM) A new model that describes a relativistic dark matter particle boosted by the annihilation of heavier dark matter participles in the galactic center or the sun. 30

Belle II B-factory experiment now running at KEK. 76, 82

Brookhaven National Laboratory (BNL) US national laboratory in Upton, NY. 181, 182

baryon-number violating (BNV) Describing an interaction where baryon number is not conserved. 27

BSM beyond the standard model. 30, 44

charge and time integrated readout chip (CATIROC) A complete read-out chip manufactured in AustriaMicroSystem designed to read arrays of 16 photomultipliers. 63

charged current (CC) Refers to an interaction between elementary particles where a charged weak force carrier (W^+ or W^-) is exchanged. 23–25, 28–30, 34, 35, 43, 47, 66, 71, 73, 110–112, 117, 118, 120, 121, 129, 130, 137–139, 142, 149, 152, 153, 161, 166, 167, 169, 171–173, 175

CCQE charged current quasielastic interaction. 111, 115–118, 166, 167

critical decision (CD) The U.S. DOE's Order 413.3B outlines a series of staged project approvals, each of which is referred to as a critical decision (CD). 21

conceptual design report (CDR) A formal project document that describes the experiment at a conceptual level. 23, 31

cold electronics (CE) Analog and digital readout electronics that operate at cryogenic temperatures. 50–52, 188

European Organization for Nuclear Research (CERN) The leading particle physics laboratory in Europe and home to the ProtoDUNEs. (In French, the Organisation Européenne pour la Recherche Nucléaire, derived from Conseil Européen pour la Recherche Nucléaire. 4, 8, 12, 13, 17, 31, 42, 76, 77, 80, 84, 88, 182, 187, 189, 193, 195

conventional facilities (CF) Pertaining to construction and operation of buildings and conventional infrastructure, and for LBNF/DUNE, CF includes the excavation caverns. 3, 7, 21, 74, 95, 188

computational fluid dynamics (CFD) High performance computer-assisted modeling of fluid dynamical systems. 54, 55

cryogenic instrumentation and slow controls (CISC) Includes equipment to monitor all detector components and LAr quality and behavior, and provides a control system for many of the detector components. 21, 55, 59, 79, 92, 102

Cabibbo-Kobayashi-Maskawa matrix (CKM matrix) Refers to the matrix describing the mixing between mass and weak eigenstates of quarks. 24

2020 JINST 15 T08008

confidence level (CL) Refers to a probability used to determine the value of a random variable given its distribution. 27

construction manager/general contractor (CMGC) The organizational unit responsible for management of the construction of conventional facilities at the underground area at the SURF site. 102

CMOS Complementary metal-oxide-semiconductor. 62

CMS Compact Muon Solenoid experiment at CERN. 46, 181, 182

cluster on board (COB) An ATCA motherboard housing four RCEs. 193

conceptual design review A project management device by which a conceptual design is reviewed. 104

charge parity (CP) Product of charge and parity transformations. 6, 24–26, 37, 38, 66, 108, 171

cathode plane assembly (CPA) The component of the SP detector module that provides the drift HV cathode. 13, 48, 50, 55

charge, parity, and time reversal symmetry (CPT) product of charge, parity and time-reversal transformations. 30

charge-parity symmetry violation (CPV) Lack of symmetry in a system before and after charge and parity transformations are applied. For CP symmetry to hold, a particle turns into its corresponding antiparticle under a charge transformation, and a parity transformation inverts its space coordinates, i.e., produces the mirror image. 2, 5, 6, 15, 25, 26, 36–38, 47, 57, 65, 118

charge-readout plane (CRP) In the DP technology, a collection of electrodes in a planar arrangement placed at a particular voltage relative to some applied E field such that drifting electrons may be collected and their number and time may be measured. 12, 13, 20, 59–62

cosmic ray tagger (CRT) Detector external to the TPC designed to tag TPC-traversing cosmic ray particles. 14, 89

computing and software consortium (CSC) DUNE computing and software consortium. 76, 78–80, 82, 84, 181, 182

central utility cavern (CUC) The utility cavern at the 4850L of SURF located between the two detector caverns. It contains utilities such as central cryogenics and other systems, and the underground data center and control room. 7, 51, 54, 100, 102, 103

data acquisition (DAQ) The data acquisition system accepts data from the detector FE electronics, buffers the data, performs a trigger decision, builds events from the selected data and delivers the result to the offline secondary DAQ buffer. 20, 51, 52, 54, 59, 63, 64, 78, 79, 84, 91, 92, 102, 103, 186, 188

DAQ back-end subsystem (DAQ BE) The portion of the DAQ that is generally toward its output end. It is responsible for accepting and executing trigger commands and marshaling the data they address to output storage buffers. 54

DAQ readout unit (DAQ RU) The first element in the data flow of the DAQ. 54

DC direct coupling. 89

DUNE detector safety system (DDSS) The system used to manage key aspects of detector safety. 56

detector module The entire DUNE far detector is segmented into four modules, each with a nominal 10 kt fiducial mass. 7, 9, 10, 12, 21, 51, 55, 61, 63, 102, 103, 119, 187, 194, 195

2020 JINST 15 T08008

DIRAC Computing workflow management designed for LHCb and now used by many HEP experiments. 182

dark matter (DM) The term given to the unknown matter or force that explains measurements of galaxy motion that are otherwise inconsistent with the amount of mass associated with the observed amount of photon production. 30, 185

DOE U.S. Department of Energy. 3, 4, 17, 18, 21, 98, 106, 188, 189

data organization, management, and access (DOMA) data organization, management, and access efforts through the HEP Software Foundation. 182

dual-phase (DP) Distinguishes one of the DUNE far detector technologies by the fact that it operates using argon in both gas and liquid phases. 8–12, 19, 31, 53, 54, 57–59, 62–64, 76, 86, 87, 102, 186, 193, 195

DP module dual-phase DUNE FD module. 10, 12, 55, 57–59, 61, 62, 84, 184, 188

detector support system (DSS) The system used to support a SP detector module within its cryostat. 55

Deep Underground Neutrino Experiment (DUNE) A leading-edge, international experiment for neutrino science and proton decay studies. 1–12, 14–23, 25–33, 36–39, 42–47, 53–55, 57, 65, 66, 68, 69, 73–80, 82–88, 92, 94–111, 113–116, 118–124, 126, 128, 129, 134, 135, 137, 159, 161, 163, 169, 171, 172, 177, 179–182, 184, 187–191, 193–195

DUNE Precision Reaction-Independent Spectrum Measurement (DUNE-PRISM) a mobile near detector that can perform measurements over a range of angles off-axis from the neutrino beam direction in order to sample many different neutrino energy distributions. 15, 16, 68, 74, 110, 111, 115, 118, 122, 123, 157–159, 162, 176, 178

executive board (EB) The highest level DUNE decision-making body for the collaboration. 19, 95, 98, 104

electromagnetic calorimeter (ECAL) A detector component that measures energy deposition of traversing particles (in the near detector conceptual design). 15, 68, 70, 73, 110, 111, 118, 137, 139, 141, 144–148, 154, 156, 162–164, 168, 175, 177, 178, 191

Experimental Facilities Interface Group (EFIG) The body responsible for the required high-level coordination between the LBNF and DUNE projects. 18, 95, 104

equivalent noise charge (ENC) The equivalent noise charge is the input charge that corresponds to a S/N = 1. 14

ERT emergency response team. 107

environment, safety and health (ES&H) A discipline and specialty that studies and implements practical aspects of environmental protection and safety at work. 94, 96, 97, 99, 101, 106, 107

European Strategy for Particle Physics (ESPP) The cornerstone of Europe's decision-making process for the long-term future of the field. Mandated by the CERN Council, it is formed through a broad consultation of the grass-roots particle physics community, it actively solicits the opinions of physicists from around the world, and it is developed in close coordination with similar processes in the USA and Japan in order to ensure coordination between regions and optimal use of resources globally. 4

earned value management system (EVMS) Earned Value Management is a systematic approach to the integration and measurement of cost, schedule, and technical (scope) accomplishments on a project or task. It provides both the government and contractors the ability to examine detailed schedule information, critical program and technical milestones, and cost data (text from the US DOE); the EVMS is a system that implements this approach. 98

2020 JINST 15 T08008

field cage (FC) The component of a LArTPC that contains and shapes the applied E field. 9, 11–13, 50, 55, 58, 59, 61, 63, 123

far detector (FD) The 70 kt total (40 kt fiducial) mass LArTPC DUNE detector, composed of four 17.5 kt total (10 kt fiducial) mass modules, to be installed at the far site at SURF in Lead, SD, USA. 1, 3–8, 10–15, 19, 21, 23, 26, 28, 30–33, 39, 42–45, 49, 51, 53–55, 65, 66, 68, 69, 71–74, 76, 77, 84–88, 94, 95, 98, 102, 103, 108–112, 114–116, 118–120, 122, 123, 138, 141, 148, 157–160, 171–173, 187, 190, 194

front-end (FE) The front-end refers a point that is "upstream" of the data flow for a particular subsystem. For example the SP front-end electronics is where the cold electronics meet the sense wires of the TPC and the front-end DAQ is where the DAQ meets the output of the electronics. 51–53, 59, 60, 62, 144, 186, 188, 195

Front-End Link eXchange (FELIX) A high-throughput interface between FE and trigger electronics and the standard PCIe computer bus. 54

front-end mother board (FEMB) Refers a unit of the SP CE that contains the FE amplifier and ADC ASICs covering 128 channels. 195

Fermi National Accelerator Laboratory (Fermilab) U.S. national laboratory in Batavia, IL. It is the laboratory that hosts DUNE and serves as its near site. 3, 4, 8, 17–19, 21, 31, 77, 79, 80, 84, 88, 95, 97, 106, 124, 127, 181, 182, 184, 189–194

FHC forward horn current (ν_μ mode). 129, 130, 136

final design review A project management device by which a final design is reviewed. 104

field programmable gate array (FPGA) An integrated circuit technology that allows the hardware to be reconfigured to execute different algorithms after its manufacture and deployment. 126, 193

Fermi Research Alliance (FRA) A joint partnership of the University of Chicago and the Universities Research Association (URA) that manages and operates Fermilab on behalf of the DOE. 106

FRP fiber-reinforced plastic. 62

far site conventional facilities (FSCF) The CF at the DUNE far detector site, SURF. 96, 97, 99, 103, 194

final-state interactions (FSI) Refers to interactions between elementary or composite particles subsequent to the initial, fundamental particle interaction, such as may occur as the products exit a nucleus. 27, 73, 112, 114, 117, 168

FTE full-time equivalent. A unit of labor for the project. One year of work from one person. 82

fiducial volume (FV) The detector volume within the TPC that is selected for physics analysis through cuts on reconstructed event position. 112, 127–130, 137, 138, 152, 165, 168–170

gaseous argon (GAr) argon in its gas phase. 102

Generates Events for Neutrino Interaction Experiments (GENIE) Software providing an object-oriented neutrino interaction simulation resulting in kinematics of the products of the interaction. 117, 150, 151, 153

Global Positioning System (GPS) A satellite-based system that provides a highly accurate 1PPS signal that may be used to synchronize clocks and determine location. 54

ground grid An electrode held electrically neutral relative to Earth ground voltage; it is installed between the cathode and the PDs in a DP module to protect the PMTs, maintaining high transparency to light. 61

2020 JINST 15 T08008

grand unified theory (GUT) A class of theories that unifies the electro-weak and strong forces. 2, 26, 27, 47

hazard analysis (HA) A first step in a process to assess risk; the result of hazard analysis is the identification of the hazards present for a task or process. 106

HEP high energy physics. 76–78, 84, 87, 181, 182

high-performance computing (HPC) high-performance computing facilities; generally computing facilities emphasizing parallel computing with aggregate power of more than a teraflop. 88, 92, 93

high-pressure gaseous argon TPC (HPgTPC) A TPC filled with gaseous argon; a possible component of the DUNE ND. 15, 16, 68, 74, 110, 112, 118, 119, 128, 137–149, 151, 152, 156, 172, 175, 178, 191

HEP Software Foundation Collaboration (HSC) A foundation that facilitates cooperation and common efforts in high energy physics software and computing internationally. 77, 82, 181

high voltage (HV) Generally describes a voltage applied to drive the motion of free electrons through some media, e.g., LAr. 10, 50, 55, 59, 61, 62, 123, 141, 143

high voltage system (HVS) The detector subsystem that provides the TPC drift field. 20

ICARUS A neutrino experiment that was located at the Laboratori Nazionali del Gran Sasso (LNGS) in Italy, then refurbished at CERN for re-use in the same neutrino beam from Fermilab used by the MiniBooNE, MicroBooNE and SBND experiments. The ICARUS detector is being reassembled at Fermilab. 8, 10, 131, 194

IFbeam Database that stores beamline information indexed by timestamp. 92

International Neutrino Council (INC) A highest-level international advisory body to the U.S. DOE and the Fermilab directorate on matters related to the LBNF and the PIP-II projects. This council is composed of representatives from the international funding agencies and CERN that make major contributions the infrastructure. 17, 18

installation readiness review A project management device by which the plan for installation is reviewed. 104, 106

integration office The office that incorporates the onsite team responsible for coordinating integration and installation activities at SURF. 94, 96, 99–102, 104, 189, 193

inner readout chamber (IROC) inner (radial) readout chamber for gaseous argon TPC. 143

Joint Project Office (JPO) The framework through which team members from the LBNF project office, integration office, and DUNE technical coordination work together to provide coherence in project support functions across the global enterprise. Its functions include global project configuration and integration, installation planning and coordination, scheduling, safety assurance, technical review planning and oversight, development of partner agreements, and financial reporting. 94–98, 103, 104

KLOE KLOE is a e^+e^- collider detector spectrometer operated at DAFNE, the ϕ-meson factory at Frascati, Rome. In DUNE it will consist of a 26 cm Pb+scintillating fiber ECAL surrounding a cylindrical open detector region that is 4.00 m in diameter and 4.30 m long. The ECAL and detector region are embedded in a 0.6 T magnetic field created by a 4.86 m diameter superconducting coil and a 475 tonne iron yoke. 70, 73, 111, 163

L/E length-to-energy ratio. 71, 112

liquid argon (LAr) Argon in its liquid phase; it is a cryogenic liquid with a boiling point of −90 °C (87 K) and density of 1.4 g/ml. 3, 5, 7–10, 12, 14, 15, 21, 43, 47, 48, 51, 53, 55, 57, 59, 61, 68, 69, 84, 89, 110, 123–127, 131, 133–137, 140, 141, 146, 148, 173, 176–178, 185, 195

LArIAT The repurposed ArgoNeuT LArTPC, modified for use in a charged particle beam, dedicated to the calibration and precise characterization of the output response of these detectors. 10

LArPix ASIC pixelated charge readout for a TPC. 126

Liquid Argon Software (LArSoft) A shared base of physics software across LArTPC experiments. 149, 181

liquid argon time-projection chamber (LArTPC) A TPC filled with liquid argon; the basis for the DUNE FD modules. 1, 3, 4, 6–11, 15, 16, 27, 31, 33, 42, 44, 47, 48, 53, 57, 58, 68, 76, 78, 82, 84, 89, 110, 112, 118, 119, 121, 123, 126–128, 137–142, 145, 148, 150, 175, 177, 181, 184, 188, 190

long-baseline (LBL) Refers to the distance between the neutrino source and the FD. It can also refer to the distance between the near and far detectors. The "long" designation is an approximate and relative distinction. For DUNE, this distance (between Fermilab and SURF) is approximately 1300 km. 114, 118, 137, 138

Long-Baseline Neutrino Committee (LBNC) The committee, composed of internationally prominent scientists with relevant expertise, charged by the Fermilab director to review the scientific, technical, and managerial progress, plans and decisions associated with DUNE. 18

LBNE Long Baseline Neutrino Experiment (a terminated US project that was reformulated in 2014 under the auspices of the new DUNE collaboration, an internationally coordinated and internationally funded program, with Fermilab as host). 4

Long-Baseline Neutrino Facility (LBNF) The organizational entity responsible for developing the neutrino beam, the cryostats and cryogenics systems, and the conventional facilities for DUNE. 3, 4, 7, 17–19, 21, 25, 31, 33, 44, 47, 53–55, 95–100, 102, 103, 105, 112, 122, 126, 150, 159, 165, 166, 175, 187, 189, 190, 192–194

LBNF Strategic Project Advisory Committee (LBNF SPAC) A committee charged by the host laboratory director to provide expert, independent advice on significant issues and strategies related to LBNF project organization, management, and risks. 17

LBNF and DUNE project (LBNF/DUNE) The overall global project, including LBNF and DUNE. 5, 7, 94–99, 101, 102, 105–107, 185

Lawrence Berkeley National Laboratory (LBNL) US national laboratory in Berkeley, CA. 88, 191

Long Baseline Neutrino Observatory (LBNO) A terminated European project that, during its six-year duration, assessed the feasibility of a next-generation deep underground neutrino observatory in Europe). 4

light-mass dark matter (LDM) Refers to dark matter particles with mass values much lower than the electroweak scale, specifically below the 1 GeV level. 30

large electron multiplier (LEM) A micro-pattern detector suitable for use in ultra-pure argon vapor; LEMs consist of copper-clad PCB boards with sub-millimeter-size holes through which electrons undergo amplification. 8, 12, 58–61

LHC Large Hadron Collider. 17, 30, 46, 54, 76, 78, 82, 143, 181, 182, 185

LHCb LHC experiment dedicated to forward physics. 82, 179

2020 JINST 15 T08008

Large Synoptic Survey Telescope (LSST) 8.4 m telescope with 3.2G-pixel camera that will start taking data in 2023. 76

LV low voltage. 62

Monte Carlo (MC) Refers to a method of numerical integration that entails the statistical sampling of the integrand function. Forms the basis for some types of detector and physics simulations. 43, 72, 149, 157, 158, 180

MicroTCA Carrier Hub (MCH) An network switching device. 63

mass hierarchy (MH) Describes the separation between the mass squared differences related to the solar and atmospheric neutrino problems. 6

MicroBooNE The LArTPC-based MicroBooNE neutrino oscillation experiment at Fermilab. 8, 10, 86, 89, 131, 141, 142, 181, 189, 194

MINERvA The MINERvA neutrino cross sections experiment at Fermilab. 86, 109, 115–117, 121, 134, 137, 159, 166, 167, 173

MINOS A long-baseline neutrino experiment, with a near detector at Fermilab and a far detector in the Soudan mine in Minnesota, designed to observe the phenomena of neutrino oscillations (ended data runs in 2012). 109, 116, 124, 161

minimum ionizing particle (MIP) Refers to a particle traversing some medium such that the particle's mean energy loss is near the minimum. 50, 52, 133

memorandum of understanding (MoU) A document summarizing an agreement between two or more parties. 98

multi-purpose detector (MPD) A component of the near detector conceptual design; it is a magnetized system consisting of a HPgTPC and a surrounding ECAL. 15, 16, 68, 74, 75, 110, 122, 123, 131, 133, 137–141, 144, 145, 147, 148, 150, 151, 161, 162, 173–175, 177, 178

Mu2e An experiment sited at Fermilab that searches for charged-lepton flavor violation and seeks to discover physics beyond the SM. 53, 147

MWPC multi-wire proportional chamber. 143

NA61 CERN hadron production experiment. 135

neutral current (NC) Refers to an interaction between elementary particles where a neutrally charged weak force carrier (Z^0) is exchanged. 23, 28, 30, 34, 43, 71, 73, 111, 112, 115, 121, 137–139, 166, 169, 172, 173

Neutrino Cost Group (NCG) A group of internationally prominent scientists with relevant experience that is charged by the Fermilab director to review the cost, schedule, and associated risks for the DUNE experiment. 18

near detector (ND) Refers to the detector(s) installed close to the neutrino source at Fermilab. 3, 4, 6, 15–17, 19, 23, 30–32, 36, 44, 45, 65, 66, 68–71, 73–75, 84, 86, 88, 102, 108–112, 114–116, 118–120, 122–124, 126–129, 134–138, 140, 141, 145, 157–159, 161–163, 167, 169, 171–177, 184, 189, 193

NERSC National Energy Research Computing Facility at LBNL. 88

NOvA The NOvA off-axis neutrino oscillation experiment at Fermilab. 33, 55, 86, 88, 109, 115, 117, 137, 159, 184

2020 JINST 15 T08008

NP04 CERN North Area hadron beamline used for the SP test beam run. 88, 89

nonstandard interaction (NSI) A general class of theory of elementary particles other than the Standard Model. 30

NuFIT 4.0 The NuFIT 4.0 global fit to neutrino oscillation data. 33, 34, 41

NuMI a set of facilities at Fermilab, collectively called "Neutrinos at the Main Injector." The NuMI neutrino beamline target system converts an intense proton beam into a focused neutrino beam. 31, 115–117, 119, 120, 126, 134, 159, 161

oxygen deficiency hazard (ODH) a hazard that occurs when inert gases such as nitrogen, helium, or argon displace room air and thus reduce the percentage of oxygen below the level required for human life. 107

operational readiness review A project management device by which the operational readiness is reviewed. 104, 106

outer readout chamber (OROC) outer (radial) readout chamber for gaseous argon TPC. 143

Open Science Grid (OSG) Open Science Grid. 76, 80, 91

Pandora The Pandora multi-algorithm approach to pattern recognition. 91

PCB printed circuit board. 60, 70, 146

photon detector (PD) The detector elements involved in measurement of the number and arrival times of optical photons produced in a detector module. 9, 11, 14, 48, 51–55, 58, 86, 89, 188

photon detection system (PD system) The detector subsystem sensitive to light produced in the LAr. 14, 15, 20, 63, 127, 184

particle ID (PID) Particle identification. 54

Proton Improvement Plan II (PIP-II) A Fermilab project for improving the protons on target delivered delivered by the LBNF neutrino production beam. This is version two of this plan and it is planned to be followed by a PIP-III. 3, 17, 18, 189

Projection Matching Algorithm (PMA) A reconstruction algorithm that combines 2D reconstructed objects to form a 3D representation. 91

Pontecorvo-Maki-Nakagawa-Sakata (PMNS) A type of matrix that describes the mixing between mass and weak eigenstates of the neutrino. 24, 25, 30, 39, 108

photomultiplier tube (PMT) A device that makes use of the photoelectric effect to produce an electrical signal from the arrival of optical photons. 12, 57, 59, 61, 63, 64, 188

parts per million (ppm) A concentration equal to one part in 10^{-6}. 49

parts per trillion (ppt) A concentration equal to one part in 10^{-12}. 49, 58

preliminary design review A project management device by which an early design is reviewed. 104

production progress review A project management device by which the progress of production is reviewed. 104

production readiness review A project management device by which the production readiness is reviewed. 104

2020 JINST 15 T08008

project integration director Responsible for integration and installation of LBNF and DUNE deliverables in South Dakota. Manages the integration office. 94–96, 99–101, 106, 107

ProtoDUNE Either of the two DUNE prototype detectors constructed at CERN. One prototype implements SP technology and the other DP. 31, 54, 77, 78, 80, 82, 87, 88, 90, 97, 115, 124, 129, 182, 184, 193

ProtoDUNE-DP The DP ProtoDUNE detector at CERN. 12–14, 61–64, 76, 77, 80, 84

ProtoDUNE-ND a prototype DUNE ND. 124

ProtoDUNE-SP The SP ProtoDUNE detector at CERN. 10, 12–15, 42, 50, 76, 77, 79, 80, 84, 88–93, 105, 181

quality assurance (QA) The set of actions taken to provide confidence that quality requirements are fulfilled, and to detect and correct poor results. 13, 56, 94, 98, 99, 105, 106, 195

quality control (QC) An aggregate of activities (such as design analysis and inspection for defects) performed to ensure adequate quality in manufactured products. 56, 99, 105

quasi-elastic (QE) Refers to interaction between elementary particles and a nucleus in an energy range where the interaction can be modeled as occurring between constituent quarks of one nucleon and resulting in no bulk recoil of the resulting nucleus. 74, 112–114, 117

resource coordinator (RC) A member of the DUNE management team responsible for coordinating the financial resources of the project effort. 19, 98

reconfigurable computing element (RCE) Data processor located outside of the cryostat on a cluster on board (COB) that contains FPGA, RAM and solid-state disk (SSD) resources, responsible for buffering data, producing trigger primitives, responding to triggered requests for data and synching SNB dumps. 195

review office An office within the integration office that organizes reviews. 104

RHC reverse horn current ($\overline{\nu}_\mu$ mode). 136

readout chamber (ROC) readout chamber for gaseous argon TPC. 143, 144

ROI region of interest. 63, 84, 85, 90, 91

ROOT A modular scientific software toolkit. It provides all the functionalities needed to deal with big data processing, statistical analysis, visualisation and storage. It is mainly written in C++ but integrated with other languages such as Python and R. 90

Resources Review Board (RRB) A part of DUNE's international project governance structure, composed of representatives of all funding agencies that sponsor the project, and of Fermilab management, established to provide coordination among funding partners and oversight of DUNE. 17, 18

Rucio Data management system originally developed by ATLAS but now open-source and shared across HEP. 77, 181, 182

signal-to-noise (S/N) signal-to-noise ratio. 8, 14, 48–50, 57, 59, 63, 84

sequential access via metadata (SAM) A data-handling system to store and retrieve files and associated metadata, including a complete record of the processing that has used the files. 181, 182

System for on-Axis Neutrino Detection (SAND) The beam monitor component of the near detector that remains on-axis at all times and serves as a dedicated neutrino spectrum monitor. 15, 69–71, 74, 75, 111, 162, 166–168, 173–176

2020 JINST 15 T08008

Short-Baseline Neutrino (SBN) A Fermilab program consisting of three collaborations, MicroBooNE, SBND, and ICARUS, to perform sensitive searches for ν_e appearance and ν_μ disappearance in the Booster Neutrino Beam. 18, 45, 87, 109

SBND The Short-Baseline Near Detector experiment at Fermilab. 8, 181, 189, 194

Scientific Computing Infrastructure (SCI) Proposed extension of the infrastructure component of WLCG to other experiments. 181

Fermilab South Dakota Services Division (SDSD) A Fermilab division responsible providing host laboratory functions at SURF in South Dakota. 95, 102, 106

South Dakota Science and Technology Authority (SDSTA) The legal entity that manages SURF, in Lead, S.D. 107

South Dakota Warehouse Facility (SDWF) Warehousing operations in South Dakota responsible for receiving LBNF and DUNE goods and coordinating shipments to the Ross shaft at SURF. 102

secondary DAQ buffer A secondary DAQ buffer holds a small subset of the full rate as selected by a trigger command. This buffer also marks the interface with the DUNE Offline. 186

signal feedthrough chimney (SFT chimney) In the DP technology, a volume above the cryostat penetration used for a signal feedthrough. 12, 59, 60, 62, 63

silicon photomultiplier (SiPM) A solid-state avalanche photodiode sensitive to single photoelectron signals. 11, 52, 53, 70, 127, 145, 146, 184

standard model (SM) Refers to a theory describing the interaction of elementary particles. 26, 27, 30, 47, 191

supernova neutrino burst (SNB) A prompt increase in the flux of low-energy neutrinos emitted in the first few seconds of a core-collapse supernova. It can also refer to a trigger command type that may be due to this phenomenon, or detector conditions that mimic its interaction signature. 2, 5, 28, 33, 42, 43, 47, 52–54, 86–88, 90, 91, 193

single-phase (SP) Distinguishes one of the DUNE far detector technologies by the fact that it operates using argon in its liquid phase only. 8–12, 19, 31, 47, 48, 53–55, 57, 59, 63, 76, 84, 85, 87, 102, 184, 187, 188, 192, 193, 195

SP module single-phase DUNE FD module. 10–12, 48, 52, 54, 55, 84–87, 148, 149

SRC short-range correlated nucleon-nucleon interactions. 113

SSC The Superconducting Super Collider was to be a huge underground ring complex beneath the area near Waxahachie, Texas, USA, that would have been the world's most energetic particle accelerator. It was begun in 1990, but canceled by the U.S. Congress in 1993 (scientificamerican.com Oct 2013). 146

solid-state disk (SSD) Any storage device that may provide sufficient write throughput to receive, both collectively and distributed, the sustained full rate of data from a detector module for many seconds. 193

Sanford Underground Research Facility (SURF) The laboratory in South Dakota where the LBNF FSCF will be constructed and the DUNE FD will be installed and operated. 3, 4, 6–8, 21, 54, 82, 94, 96–99, 101, 102, 106, 107, 186, 190, 194

T2K T2K (Tokai to Kamioka) is a long-baseline neutrino experiment in Japan studying neutrino oscillations. 25, 33, 86, 109, 115, 120, 137, 163, 195

2020 JINST 15 T08008

technical board (TB) The DUNE organization responsible for evaluating technical decisions. 104

technical coordinator (TC) A member of the DUNE management team responsible for organizing the technical aspects of the project effort; is head of technical coordination. 19, 94, 97–99, 106

temporary construction opening (TCO) An opening in the side of a cryostat through which detector elements are brought into the cryostat; utilized during construction and installation. 55

technical design report (TDR) A formal project document that describes the experiment at a technical level. 1, 3–5, 7, 10, 15, 17–19, 21, 31, 32, 82, 102

technical coordination The DUNE organization responsible for overall integration of the detector elements and successful execution of the detector construction project; areas of responsibility include general project oversight, systems engineering, QA and safety. 94, 96, 98–100, 102, 104–106, 189, 195

tetra-phenyl butadiene (TPB) A WLS material. 63

time projection chamber (TPC) A type of particle detector that uses an E field together with a sensitive volume of gas or liquid, e.g., LAr, to perform a 3D reconstruction of a particle trajectory or interaction. The activity is recorded by digitizing the waveforms of current induced on the anode as the distribution of ionization charge passes by or is collected on the electrode. 9, 10, 14, 15, 20, 50, 54, 55, 58, 60, 64, 68, 70, 73, 77, 84, 89–91, 111, 115, 123–126, 128, 143, 144, 162–164, 175, 188–190, 192, 193

trigger candidate Summary information derived from the full data stream and representing a contribution toward forming a trigger decision. 195

trigger command Information derived from one or more trigger candidates that directs elements of the detector module to read out a portion of the data stream. 194, 195

trigger decision The process by which trigger candidates are converted into trigger commands. 186, 195

UA1 UA1 (Underground Area 1) was a particle detector at CERN's Super Proton Synchrotron (SPS). It ran from 1981 until 1990, when the SPS was used as a proton-antiproton collider, searching for traces of W and Z particles in collisions. (CERN) The UA1 dipole magnet was reused in the NOMAD experiment and currently provides the magnetic field for the T2K ND280 detector. 146

VUV vacuum ultra-violet. 48, 52

WA105 DP demonstrator The $3 \times 1 \times 1\ \mathrm{m}^3$ WA105 DP prototype detector at CERN. 8

work breakdown structure (WBS) An organizational project management tool by which the tasks to be performed are partitioned in a hierarchical manner. 21, 102, 104

warm interface board (WIB) Digital electronics situated just outside the SP cryostat that receives digital data from the front-end mother boards (FEMBs) over cold copper connections and sends it to the reconfigurable computing element (RCE) FE readout hardware. 51

weakly-interacting massive particle (WIMP) A hypothesized particle that may be a component of dark matter. 30

Wire-Cell A tomographic automated 3D neutrino event reconstruction method for LArTPCs. 91

Worldwide LHC Computing Grid (WLCG) Worldwide LHC Computing Grid. 76, 80, 82, 91, 181, 194

wavelength-shifting (WLS) A material or process by which incident photons are absorbed by a material and photons are emitted at a different, typically longer, wavelength. 52, 57, 63, 163, 195, 196

2020 JINST 15 T08008

White Rabbit (WR) A component of the timing system that forwards clock signal and time-of-day reference data to the master timing unit. 63, 196

White Rabbit μTCA Carrier Hub (WR-MCH) A card mounted in μTCA crate that recieves time syncronization information and trigger data packets over WR network and disributes them to the AMC over μTCA backplane. 63

X-ARAPUCA Extended ARAPUCA design with WLS coating on only the external face of the dichroic filter window(s) but with a WLS doped plate inside the cell. 52, 53

Bibliography

[1] LBNE collaboration, *The Long-Baseline Neutrino Experiment: Exploring Fundamental Symmetries of the Universe*, in proceerings of *Snowmass 2013: Workshop on Energy Frontier Seattle, USA, June 30–July 3, 2013*, 2013, http://lss.fnal.gov/archive/2014/pub/fermilab-pub-14-022.pdf [arXiv:1307.7335] [INSPIRE].

[2] P. Derwent et al., *Proton Improvement Plan-II*, (2013), http://projectx-docdb.fnal.gov/cgi-bin/RetrieveFile?docid=1232&filename=1.2%20MW%20Report_Rev5.pdf&version=3.

[3] Particle Physics Project Prioritization Panel, *US Particle Physics: Scientific Opportunities; A Strategic Plan for the Next Ten Years*, (2008), https://science.osti.gov/-/media/hep/pdf/files/pdfs/p5_report_06022008.pdf.

[4] LAGUNA-LBNO collaboration, *Optimised sensitivity to leptonic CP-violation from spectral information: the LBNO case at 2300 KM baseline*, arXiv:1412.0593 [INSPIRE].

[5] *Nucl. Instrum. Meth.* **A 527** (2004) 329. ICARUS collaboration, *Design, construction and tests of the ICARUS T600 detector*, *Nucl. Instrum. Meth.* **A 527** (2004) 329 [INSPIRE].

[6] MicroBooNE collaboration, *Design and Construction of the MicroBooNE Detector*, 2017 *JINST* **12** P02017 [arXiv:1612.05824] [INSPIRE].

[7] C. Anderson et al., *The ArgoNeuT Detector in the NuMI Low-Energy beam line at Fermilab*, 2012 *JINST* **7** P10019 [arXiv:1205.6747] [INSPIRE].

[8] LArIAT collaboration, *LArIAT: Liquid Argon In A Testbeam*, arXiv:1406.5560 [INSPIRE].

[9] DUNE collaboration, *The Single-Phase ProtoDUNE Technical Design Report*, arXiv:1706.07081 [INSPIRE].

[10] Particle Data Group collaboration, *Review of Particle Physics*, *Phys. Rev.* **D 98** (2018) 030001 [INSPIRE].

[11] T2K collaboration, *Constraint on the Matter-Antimatter Symmetry-Violating Phase in Neutrino OscillationsConstraint on the matter–antimatter symmetry-violating phase in neutrino oscillations*, *Nature* **580** (2020) 339 [arXiv:1910.03887] [INSPIRE].

[12] H. Nunokawa, S.J. Parke and J.W.F. Valle, *CP Violation and Neutrino Oscillations*, *Prog. Part. Nucl. Phys.* **60** (2008) 338 [arXiv:0710.0554] [INSPIRE].

[13] M. Bass et al., *Baseline Optimization for the Measurement of CP-violation, Mass Hierarchy and θ_{23} Octant in a Long-Baseline Neutrino Oscillation Experiment*, *Phys. Rev.* **D 91** (2015) 052015 [arXiv:1311.0212] [INSPIRE].

[14] K.S. Babu et al., *Working Group Report: Baryon Number Violation*, in *Proceedings, 2013 Community Summer Study on the Future of U.S. Particle Physics: Snowmass on the Mississippi (CSS2013): Minneapolis, MN, USA, July 29-August 6, 2013*, 2013, http://www.slac.stanford.edu/econf/C1307292/docs/IntensityFrontier/BaryonNo-13.pdf [arXiv:1311.5285] [INSPIRE].

[15] R.M. Bionta et al., *Observation of a Neutrino Burst in Coincidence with Supernova SN 1987a in the Large Magellanic Cloud*, *Phys. Rev. Lett.* **58** (1987) 1494 [INSPIRE].

2020 JINST 15 T08008

[16] Kamiokande-II collaboration, *Observation of a Neutrino Burst from the Supernova SN 1987a*, *Phys. Rev. Lett.* **58** (1987) 1490 [INSPIRE].

[17] D.N. Schramm and J.W. Truran, *New physics from Supernova SN1987A*, *Phys. Rept.* **189** (1990) 89 [INSPIRE].

[18] F. Vissani, *Comparative analysis of SN1987A antineutrino fluence*, *J. Phys.* **G 42** (2015) 013001 [arXiv:1409.4710] [INSPIRE].

[19] A. Mirizzi, I. Tamborra, H.-T. Janka, N. Saviano, K. Scholberg, R. Bollig et al., *Supernova Neutrinos: Production, Oscillations and Detection*, *Riv. Nuovo Cim.* **39** (2016) 1 [arXiv:1508.00785] [INSPIRE].

[20] S. Horiuchi and J.P. Kneller, *What can be learned from a future supernova neutrino detection?*, *J. Phys.* **G 45** (2018) 043002 [arXiv:1709.01515] [INSPIRE].

[21] L. Hudepohl, B. Müller, H.T. Janka, A. Marek and G.G. Raffelt, *Neutrino Signal of Electron-Capture Supernovae from Core Collapse to Cooling*, *Phys. Rev. Lett.* **104** (2010) 251101 [*Erratum ibid.* **105** (2010) 249901] [arXiv:0912.0260] [INSPIRE].

[22] K. Scholberg, *Supernova Neutrino Detection*, *Ann. Rev. Nucl. Part. Sci.* **62** (2012) 81 [arXiv:1205.6003] [INSPIRE].

[23] I. Esteban, M.C. Gonzalez-Garcia, A. Hernandez-Cabezudo, M. Maltoni and T. Schwetz, *Global analysis of three-flavour neutrino oscillations: synergies and tensions in the determination of θ_{23}, δ_{CP} and the mass ordering*, *JHEP* **01** (2019) 106 [arXiv:1811.05487] [INSPIRE].

[24] *Nufit4.0.*, http://www.nu-fit.org/.

[25] P.F. de Salas, D.V. Forero, C.A. Ternes, M. Tortola and J.W.F. Valle, *Status of neutrino oscillations 2018: 3σ hint for normal mass ordering and improved CP sensitivity*, *Phys. Lett.* **B 782** (2018) 633 [arXiv:1708.01186] [INSPIRE].

[26] F. Capozzi, E. Lisi, A. Marrone, D. Montanino and A. Palazzo, *Status and prospects of global analyses of neutrino mass-mixing parameters*, *J. Phys. Conf. Ser.* **888** (2017) 012037 [INSPIRE].

[27] NOvA collaboration, *First Measurement of Neutrino Oscillation Parameters using Neutrinos and Antineutrinos by NOvA*, *Phys. Rev. Lett.* **123** (2019) 151803 [arXiv:1906.04907] [INSPIRE].

[28] T2K collaboration, *Search for CP-violation in Neutrino and Antineutrino Oscillations by the T2K Experiment with 2.2×10^{21} Protons on Target*, *Phys. Rev. Lett.* **121** (2018) 171802 [arXiv:1807.07891] [INSPIRE].

[29] Super-Kamiokande collaboration, *Search for proton decay via $p \to \nu\nu K^+$ using 260 kiloton·year data of Super-Kamiokande*, *Phys. Rev.* **D 90** (2014) 072005 [arXiv:1408.1195] [INSPIRE].

[30] H. Minakata, H. Nunokawa, R. Tomas and J.W.F. Valle, *Parameter Degeneracy in Flavor-Dependent Reconstruction of Supernova Neutrino Fluxes*, *JCAP* **12** (2008) 006 [arXiv:0802.1489] [INSPIRE].

[31] I. Tamborra, B. Müller, L. Hudepohl, H.-T. Janka and G. Raffelt, *High-resolution supernova neutrino spectra represented by a simple fit*, *Phys. Rev.* **D 86** (2012) 125031 [arXiv:1211.3920] [INSPIRE].

[32] K. Nakazato, K. Sumiyoshi, H. Suzuki, T. Totani, H. Umeda and S. Yamada, *Supernova Neutrino Light Curves and Spectra for Various Progenitor Stars: From Core Collapse to Proto-neutron Star Cooling*, *Astrophys. J. Suppl.* **205** (2013) 2 [arXiv:1210.6841] [INSPIRE].

[33] L. Huedepohl, *Neutrinos from the Formation, Cooling and Black Hole Collapse of Neutron Stars*. Ph.D. thesis, Technische Universitat Munchen (2014), https://wwwmpa.mpa-garching.mpg.de/ccsnarchive/data/Huedepohl2014_phd_thesis/.

[34] CMS collaboration, *Search for an $L_\mu - L_\tau$ gauge boson using $Z \to 4\mu$ events in proton-proton collisions at $\sqrt{s} = 13$ TeV*, *Phys. Lett.* **B 792** (2019) 345 [arXiv:1808.03684] [INSPIRE].

[35] BaBar collaboration, *Search for a muonic dark force at BABAR*, *Phys. Rev.* **D 94** (2016) 011102 [arXiv:1606.03501] [INSPIRE].

2020 JINST 15 T08008

[36] CCFR collaboration, *Neutrino tridents and W Z interference*, *Phys. Rev. Lett.* **66** (1991) 3117 [INSPIRE].

[37] W. Altmannshofer, S. Gori, M. Pospelov and I. Yavin, *Neutrino Trident Production: A Powerful Probe of New Physics with Neutrino Beams*, *Phys. Rev. Lett.* **113** (2014) 091801 [arXiv:1406.2332] [INSPIRE].

[38] G. Bellini et al., *Precision measurement of the 7Be solar neutrino interaction rate in Borexino*, *Phys. Rev. Lett.* **107** (2011) 141302 [arXiv:1104.1816] [INSPIRE].

[39] R. Harnik, J. Kopp and P.A.N. Machado, *Exploring nu Signals in Dark Matter Detectors*, *JCAP* **07** (2012) 026 [arXiv:1202.6073] [INSPIRE].

[40] BOREXINO collaboration, *First Simultaneous Precision Spectroscopy of pp, ^{7}Be and pep Solar Neutrinos with Borexino Phase-II*, *Phys. Rev.* **D 100** (2019) 082004 [arXiv:1707.09279] [INSPIRE].

[41] B. Ahlgren, T. Ohlsson and S. Zhou, *Comment on "Is Dark Matter with Long-Range Interactions a Solution to All Small-Scale Problems of Λ Cold Dark Matter Cosmology?"*, *Phys. Rev. Lett.* **111** (2013) 199001 [arXiv:1309.0991] [INSPIRE].

[42] A. Kamada and H.-B. Yu, *Coherent Propagation of PeV Neutrinos and the Dip in the Neutrino Spectrum at IceCube*, *Phys. Rev.* **D 92** (2015) 113004 [arXiv:1504.00711] [INSPIRE].

[43] C. Rubbia, *The Liquid Argon Time Projection Chamber: A New Concept for Neutrino Detectors*, techical report (1977) CERN-EP-INT-77-08.

[44] MU2E collaboration, *Mu2e Technical Design Report*, arXiv:1501.05241 [INSPIRE].

[45] A. Friedland and S.W. Li, *Understanding the energy resolution of liquid argon neutrino detectors*, *Phys. Rev.* **D 99** (2019) 036009 [arXiv:1811.06159] [INSPIRE].

[46] HEP SOFTWARE FOUNDATION collaboration, *A Roadmap for HEP Software and Computing R&D for the 2020s*, *Comput. Softw. Big Sci.* **3** (2019) 7 [arXiv:1712.06982] [INSPIRE].

[47] M. Barisits et al., *Rucio - Scientific data management*, *Comput. Softw. Big Sci.* **3** (2019) 11 [arXiv:1902.09857] [INSPIRE].

[48] H. Schellman at al., *Computing Consortium Governance Document*, DUNE doc 12751, Oregon State University (2019), http://docs.dunescience.org/cgi-bin/ShowDocument?docid=12751&asof=2019-11-1.

[49] G. Karagiorgi, D. Newbold, A. Norman and H. Schellman, *DUNE FD Interface Document: Software and Computing to Joint DAQ*, DUNE doc 7123, Columbia, Bristol, Fermilab, and Oregon State (2018), http://docs.dunescience.org/cgi-bin/ShowDocument?docid=7123&asof=2019-11-1.

[50] S. Gollapinni et al., *DUNE FD Interface Document: Software and Computing to Joint CISC*, http://docs.dunescience.org/cgi-bin/ShowDocument?docid=7126&version=1.

[51] D. Adams, *ProtoDUNE Data Preparation*, DUNE doc 12349, BNL (2018), http://docs.dunescience.org/cgi-bin/ShowDocument?docid=12349&asof=2019-11-1.

[52] MICROBOONE collaboration, *The Pandora multi-algorithm approach to automated pattern recognition of cosmic-ray muon and neutrino events in the MicroBooNE detector*, *Eur. Phys. J.* **C 78** (2018) 82 [arXiv:1708.03135] [INSPIRE].

[53] X. Qian, B. Viren and C. Zhang, *Wire-Cell. Software Package for Liquid Argon TPC*, https://www.phy.bnl.gov/wire-cell/.

[54] R. Sulej and D. Stefan, *LArSoft Single Record Algorithm*, http://larsoft.org/single-record/?pdb=102.

[55] M. Andrews, *Integrated Environment, Safety and Health Management Plan*, DUNE doc 291 (2016). https://docs.dunescience.org/cgi-bin/private/ShowDocument?docid=291&asof=2019-11-1.

[56] A. Bross at al., *High-Pressure Argon gas TPC Option for the DUNE Near Detector*, DUNE doc 12388 (2019), http://docs.dunescience.org/cgi-bin/ShowDocument?docid=12388&asof=2019-11-1

2020 JINST 15 T08008

[57] R.A. Smith and E.J. Moniz, *Neutrino reactions on nuclear targets*, *Nucl. Phys.* **B 43** (1972) 605 [*Erratum ibid.* **B 101** (1975) 547] [INSPIRE].

[58] A. Bodek, M.E. Christy and B. Coopersmith, *Effective spectral function for quasielastic scattering on nuclei from* ${}^{2}_{1}H$ *to* ${}^{208}_{82}Pb$, *AIP Conf. Proc.* **1680** (2015) 020003 [arXiv:1409.8545] [INSPIRE].

[59] MINERvA collaboration, *Measurement of Quasielastic-Like Neutrino Scattering at* $\langle E_\nu \rangle \sim 3.5$ *GeV on a Hydrocarbon Target*, *Phys. Rev.* **D 99** (2019) 012004 [arXiv:1811.02774] [INSPIRE].

[60] NOvA collaboration, *New constraints on oscillation parameters from* ν_e *appearance and* ν_μ *disappearance in the NOvA experiment*, *Phys. Rev.* **D 98** (2018) 032012 [arXiv:1806.00096] [INSPIRE].

[61] J. Wolcott, *Impact of cross section modeling on NOvA oscillation analyses*, (2018), ,https://indico.cern.ch/event/703880/contributions/3159021/attachments/1735451/2806895/2018-10-17_Wolcott_XS_unc_on_NOvA_osc_-_NuInt.pdf.

[62] D. Jena, *MINERvA adventures in flux determination*, in proceedings of *NuInt 2018*, Fermilab, October 2018, https://indico.cern.ch/event/703880/contributions/3159052/attachments/1735968/2817449/NuInt2018_DeepikaJena_Flux.pdf.

[63] MiniBooNE collaboration, *Measurement of the Neutrino Neutral-Current Elastic Differential Cross Section on Mineral Oil at* $E_\nu \sim 1$ *GeV*, *Phys. Rev.* **D 82** (2010) 092005 [arXiv:1007.4730] [INSPIRE].

[64] K2K collaboration, *Measurement of the quasi-elastic axial vector mass in neutrino-oxygen interactions*, *Phys. Rev.* **D 74** (2006) 052002 [hep-ex/0603034] [INSPIRE].

[65] MINOS collaboration, *Study of quasielastic scattering using charged-current* $\nu\mu$ *-iron interactions in the MINOS near detector*, *Phys. Rev.* **D 91** (2015) 012005 [arXiv:1410.8613] [INSPIRE].

[66] M. Martini, M. Ericson and G. Chanfray, *Energy reconstruction effects in neutrino oscillation experiments and implications for the analysis*, *Phys. Rev.* **D 87** (2013) 013009 [arXiv:1211.1523] [INSPIRE].

[67] NOvA collaboration, *First measurement of muon-neutrino disappearance in NOvA*, *Phys. Rev.* **D 93** (2016) 051104 [arXiv:1601.05037] [INSPIRE].

[68] C. Andreopoulos et al., *The GENIE Neutrino Monte Carlo Generator*, *Nucl. Instrum. Meth.* **A 614** (2010) 87 [arXiv:0905.2517] [INSPIRE].

[69] A. Bodek and J.L. Ritchie, *Further Studies of Fermi Motion Effects in Lepton Scattering from Nuclear Targets*, *Phys. Rev.* **D 24** (1981) 1400 [INSPIRE].

[70] S. Dytman, *Neutrino event generators*, *AIP Conf. Proc.* **896** (2007) 178 [INSPIRE].

[71] P. Rodrigues, C. Wilkinson and K. McFarland, *Constraining the GENIE model of neutrino-induced single pion production using reanalyzed bubble chamber data*, *Eur. Phys. J.* **C 76** (2016) 474 [arXiv:1601.01888] [INSPIRE].

[72] J. Nieves, J.E. Amaro and M. Valverde, *Inclusive quasi-elastic neutrino reactions*, *Phys. Rev.* **C 70** (2004) 055503 [*Erratum ibid.* **C 72** (2005) 019902] [nucl-th/0408005] [INSPIRE].

[73] R. Gran, *Model Uncertainties for Valencia RPA Effect for MINERvA*, arXiv:1705.02932 [INSPIRE].

[74] J. Nieves, I. Ruiz Simo and M.J. Vicente Vacas, *Inclusive Charged–Current Neutrino–Nucleus Reactions*, *Phys. Rev.* **C 83** (2011) 045501 [arXiv:1102.2777] [INSPIRE].

[75] R. Gran, J. Nieves, F. Sanchez and M.J. Vicente Vacas, *Neutrino-nucleus quasi-elastic and 2p2h interactions up to 10 GeV*, *Phys. Rev.* **D 88** (2013) 113007 [arXiv:1307.8105] [INSPIRE].

[76] J. Schwehr, D. Cherdack and R. Gran, *GENIE implementation of IFIC Valencia model for QE-like 2p2h neutrino-nucleus cross section*, arXiv:1601.02038 [INSPIRE].

[77] M. Alam et al., *GENIE Production Release 2.10.0*, arXiv:1512.06882 [INSPIRE].

2020 JINST 15 T08008

[78] A. Bercellie, *Pion production at MINERvA*, in proceedings of *NuInt 2018*, Fermilab, October 2018, https://indico.cern.ch/event/703880/contributions/3157434/attachments/1734544/2808228/Minerva_LE_Pions_NUINT2018.pdf.

[79] MINERvA collaboration, *Measurement of ν_μ charged-current single π^0 production on hydrocarbon in the few-GeV region using MINERvA*, *Phys. Rev.* **D 96** (2017) 072003 [arXiv:1708.03723] [INSPIRE].

[80] MINERvA collaboration, *Single Neutral Pion Production by Charged-Current $\bar{\nu}_\mu$ Interactions on Hydrocarbon at $\langle E_\nu \rangle$ =3.6 GeV*, *Phys. Lett.* **B 749** (2015) 130 [arXiv:1503.02107] [INSPIRE].

[81] MINERvA collaboration, *Cross sections for ν_μ and $\bar{\nu}_\mu$ induced pion production on hydrocarbon in the few-GeV region using MINERvA*, *Phys. Rev.* **D 94** (2016) 052005 [arXiv:1606.07127] [INSPIRE].

[82] NOvA and M. collaborations, private communication.

[83] M. Day and K.S. McFarland, *Differences in Quasi-Elastic Cross-Sections of Muon and Electron Neutrinos*, *Phys. Rev.* **D 86** (2012) 053003 [arXiv:1206.6745] [INSPIRE].

[84] MINERvA collaboration, *Constraint of the MINERvA medium energy neutrino flux using neutrino-electron elastic scattering*, *Phys. Rev.* **D 100** (2019) 092001 [arXiv:1906.00111] [INSPIRE].

[85] R. Belusevic and D. Rein, *Neutrino Reactions in the Low Y Region*, *Phys. Rev.* **D 38** (1988) 2753 [INSPIRE].

[86] A. Bodek, U. Sarica, D. Naples and L. Ren, *Methods to Determine Neutrino Flux at Low Energies:Investigation of the Low ν Method*, *Eur. Phys. J.* **C 72** (2012) 1973 [arXiv:1201.3025] [INSPIRE].

[87] DUNE collaboration, *Long-Baseline Neutrino Facility (LBNF) and Deep Underground Neutrino Experiment (DUNE)*, arXiv:1601.05471 [INSPIRE].

[88] DUNE collaboration, *Long-Baseline Neutrino Facility (LBNF) and Deep Underground Neutrino Experiment (DUNE)*, arXiv:1512.06148 [INSPIRE].

[89] ArgonCube collaboration, *ArgonCube: a novel, fully-modular approach for the realization of large-mass liquid argon TPC neutrino detectors*, CERN, Geneva (2015), CERN-SPSC-2015-009, SPSC-I-243

[90] J. Asaadi et al., *First Demonstration of a Pixelated Charge Readout for Single-Phase Liquid Argon Time Projection Chambers*, *Instruments* **4** (2020) 9 [arXiv:1801.08884] [INSPIRE].

[91] D.A. Dwyer et al., *LArPix: Demonstration of low-power 3D pixelated charge readout for liquid argon time projection chambers*, 2018 *JINST* **13** P10007 [arXiv:1808.02969] [INSPIRE].

[92] M. Auger, Y. Chen, A. Ereditato, D. Goeldi, I. Kreslo, D. Lorca et al., *ArCLight—A Compact Dielectric Large-Area Photon Detector*, *Instruments* **2** (2018) 3 [arXiv:1711.11409] [INSPIRE].

[93] M. Auger et al., *A Concept for the Fourth DUNE Far Detector Module*, DUNE doc 10419 (2018), http://docs.dunescience.org/cgi-bin/ShowDocument?docid=10419&asof=2019-11-1.

[94] A. Ereditato, C.C. Hsu, S. Janos, I. Kreslo, M. Messina, C. Rudolf von Rohr et al., *Design and operation of ARGONTUBE: a 5 m long drift liquid argon TPC*, 2013 *JINST* **8** P07002 [arXiv:1304.6961] [INSPIRE].

[95] M. Zeller et al., *First measurements with ARGONTUBE, a 5m long drift Liquid Argon TPC*, *Nucl. Instrum. Meth.* **A 718** (2013) 454 [INSPIRE].

[96] A. Ereditato, D. Goeldi, S. Janos, I. Kreslo, M. Luethi, C. Rudolf von Rohr et al., *Performance of cryogenic charge readout electronics with the ARGONTUBE LAr TPC*, 2014 *JINST* **9** P11022 [arXiv:1408.7046] [INSPIRE].

[97] M. Auger et al., *ProtoDUNE-ND: proposal to place the ArgonCube 2x2 Demonstrator on-axis in NuMI*, DUNE doc 12571 (2019), https://docs.dunescience.org/cgi-bin/private/ShowDocument?docid=12571&asof=2019-11-1.

2020 JINST 15 T08008

[98] E. Tuncer, I. Sauers, D. R. James and A. R. Ellis, *Electrical insulation characteristics of glass fiber reinforced resins*, *IEEE Transactions on Applied Superconductivity* **19** (2009) 2359.

[99] P. Adamson et al., *The NuMI Neutrino Beam*, *Nucl. Instrum. Meth.* **A 806** (2016) 279 [arXiv:1507.06690] [INSPIRE].

[100] E. Grace and J.A. Nikkel, *Index of refraction, Rayleigh scattering length and Sellmeier coefficients in solid and liquid argon and xenon*, *Nucl. Instrum. Meth.* **A 867** (2017) 204 [arXiv:1502.04213] [INSPIRE].

[101] C.M. Marshall, *LArTPC - optimal height of detector*, in *DUNE Collaboration Meeting*, 2 (2018), http://docs.dunescience.org/cgi-bin/ShowDocument?docid=19809&asof=2020-06-19.

[102] T. Heindl, T. Dandl, A. Fedenev, M. Hofmann, R. Krücken, L. Oberauer et al., *Table-top setup for investigating the scintillation properties of liquid argon*, 2011 *JINST* **6** P02011 [arXiv:1511.07720] [INSPIRE].

[103] S. Kubota, M. Hishida, M. Suzuki and J.-z. Ruan(Gen, *Dynamical behavior of free electrons in the recombination process in liquid argon, krypton and xenon*, *Phys. Rev.* **B 20** (1979) 3486 [INSPIRE].

[104] A. Hitachi, T. Takahashi, N. Funayama, K. Masuda, J. Kikuchi and T. Doke, *Effect of ionization density on the time dependence of luminescence from liquid argon and xenon*, *Phys. Rev.* **B 27** (1983) 5279 [INSPIRE].

[105] E.M. Gushchin, A.A. Kruglov and I.M. Obodovskii, *Electron dynamics in condensed argon and xenon*, *Journal of Experimental and Theoretical Physics* **55** (1982) 650.

[106] V. Chepel and H. Araujo, *Liquid noble gas detectors for low energy particle physics*, 2013 *JINST* **8** R04001 [arXiv:1207.2292] [INSPIRE].

[107] MicroBooNE collaboration, *Determination of muon momentum in the MicroBooNE LArTPC using an improved model of multiple Coulomb scattering*, 2017 *JINST* **12** P10010 [arXiv:1703.06187] [INSPIRE].

[108] MINERvA collaboration, *Measurement of Neutrino Flux from Neutrino-Electron Elastic Scattering*, *Phys. Rev.* **D 93** (2016) 112007 [arXiv:1512.07699] [INSPIRE].

[109] C.M. Marshall, K.S. McFarland and C. Wilkinson, *Neutrino-electron elastic scattering for flux determination at the DUNE oscillation experiment*, *Phys. Rev.* **D 101** (2020) 032002 [arXiv:1910.10996] [INSPIRE].

[110] NA61/SHINE collaboration, *The NA61/SHINE Experiment at the CERN SPS*, *Nucl. Phys.* **A 830** (2009) 559C [arXiv:0907.4493] [INSPIRE].

[111] ALICE collaboration, *ALICE time projection chamber: Technical Design Report*, Tech. Rep., CERN, Geneva (2000), CERN-OPEN-2000-183, CERN-LHCC-2000-001.

[112] J. Alme et al., *The ALICE TPC, a large 3-dimensional tracking device with fast readout for ultra-high multiplicity events*, *Nucl. Instrum. Meth.* **A 622** (2010) 316 [arXiv:1001.1950] [INSPIRE].

[113] F. Simon, C. Soldner and L. Weuste, *T3B — an experiment to measure the time structure of hadronic showers*, 2013 *JINST* **8** P12001 [arXiv:1309.6143] [INSPIRE].

[114] CALICE collaboration, *Construction and Commissioning of the CALICE Analog Hadron Calorimeter Prototype*, 2010 *JINST* **5** P05004 [arXiv:1003.2662] [INSPIRE].

[115] L. Emberger and F. Simon, *A highly granular calorimeter concept for long baseline near detectors*, *J. Phys. Conf. Ser.* **1162** (2019) 012033 [arXiv:1810.03677] [INSPIRE].

[116] J. Layter, *Results from pep-4 tpc*, in *Electroweak Effects at High Energies*, pp. 201–213. Springer (1985).

[117] PEP4 collaboration, *First Operation of the TPC Facility at PEP*, *J. Phys. Colloq.* **43** (1982) 42 [INSPIRE].

[118] TPC/Two Gamma collaboration, *Spatial resolution of the PEP-4 time projection chamber*, *IEEE Trans. Nucl. Sci.* **30** (1983) 76 [INSPIRE].

2020 JINST 15 T08008

[119] ALICE collaboration, *ALICE: Physics performance report, volume II*, *J. Phys.* **G 32** (2006) 1295 [INSPIRE].

[120] C. Cheshkov, *Fast Hough-transform track reconstruction for the ALICE TPC*, *Nucl. Instrum. Meth.* **A 566** (2006) 35 [INSPIRE].

[121] C. Grupen, *Physics of particle detection*, *AIP Conf. Proc.* **536** (2000) 3 [physics/9906063] [INSPIRE].

[122] C. Lippmann, *Performance of the ALICE Time Projection Chamber*, *Phys. Procedia* **37** (2012) 434 [INSPIRE].

[123] ALICE collaboration, *Performance of the ALICE Experiment at the CERN LHC*, *Int. J. Mod. Phys.* **A 29** (2014) 1430044 [arXiv:1402.4476] [INSPIRE].

[124] GEANT4 collaboration, *GEANT4: A Simulation toolkit*, *Nucl. Instrum. Meth.* **A 506** (2003) 250 [INSPIRE].

[125] *Garsoft redmine repository*, https://cdcvs.fnal.gov/redmine/projects/garsoft (accessed Feb. 19, 2019).

[126] A. Holin, *NUMI beam lessons and work in progress MINOS/MINOS+*, (2017), https://indico.cern.ch/event/674901/contributions/2799260/.

[127] J. Hylen, *NuMI Horn 1 mis-alignment*, (2016), https://indico.fnal.gov/event/13292/.

[128] A. Blondel et al., *A fully active fine grained detector with three readout views*, 2018 *JINST* **13** P02006 [arXiv:1707.01785] [INSPIRE].

[129] T2K collaboration, *T2K ND280 Upgrade - Technical Design Report*, arXiv:1901.03750 [INSPIRE].

[130] O. Mineev et al., *Beam test results of 3D fine-grained scintillator detector prototype for a T2K ND280 neutrino active target*, *Nucl. Instrum. Meth.* **A 923** (2019) 134 [arXiv:1808.08829] [INSPIRE].

[131] MINERvA collaboration, *Neutron measurements from antineutrino hydrocarbon reactions*, *Phys. Rev.* **D 100** (2019) 052002 [arXiv:1901.04892] [INSPIRE].

[132] T2K collaboration, *Characterization of nuclear effects in muon-neutrino scattering on hydrocarbon with a measurement of final-state kinematics and correlations in charged-current pionless interactions at T2K*, *Phys. Rev.* **D 98** (2018) 032003 [arXiv:1802.05078] [INSPIRE].

[133] E.L. Snider and G. Petrillo, *LArSoft: Toolkit for Simulation, Reconstruction and Analysis of Liquid Argon TPC Neutrino Detectors*, *J. Phys. Conf. Ser.* **898** (2017) 042057 [INSPIRE].

[134] I. Bird et al., *Update of the Computing Models of the WLCG and the LHC Experiments*, CERN, Geneva (2014), CERN-LHCC-2014-014, LCG-TDR-002.

[135] W.O. Board, *Evolution of scientific computing in the next, decade: Hep and beyond*, http://wlcg-docs.web.cern.ch/wlcg-docs/technical_documents/HEP-Computing-Evolution.pdf.

[136] D. Berzano et al., *HEP Software Foundation Community White Paper Working Group – Data Organization, Management and Access (DOMA)*, arXiv:1812.00761 [INSPIRE].

[137] M. Ritter et al., *Belle II Conditions Database*, *J. Phys. Conf. Ser.* **1085** (2018) 032032 [INSPIRE].

[138] M. Bracko, M. Clemencic, D. Dykstra, A. Formica, G. Govi, M. Jouvin et al., *HEP Software Foundation Community White Paper Working Group – Conditions Data*, arXiv:1901.05429 [INSPIRE].

[139] LHCB collaboration, *LHCb distributed computing in run II and its evolution towards run III*, in *proceedings of 38th International Conference on High Energy Physics (ICHEP2016)*, *PoS* **ICHEP** (2016) 191.

[140] ATLAS collaboration, *PanDA for ATLAS distributed computing in the next decade*, *J. Phys. Conf. Ser.* **898** (2017) 052002 [INSPIRE].

2020 JINST 15 T08008

The DUNE collaboration

B. Abi,[1] R. Acciarri,[2] M.A. Acero,[3] G. Adamov,[4] D. Adams,[5] M. Adinolfi,[6] Z. Ahmad,[7] J. Ahmed,[8] T. Alion,[9] S. Alonso Monsalve,[10] C. Alt,[11] J. Anderson,[12] C. Andreopoulos,[14,13] M. Andrews,[2] F. Andrianala,[15] S. Andringa,[16] A. Ankowski,[17] M. Antonova,[18] S. Antusch,[19] A. Aranda-Fernandez,[20] A. Ariga,[21] L.O. Arnold,[22] M.A. Arroyave,[23] J. Asaadi,[24] A. Aurisano,[25] V. Aushev,[26] D. Autiero,[27] F. Azfar,[1] H. Back,[28] J.J. Back,[8] C. Backhouse,[29] P. Baesso,[6] L. Bagby,[2] R. Bajou,[30] S. Balasubramanian,[31] P. Baldi,[32] B. Bambah,[33] F. Barao,[16,34] G. Barenboim,[18] G. Barker,[8] W. Barkhouse,[35] C. Barnes,[36] G. Barr,[1] J. Barranco Monarca,[37] N. Barros,[16,38] J.L. Barrow,[39,2] A. Bashyal,[40] V. Basque,[41] F. Bay,[42] J. Bazo Alba,[43] J.F. Beacom,[44] E. Bechetoille,[27] B. Behera,[45] L. Bellantoni,[2] G. Bellettini,[46] V. Bellini,[48,47] O. Beltramello,[10] D. Belver,[49] N. Benekos,[10] F. Bento Neves,[16] J. Berger,[50] S. Berkman,[2] P. Bernardini,[51] R.M. Berner,[21] H. Berns,[52] S. Bertolucci,[54,53] M. Betancourt,[2] Y. Bezawada,[52] M. Bhattacharjee,[55] B. Bhuyan,[55] S. Biagi,[56] J. Bian,[32] M. Biassoni,[57] K. Biery,[2] B. Bilki,[58] M. Bishai,[5] A. Bitadze,[41] A. Blake,[59] B. Blanco Siffert,[60] F. Blaszczyk,[2] G. Blazey,[61] E. Blucher,[62] J. Boissevain,[63] S. Bolognesi,[64] T. Bolton,[65] M. Bonesini,[57,66] M. Bongrand,[67] F. Bonini,[5] A. Booth,[9] C. Booth,[68] S. Bordoni,[10] A. Borkum,[9] T. Boschi,[69] N. Bostan,[70] P. Bour,[71] S. Boyd,[8] D. Boyden,[61] J. Bracinik,[72] D. Braga,[2] D. Brailsford,[59] A. Brandt,[24] J. Bremer,[10] C. Brew,[14] E. Brianne,[41] S.J. Brice,[2] C. Brizzolari,[57,66] C. Bromberg,[73] G. Brooijmans,[22] J. Brooke,[6] A. Bross,[2] G. Brunetti,[74] N. Buchanan,[45] H. Budd,[75] D. Caiulo,[27] P. Calafiura,[76] J. Calcutt,[73] M. Calin,[77] S. Calvez,[45] E. Calvo,[49] L. Camilleri,[22] A. Caminata,[78] M. Campanelli,[29] D. Caratelli,[2] G. Carini,[5] B. Carlus,[27] P. Carniti,[57] I. Caro Terrazas,[45] H. Carranza,[24] A. Castillo,[79] C. Castromonte,[80] C. Cattadori,[57] F. Cavalier,[67] F. Cavanna,[2] S. Centro,[74] G. Cerati,[2] A. Cervelli,[54] A. Cervera Villanueva,[18] M. Chalifour,[10] C. Chang,[81] E. Chardonnet,[30] A. Chatterjee,[50] S. Chattopadhyay,[7] J. Chaves,[82] H. Chen,[5] M. Chen,[32] Y. Chen,[21] D. Cherdack,[83] C. Chi,[22] S. Childress,[2] A. Chiriacescu,[77] K. Cho,[84] S. Choubey,[85] A. Christensen,[45] D. Christian,[2] G. Christodoulou,[10] E. Church,[28] P. Clarke,[86] T.E. Coan,[87] A.G. Cocco,[88] J. Coelho,[67] E. Conley,[89] J. Conrad,[90] M. Convery,[17] L. Corwin,[91] P. Cotte,[64] L. Cremaldi,[92] L. Cremonesi,[29] J.I. Crespo-Anadón,[49] E. Cristaldo,[93] R. Cross,[59] C. Cuesta,[49] Y. Cui,[81] D. Cussans,[6] M. Dabrowski,[5] H. Da Motta,[94] L. Da Silva Peres,[60] Q. David,[27] G.S. Davies,[92] S. Davini,[78] J. Dawson,[30] K. De,[24] R.M. De Almeida,[95] P. Debbins,[70] I. De Bonis,[96] M. Decowski,[42,97] A. De Gouvea,[98] P.C. De Holanda,[99] I.L. De Icaza Astiz,[9] A. Deisting,[100] P. De Jong,[42,97] A. Delbart,[64] D. Delepine,[37] M. Delgado,[101] A. Dell'Acqua,[10] P. De Lurgio,[12] J.R. De Mello Neto,[60] D.M. DeMuth,[102] S. Dennis,[103] C. Densham,[14] G. Deptuch,[2] A. De Roeck,[10] V. De Romeri,[18] J. De Vries,[103] R. Dharmapalan,[104] M. Dias,[105] F. Diaz,[43] J. Diaz,[106] S. Di Domizio,[78] L. Di Giulio,[10] P. Ding,[2] L. Di Noto,[78] C. Distefano,[56] R. Diurba,[107] M. Diwan,[5] Z. Djurcic,[12] N. Dokania,[108] M. Dolinski,[109] L. Domine,[17] D. Douglas,[73] F. Drielsma,[17] D. Duchesneau,[96] K. Duffy,[2] P. Dunne,[110] T. Durkin,[14] H. Duyang,[111] O. Dvornikov,[104] D. Dwyer,[76] A. Dyshkant,[61] M. Eads,[61] D. Edmunds,[73] J. Eisch,[112] S. Emery,[64] A. Ereditato,[21] C. Escobar,[2] L. Escudero Sanchez,[103] J.J. Evans,[41] E. Ewart,[106] A.C. Ezeribe,[68] K. Fahey,[2] A. Falcone,[57,66] C. Farnese,[74] Y. Farzan,[113] J. Felix,[37] E. Fernandez-Martinez,[114] P. Fernandez Menendez,[18] F. Ferraro,[78] L. Fields,[2] A. Filkins,[115] F. Filthaut,[42,116] R.S. Fitzpatrick,[36] W. Flanagan,[117] B. Fleming,[31] R. Flight,[75] J. Fowler,[89] W. Fox,[106] J. Franc,[71] K. Francis,[61] D. Franco,[31] J. Freeman,[2] J. Freestone,[41] J. Fried,[5] A. Friedland,[17] S. Fuess,[2]

2020 JINST 15 T08008

I. Furic,[118] A.P. Furmanski,[107] A. Gago,[43] H. Gallagher,[119] A. Gallego-Ros,[49] N. Gallice,[121,120] V. Galymov,[27] E. Gamberini,[10] T. Gamble,[68] R. Gandhi,[85] R. Gandrajula,[73] S. Gao,[5] D. Garcia-Gamez,[122] M.Á. García-Peris,[18] S. Gardiner,[2] D. Gastler,[123] G. Ge,[22] B. Gelli,[99] A. Gendotti,[11] S. Gent,[124] Z. Ghorbani-Moghaddam,[78] D. Gibin,[74] I. Gil-Botella,[49] C. Girerd,[27] A. Giri,[125] D. Gnani,[76] O. Gogota,[26] M. Gold,[126] S. Gollapinni,[63] K. Gollwitzer,[2] R.A. Gomes,[127] L. Gomez Bermeo,[79] L.S. Gomez Fajardo,[79] F. Gonnella,[72] J. Gonzalez-Cuevas,[93] M.C. Goodman,[12] O. Goodwin,[41] S. Goswami,[128] C. Gotti,[57] E. Goudzovski,[72] C. Grace,[76] M. Graham,[17] E. Gramellini,[31] R. Gran,[129] E. Granados,[37] A. Grant,[130] C. Grant,[123] D. Gratieri,[95] P. Green,[41] S. Green,[103] L. Greenler,[131] M. Greenwood,[40] J. Greer,[6] C. Griffith,[9] M. Groh,[106] J. Grudzinski,[12] K. Grzelak,[132] W. Gu,[5] V. Guarino,[12] R. Guenette,[133] A. Guglielmi,[74] B. Guo,[111] K. Guthikonda,[134] R. Gutierrez,[101] P. Guzowski,[41] M.M. Guzzo,[99] S. Gwon,[135] A. Habig,[129] A. Hackenburg,[31] H. Hadavand,[24] R. Haenni,[21] A. Hahn,[2] J. Haigh,[8] J. Haiston,[91] T. Hamernik,[2] P. Hamilton,[110] J. Han,[50] K. Harder,[14] D.A. Harris,[2,136] J. Hartnell,[9] T. Hasegawa,[137] R. Hatcher,[2] E. Hazen,[123] A. Heavey,[2] K.M. Heeger,[31] K. Hennessy,[13] S. Henry,[75] M. Hernandez Morquecho,[37] K. Herner,[2] L. Hertel,[32] A.S. Hesam,[10] J. Hewes,[25] A. Higuera Pichardo,[83] T. Hill,[138] S.J. Hillier,[72] A. Himmel,[2] J. Hoff,[2] C. Hohl,[19] A. Holin,[29] E. Hoppe,[28] G.A. Horton-Smith,[65] M. Hostert,[69] A. Hourlier,[90] B. Howard,[106] R. Howell,[75] J. Huang,[139] J. Huang,[52] J. Hugon,[140] G. Iles,[110] A.M. Iliescu,[54] R. Illingworth,[2] A. Ioannisian,[141] R. Itay,[17] A. Izmaylov,[18] E. James,[2] B. Jargowsky,[32] F. Jediny,[71] C. Jesús-Valls,[142] X. Ji,[5] L. Jiang,[143] S. Jiménez,[49] A. Jipa,[77] A. Joglekar,[81] C. Johnson,[45] R. Johnson,[25] B. Jones,[24] S. Jones,[29] C. Jung,[108] T. Junk,[2] Y. Jwa,[22] M. Kabirnezhad,[1] A. Kaboth,[14] I. Kadenko,[26] F. Kamiya,[144] G. Karagiorgi,[22] A. Karcher,[76] M. Karolak,[64] Y. Karyotakis,[96] S. Kasai,[145] S.P. Kasetti,[140] L. Kashur,[45] N. Kazaryan,[141] E. Kearns,[123] P. Keener,[82] K.J. Kelly,[2] E. Kemp,[99] W. Ketchum,[2] S. Kettell,[5] M. Khabibullin,[146] A. Khotjantsev,[146] A. Khvedelidze,[4] D. Kim,[10] B. King,[2] B. Kirby,[5] M. Kirby,[2] J. Klein,[82] K. Koehler,[131] L.W. Koerner,[83] S. Kohn,[147,76] P.P. Koller,[21] M. Kordosky,[115] T. Kosc,[27] U. Kose,[10] V. Kostelecky,[106] K. Kothekar,[6] F. Krennrich,[112] I. Kreslo,[21] Y. Kudenko,[146] V. Kudryavtsev,[68] S. Kulagin,[146] J. Kumar,[104] R. KUMAR,[148] C. Kuruppu,[111] V. Kus,[71] T. Kutter,[140] A. Lambert,[76] K. Lande,[82] C.E. Lane,[109] K. Lang,[139] T. Langford,[31] P. Lasorak,[9] D. Last,[82] C. Lastoria,[49] A. Laundrie,[131] A. Lawrence,[76] I. Lazanu,[77] R. LaZur,[45] T. Le,[119] J. Learned,[104] P. LeBrun,[27] G. Lehmann Miotto,[10] R. Lehnert,[106] M. Leigui de Oliveira,[144] M. Leitner,[76] M. Leyton,[142] L. Li,[32] S. Li,[5] S. Li,[17] T. Li,[86] Y. Li,[5] H. Liao,[65] C. Lin,[76] S. Lin,[140] A. Lister,[131] B.R. Littlejohn,[149] J. Liu,[32] S. Lockwitz,[2] T. Loew,[76] M. Lokajicek,[150] I. Lomidze,[4] K. Long,[110] K. Loo,[151] D. Lorca,[21] T. Lord,[8] J. LoSecco,[152] W.C. Louis,[63] K. Luk,[147,76] X. Luo,[153] N. Lurkin,[72] T. Lux,[142] V.P. Luzio,[144] D. MacFarland,[17] A. Machado,[99] P. Machado,[2] C. Macias,[106] J. Macier,[2] A. Maddalena,[154] P. Madigan,[147,76] S. Magill,[12] K. Mahn,[73] A. Maio,[16,38] J.A. Maloney,[155] G. Mandrioli,[54] J.C. Maneira,[16,38] L. Manenti,[29] S. Manly,[75] A. Mann,[119] K. Manolopoulos,[14] M. Manrique Plata,[106] A. Marchionni,[2] W. Marciano,[5] D. Marfatia,[104] C. Mariani,[143] J. Maricic,[104] F. Marinho,[156] A.D. Marino,[157] M. Marshak,[107] C. Marshall,[76] J. Marshall,[8] J. Marteau,[27] J. Martin-Albo,[18] N. Martinez,[158] D.A. Martinez Caicedo,[91] S. Martynenko,[108] K. Mason,[119] A. Mastbaum,[159] M. Masud,[18] S. Matsuno,[104] J. Matthews,[140] C. Mauger,[82] N. Mauri,[54,53] K. Mavrokoridis,[13] R. Mazza,[57] A. Mazzacane,[2] E. Mazzucato,[64] E. McCluskey,[2] N. McConkey,[41] K.S. McFarland,[75] C. McGrew,[108] A. McNab,[41] A. Mefodiev,[146] P. Mehta,[160] P. Melas,[161] M. Mellinato,[57,66] O. Mena,[18] S. Menary,[136] H. Mendez,[158] A. Menegolli,[162] G. Meng,[74] M. Messier,[106] W. Metcalf,[140] M. Mewes,[106] H. Meyer,[163] T. Miao,[2] G. Michna,[124] T. Miedema,[42,116] J. Migenda,[68] R. Milincic,[104] W. Miller,[107] J. Mills,[119] C. Milne,[138] O. Mineev,[146] O.G. Miranda,[164] S. Miryala,[5] C. Mishra,[2] S. Mishra,[111] A. Mislivec,[107] D. Mladenov,[10] I. Mocioiu,[165] K. Moffat,[69] N. Moggi,[54,53] R. Mohanta,[33] T.A. Mohayai,[2] N. Mokhov,[2] J.A. Molina,[93] L. Molina Bueno,[11] A. Montanari,[54] C. Montanari,[162] D. Montanari,[2] L.M. Montano Zetina,[164] J. Moon,[90] M. Mooney,[45] A. Moor,[103] D. Moreno,[101] B. Morgan,[8] C. Morris,[83] C. Mossey,[2] E. Motuk,[29] C.A. Moura,[144] J. Mousseau,[36] W. Mu,[2] L. Mualem,[166] J. Mueller,[45] M. Muether,[163] S. Mufson,[106] F. Muheim,[86] A. Muir,[130] M. Mulhearn,[52] H. Muramatsu,[107] S. Murphy,[11] J. Musser,[106] J. Nachtman,[70] S. Nagu,[167] M. Nalbandyan,[141]

2020 JINST 15 T08008

R. Nandakumar,[14] D. Naples,[50] S. Narita,[168] D. Navas-Nicolás,[49] N. Nayak,[32] M. Nebot-Guinot,[86] L. Necib,[166] K. Negishi,[168] J.K. Nelson,[115] J. Nesbit,[131] M. Nessi,[10] D. Newbold,[14] M. Newcomer,[82] D. Newhart,[2] R. Nichol,[29] E. Niner,[2] K. Nishimura,[104] A. Norman,[2] R. Northrop,[62] P. Novella,[18] J.A. Nowak,[59] M. Oberling,[12] A. Olivares Del Campo,[69] A. Olivier,[75] Y. Onel,[70] Y. Onishchuk,[26] J. Ott,[32] L. Pagani,[52] S. Pakvasa,[104] O. Palamara,[2] S. Palestini,[10] J.M. Paley,[2] M. Pallavicini,[78] C. Palomares,[49] E. Pantic,[52] V. Paolone,[50] V. Papadimitriou,[2] R. Papaleo,[56] A. Papanestis,[14] S. Paramesvaran,[6] S. Parke,[2] Z. Parsa,[5] M. Parvu,[77] S. Pascoli,[69] L. Pasqualini,[54,53] J. Pasternak,[110] J. Pater,[41] C. Patrick,[29] L. Patrizii,[54] R.B. Patterson,[166] S. Patton,[76] T. Patzak,[30] A. Paudel,[65] B. Paulos,[131] L. Paulucci,[144] Z. Pavlovic,[2] G. Pawloski,[107] D. Payne,[13] V. Pec,[68] S.J. Peeters,[9] Y. Penichot,[64] E. Pennacchio,[27] A. Penzo,[70] O.L. Peres,[99] J. Perry,[86] D. Pershey,[89] G. Pessina,[57] G. Petrillo,[17] C. Petta,[48,47] R. Petti,[111] F. Piastra,[21] L. Pickering,[73] F. Pietropaolo,[10,74] J. Pillow,[8] R. Plunkett,[2] R. Poling,[107] X. Pons,[10] N. Poonthottathil,[112] S. Pordes,[2] M. Potekhin,[5] R. Potenza,[48,47] B.V. Potukuchi,[169] J. Pozimski,[110] M. Pozzato,[54,53] S. Prakash,[99] T. Prakash,[76] S. Prince,[133] G. Prior,[16] D. Pugnere,[27] K. Qi,[108] X. Qian,[5] J. Raaf,[2] R. Raboanary,[15] V. Radeka,[5] J. Rademacker,[6] B. Radics,[11] A. Rafique,[12] E. Raguzin,[5] M. Rai,[8] M. Rajaoalisoa,[25] I. Rakhno,[2] H. Rakotondramanana,[15] L. Rakotondravohitra,[15] Y. Ramachers,[8] R. Rameika,[2] M. Ramirez Delgado,[37] B. Ramson,[2] A. Rappoldi,[162] G. Raselli,[162] P. Ratoff,[59] S. Ravat,[10] H. Razafinime,[15] J. Real,[170] B. Rebel,[131,2] D. Redondo,[49] M. Reggiani-Guzzo,[99] T. Rehak,[109] J. Reichenbacher,[91] S.D. Reitzner,[2] A. Renshaw,[83] S. Rescia,[5] F. Resnati,[10] A. Reynolds,[1] G. Riccobene,[56] L.C. Rice,[50] K. Rielage,[63] Y. Rigaut,[11] D. Rivera,[82] L. Rochester,[17] M. Roda,[13] P. Rodrigues,[1] M. Rodriguez Alonso,[10] J. Rodriguez Rondon,[91] A. Roeth,[89] H. Rogers,[45] S. Rosauro-Alcaraz,[114] M. Rossella,[162] J. Rout,[160] S. Roy,[85] A. Rubbia,[11] C. Rubbia,[171] B. Russell,[76] J. Russell,[17] D. Ruterbories,[75] R. Saakyan,[29] S. Sacerdoti,[30] T. Safford,[73] N. Sahu,[125] P. Sala,[121,10] N. Samios,[5] M. Sanchez,[112] D.A. Sanders,[92] D. Sankey,[14] S. Santana,[158] M. Santos-Maldonado,[158] N. Saoulidou,[161] P. Sapienza,[56] C. Sarasty,[25] I. Sarcevic,[172] G. Savage,[2] V. Savinov,[50] A. Scaramelli,[162] A. Scarff,[68] A. Scarpelli,[30] T. Schaffer,[129] H. Schellman,[40,2] P. Schlabach,[2] D. Schmitz,[62] K. Scholberg,[89] A. Schukraft,[2] E. Segreto,[99] J. Sensenig,[82] I. Seong,[32] A. Sergi,[72] F. Sergiampietri,[108] D. Sgalaberna,[11] M. Shaevitz,[22] S. Shafaq,[160] M. Shamma,[81] H.R. Sharma,[169] R. Sharma,[5] T. Shaw,[2] C. Shepherd-Themistocleous,[14] S. Shin,[173] D. Shooltz,[73] R. Shrock,[108] L. Simard,[67] N. Simos,[5] J. Sinclair,[21] G. Sinev,[89] J. Singh,[167] J. Singh,[167] V. Singh,[174,175] R. Sipos,[10] F. Sippach,[22] G. Sirri,[54] A. Sitraka,[91] K. Siyeon,[135] D. Smargianaki,[108] A. Smith,[89] A. Smith,[103] E. Smith,[106] P. Smith,[106] J. Smolik,[71] M. Smy,[32] P. Snopok,[149] M. Soares Nunes,[99] H. Sobel,[32] M. Soderberg,[176] C.J. Solano Salinas,[80] S. Söldner-Rembold,[41] N. Solomey,[163] V. Solovov,[16] W.E. Sondheim,[63] M. Sorel,[18] J. Soto-Oton,[49] A. Sousa,[25] K. Soustruznik,[177] F. Spagliardi,[1] M. Spanu,[5] J. Spitz,[36] N.J. Spooner,[68] K. Spurgeon,[176] R. Staley,[72] M. Stancari,[2] L. Stanco,[74] H. Steiner,[76] J. Stewart,[5] B. Stillwell,[62] J. Stock,[91] F. Stocker,[10] T. Stokes,[140] M. Strait,[107] T. Strauss,[2] S. Striganov,[2] A. Stuart,[20] D. Summers,[92] A. Surdo,[51] V. Susic,[19] L. Suter,[2] C. Sutera,[48,47] R. Svoboda,[52] B. Szczerbinska,[178] A. Szelc,[41] R. Talaga,[12] H. Tanaka,[17] B. Tapia Oregui,[139] A. Tapper,[110] S. Tariq,[2] E. Tatar,[138] R. Tayloe,[106] A. Teklu,[108] M. Tenti,[54] K. Terao,[17] C.A. Ternes,[18] F. Terranova,[57,66] G. Testera,[78] A. Thea,[14] J.L. Thompson,[68] C. Thorn,[5] S. Timm,[2] A. Tonazzo,[30] M. Torti,[57,66] M. Tortola,[18] F. Tortorici,[48,47] D. Totani,[2] M. Toups,[2] C. Touramanis,[13] J. Trevor,[166] W.H. Trzaska,[151] Y.T. Tsai,[17] Z. Tsamalaidze,[4] K. Tsang,[17] N. Tsverava,[4] S. Tufanli,[10] C. Tull,[76] E. Tyley,[68] M. Tzanov,[140] M.A. Uchida,[103] J. Urheim,[106] T. Usher,[17] M. Vagins,[179] P. Vahle,[115] G. Valdiviesso,[180] E. Valencia,[115] Z. Vallari,[166] J.W. Valle,[18] S. Vallecorsa,[10] R. Van Berg,[82] R.G. Van de Water,[63] D. Vanegas Forero,[99] F. Varanini,[74] D. Vargas,[142] G. Varner,[104] J. Vasel,[106] G. Vasseur,[64] K. Vaziri,[2] S. Ventura,[74] A. Verdugo,[49] S. Vergani,[103] M.A. Vermeulen,[42] M. Verzocchi,[2] H. Vieira de Souza,[99] C. Vignoli,[154] C. Vilela,[108] B. Viren,[5] T. Vrba,[71] T. Wachala,[181] A.V. Waldron,[110] M. Wallbank,[25] H. Wang,[182] J. Wang,[52] Y. Wang,[182] Y. Wang,[108] K. Warburton,[112] D. Warner,[45] M. Wascko,[110] D. Waters,[29] A. Watson,[72] P. Weatherly,[109] A. Weber,[14,1] M. Weber,[21] H. Wei,[5] A. Weinstein,[112] D. Wenman,[131] M. Wetstein,[112] M.R. While,[91] A. White,[24] L.H. Whitehead,[103] D. Whittington,[176] M.J. Wilking,[108] C. Wilkinson,[21] Z. Williams,[24] F. Wilson,[14]

2020 JINST 15 T08008

R.J. Wilson,[45] J. Wolcott,[119] T. Wongjirad,[119] K. Wood,[108] L. Wood,[28] E. Worcester,[5] M. Worcester,[5] C. Wret,[75] W. Wu,[2] W. Wu,[32] Y. Xiao,[32] G. Yang,[108] T. Yang,[2] N. Yershov,[146] K. Yonehara,[2] T. Young,[35] B. Yu,[5] J. Yu,[24] J. Zalesak,[150] L. Zambelli,[96] B. Zamorano,[122] A. Zani,[121] L. Zazueta,[115] G. Zeller,[2] J. Zennamo,[2] K. Zeug,[131] C. Zhang,[5] M. Zhao,[5] E. Zhivun,[5] G. Zhu,[44] E.D. Zimmerman,[157] M. Zito,[64] S. Zucchelli,[54,53] J. Zuklin,[150] V. Zutshi[61] and R. Zwaska[2]

1 *University of Oxford, Oxford, OX1 3RH, United Kingdom*
2 *Fermi National Accelerator Laboratory, Batavia, IL 60510, USA*
3 *Universidad del Atlantico, Carrera 30 Número 8- 49 Puerto Colombia - Atlántico, Colombia*
4 *Georgian Technical University, 77 Kostava Str. 0160, Tbilisi, Georgia*
5 *Brookhaven National Laboratory, Upton, NY 11973, USA*
6 *University of Bristol, H. H. Wills Physics Laboratory, Tyndall Avenue Bristol BS8 1TL, United Kingdom*
7 *Variable Energy Cyclotron Centre, 1/AF, Bidhannagar Kolkata - 700 064 West Bengal, India*
8 *University of Warwick, Coventry CV4 7AL, United Kingdom*
9 *University of Sussex, Brighton, BN1 9RH, United Kingdom*
10 *CERN, European Organization for Nuclear Research 1211 Genève 23, Switzerland, CERN*
11 *ETH Zurich, Institute for Particle Physics, Zurich, Switzerland*
12 *Argonne National Laboratory, Argonne, IL 60439, USA*
13 *University of Liverpool, L69 7ZE, Liverpool, United Kingdom*
14 *STFC Rutherford Appleton Laboratory, OX11 0QX Harwell Campus, Didcot, United Kingdom*
15 *University of Antananarivo, BP 566, Antananarivo 101, Madagascar*
16 *Laboratório de Instrumentação e Física Experimental de Partículas, Av. Gama Pinto, n.2, Lisboa, Complexo Interdisciplinar (3is) 1649-003 Portugal*
17 *SLAC National Acceleratory Laboratory, Menlo Park, CA 94025, USA*
18 *Instituto de Fisica Corpuscular, Catedratico Jose Beltran, 2 E-46980 Paterna (Valencia), Spain*
19 *University of Basel, Klingelbergstrasse 82, CH-4056 Basel, Switzerland*
20 *Universidad de Colima, 340 Colonia Villa San Sebastian Colima, Colima, Mexico*
21 *University of Bern, Sidlerstrasse 5, CH-3012 Bern, Switzerland*
22 *Columbia University, New York, NY 10027, USA*
23 *Universidad EIA, Via José María Córdoba #km 2 + 200, Envigado, Antioquia*
24 *University of Texas at Arlington, Arlington, TX 76019, USA*
25 *University of Cincinnati, Cincinnati, OH 45221, USA*
26 *Kyiv National University, 64, 01601 Kyiv, Ukraine*
27 *Institut de Physique des 2 Infinis de Lyon, Rue E. Fermi 4 69622 Villeurbanne, France*
28 *Pacific Northwest National Laboratory, Richland, WA 99352, USA*
29 *University College London, London, WC1E 6BT, United Kingdom*
30 *Université de Paris, CNRS, Astroparticule et Cosmologie, F-75006, Paris, France*
31 *Yale University, New Haven, CT 06520, USA*
32 *University of California Irvine, Irvine, CA 92697, USA*
33 *University of Hyderabad, Gachibowli, Hyderabad - 500 046, India*
34 *Instituto Superior T'ecnico - IST, Univ. de Lisboa, Portugal*
35 *University of North Dakota, 3501 University Ave Grand Forks, ND 58202-8357, USA*
36 *University of Michigan, Ann Arbor, MI 48109, USA*
37 *Universidad de Guanajuato, Gto., C.P. 37000, Mexico*
38 *Faculdade de Ci^encias - FCUL, Univ. de Lisboa, Portugal*
39 *University of Tennessee at Knoxville, TN, 37996, USA*
40 *Oregon State University, Corvallis, OR 97331, USA*
41 *University of Manchester, Oxford Road, Manchester M13 9PL, United Kingdom*
42 *Nikhef National Institute of Subatomic Physics, Science Park, Amsterdam, Netherlands*
43 *Pontificia Universidad Católica del Perú, Apartado 1761, Lima, Perú*
44 *Ohio State University, 191 W. Woodruff Ave. Columbus, OH 43210, USA*
45 *Colorado State University, Fort Collins, CO 80523, USA*

2020 JINST 15 T08008

46 *Università di Pisa, Theor. Division; Largo B. Pontecorvo 3, Ed. B-C, I-56127 Pisa, Italy*
47 *Istituto Nazionale di Fisica Nucleare Sezione di Catania, Via Santa Sofia 64, I-95123 Catania, Italy*
48 *Università di Catania, Dipartimento di Fisica e Astronomia "E. Majorana", Italy*
49 *CIEMAT, Centro de Investigaciones Energéticas, Medioambientales y Tecnológicas, Av. Complutense, 40, E-28040 Madrid, Spain*
50 *University of Pittsburgh, Pittsburgh, PA 15260, USA*
51 *Università del Salento and Istituto Nazionale Fisica Nucleare, Via Provinciale per Arnesano, 73100 Lecce, Italy*
52 *University of California Davis, Davis, CA 95616, USA*
53 *University of Bologna, Department of Physics and Astronomy, viale Berti Pichat 6/2, 40127 Bologna, Italy*
54 *Istituto Nazionale di Fisica Nucleare Bologna, 40127 Bologna BO, Italy*
55 *Indian Institute of Technology Guwahati, Guwahati, 781 039, India*
56 *Laboratori Nazionali del Sud, Via S. Sofia 62, 95123 Catania, Italy*
57 *Istituto Nazionale di Fisica Nucleare Sezione di Milano Bicocca , Piazza della Scienza, 3 - I-20126 Milano, Italy*
58 *Beykent University, Istanbul*
59 *Lancaster University, Bailrigg, Lancaster LA1 4YB, United Kingdom*
60 *Universidade Federal do Rio de Janeiro, Rio de Janeiro - RJ, 21941-901, Brazil*
61 *Northern Illinois University, Department of Physics, DeKalb, Illinois 60115, USA*
62 *University of Chicago, Chicago, IL 60637, USA*
63 *Los Alamos National Laboratory, Los Alamos, NM 87545, USA*
64 *CEA/Saclay, IRFU Institut de Recherche sur les Lois Fondamentales de l'Univers, F-91191 Gif-sur-Yvette CEDEX, France*
65 *Kansas State University, Manhattan, KS 66506, USA*
66 *University of Milano-Bicocca, Dep. of Physics "G. Occhialini", Piazza della Scienza 3, Milano, Italy*
67 *Laboratoire de l'Accélérateur Linéaire , Bâtiment 200, 91440 Orsay, France*
68 *University of Sheffield, Department of Physics and Astronomy, Sheffield S3 7RH, United Kingdom*
69 *Durham University, South Road, Durham DH1 3LE, United Kingdom*
70 *University of Iowa, Department of Physics and Astronomy 203 Van Allen Hall Iowa City, IA 52242, USA*
71 *Czech Technical University in Prague, Břehová 78/7, 115 19 Prague 1, Czech Republic*
72 *University of Birmingham, Edgbaston, Birmingham B15 2TT, United Kingdom*
73 *Michigan State University, East Lansing, MI 48824, USA*
74 *Universtà Degli Studi di Padova, Dip. Fisica e Astronomia G. Galilei and INFN Sezione di Padova, I-35131 Padova, Italy*
75 *University of Rochester, Rochester, NY 14627, USA*
76 *Lawrence Berkeley National Laboratory, Berkeley, CA 94720, USA*
77 *University of Bucharest, Faculty of Physics, Bucharest, Romania*
78 *Università degli studi di Genova, Istituto Nazionale di Fisica Nucleare Genova, 16126 Genova GE, Italy*
79 *Universidad Sergio Arboleda, Cll 74 -14 -14, 11022 Bogotá, Colombia*
80 *Universidad Nacional de Ingeniería, Av. Tupac Amaru 210, Lima 25, Perú*
81 *University of California Riverside, 900 University Ave, Riverside CA 92521*
82 *University of Pennsylvania, Philadelphia, PA 19104, USA*
83 *University of Houston, Houston, TX 77204, USA*
84 *Korea Institute of Science and Technology Information, Daejeon, 34141, South Korea*
85 *Harish-Chandra Research Institute, Jhunsi, Allahabad 211 019, India*
86 *University of Edinburgh, Edinburgh EH8 9YL, United Kingdom*
87 *Southern Methodist University, Dallas, TX 75275, USA*
88 *Istituto Nazionale di Fisica Nucleare Sezione di Napoli, Complesso Universitario di Monte S. Angelo, I-80126 Napoli, Italy*
89 *Duke University, Durham, NC 27708, USA*
90 *Massachusetts Institute of Technology, Cambridge, MA 02139, USA*
91 *South Dakota School of Mines and Technology, Rapid City, SD 57701, USA*
92 *University of Mississippi, P.O. Box 1848, University, MS 38677 USA*
93 *Universidad Nacional de Asunción, San Lorenzo, Paraguay*

2020 JINST 15 T08008

94 *Centro Brasileiro de Pesquisas Físicas, Rio de Janeiro, RJ 22290-180, Brazil*
95 *Fluminense Federal University, Rua Miguel de Frias, 9 Icaraí Niterói - RJ, 24220-900, Brazil*
96 *Laboratoire d'Annecy-le-Vieux de Physique des Particules, CNRS/IN2P3 and Université Savoie Mont Blanc, CNRS/IN2P3 and Université Savoie Mont Blanc, 74941 Annecy-le-Vieux, France*
97 *University of Amsterdam, Science Park 105, NL-1098 XG Amsterdam, The Netherlands*
98 *Northwestern University, Evanston, Il 60208, USA*
99 *Universidade Estadual de Campinas, Campinas - SP, 13083-970, Brazil*
100 *Royal Holloway College London, Egham, Surrey, TW20 0EX*
101 *Universidad Antonio Nariño, Cra 3 Este No 47A-15, Bogotá, Colombia*
102 *Valley City State University, Valley City, ND 58072, USA*
103 *University of Cambridge, JJ Thomson Avenue, Cambridge CB3 0HE, United Kingdom*
104 *University of Hawaii, Honolulu, HI 96822, USA*
105 *São Paulo Federal University, Departamento de Física-Campus Diadema,09913-030, São Paulo, Brazil*
106 *Indiana University, Bloomington, IN 47405, USA*
107 *University of Minnesota Twin Cities, Minneapolis, MN 55455, USA*
108 *Stony Brook University, SUNY, Stony Brook, New York 11794, USA*
109 *Drexel University, Philadelphia, PA 19104, USA*
110 *Imperial College of Science Technology and Medicine, Blackett Laboratory Prince Consort Road, London SW7 2BZ, United Kingdom*
111 *University of South Carolina, Columbia, SC 29208, USA*
112 *Iowa State University, Ames, Iowa 50011, USA*
113 *Institute for Research in Fundamental Sciences , Farmanieh St. Tehran, 19538-33511, Iran*
114 *Madrid Autonoma University and IFT UAM/CSIC, Ciudad Universitaria de Cantoblanco 28049 Madrid, Spain*
115 *College of William and Mary, Williamsburg, VA 23187, USA*
116 *Radboud University, Heyendaalseweg 135, NL-6525 AJ Nijmegen, The Netherlands*
117 *University of Dallas, Irving, TX 75062-4736, USA*
118 *University of Florida, PO Box 118440 Gainesville, FL 32611-8440, USA*
119 *Tufts University, Medford, MA 02155, USA*
120 *Università degli Studi di Milano, Dipartimento di Fisica, I-20133 Milano, Italy*
121 *INFN sezione di Milano, via Celoria 16, 20133 Milano, Italy*
122 *University of Granada & CAFPE, Campus Fuentenueva (Edif. Mecenas), 18002 Granada, Spain*
123 *Boston University, Boston, MA 02215, USA*
124 *South Dakota State University, Brookings, SD 57007, USA*
125 *Indian Institute of Technology Hyderabad, Hyderabad, 502285, India*
126 *University of New Mexico, 1919 Lomas Blvd. N.E. Albuquerque, NM 87131, USA*
127 *Universidade Federal de Goias, Goiania, GO 74690-900, Brazil*
128 *Physical Research Laboratory, Ahmedabad 380 009, India*
129 *University of Minnesota Duluth, Duluth, MN 55812, USA*
130 *Daresbury Laboratory, Daresbury Warrington, Cheshire WA4 4AD, United Kingdom*
131 *University of Wisconsin Madison, Madison, WI 53706, USA*
132 *University of Warsaw, Faculty of Physics ul. Pasteura 5 02-093 Warsaw, Poland*
133 *Harvard University, 17 Oxford St. Cambridge, MA 02138, USA*
134 *K L University, K L E F, Green Fields, Guntur - 522 502, AP, India*
135 *Chung-Ang University, Dongjak-Gu, Seoul 06974, South Korea*
136 *York University, Physics and Astronomy Department, 4700 Keele St. Toronto M3J 1P3, Canada*
137 *High Energy Accelerator Research Organization (KEK), Ibaraki, 305-0801, Japan*
138 *Idaho State University, Department of Physics, Pocatello, ID 83209, USA*
139 *University of Texas at Austin, Austin, TX 78712, USA*
140 *Louisiana State University, Baton Rouge, LA 70803, USA*
141 *Yerevan Institute for Theoretical Physics and Modeling, Halabian Str. 34, Yerevan 0036, Armenia*
142 *Institut de Fìsica d'Altes Energies , Campus UAB, Facultat Ciències Nord, 08193 Bellaterra, Barcelona, Spain*
143 *Virginia Tech, Blacksburg, VA 24060, USA*

2020 JINST 15 T08008

144 *Universidade Federal do ABC, Av. dos Estados 5001, Santo André - SP, 09210-580 Brazil*
145 *National Institute of Technology, Kure College, Kure College, Hiroshima, 737-8506, Japan*
146 *Institute for Nuclear Research of the Russian Academy of Sciences, prospekt 60-letiya Oktyabrya 7a, Moscow 117312, Russia*
147 *University of California Berkeley, Berkeley, CA 94720, USA*
148 *Punjab Agricultural University, Department of Math. Stat. & Physics, Ludhiana 141004, India*
149 *Illinois Institute of Technology, Chicago, IL 60616, USA*
150 *Institute of Physics, Czech Academy of Sciences, Na Slovance 2, 182 21 Praha 8, Czech Republic*
151 *University of Jyvaskyla, P.O. Box 35, FI-40014, Finland*
152 *University of Notre Dame, Notre Dame, IN 46556, USA*
153 *University of California Santa Barbara, Santa Barbara, California 93106 USA*
154 *Laboratori Nazionali del Gran Sasso, I-67010 Assergi, AQ, Italy*
155 *Dakota State University, Madison, SD 57042, USA*
156 *Universidade Federal de São Carlos, Araras - SP, 13604-900, Brazil*
157 *University of Colorado Boulder, Boulder, CO 80309, USA*
158 *University of Puerto Rico, Mayaguez, 00681, USA*
159 *Rutgers University, Piscataway, NJ, 08854, USA*
160 *Jawaharlal Nehru University, School of Physical Sciences, New Delhi 110067, India*
161 *University of Athens, University Campus, Zografou GR 157 84, Greece*
162 *Università degli studi di Pavia, Istituto Nazionale di Fisica Nucleare Sezione di Pavia, I-27100 Pavia, Italy*
163 *Wichita State University, Physics Division, Wichita, KS 67260, USA*
164 *Centro de Investigacion y de Estudios Avanzados del IPN (Cinvestav), Mexico City*
165 *Pennsylvania State University, University Park, PA 16802, USA*
166 *California Institute of Technology, Pasadena, CA 91125, USA*
167 *University of Lucknow, Lucknow 226007, Uttar Pradesh, India*
168 *Iwate University, Morioka, Iwate 020-8551, Japan*
169 *University of Jammu, Physics Department, JAMMU-180006, India*
170 *University Grenoble Alpes, CNRS, Grenoble INP, LPSC-IN2P3, 38000 Grenoble, France*
171 *Gran Sasso Science Institute, Viale Francesco Crispi 7, L'Aquila, Italy*
172 *University of Arizona, 1118 E. Fourth Street Tucson, AZ 85721, USA*
173 *Jeonbuk National University, 414, Natural Science Building #5 Department of Physics 567 Baekjedaero, Deogjin-gu Jeonju, Jeonrabuk-do 54896*
174 *Central University of South Bihar, Department of Physics SH-7, Gaya Panchanpur Road, Gaya - 824236*
175 *Banaras Hindu University, Department of Physics, Varanasi - 221 005, India*
176 *Syracuse University, Syracuse, NY 13244, USA*
177 *Institute of Particle and Nuclear Physics of the Faculty of Mathematics and Physics of the Charles University in Prague, V Holešovičkách 747/2, 180 00 Praha 8-Libeň, Czech Republic*
178 *Texas A&M University (Corpus Christi), Corpus Christi, TX 78412, USA*
179 *Kavli Institute for the Physics and Mathematics of the Universe, Kashiwa, Chiba 277-8583, Japan*
180 *Universidade Federal de Alfenas, Poços de Caldas - MG, 37715-400, Brazil*
181 *H. Niewodniczański Institute of Nuclear Physics, Polish Academy of Sciences, Cracow, Poland*
182 *University of California Los Angeles, Los Angeles, CA 90095, USA*

2020 JINST 15 T08008